

---

# Dynamics of Bose-Einstein condensates in novel optical potentials

---

**Dynamik von Bose-Einstein-Kondensaten in neuartigen optischen Potentialen**

Dissertation approved by the Department of Physics of the Technische Universität Darmstadt in fulfillment of the requirements for the degree of Doctor of Natural Sciences (Dr. rer. nat.) by Johannes Küber, MSc from Frankfurt am Main

July 2014 – Darmstadt – D 17

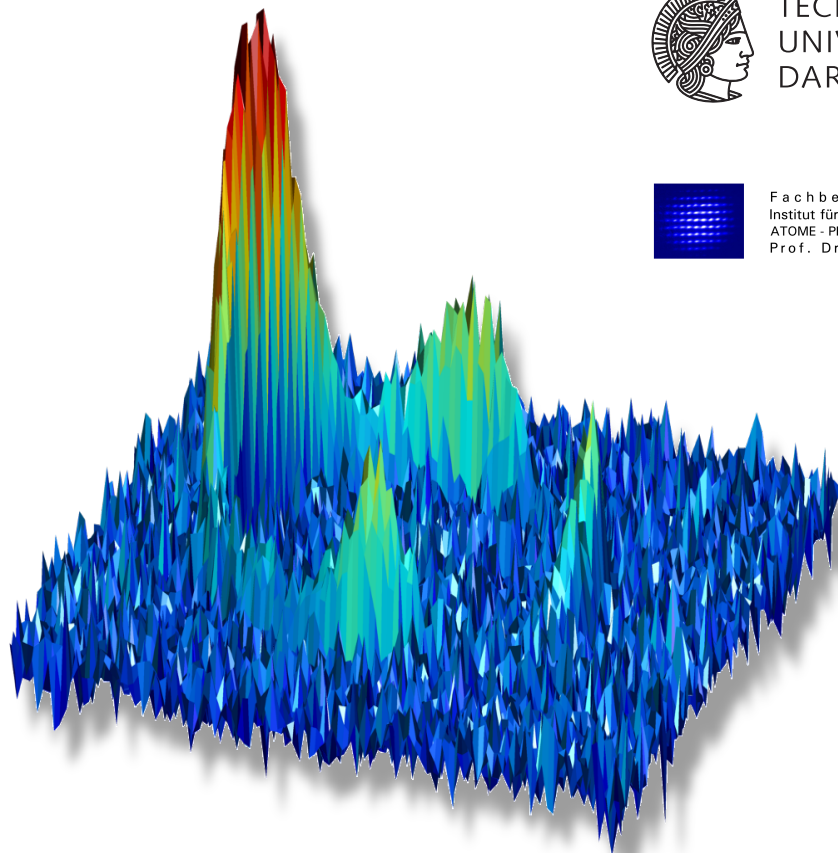
---



TECHNISCHE  
UNIVERSITÄT  
DARMSTADT



Fachbereich Physik  
Institut für Angewandte Physik  
ATOME - PHOTONEN - QUANTEN  
Prof. Dr. Gerhard Birkl





# Dynamics of Bose-Einstein condensates in novel optical potentials

Dissertation  
approved by the Department of Physics  
of the Technische Universität Darmstadt  
in fulfillment of the requirements for the degree of  
Doctor of Natural Sciences (Dr. rer. nat.)

by Johannes Küber, MSc  
from Frankfurt am Main

1st Referee: Prof. Dr. Gerhard Birkl  
2nd Referee: Prof. Dr. Thomas Walther

Submission date: 1. July 2014  
Examination date: 21. July 2014

Darmstadt 2014  
D 17



---

*From this day to the ending of the world,  
But we in it shall be remembered  
We few, we happy few, we band of brothers  
For he to-day that sheds his blood with me  
Shall be my brother*

Heinrich V, The Life of Henry the Fifth

---

---

Cover picture: A Bose-Einstein condensate loaded into a toroidal waveguide. After the loading process is complete it is split and accelerated. Multiple accelerated wave packets travel along a toroidal wave guide.

Bitte zitieren Sie dieses Dokument als:

URN: urn:nbn:de:tuda-tuprints-40377

URL: <http://tuprints.ulb.tu-darmstadt.de/4037>

Dieses Dokument wird bereitgestellt von tuprints,

E-Publishing-Service der TU Darmstadt

<http://tuprints.ulb.tu-darmstadt.de>

[tuprints@ulb.tu-darmstadt.de](mailto:tuprints@ulb.tu-darmstadt.de)



Die Veröffentlichung steht unter folgender Creative Commons Lizenz:

Namensnennung – Keine kommerzielle Nutzung – Keine Bearbeitung 2.0

Deutschland

<http://creativecommons.org/licenses/by-nc-nd/2.0/de/>

---

---

---

## Abstract

---

Matter wave interferometry offers a novel approach for high precision measurements, such as the determination of physical constants like the local gravity constant  $g$  or the fine-structure constant. Since its early demonstration, it has become an important tool in the fields of fundamental and applied physics. The present work covers the implementation of matter wave interferometers as well as the creation of novel guiding potentials for ultra-cold ensembles of atoms and Bose-Einstein condensates for this purpose. In addition, novel techniques for the manipulation of atoms with Bragg lattices are presented, serving as elements for interferometry.

The measurements in this work are performed with a Bose-Einstein condensate of 25000  $^{87}\text{Rb}$  atoms created in a crossed optical dipole trap. The crossed optical dipole trap is loaded from a magneto-optical trap and allows a measurement every 25 s.

This work introduces the novel technique of double Bragg diffraction as a tool for atom optics for the first time experimentally. The creation of beamsplitters and mirrors for advanced interferometric measurements is characterized. An in depth discussion on the momentum distribution of atomic clouds and its influence on double Bragg diffraction is given. Additionally experimental results for higher-order Bragg diffraction are explained and double Bragg diffraction is used to implement a full Ramsey-type interferometer.

A second central result of this work is the implementation of novel guiding structures for ultra-cold atoms. These structures are created with conical refraction, an effect that occurs when light is guided along one of the optical axis of a bi-axial crystal. The conical refraction crystal used to operate the novel trapping geometries is a  $\text{KGd}(\text{WO}_4)_2$  crystal that has been specifically cut orthogonal to one of the optical axis. Two regimes are discussed in detail: the creation of a toroidal matter wave guide and the implementation of a three-dimensional dark focus. Additional geometries accessible with conical refraction are introduced and possible applications are shown.

The first regime characterized in detail is the creation of a toroidal wave guide for ultra-cold atoms and Bose-Einstein condensates. With the aid of a lightsheet potential atoms are trapped in a quasi two-dimensional ring geometry. Inside of the geometry atoms are accelerated, decelerated and held for extended storage times of up to two seconds. First attempts for the implementation of a Mach-Zehnder-type interferometer in a toroidal trap are presented. The second regime shown is the creation of a three-dimensional dark focus that is used to trap atoms in a repulsive confinement of light. The parameters of the dark focus are investigated in detail. Future application of a two-dimensional array of dark foci is shown by demonstrating the respective light field.



---

---

## Zusammenfassung

---

Materiewelleninterferometrie bietet einen neuartigen Zugang zu Hochpräzisionsmessungen physikalischer Konstanten, wie beispielsweise die Messung der lokalen Erdbeschleunigung  $g$  oder der Feinstrukturkonstante. Seit ihrer ersten Demonstration hat sie sich zu einem wichtigen Werkzeug der Grundlagen- sowie der angewandten Physik entwickelt. Die vorliegende Arbeit beschäftigt sich mit der Konstruktion von Materiewelleninterferometern, sowie mit der Erzeugung neuartiger Potentiale für ultra-kalte Atome und Bose-Einstein-Kondensate für diesen Einsatzbereich. Ebenfalls werden neuartige Techniken für die Manipulation von Atomen mittels Bragg Gitter vorgestellt, welche ihre Anwendung in der Interferometrie finden.

Die atomoptischen Messungen in dieser Arbeit werden mit einem Bose-Einstein-Kondensat von 25000  $^{87}\text{Rb}$  Atomen durchgeführt. Dieses wird in einer gekreuzten Dipolfalle erzeugt, welche aus einer magnetooptischen Falle geladen wird. Der Experimentzyklus beträgt typischerweise 25 s.

Diese Arbeit führt erstmals Doppel-Bragg Beugung als experimentelle Technik der Atomoptik ein. Die Erzeugung von Strahlteilern sowie Spiegeln für Materiewellen für fortschrittliche interferometrische Messungen wird charakterisiert. Eine tiefgreifende Diskussion in Bezug auf die Impulsbreite von atomaren Ensembles und ihren Einfluss auf Doppel-Bragg Beugung wird geführt. Ebenfalls wird Doppel-Bragg Beugung höherer Ordnung sowie die experimentelle Umsetzung eines Ramsey-Interferometers mittels Doppel-Bragg Beugung gezeigt.

Ein zweites, zentrales Ergebnis dieser Arbeit ist die Erzeugung von neuartigen Wellenleitern für ultra-kalte Atome. Diese werden mit Hilfe konischer Refraktion erzeugt, ein Effekt welcher auftritt, wenn Licht entlang einer optischen Achse eines biaxialen Kristalls eingestrahlt wird. Zur Untersuchung der konischen Refraktion wird ein  $\text{KGd}(\text{WO}_4)_2$  Kristall eingesetzt. Zwei Parameterbereiche werden im Detail diskutiert: die Erzeugung eines toroidalen Materiewellenleiters sowie die Erzeugung eines dreidimensional dunklen Fokus. Zusätzliche, mittels konischer Refraktion realisierbare Geometrien, werden vorgestellt und ihre Anwendungsgebiete werden aufgezeigt.

Der erste Parameterbereich beschreibt die Erzeugung des toroidalen Wellenleiters für ultra-kalte Atome und Bose-Einstein-Kondensate. Mit Hilfe eines zusätzlichen Lichtteppichs wird ein quasi zweidimensionaler Einschluss erzeugt. In diesem können Atome beschleunigt, abgebremst und für bis zu zwei Sekunden gehalten werden. Erste Versuche zur Implementierung eines Mach-Zehnder Interferometers in einer kreisförmigen Falle werden präsentiert. Der zweite Parameterbereich beschreibt die Erzeugung eines dreidimensional dunklen Fokus. Dieser wird als repulsiver Einschluss genutzt und seine Eigenschaften werden im Detail diskutiert. Zusätzlich wird die zukünftige Anwendung in einer zweidimensionalen Registeranordnung experimentell vorgestellt, indem die dafür notwendigen Lichtfelder charakterisiert werden.



---

---

# Contents

<b>1</b>	<b>Introduction</b>	<b>1</b>
<b>2</b>	<b>Preparation and detection of ultra-cold atoms and Bose-Einstein condensates</b>	<b>5</b>
2.1	Optical dipole potentials . . . . .	5
2.1.1	Specific beam shapes . . . . .	7
2.2	Bose-Einstein condensates . . . . .	9
2.2.1	Non-interacting Bose-Einstein condensate . . . . .	9
2.2.2	Interacting Bose-Einstein condensate . . . . .	11
2.2.3	Expansion of Bose-Einstein condensates in trapped geometries . . . . .	12
2.3	The ATOMICS experiment . . . . .	15
2.3.1	Creation of ultra-cold atoms in a magneto-optical trap . . .	15
2.3.2	Creation of Bose-Einstein condensates . . . . .	16
2.3.3	Detection of cold atom ensembles . . . . .	17
<b>3</b>	<b>Bragg diffraction and double Bragg diffraction</b>	<b>21</b>
3.1	Bragg diffraction . . . . .	21
3.1.1	Spatially periodic optical potentials . . . . .	22
3.1.2	Method of averaging . . . . .	23
3.1.3	Time evolution of momentum states of Bragg diffracted atoms . . . . .	25
3.2	Double Bragg diffraction theory . . . . .	27
3.2.1	Rabi oscillations induced by Double Bragg diffraction . . .	28
3.2.2	Influences of a finite momentum distribution on double Bragg diffraction . . . . .	30
3.2.3	Influences of the lattice depth on double Bragg diffraction	33
3.2.4	Beamsplitter and mirror for atoms . . . . .	33
3.3	Experimental realization of double Bragg diffraction . . . . .	34
3.3.1	Experimental setup . . . . .	35
3.3.2	Observing double Bragg diffraction experimentally . . . . .	38
3.4	Higher-order double Bragg diffraction . . . . .	41
3.4.1	Second-order double Bragg diffraction . . . . .	41
3.4.2	Third-order double Bragg diffraction . . . . .	43
3.4.3	Quality of Bragg diffraction beamsplitters . . . . .	45

3.5	Influences of the BEC momentum distribution on double Bragg diffraction . . . . .	48
3.5.1	Fourier width of a Gaussian lattice pulse . . . . .	48
3.5.2	Bragg spectroscopy of a Bose-Einstein condensate . . . . .	50
3.5.3	Experimental realisation of long-pulse double Bragg diffraction . . . . .	53
3.5.4	Measuring the mean-field expansion of a BEC with double Bragg diffraction . . . . .	59
3.6	Other methods of coherent Beam splitting . . . . .	61
3.6.1	Three-frequency Bragg diffraction . . . . .	61
3.6.2	'Pendellösung' in a non-moving optical lattice . . . . .	62
3.6.3	Modifications to the experimental setup . . . . .	63
3.6.4	Comparison of different beam splitting configurations . . . . .	64
3.7	Matter wave interferometry with double Bragg diffraction . . . . .	67
3.7.1	Experimental procedure of a Ramsey-type interferometer . . . . .	68
3.7.2	Fringe period of interferometric measurements . . . . .	69
3.7.3	Analyses of spatially periodic density profiles . . . . .	71
3.7.4	Matter wave interferometry with double Bragg diffraction . . . . .	74
3.7.5	Interferometry with higher order double Bragg diffraction . . . . .	75
<b>4</b>	<b>Conical Refraction</b>	<b>81</b>
4.1	Birefringence . . . . .	81
4.2	Birefringence in bi-axial crystals . . . . .	82
4.3	Conical refraction . . . . .	84
4.3.1	Polarisation dependence of conical refraction light field . . . . .	85
4.3.2	Important parameters of conical refraction setups . . . . .	86
4.3.3	Intensity distribution of conical refraction . . . . .	87
4.4	Intensity distribution for varying $\rho_0$ . . . . .	88
4.4.1	Creation of a double ring structure with conical refraction . . . . .	90
4.4.2	Creation of a three-dimensional dark focus with conical refraction . . . . .	93
4.5	Additional intensity distributions created with conical refraction . . . . .	96
4.5.1	Lightsheet potential with conical refraction . . . . .	96
4.5.2	Single ring with central barrier . . . . .	97
4.5.3	Single ring in a double ring configuration . . . . .	98
<b>5</b>	<b>Toroidal waveguide for ultra-cold atoms and BECs</b>	<b>101</b>
5.1	Experimental realisation of ring potential . . . . .	101
5.1.1	Optical setup for the ring shaped potential . . . . .	102
5.1.2	Lightsheet potential . . . . .	104
5.2	Analysis of ring shaped density profiles . . . . .	106
5.3	Loading and expansion of a Bose-Einstein condensate . . . . .	111
5.3.1	Horizontal alignment of the conical refraction potential . . . . .	112



5.3.2	Adiabatic loading of the toroidal trapping potential . . . .	114
5.3.3	Vertical alignment of the conical refraction beam . . . . .	115
5.3.4	Properties of the potential in the focal plane . . . . .	118
5.3.5	Expansion of atomic ensembles in the ring potential . . . .	122
5.3.6	Lifetime of trapped atomic ensembles in the toroidal trap .	125
5.4	Transport of BEC in ring shaped trapping potentials . . . . .	130
5.4.1	Additions to the optical setup . . . . .	131
5.4.2	Accelerated atoms in a toroidal trapping geometry . . . .	132
5.4.3	Symmetric splitting of wave packets inside the toroidal potential . . . . .	140
5.4.4	Behaviour for long storage times . . . . .	142
5.5	Dynamic loading and release of atoms in ring shaped guiding structure . . . . .	144
5.5.1	Loading a moving wave packet into the ring potential . . .	145
5.5.2	Releasing atoms from the ring potential . . . . .	149
5.6	Matter wave interferometry in ring shaped dipole potentials . . .	152
5.6.1	Experimental implementation of interferometric mea- surements with Bragg diffraction . . . . .	153
5.6.2	Discussion on limiting factors for matter wave interfer- ometers in wave guides . . . . .	157
5.6.3	Consequences for future interferometric measurements . .	161

**6 Novel three dimensional dark focus trap 163**

6.1	Experimental realization of a three dimensional dark focus trap .	163
6.1.1	Experimental setup of a three dimensional dark focus beam	164
6.1.2	Intensity distribution along the beam path . . . . .	165
6.1.3	Properties of the focal plane . . . . .	171
6.2	Atom trapping in a three-dimensional dark focus . . . . .	174
6.2.1	Experimental alignment . . . . .	174
6.2.2	Vertical alignment and trapping of ultra-cold atoms . . . .	177
6.2.3	Loading of BECs into the dark focus potential . . . . .	181
6.2.4	Lifetime of atoms in the dark focus trap . . . . .	181
6.2.5	Trapping frequencies of the dark focus potential . . . . .	184
6.3	Two dimensional array of dark-foci . . . . .	185
6.3.1	Two-dimensional lens arrays . . . . .	186
6.3.2	Experimental realisation of a two-dimensional array of dark foci . . . . .	186
6.3.3	Experimental implementation of a two-dimensional array of dark foci . . . . .	190
6.3.4	Comparison of central traps and off-centre traps . . . . .	191
6.3.5	Towards two-dimensional registers of atoms traps with conical refraction . . . . .	195

---

<b>7 Summary and Outlook</b>	<b>197</b>
<b>Appendix</b>	<b>201</b>
<b>A Rb Data</b>	<b>203</b>
A.1 $^{87}\text{Rb}$ level scheme . . . . .	203
A.2 $^{87}\text{Rb}$ properties . . . . .	204
A.3 $^{87}\text{Rb}$ in optical lattices . . . . .	204
<b>B ATOMICS Experiment</b>	<b>205</b>
B.1 Lightsheet properties . . . . .	205
B.2 Double ring potential properties . . . . .	206
B.3 Dark focus beam properties . . . . .	207
<b>C Conical Refraction</b>	<b>209</b>
C.1 Overview on conical refraction crystals . . . . .	209
<b>D Computer-operated laboratory monitoring system</b>	<b>211</b>
D.1 Hardware . . . . .	211
D.2 Software . . . . .	212
D.2.1 Setup of a new monitoring system . . . . .	212
D.2.2 Overview of the installed systems . . . . .	214
D.3 Export data via command line . . . . .	214
D.4 First experimental observations . . . . .	215
<b>Bibliography</b>	<b>217</b>
<b>Publications</b>	<b>235</b>

---

# 1 Introduction

Interferometric measurements with light waves are one of the most well-known physical measurement methods. By exploiting the coherence of photons in depth, new knowledge on a multitude of different phenomena is gained. Interferometric experiments have shown to be one of the most sensitive measurement methods. For example Michelson-Fabry-Perot interferometers are used to measure gravitational waves at the Laser Interferometer Gravitational-Wave Observatory (LIGO) [1]. Also optical coherence tomography (OCT) is used in clinical environments to image the retina and to gain insight on disease patterns [2]. Another example, the famously failed experiment to show that electromagnetic fields propagate in a medium called ether, by A. Michelson and E. Morley in 1887, is a well known example for a measurement exploiting the interference of light waves [3]. The ongoing improvement of the precision of these measurements spawned the field of matter wave interferometry.

Since the predictions of the wave-like behaviour of matter by L. de Broglies in 1924 [4] and the experimental proof by C. Davisson and L. Germer, the focus for high precision interferometric measurements extended towards massive particles like atoms, electrons, or neutrons [5]. The wave nature of matter showed scattering of electrons in a single nickel crystal [6] in the same way as X-rays are scattered by crystals [7]. Due to the shorter wavelength of matter waves, the expected precision of interferometric measurements is predicted to be higher. Matter wave interferometers have been successfully used to measure the earth's gravitational force [8–11] or the fine structure constant [12, 13] with high precision. They also serve as a tool for measurements in micro-gravitational environments [14–16]. A reliable source for coherent atoms is a key point for matter wave interferometry.

Bose-Einstein condensates, firstly predicted in 1924 by S.N. Bose and A. Einstein [17–19], offer a mesoscopic number of identical particles with the ability to interfere, due to their large coherence length. These properties make Bose-Einstein condensates ideal for interferometric measurements. 70 years after the initial discussion, the first ever Bose-Einstein condensate could be produced experimentally in 1995 [20, 21] in a magnetic trap. For their work, E.A. Cornell, W. Ketterle, and C.E. Wieman received the Noble Prize in Physics in 2001. The experimental success of the creation of a BEC was preceded by a long series of experimental breakthroughs in the creation of ultra-cold atoms. Most noticeable is the technique of laser-cooling [22] and the first magneto-optical trap as a source for ultra-cold atoms [23–25], work for which W.D. Phillips, S. Chu, and C. Cohen-Tannoudji have been awarded with the Nobel Prize in Physics in

---

1997. In order to provide a fast and reliable process for the creation of condensed atoms a multitude of novel techniques exists.

Supplementary to the creation of Bose-Einstein condensates in magnetic traps an additional experimental method for the creation of ultra-cold atoms has been developed: Optical dipole potentials exploit the electric dipole interaction of atoms with far-detuned light to create attractive or repulsive potentials [26]. By lowering the trap depth, an efficient evaporation mechanism is found that is used to cool atoms to quantum degeneracy [27]. In 2001 a first all-optical Bose-Einstein condensate could be demonstrated in a crossed optical dipole trap with rubidium atoms [28]. The simple beam shaping mechanism of dipole potentials with standard optical elements, such as lenses and mirrors, offers high flexibility and adaptability in the creation of novel potential shapes and structures. These structures are a valuable tool to store and guide atoms for advanced interferometric measurements. Developing novel types of trapping geometries enables the usage of experiments impossible until now.

An important tool for the creation of exotic and unique beam shapes in this work is conical refraction. Since its prediction in 1832 by Hamilton [29] and the soon after experimental observation by Lloyd in 1833 [30], conical refraction has been a phenomenon of constant experimental and theoretical research. Only after its theoretical discussion by A.M. Belskii and A.P. Khapalyuk [31] in 1978 and its reformulation by A.M. Belskii and M.A. Stepanov [32,33] in 1999, a full theoretical description of the phenomenon is possible. The rotationally symmetric, cone shaped light field formed inside a bi-axial crystal has recently been discovered as a tool for atom optics and solid state physics [34–36].

In addition to the experimental creation of optical potentials for atom optics and matter wave interferometry, beamsplitters and mirrors for atoms are implemented, similar to interferometers with light waves. For ultra-cold atoms and Bose-Einstein condensates optical lattices [37], created by standing light waves, have shown to be a great tool for atom manipulation [38, 39]. They offer the possibility to accelerate, decelerate and coherently split atomic ensembles and were first used experimentally for matter wave interferometry in 1991 [40].

The present work is devoted to the investigation of the dynamics of Bose-Einstein condensates in novel dipole potentials. The long term goal of this work is the creation of compact and scalable tools for atom optics, interferometers and quantum information processing. This work has been carried out at the *ATOMICS* experiment of the *Atome-Photonen-Quanten* group at the Institute of Applied Physics at the Technische Universität Darmstadt. The acronym *ATOMICS* stands for 'ATom Optics with MICRo Structures'.

In addition to this introduction, this work is divided into six chapters:

**Chapter 2** introduces the *ATOMICS* experiment and the preceding work that leads to the experiments in this work. It will be shown how the efficient cre-

---

ation of all-optical Bose-Einstein condensates is carried out and characteristics of the experimental setup are discussed. In addition basic properties of optical potentials and Bose-Einstein condensates are given. Especially, the dynamics of interacting ensembles of atoms in trapped geometries are investigated.

**Chapter 3** is dedicated to the discussion of double Bragg diffraction as a novel tool for atom optics and atom interferometry. A discussion on the theoretical description of Bragg diffraction and double Bragg diffraction will be given. Subsequently, the experimental demonstration of double Bragg diffraction will be shown for the first time. The following sections will identify important experimental parameters that define the applicability of double Bragg diffraction. In addition, higher-order Bragg diffraction will be implemented and the quality of double Bragg diffraction as a beamsplitter and mirror is conducted. Finally, a full interferometer sequence using double Bragg diffraction will be shown. In particular, differences of double Bragg diffraction and Bragg diffraction for interferometric applications will be discussed.

**Chapter 4** gives an introduction to conical refraction, a phenomenon occurring in bi-axial birefringent crystals. After a short summary on birefringence in uni-axial crystals the theory describing conical refraction will be presented. The discussion is led to different regimes of conical refraction structures. Two important regimes, the double ring structure with the Poggendorff dark ring and the three-dimensional dark focus, are explained in detail. Special attention is given to the applicability of these potentials towards trapping and guiding of ultra-cold atoms in these structures. Furthermore a discussion on additional optical potentials realizable with conical refraction is given.

**Chapter 5** is devoted to the experimental implementation of toroidal trapping potentials with conical refraction. The creation of toroidal wave guides with conical refraction and their properties are explained in detail and verified experimentally. The toroidal wave guide is used as a storage potential for moving ensembles of ultra-cold atoms and a scheme for dynamically loading the ring shaped potential is demonstrated. The discussion is followed by first results on an experimental implementation of a Mach-Zehnder like interferometer in the toroidal wave guide. Experimental problems impeding the interferometer will be shown and a possible outlook on future improvements will be given.

**Chapter 6** presents the first ever implementation of a three-dimensional dark focus created with conical refraction as a trap for ultra-cold atoms and BECs. In conjunction with the experimental implementation of the potential, important trapping parameters are characterized. Supplementary an experimental demonstration will be shown, which illustrates the scalability of the dark focus structure. An implementation of the optical configuration a two dimensional register of dark foci is performed and its use for quantum information processing is discussed.

**Chapter 7** summarizes the experimental insight gained in this work and gives an outlook on future developments and improvements of the experiment.



---

## 2 Preparation and detection of ultra-cold atoms and Bose-Einstein condensates

After the first ever realization of Bose-Einstein condensation of an atomic vapour [41, 42] in a magnetic trap additional methods for the creation of BECs emerged. Even though magnetic traps are most frequently used to create BECs of up to  $120 \times 10^6$  atoms [43], the use of far detuned optical dipole potentials has shown to be advantageous in certain situations. On the one hand atoms without magnetic moment are trappable and on the other hand, in contrast to magnetic traps, optical traps are capable of trapping atoms regardless of which magnetic state the atoms have [27]. In addition optical dipole potentials generally feature smaller experimental setups and do not need huge magnetic coils to create sufficient trapping potentials. The implementation of optical dipole potentials peaked with the first ever all-optical BECs created in 2001 [28].

Since 2008 the group Atome-Photonen-Quanten at the Technische Universität Darmstadt is capable of producing all-optical BECs [44, 45]. The chosen wavelength of 1070 nm enables the use of commercially available optics. In addition to the implemented scheme at the ATOMICS experiment additional techniques emerged to efficiently create BECs with optical potentials [46–49]. All of these implementations aim to reduce the impact of reduced trapping frequencies [50] in all-optical configurations during the evaporation process, which allows for faster evaporation.

This chapter will introduce optical dipole potentials used to create ensembles of ultra-cold atoms and BECs (see Sec. 2.1). In addition basic properties of Bose-Einstein condensates will be explained in Sec. 2.2. The chapter closes with the explanation of the experimental setup used at the ATOMICS experiment for the creation of ultra-cold atoms and BECs (see Sec. 2.3).

---

### 2.1 Optical dipole potentials

---

The interaction of atoms and light is mainly dependent on the frequency of the incident light  $\omega$  and the transitions of the atom species. The rate at which

photons resonantly excite a transition with frequency  $\omega_0$  is given by the spontaneous scattering rate  $\Gamma_{\text{SC}}$ :

$$\Gamma_{\text{SC}}(\vec{r}) = -\frac{3\pi c^2 \Gamma}{2\hbar \omega_0^3} \left( \frac{\omega}{\omega_0^3} \right)^3 \left( \frac{1}{\omega_0 - \omega} + \frac{1}{\omega_0 + \omega} \right)^2 I(\vec{r}) \quad (2.1)$$

where  $\Gamma$  is the decay rate of the transition, and  $I(\vec{r})$  is the intensity of the incident light at the position  $\vec{r}$ . Scattering of photons introduces heating, which is not desired in an experimental environment of ultra-cold atoms. Especially interferometers suffer from spontaneous scattering as they are a main contributor to decoherence, and therefore the loss of contrast.

Introducing a detuning  $\Delta = \omega - \omega_0$  reduces the scattering rate and gives rise to an additional phenomenon. Detuned light fields produce conservative potentials that can be used to store or guide atoms. Depending on the detuning  $\Delta$  an energy shift  $\Delta E$  is introduced that creates attractive or repulsive potentials, which are directly dependent on the intensity  $I(\vec{r})$ . The energy shift can be calculated by perturbation theory and is given by [26]:

$$\Delta E_i(\vec{r}) = \frac{3}{2} \pi c^2 \times I(\vec{r}) \sum_{i \neq j} \frac{\Gamma_{ij} c_{ij}^2}{\omega_{0,ij}^3 \Delta_{ij}}. \quad (2.2)$$

The energy shift  $\Delta E_i$  of each state  $i$  is given by the sum over all other states  $j$ .  $\Gamma_{ij}$  gives the decay rate of the transition and  $\omega_{0,ij}$  is frequency.  $I(\vec{r})$  gives the local intensity and  $c$  denotes the speed of light. The frequency detuning  $\Delta_{ij} = \omega - \omega_{ij}$  defines the detuning with respect to the transition  $j$ . The coupling strength is given by the Glebsch-Gordon coefficients  $c_{ij} = \langle e_i | \hat{\mu} | e_j \rangle / \|\mu\|$  and is listed in [51, 52].

The used isotope in this work of  $^{87}\text{Rb}$  features a fine-splitting of the excited P state. The two transitions  $D_1$  and  $D_2$  of feature wavelength of  $\lambda_{D_1} = 794.987$  nm and  $\lambda_{D_2} = 780.241$  nm. For  $^{87}\text{Rb}$  the shift of the states of the atomic transitions is then given by:

$$\begin{aligned} U_{\text{dip}}(\vec{r}) &= -\frac{\pi c^2 \Gamma_{D_2}}{2\omega_{D_2}^3} \left( \frac{2}{\omega_{D_2} + \omega} - \frac{2}{\omega_{D_2} - \omega} \right) I(\vec{r}) \\ &\quad - \frac{\pi c^2 \Gamma_{D_1}}{2\omega_{D_1}^3} \left( \frac{1}{\omega_{D_1} + \omega} - \frac{1}{\omega_{D_1} - \omega} \right) I(\vec{r}). \quad (2.3) \\ U_{\text{dip}}(\vec{r}) &= -\hat{U}_{\text{Rb}} I(\vec{r}) \end{aligned}$$

The values for Eq. 2.3 are summarized in App. A or can be taken from [52]. The values of  $\hat{U}_{\text{Rb}}$  used at the ATOMICS experiment are composed in Table 2.1.

Wavelength[nm]	Laser system	$\hat{U}_{Rb} [m^2s]$
782.5	Lightsheet laser	$9.985 \times 10^{-35}$
792.5	Ring and dark focus laser	$3.101 \times 10^{-35}$
1070	Crossed dipole trap laser	$2.076 \times 10^{-36}$

**Table 2.1:** Compilation of  $\hat{U}_{Rb}$  for different laser system used at the ATOMICS experiment.

### 2.1.1 Specific beam shapes

A Gaussian beam is the fundamental transverse, or  $TEM_{00}$  mode of an optical resonator. Gaussian beam profiles are typically emitted from lasers and widely used for atom optic experiments, such as dipole traps [27] and optical lattices [53]. Focussed Gaussian beams used for atom trapping exhibit basic properties which will be discussed in this section.

#### Focussed gaussian beam

The intensity profile of a Gaussian beam propagating along the  $z$ -axis is given by:

$$I(r, z) = \frac{2P}{\pi w(z)^2} e^{-\frac{2r^2}{w(z)^2}}, \quad (2.4)$$

where  $P$  is the input power,  $w(z)$  the waist at position  $z$ , and  $z_R$  the Rayleigh range of the beam. The Rayleigh range gives the distance from  $z = 0$ , the focal point, where the waist is increased by a factor of  $\sqrt{2}w_0$ . The Rayleigh range is defined as:

$$z_R = \frac{\pi w_0^2}{\lambda}, \quad (2.5)$$

with  $\lambda$  being the wavelength of the incident beam. The waist  $w_0$  of a focussed laser beam in the focal plane is calculated with:

$$w_0 = \frac{\lambda f}{\pi w_i}, \quad (2.6)$$

where  $f$  is the focal length of the lens and  $w_i$  is the incident beam waist. The evolution of the waist along the  $z$  axis is given by:

$$w(z) = w_0 \sqrt{1 + \left(\frac{\lambda z}{\pi w_0^2}\right)^2} = w_0 \sqrt{1 + \left(\frac{z}{z_R}\right)^2}. \quad (2.7)$$

Eq. (2.4) put in Eq. (2.3) gives the possibility to calculate the trap depth of a red detuned focussed Gaussian beam. A blue detuned beam would create a equivalent repulsive potential. An attractive potential near the focal plane be described as harmonic and the trapping frequencies in the radial direction  $\omega_r$  and along the beam propagation  $\omega_z$  are given by:

$$\omega_r = \sqrt{\frac{8P\hat{U}_{Rb}}{\pi m w_0^4}}, \quad (2.8)$$

$$\omega_z = \sqrt{\frac{4P\hat{U}_{Rb}}{\pi m w_0^2 z_R^2}}. \quad (2.9)$$

In the ATOMICS experiment Gaussian beams used for the creation of Bose-Einstein condensates feature a beam waist of  $w_0 \approx 45 \mu\text{m}$  and don't feature sufficient trapping frequencies in the longitudinal direction to efficiently evaporate atoms. The creation of BECs is therefore done in crossed optical dipole beams.

---

### Crossed focussed gaussian beams

---

The combination of two crossed focussed Gaussian beams is used to create an efficient confinement in all three dimensions. The achieved confinement is sufficient to evaporate atoms and to achieve Bose-Einstein condensation. The two beams propagate along the  $x$  and the  $y$  direction and feature the waist  $w_1(x)$  and  $w_2(y)$  respectively. The intensity distribution is given by:

$$I(r, z) = \frac{2P_1}{\pi w_1(x)^2} e^{-\frac{2(y^2+z^2)}{w_1(x)^2}} + \frac{2P_2}{\pi w_2(y)^2} e^{-\frac{2(x^2+z^2)}{w_2(y)^2}} \quad (2.10)$$

with  $P_1$  and  $P_2$  being the optical power of the two beams. The trapping frequencies of the beams are defined as:

$$\omega_x = \sqrt{\frac{4\hat{U}_{Rb}}{\pi m} \left( \frac{2P_2}{w_{0,2}^4} + \frac{P_1}{w_{0,1}^2 z_{R,1}^2} \right)}, \quad (2.11)$$

$$\omega_y = \sqrt{\frac{4\hat{U}_{Rb}}{\pi m} \left( \frac{2P_1}{w_{0,1}^4} + \frac{P_2}{w_{0,2}^2 z_{R,2}^2} \right)}, \quad (2.12)$$

$$\omega_z = \sqrt{\frac{8\hat{U}_{Rb}}{\pi m} \left( \frac{P_1}{w_{0,1}^4} + \frac{P_2}{w_{0,2}^4} \right)}, \quad (2.13)$$

with  $z_{R,1}$  and  $z_{R,2}$  being the Rayleigh ranges of each of the beams.

---

## Elliptically focussed gaussian beam

---

An elliptical Gaussian beam is produced with lenses that feature different focal length  $f_x$  and  $f_y$ . Elliptical lenses are used to create lightsheet potentials with (see Sec. 5.1.2) and without conical refraction (see Sec. 4.5.1). The intensity distribution of an elliptical focussed Gaussian beam propagating in  $z$ -direction is:

$$I(x, y, z) = \frac{2P}{\pi w_x(z) w_y(z)} e^{-\left(\frac{x^2}{w_x(z)^2} + \frac{y^2}{w_y(z)^2}\right)}, \quad (2.14)$$

where  $w_x(z)$  and  $w_y(z)$  are the waists and  $P$  the input power of the beam. The trapping frequencies are given by:

$$\omega_x = \sqrt{\frac{4P\hat{U}_{Rb}}{\pi m w_{0,x}^3 w_{0,y}}}, \quad (2.15)$$

$$\omega_y = \sqrt{\frac{4P\hat{U}_{Rb}}{\pi m w_{0,x} w_{0,y}^3}}, \quad (2.16)$$

$$\omega_z = \sqrt{\frac{2P\hat{U}_{Rb}}{\pi m w_{0,x} w_{0,y}} \left( \frac{1}{z_{R,x}^2} + \frac{1}{z_{R,y}^2} \right)}, \quad (2.17)$$

where  $P$  denotes the input beam power and  $z_{R,x}$  and  $z_{R,y}$  are the respective Rayleigh ranges.

---

## 2.2 Bose-Einstein condensates

---

This section gives an introduction to Bose-Einstein condensates as well as important parameters used throughout this work. An in depth discussion on Bose-Einstein condensates can be found in [54–56].

---

### 2.2.1 Non-interacting Bose-Einstein condensate

---

The occupation number  $\bar{n}(\epsilon)$  of a state with energy  $\epsilon$  of non-interacting bosons in thermal equilibrium is given by the grand canonical ensemble [57]:

$$\bar{n}(\epsilon) = \frac{1}{e^{\beta(\epsilon-\mu)} - 1}, \quad (2.18)$$

where  $\beta = 1/k_B T$ , with the temperature  $T$  and  $k_B$  the Boltzmann constant.  $\mu = \delta E / \delta N$  is the chemical potential, which gives the change in energy for

varying atom numbers  $N$ . As temperature declines the chemical potential rises up to the energie of the ground state  $\epsilon_0$ . Higher chemical potentials are not possible, because these would yield negative occupation numbers.

The total number of atoms  $N$  is defined as sum over the atoms in the ground state  $N_0$  and and all higher states  $N_T$ :

$$N = N_0 + N_T = \bar{n}_{\epsilon_0} + \sum_{i \neq 0} \bar{n}_{\epsilon_i}. \quad (2.19)$$

The occupation number  $N_T$  for low temperatures gives a critical point where  $N_T < N$  and  $N_0 > 0$ .  $N_T$  is given by:

$$N_T = \frac{V}{\lambda_{DB}^3} g_{3/2}(e^{\beta\mu}), \quad (2.20)$$

where  $V$  is the volume and  $g_{3/2}$  is defined as  $g_\eta(z) = \sum_{t=1}^{\infty} z^t / t^\eta$ .  $\lambda_{DB}$  is the thermal de Broglie wavelength:

$$\lambda_{DB} = \sqrt{\frac{2\pi\hbar^2}{mk_B T}}, \quad (2.21)$$

with  $m$  the mass, and  $\hbar = h/2\pi$  the Dirac constant. The temperature dependent occupation of  $N_0$  and  $N_T$  yields a critical temperature for which  $N_0 > 0$  and is given by:

$$k_B T_C = \frac{2\pi\hbar^2}{m} \left( \frac{n}{g_{3/2}(1)} \right)^{2/3}. \quad (2.22)$$

The temperature dependant occupation of the ground state in terms of the critical temperature  $T_C$  is then defined as:

$$N_0(T) = N \times \left( 1 - \frac{T}{T_C}^\alpha \right), \quad (2.23)$$

with  $\alpha = 3/2$  in a three-dimensional box potential and  $\alpha = 3$  in a three-dimensional harmonic potential. For temperatures below  $T_C$  a macroscopic occupation of  $N_0$  observable with  $N_0 = N$  at zero temperature.

With the definition  $\rho_{psd} = n\lambda_{DB}^3$ , the phase space density, a criterion is found for which Bose-Einstein condensation is observable:

$$\rho_{psd} = n\lambda_{DB}^3 > g_{3/2}(1) = 2.612 \quad (2.24)$$

The wave function of a non-interacting Bose-Einstein condensate is given as the product of the single particle wave function  $\varphi_0(\vec{r}_i)$ :

$$\Phi(\vec{r}_1, \dots, \vec{r}_N) = \prod_{i=1}^N \varphi_0(\vec{r}_i). \quad (2.25)$$

This results in a density  $n(\vec{r})$  of:

$$n(\vec{r}) = \left| \prod_{i=1}^N \varphi_0(\vec{r}_i) \right|^2 = N \left| \varphi_0(\vec{r}_i) \right|^2, \quad (2.26)$$

which is the scaled density of a single particle wave function, which, in a harmonic potential, is defined as:

$$\varphi_0(\vec{r}) = \left( \frac{1}{\pi a_{ho}} \right)^{\frac{3}{4}} e^{\left[ -\frac{m}{2\hbar} (\omega_x x^2 + \omega_y y^2 + \omega_z z^2) \right]}, \quad (2.27)$$

where  $a_{ho}$  is the oscillator length:

$$a_{ho} = \sqrt{\frac{\hbar}{m\bar{\omega}}}, \quad (2.28)$$

a characteristic length that gives the spatial expansion of the non-interacting condensate in a harmonic potential.  $\bar{\omega}$  gives the mean trapping frequency of the harmonic potential and is given by:

$$\bar{\omega} = \left( \omega_x \omega_y \omega_z \right)^{\frac{1}{3}}. \quad (2.29)$$

---

## 2.2.2 Interacting Bose-Einstein condensate

---

Up until now interaction of atoms has been neglected. For a complete discussion the interaction of atoms has to be taken into account. In a dilute vapour, the interaction can be expressed by a simple contact-interaction of the form  $V(\vec{r}' - \vec{r}) = g\delta(\vec{r}' - \vec{r})$ , where the constant  $g$  is given by  $g = 4\pi\hbar a/m$ . The s-wave scattering length  $a$  is defined by the interacting particles.

The resulting system can be described with a classical field  $\Psi(r, t)$  for very low temperatures and is given by the Gross-Pitaevskii equation:

$$i\hbar \frac{\partial}{\partial t} \Psi(\vec{r}, t) = \left( -\frac{\hbar^2 \nabla^2}{2m} + V_{\text{ext}}(\vec{r}, t) + g \left| \Psi(\vec{r}, t) \right|^2 \right) \Psi(\vec{r}, t), \quad (2.30)$$

where  $V_{\text{ext}}(\vec{r}, t)$  describes the external potential. The interaction of the system takes into account the mean interaction of all particles, thus the term mean-field emerged to describe the interaction. For non-interacting particles the system collapses to the Schrödinger equation. In order to provide normalized solution  $N = \int d\vec{r} |\Psi(\vec{r}, t)|^2$  has to be fulfilled.

Stationary solutions of simplify the description and rule out the time-dependence. The resulting time-independent Gross-Pitaevskii equation is given by:

$$\left( -\frac{\hbar^2 \nabla^2}{2m} + V_{\text{ext}}(\vec{r}) - \mu + g |\Psi(\vec{r})|^2 \right) \Psi(\vec{r}) = 0. \quad (2.31)$$

For repulsive interaction and a large particle numbers the kinetic energy of the particles is negligible. This approximation is known as the Thomas-Fermi limit. Eq. (2.31) can be reduced to:

$$\left( V_{\text{ext}}(\vec{r}) + g |\Psi(\vec{r})|^2 \right) \Psi(\vec{r}) = \mu \Psi(\vec{r}), \quad (2.32)$$

and a solution for  $V_{\text{ext}}(\vec{r}) < \mu$  is:

$$|\Psi(\vec{r})|^2 = n(\vec{r}) = \frac{\mu - V_{\text{ext}}(\vec{r})}{g}. \quad (2.33)$$

The obtained density distribution has the inverse shape of the external potential and is filled up to the energie of the chemical potential. For locations with  $V_{\text{ext}}(\vec{r}) > \mu$  the obtained density is  $n(\vec{r}) = 0$ . In harmonic potentials, as used in this work, the radius  $R_{\text{TF}, i}$  in the spatial dimensions  $i$  of the density distribution is called Thomas-Fermi radius and is defined as:

$$R_{\text{TF}, i} = \sqrt{\frac{2\mu}{m\omega_i}} = \left( \frac{15\hbar N \bar{\omega}^3}{m^2 \omega_i^5} \right)^{\frac{1}{5}}, \quad (2.34)$$

Experimental realizations of condensed atoms clouds in all-optical potentials typically feature a bimodal distribution. The bimodal distribution consists of a thermal cloud of atoms, which is not condensed, and a condensed cloud of atoms. The fraction of condensed atoms is given by the condensate fraction  $N_0/N$ . The resulting density distribution shows the quadratic density given by the harmonic external potential on top of the cloud of thermal atoms.

---

### 2.2.3 Expansion of Bose-Einstein condensates in trapped geometries

---

A cloud of condensed atoms in a harmonic trap will keep its shape as long as the trapping potential itself is kept harmonic [58–60]. This is also true if atoms are loaded from one potential into another as long as the loading itself is adiabatic (see Sec. 5.3.2). The temporal evolution of the cloud can then be described by a linear scaling law:

$$R_i(t) = \lambda_i(t) R_i(0). \quad (2.35)$$

The size  $R_i$  of a condensate at different times  $t$  is dependent on the initial size  $R_i(0)$  and the scaling parameter  $\lambda_i(t)$ . The three dimensions  $i$  are independent of each other. The scaling parameter  $\lambda_i(t)$  fulfils:

$$\ddot{\lambda}_i(t) = \frac{\omega_i(0)^2}{\lambda_i(t)\lambda_1(t)\lambda_2(t)\lambda_3(t)} - \omega_i^2(t)\lambda_i(t), \quad (2.36)$$

where  $\omega_i(t)$  (see Sec. 2.1) are the trapping frequencies of the harmonic potential. In general  $R_i$  can be chosen arbitrarily as a distance from the centre of mass of the atomic cloud. The Thomas-Fermi radius (see Eq. (2.34)) is a meaningful choice to describe the evolution of a BEC. The velocity field of the the cloud is given by [58]:

$$v_i(\vec{r}, t) = \frac{\hbar}{m} \nabla \phi(\vec{r}, t). \quad (2.37)$$

In general the time evolution of the velocity field and the phase profile  $\phi(\vec{r}, t)$  of a condensate is given by [60]:

$$v_i(\vec{r}, t) = \frac{\hbar}{m} \nabla \phi(\vec{r}, t). \quad (2.38)$$

Since the evolution of the phase profile of the condensate follows the evolution of the density profile [58] a valid ansatz for the phase profile is:

$$\phi(\vec{r}, t) = \frac{\alpha_i(t)}{2} x_i^2 + \beta_i(t) x_i. \quad (2.39)$$

By using Eq. (2.37) and Eq. (2.38) a solution for  $\alpha(t)$  can be found. For simplicity this is given in a single dimension  $x$ :

$$\alpha(t) = \frac{m \dot{\lambda}_x(t)}{\hbar \lambda_x(t)}. \quad (2.40)$$

Fig. 2.1 shows the solution of Eq. (2.36) for the initial values of  $\lambda_x = \lambda_y = \lambda_z = 1$  and  $\dot{\lambda}_x = \dot{\lambda}_y = \dot{\lambda}_z = 0$ . The trapping frequencies are chose to be  $\omega_x = \omega_y = \omega$ ,  $\omega_z = (\omega_x^2 + \omega_y^2)^{1/2}$ ,  $\omega_x(t) = 2\pi \times 1 \text{ Hz}$ , and  $\omega_y(t) = \omega_z(t) = 2 \times \omega$ . Where  $\omega$  is given three different initial values. The system represents the time evolution of a BEC loaded from the crossed optical dipole trap into a quasi-one-dimensional wave guide. The solution in the guided direction is shown where experimental procedures like guiding or interferometric measurements are performed. After an initial mean-field expansion a ballistic expansion dominates. Mean-field typically stops after 5 ms for experimental values obtained at the ATOMICS experiment. This can easily be observed by the velocity  $\dot{\lambda}_x$  that asymptotically converges a fixed value. The value itself is dependent on the trapping parameters and the initial trap after the loading process.

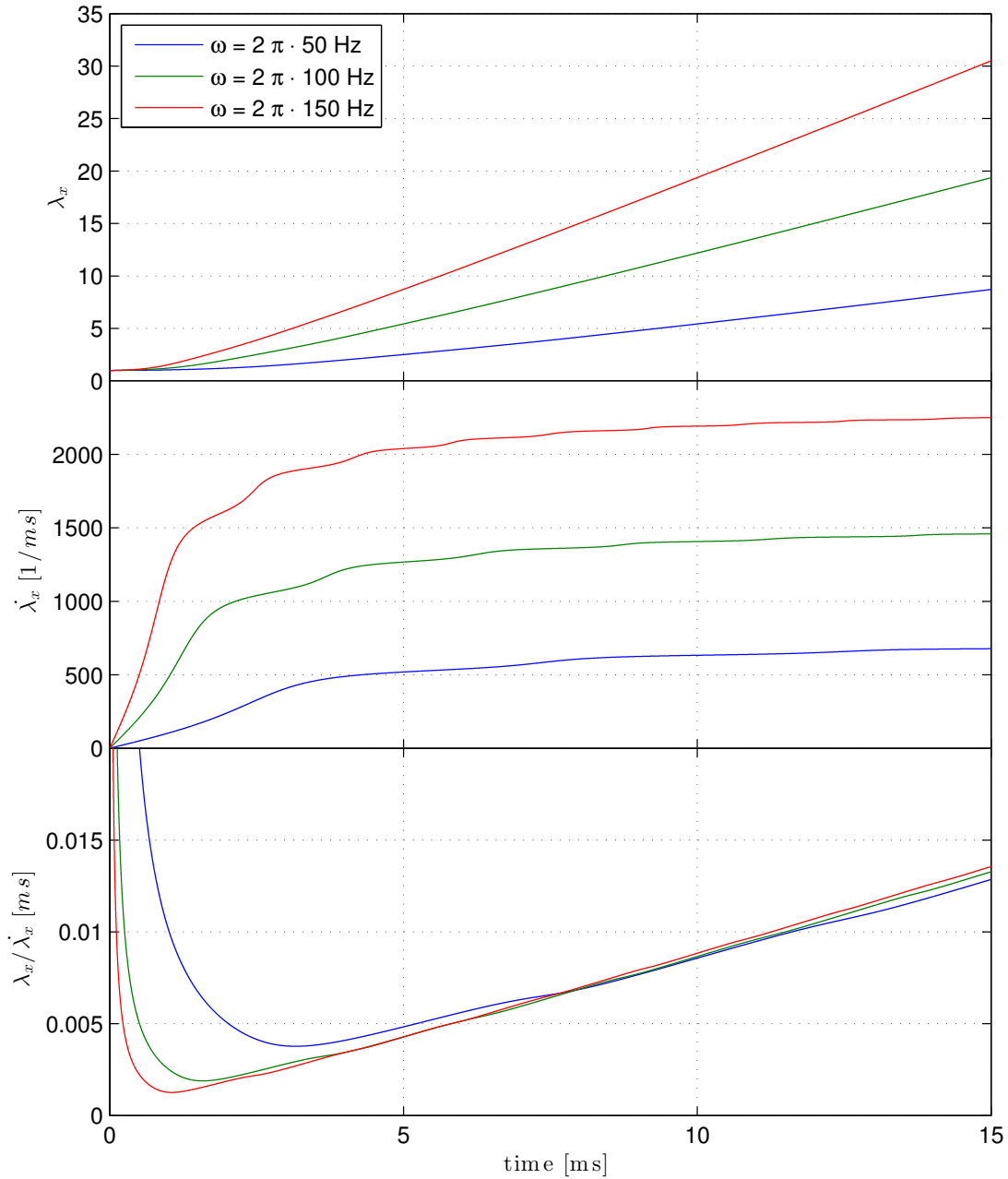


**Figure 2.1:** Numerical solution of Eq. 2.36 for three different values of  $\omega$ . The calculations were carried out with  $\omega_x = \omega_y = \omega$ ,  $\omega_z = (\omega_x^2 + \omega_y^2)^{1/2}$ ,  $\omega_x(t) = 2\pi \times 1$  Hz, and  $\omega_y(t) = \omega_z(t) = 2 \times \omega$ . The calculation describes the creation of the BEC in a crossed dipole trap and the free expansion in one of the dipole trap legs after the other has been shot off. The top section shows the time evolution of the scaling factor  $\lambda_x$ . The middle section shows its derivative  $\dot{\lambda}_x$  and the bottom section its quotient  $\lambda_x/\dot{\lambda}_x$ .

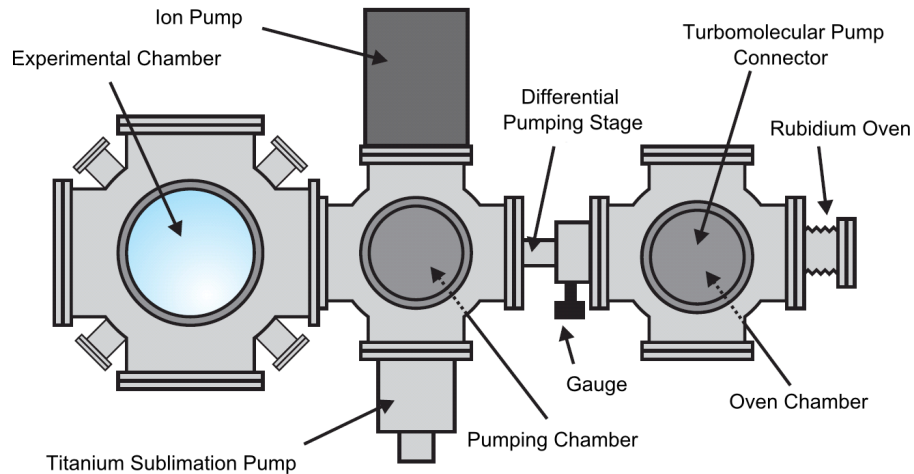


**Figure 2.2:** Drawing of the vacuum system [45, 61].

---

## 2.3 The ATOMICS experiment

---

In this thesis ultra-cold atomic ensembles and Bose-Einstein condensates of  $^{87}\text{Rb}$  have been investigated. The cooling of  $^{87}\text{Rb}$  atoms to quantum degeneracy is a multi-step process and the implemented procedure at the ATOMICS experiment will be explained shortly in this section. The ATOMICS experiment is has the capability to produce an all-optical BEC of 25000  $^{87}\text{Rb}$  atoms every 25 seconds with a condensate fraction of  $N_0/N > 0.8$  [61]. In addition the detection system of the ATOMICS experiment will be discussed (see Sec. 2.3.3). A mathematical system to further improve the quality of the obtained images will be introduced.

---

### 2.3.1 Creation of ultra-cold atoms in a magneto-optical trap

---

The ATOMICS experiment consists of a combination of two vacuum chambers [45]. The first vacuum chamber has a pressure of  $\approx 10^{-6}$  mbar and is used to house the oven used as an atom source for the experiment. The second vacuum chamber is connected to the first vacuum chamber via a differential pumping stage and is used as the experimental chamber. It features a pressure of  $\approx 3 \times 10^{-11}$  mbar and its vacuum is provided by titan sublimation pump in combination with ion-getter pump.

The oven housed in the first vacuum chamber is filled with rubidium. By heating the oven to  $\approx 100^\circ$  a vapour of rubidium atoms is created. The opening of the rubidium oven is pointed at the differential pumping stage and the beam of hot rubidium atoms is aligned to pass through the stage into the experimental vacuum chamber. In order to efficiently load the magneto-optical trap a chirp laser system [62] is used to pre-cool the atoms along their passage into

---

the experimental vacuum chamber. The chirp laser system cools the atoms by spatially The atomic beam is aligned next to the magneto-optical trap, which is constantly loaded by the chirp-cooled beam of atoms [63].

The magneto-optical trap of the ATOMICS experiment consists of three beams covering all three dimensions. The circular polarized beams are retro-reflected and a  $\lambda/4$  waveplate in front of each mirror creates the needed polarization in order to create a magneto-optical trap. The light for each beam is provided by a master oscillator power amplifier (MOPA) laser system that provides up to 300 mW of optical power and detuned by 10 MHz to the red in respect to the  $D_2$   $F = 2 \rightarrow F' = 3$  transition of  $^{87}\text{Rb}$ . The needed magnetic field gradient is created by two magnetic coils in anti-Helmholtz configuration, which are placed inside the vacuum chamber. Additional details to the magneto-optical trap in the ATOMICS experiment can be found in [44, 45, 61, 63–67]. The atomic ensemble created by the magneto-optical trap typically consists of  $5 \times 10^7$   $^{87}\text{Rb}$  atoms slightly above the Doppler-temperature of  $^{87}\text{Rb}$  which is  $145 \mu\text{K}$ . The loading time of the MOT during the experimental procedure is typically 8 s.

---

### 2.3.2 Creation of Bose-Einstein condensates

---

The all-optical creation of Bose-Einstein condensates has been investigated in detail before [45, 61, 68]. Therefore only a brief compilation of the experimental parameters will be given.

The creation of BECs at the ATOMICS experiment is performed in a crossed optical dipole trap setup [69]. Each of the beams is focussed down to a waist of  $\approx 45 \mu\text{m}$ . The ytterbium doped fibre laser<sup>1</sup> with a maximum optical output power of 50 W is at 1070 nm provides the light for both laser beams. Each beam is guided through an AOM separately to control the intensity of the beams for the evaporation process. In addition a frequency shift is imprinted to reduce interference effects between the laser beams in the cross section of the dipole trap. The maximum optical power used for the creation of a BEC is 10 W per beam.

The beams are aligned in the horizontal plane and guided into the experimental vacuum chamber. They intersect under an angle of  $90^\circ$  in the centre of the MOT. The crossed dipole trap is loaded directly from the magneto-optical trap with the aid of an optical molasses to further cool the atoms. The cross section of the dipole trap contains up to 350.000  $^{87}\text{Rb}$  atoms at a temperature of  $100 \mu\text{K}$ . The achieved phase space density is  $\rho_{\text{PSD}} = 2 \times 10^{-5}$ . To further reach Bose-Einstein condensation evaporative cooling is used [27].

Evaporative cooling relies on the principle that elastic collisions in a confined atomic vapour create a thermodynamic equilibrium state. By removing the hottest atoms from the ensemble the system has to re-thermalize to a state

---

<sup>1</sup> IPG, YLR-50-1070-LP

---

of lower mean energy and therefore lower temperature. In the case of optical dipole potentials, evaporation is done by lowering the intensity of the trap beam. The lowered potential allows the hottest atoms to escape and the remaining atoms are left at lower temperature. The drawback of this method is the loss of atoms. By choosing the appropriate intensity ramp a gain in phase-space density is achieved until the atomic ensemble is cold enough to condense into a Bose-Einstein condensate. The experimental details on the evaporation strategy and characterization measurements can be found in [65,68]. The produced Bose-Einstein condensates consists of up to  $N = 25000$  atoms with a condensate fraction of up to  $N_0/N = 0.8$ . The calculated Thomas-Fermi radius of the BEC is  $R_{TF} = (3.02 \pm 0.12) \mu\text{m}$ . After the evaporation the temperature of the non-condensed atoms is well below  $T = 100\text{nK}$ .

---

### 2.3.3 Detection of cold atom ensembles

---

The detection of atom clouds in this work is done via absorption imaging [70]. A cloud of atoms is illuminated with light and due to scattering of light with the atoms a shadow is cast. This shadow is imaged with a CCD camera and the incoming intensity is used to determine the spatially resolved density of the cloud and therefore the atom number. Due to scattering this measurement is destructive and each cloud can only be measured once. Every measurement must begin with the complete experimental procedure from the beginning in order to achieve a new experimental image.

The ATOMICS experiment features two absorption detection systems that are used to detect the atomic distribution along two axes (see Fig. 2.3). In vertical direction a *Roper-Scientific Sensys* camera is used for detection. The shadow cast by the atom ensemble is re-imaged with a combination of two achromatic lenses  $f_3$  and  $f_4$ . The diameter of the lenses is  $D = 75\text{ mm}$  and the diffraction limit of the optical setup is  $\Delta d = 1.22\lambda f/D = 3.8\mu\text{m}$ . This camera is mainly used to detect atomic distributions. The second camera used is a *PCO Pixelfly* camera, which detects along the horizontal direction. Similar to the other imaging system the shadow of the atoms is re-imaged by a pair of achromatic lenses ( $f_1$  and  $f_2$ ). The diameter of the lenses is  $50.8\text{ mm}$  giving a diffraction limit of  $\Delta d = 4.8\mu\text{m}$ .

To calculate the space-resolved atom density  $n(x, y)$ , integrated along the  $z$  direction, three images have to be taken. The first image is the image of the atomic ensemble  $I_A(x, y)$ . The second image, the reference image  $I_R(x, y)$ , is taken after a waiting time of 1 s, again with detection light but without atoms. For all images the detection light illuminates the atoms for a duration of  $200\mu\text{s}$ .

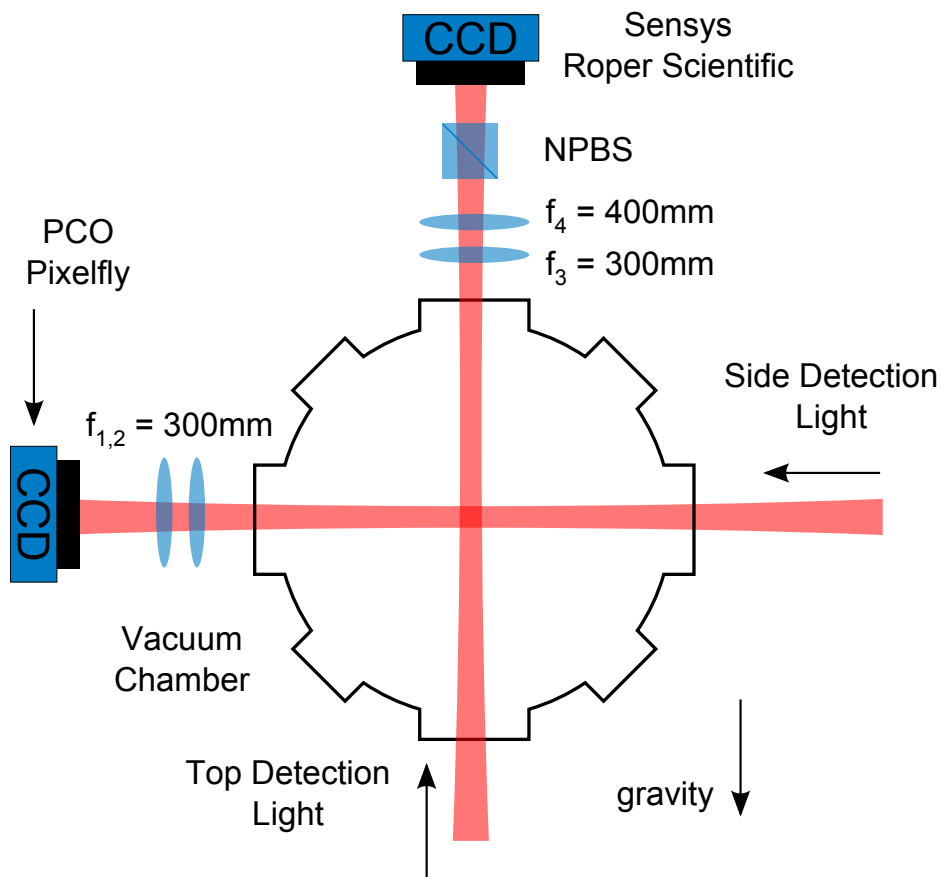


**Figure 2.3:** Setup of the imaging system used at the ATOMICS experiment. Two independent setups are used to image the density distribution of an atomic ensemble in the vacuum chamber. The main detection line used is the vertical direction, whereas the horizontal line is used for alignment of beams in the vertical direction.

The third image, the dark picture  $I_D(x, y)$ , taken without detection light. The density can be calculated using [70]:

$$n(x, y) = \frac{2I_0}{\hbar\omega\Gamma} \ln \left( \frac{I_R(x, y) - I_D(x, y)}{I_A(x, y) - I_D(x, y)} \right) \quad (2.41)$$

where  $I_0$  is the saturation intensity of the transition:

$$I_0 = \frac{2\pi^2\hbar c\Gamma}{3\lambda^3}, \quad (2.42)$$

and  $\Gamma$  is the line width of the transition.

Due to the large temporal separation of the images intensity modulations of the detection light may occur. In addition small dust particles in the beam path may change their position or elements may vibrate, and therefore small impurities are imprinted in the experimentally obtained images. As long as they are the same for all images the detection algorithm is robust enough to cancel them out. If these disturbances change during the detection process, additional, non-desired patterns are visible in the final density distribution  $n(x, y)$ . In the worst case these spatial fluctuations are in the same order as periodic structures that are measured at the ATOMICS experiment. As a consequence an additional step is taken to rule these errors out. An in depth discussion can be found here and only the main concept will be drawn out shortly [65, 71].

Typically a series of measurements has between 50 and 300 experimental images with different unwanted interference effects each. Even though they are different from image to image, they are similar. The entirety of these images spans a vector space. The implemented algorithm now finds a basis for said vector space and each image is projected onto said basis. The idea behind this is, that not the complete image is taken but only the area without atoms. Periodic errors outside the interesting experimental area should be the same as on the inside of the interesting area. By taking only the outside area of the images a weighting is found that describes the occurrence of these disturbances by the weighted fractions of the whole vector space. By subtracting the errors for the whole picture the detected errors without atoms cleanse the area filled with atoms.

The algorithm has been implemented in Python [72] and allows an easy and fast correction of all images from a series of measurements. Without the additional corrections most of the measurements in this work would have been impossible.



---

## 3 Bragg diffraction and double Bragg diffraction

Bragg scattering or Bragg diffraction was first observed as the diffraction of X-rays in crystals [73]. In atom optics Bragg diffraction allows the controlled manipulation of ultra-cold atom ensembles and BECs with moving optical lattices [38, 74–76]. Acceleration, deceleration, as well as splitting of atomic ensembles into multiple moving and non-moving parts has been demonstrated [77]. The key advantage of Bragg diffraction is the resonant excitation of discrete momentum states of natural multiples of  $|2\hbar k\rangle$ . The quantized manipulation of atoms serves as basic tool for atom manipulation [78], spectroscopy of motional states [79], and matter wave interferometry [80]. Double Bragg diffraction extends Bragg diffraction towards a symmetric splitting of atomic ensembles in positive and negative momentum states simultaneously, thus in opposite directions. It was first theoretically discussed in [81] and implemented in this work for the first time. Double Bragg diffraction offers a new way of creating matter wave beamsplitters and mirrors and serves as a new tool for matter wave optics. This chapter introduces the effect of Bragg diffraction that occurs when atoms are illuminated by periodic optical potentials (see Sec. 3.1). Sec. 3.2 expands the theoretical description to the coherent splitting of ensembles with double Bragg diffraction. Sec. 3.3 describes the experimental implementation and the first successful observation of double Bragg diffraction. The expansion of double Bragg diffraction towards higher momenta is shown in Sec. 3.4. Next Sec. 3.5 characterizes the influences of pulse length and initial ensemble momentum width on the quality of double Bragg diffraction. Sec. 3.6 compares double Bragg diffraction to other methods of coherent beam splitting. This chapter concludes with the implementation of a complete matter wave interferometer using double Bragg diffraction lattice pulses (Sec. 3.7).

---

### 3.1 Bragg diffraction

---

Bragg diffraction is a versatile tool at the ATOMICS experiment. It is used to accelerate, decelerate, and split atomic clouds. It is also used to measure the potential depth and the trapping frequencies of matter wave guides. Additionally it serves as a tool for matter wave interferometry (see Chapter 5 and Chapter 6).

Bragg diffraction is a resonant excitation of momentum states in periodic potentials. It offers a high state selectivity and the possibility to transfer multiple

momenta of  $2\hbar k$ . In Sec. 3.1.1 an introduction to periodic optical potentials will be given. To describe the dynamics of Bragg diffraction the method of averaging [82] is introduced in Sec. 3.1.2 before it is applied in Sec. 3.1.3 to describe the temporal evolution of momentum states excited by Bragg diffraction. Previous experimental implementation and characterization of Bragg diffraction at the ATOMICS experiment are described in [61, 65, 83].

---

### 3.1.1 Spatially periodic optical potentials

---

Spatially periodic optical potentials, or optical lattices, show a high degree of similarities to the observation of Bragg diffraction in crystals [84]. The diffraction of atoms in spatially periodic optical potentials can be described in the same way as the diffraction of light in spatially periodic crystals. Additionally Bragg diffraction can also be seen as a two-photon process as depicted in Fig. 3.1. Two beams are superimposed to each other at an angle  $\Theta$ . An atom resides in the cross section and absorbs a photon from one of the beams. It then emits a photon stimulated into the other beam. The potential detuning  $\Delta\omega$  of the two beams yields a small energy transfer  $\Delta E = \hbar\Delta\omega$ . Due to energy and momentum conservation the following criterion has to be met:

$$n \times \frac{P^2}{2m} = \hbar \times \Delta\omega, \quad (3.1)$$

where  $n$  gives the order of Bragg diffraction and  $P = 2\hbar k \sin(\Theta/2)$  the momentum transfer of a single Bragg diffraction process. Counter propagating laser beams have  $\Theta = 180^\circ$  which yields  $\Delta\omega = 4 \times \omega_R = 2\pi \times 15.08 \text{ kHz}$  for  $n = 1$ .  $\omega_R = \hbar k^2/2m$  is the recoil frequency, with  $k$  the wave vector of the incident beam and  $m$  the mass of the atom. Table A.2 compiles a list of experimentally used values for  $\Delta\omega$  as well as the correspondent velocity of a  $^{87}\text{Rb}$  atom after the momentum transfer.

The light field in one dimension depicted in Fig. 3.1 can be represented as follows:

$$E(z, t) = E_z e^{i(kz - \omega t)} + E_z e^{i(-kz - (\omega + \Delta\omega)t)} + \text{h.c.} \quad (3.2)$$

The combined electric field  $E(\vec{r}, t)$  consists of two light fields of equal amplitude  $E_z$ . They are counter propagating and aligned on top of each other, indicated by the sign of the wave vectors  $k$ . As shown in Sec. 2.1 the optical potential is proportional to the intensity of the light, which is given by the square of the electric field:

$$U_{1D}(\vec{r}, t) = 4\hat{U} \frac{2P}{\pi w^2(z)} \cos^2\left(kz + \frac{\Delta\omega}{2}t\right) e^{\frac{2(x^2+y^2)}{w^2(z)}}. \quad (3.3)$$

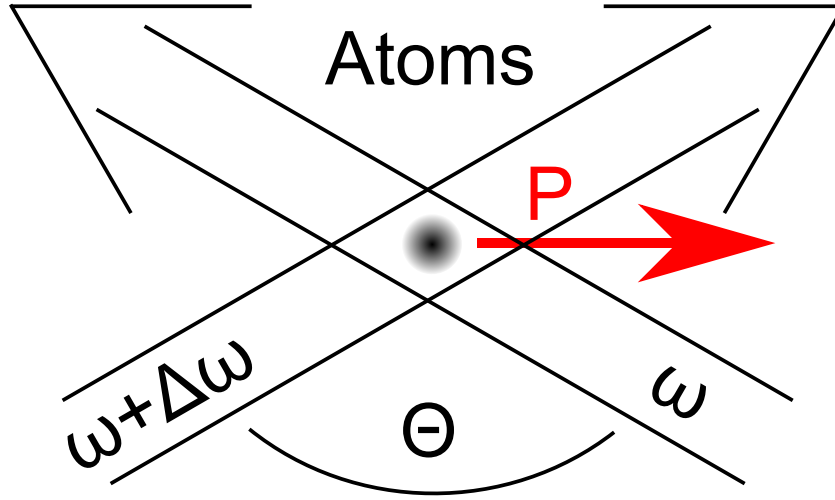


**Figure 3.1:** Two incident beams with frequency  $\omega$  and  $\omega + \Delta\omega$  are aligned to intersect at the angle  $\Theta$ . Atoms positioned in the cross section experience a momentum transfer after the absorption of light from one of the beams and the stimulated emission of light of the other beams.

The depth of an optical potential is four times the depth of a single beam with the same optical power per beam and shape. The maximum depth of the optical lattice is given by the  $U_{1D}(0)$  and normalized by the recoil energy  $E_R = \hbar^2 k^2 / 2m = \hbar\omega_R$ . The introduction of  $E_R$  simplifies the comparison of optical lattices used for different atomic species.  $U_{1D}(0)$  in orders of the recoil energy  $E_R$  is given by:

$$\frac{U_{1D}(0)}{E_R} = \frac{2m}{\hbar^2 k^2} 8\hat{U} \frac{P}{\pi w_0^2}. \quad (3.4)$$

Several one-dimensional optical lattices can be used in combination to produce two- or three-dimensional lattice systems. The time evolution of atoms in such an optical lattice will be discussed in Sec. 3.1.3. For the minimum energy transfer the Fourier limit yields a minimum pulse time  $\tau_{min}$  of

$$\tau_{min} > \frac{1}{2\omega_R} = 21.1 \mu s, \quad (3.5)$$

which will not be undercut during the experimental procedure in this work.

---

### 3.1.2 Method of averaging

---

The method of averaging gives an elegant way to solve a system of coupled differential equations. It was first discussed in [82] and can be applied to describe the time evolution of Bragg diffraction (see Sec. 3.1.3) and double Bragg

diffraction (see Sec. 3.2.1). A short overview on the method will be given in this section. The notation used is taken from [81] which differs from [82]. A system of  $n$  coupled differential equations can be written as:

$$\dot{g} = i\epsilon H g \equiv i\epsilon H_0 g + i\epsilon \sum_{j \neq 0} e^{ij\omega_r t} H_j g \quad (3.6)$$

$g$  is the representation of the state,  $H$ ,  $H_0$ , and  $H_j$  represent complex time-independent matrices. Additionally a frequency  $\omega_r$  has been introduced and the adiabaticity parameter  $\epsilon$ . Eq. (3.6) is separated in fast and slow oscillating terms  $\gamma^{(m)}$ :

$$g^{(m)} = \gamma^{(m)} + \sum_{j=1}^m \epsilon^j f_j(\gamma^{(m)}), \quad (3.7)$$

where  $f_j(\gamma^{(m)})$  is a solution of the original differential equation, that can be found up to the order  $\epsilon^m$ . Choosing  $m = 1$  eliminates all higher orders and yields a set of equations for which Bragg diffraction and double Bragg diffraction can be described. In order to solve the time dependency of the system it is assumed that  $\gamma^{(m)}$  fulfils:

$$\dot{\gamma}^{(m)} = i\epsilon H_0 \gamma^{(m)} + i \sum_{j=2}^m \epsilon^j p_j(\gamma^{(m)}). \quad (3.8)$$

$f_j(\gamma^{(m)})$  can be determined by grouping parts of equal  $\epsilon$  for Eq. (3.7) satisfying:

$$\dot{g}^{(m)} = i\epsilon H g^{(m)} + \mathcal{O}(\epsilon^{m+1}). \quad (3.9)$$

Creating the time derivative of Eq. (3.7) and using the definition of Eq. (3.8) yields a solution for  $f_j(\gamma^{(m)})$  that can be used to solve equation Eq. (3.7).

For  $m = 1$  a first-order solution can be found which solves the system of  $n$  coupled differential equations up to  $\epsilon^1$ . Then Eq. (3.8) simplifies to:

$$\dot{\gamma}^{(1)} = i\epsilon H_0 \gamma^{(1)}. \quad (3.10)$$

A solution for this differential equation is:

$$\gamma^{(1)}(t) = e^{i\epsilon H_0 t} \gamma^{(1)}(0). \quad (3.11)$$

Where  $H_0$  is a square matrix of dimension  $n \times n$ . It is specific to the system described by the set of differential equations. By using the solution of  $f_1$  [81]:

$$f_1(\gamma^{(m)}, t) = \sum_{j \neq 0} \frac{e^{ij\omega_r t}}{j\omega_r} H_j \gamma^{(m)}(t), \quad (3.12)$$

For  $m = 1$  Eq. (3.7) can now be written as:

$$g^{(1)}(t) = \left[ 1 + \epsilon \sum_{j \neq 0} \frac{e^{ij\omega_r t}}{j\omega_r} H_j \right] \gamma^{(1)}(t). \quad (3.13)$$

The solution of the coupled system of differential equations can be found by determining the appropriate matrices  $H_0$  and  $H_j$ . Depending on the adiabaticity parameter  $\epsilon$  fast oscillating terms of the order  $j\omega_R$  are suppressed. In order to find higher order solutions an analogous method can be applied to find  $f_2$  [81]. In principle this method is capable of being extended to higher-orders of  $\epsilon$ . For the experimental value of  $\epsilon < 0.1$  a strong suppression of higher order terms is already present. Therefore only first-order solutions are used in the following discussion.

### 3.1.3 Time evolution of momentum states of Bragg diffracted atoms

Atoms in the field of an optical lattice experience the interaction between two counter propagating light fields (see Sec. 3.1.1). Eq. (3.2) describes two classical fields that interact with the atom in place. The interaction of light and atom by absorption and emission, and the resulting momentum transfer, can be expressed quantum mechanically with an operator of the form:

$$e^{\pm ikz} = \int dp |p \pm \hbar k\rangle \langle p|. \quad (3.14)$$

The operator shifts the momentum of a given state by a margin of  $\pm \hbar k$  and depending of the direction of the incident light beam. This is true for both, absorption and emission processes, either from the ground state  $|g\rangle$  or the excited state  $|e\rangle$ . The ground state  $|g\rangle$  follows the dispersion relation of a free atom  $E = p^2/2m$ . Due to the optical lattice this dispersion relation is modified and Bloch bands emerge [53]. These bands shift the energy of the state but do not interfere with the discussion of Bragg diffraction as long as the intensity of the lattice is sufficiently small. Increasing the intensity yields additional dynamics of fast oscillating terms and the excitation of non-resonant momentum states. To distinguish between both regimes the adiabaticity parameter  $\epsilon$  is used. For  $\epsilon < 0.1$  the deep Bragg regime can be assumed, where fast oscillating terms are neglected [81]. For higher values of  $\epsilon$  this is no longer valid and higher order oscillations are no longer suppressed. This regime is called quasi-Bragg regime. In order to apply the method of averaging [85, 86] the representation of the system has to be transformed into a similar form as Eq. (3.6), a system of n-coupled differential equation. The initial description of the system is given by the Hamiltonian [87]:

$$\hat{H} = \frac{p^2}{2m} + \hbar\omega_{eg} |e\rangle \langle e| + \hbar \left[ \Omega_a e^{i(kz - \omega t)} + \Omega_b e^{i(-kz - (\omega + \Delta\omega)t)} \right] |e\rangle \langle g| + \text{h.c.}, \quad (3.15)$$

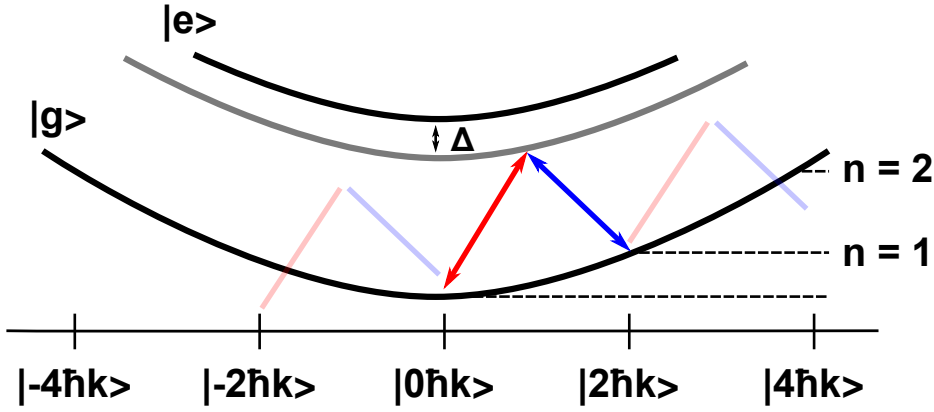


**Figure 3.2:** Energy scheme for Bragg diffraction system. A two photon process resonantly excites an oscillation between the neighbouring momentum states  $|0\hbar k\rangle$  and  $|2\hbar k\rangle$ . Due to the quadratic dispersion relation higher order momentum states are not excited resonantly.

where  $\Omega_a$  and  $\Omega_b$  are the single-photon Rabi frequencies [51] and  $\omega_{eg}$  the eigenfrequency of the system. This description assumes that fast oscillating terms are negligible (see rotating wave approximation [88]). Solving the Schrödinger equation for this system on an arbitrary state

$$|\varphi\rangle = \int dp \left( g(p) |g, p\rangle + e(p) |e, p\rangle \right), \quad (3.16)$$

yields a system of coupled differential equations. This system can be expressed in the form of Eq. (3.6) and a solution for the time evolution of the system is found via the method of averaging. The introduction of a detuning  $\Delta$  eliminates transfer to the excited state and yields a solution where only the ground states  $|g\rangle$  of different momenta are present. A schematic representation of the described system is shown in Fig. 3.2. The resonant oscillations between the neighbouring states  $|0\hbar k\rangle$  and  $|2\hbar k\rangle$  is excited by the incident light beams. The detuning  $\Delta$  with respect to the excited state yields an effective suppression of  $|e\rangle$  and higher order momenta are suppressed due to the quadratic dispersion relation of the free particle.

In order to apply the method of averaging the following definitions are used: The adiabaticity parameter  $\epsilon$  in a Bragg diffraction system is given by:

$$\epsilon \equiv \frac{\Omega}{8\omega_R}. \quad (3.17)$$

$\epsilon$  is used to determine the different regimes of Bragg diffraction and quasi-Bragg diffraction. The effective Rabi frequency is defined as  $\Omega = \Omega_a \Omega_b / 2\Delta$  [89, 90]. For Bragg diffraction the effective 2-photon-Rabi frequency is given by [51]:

$$\Omega = \frac{U_{1D}(0)}{2\hbar}. \quad (3.18)$$

The application of the method of averaging follows the discussing in Sec. 3.1.2. For  $m = 1$  the state of the system is defined as:

$$\gamma^{(1)}(t) = \left( \gamma_0^{(1)}(t), \gamma_2^{(1)}(t) \right)^T. \quad (3.19)$$

$\gamma_0^{(1)}(t)$  represents the state  $|0\hbar k\rangle$  and  $\gamma_2^{(1)}$  the state  $|2\hbar k\rangle$  having an additional momentum of  $2\hbar k$ . Following Eq. (3.10) the following differential equation has to be solved:

$$\dot{\gamma}^{(1)} = i\epsilon H_0 \gamma^{(1)} = i\Omega \begin{pmatrix} 0 & 1 \\ 1 & 0 \end{pmatrix} \gamma^{(1)}. \quad (3.20)$$

A solution for this equation is:

$$\gamma(t) = \left[ \cos\left(\frac{\Omega}{2}t\right) \begin{pmatrix} 1 & 0 \\ 0 & 1 \end{pmatrix} + i \sin\left(\frac{\Omega}{2}t\right) \begin{pmatrix} 1 & 0 \\ 0 & 1 \end{pmatrix} \right] \gamma(0), \quad (3.21)$$

and the population  $P(t)$  of the momentum states after time  $t$  is:

$$P(t) = |\gamma^{(1)}(t)|^2 = \left( P_{0\hbar k}(t), P_{2\hbar k}(t) \right). \quad (3.22)$$

Eq. (3.21) is completely independent of the adiabaticity parameter  $\epsilon$ . Correction due to reaching the quasi Bragg regime can be included by solving Eq. (3.11). This will be discussed in Sec. 3.2.3 for double Bragg diffraction, where an increased influence of higher frequency fluctuations are more dominant.

One of the main applications of Bragg diffraction is matter wave interferometry (see Sec. 5.6). For matter wave interferometry well defined light pulses of optical lattices are used to create superposition of multiple momentum states. Two pulse durations  $\tau$  are of interest: On the one hand a  $\pi/2$ -pulse creates a coherent superposition of two momentum states where both states have an equal population. The length of the pulse is defined as  $\pi/2 = \Omega\tau_{\pi/2}$ . On the other hand a  $\pi$ -pulse inverts the population of a system. For example if all atoms are at rest in the beginning, all are transferred to momentum state  $|2\hbar k\rangle$  after the  $\pi$ -pulse and vice versa. The pulse length is defined as  $\pi = \Omega\tau_{\pi}$ .

---

## 3.2 Double Bragg diffraction theory

---

Bragg diffraction is used to coherently split atoms in multiple wave packets with different momenta. A drawback of Bragg diffraction is, that its acceleration is directed in one direction only. To create a beamsplitter, where atoms are accelerated in opposite directions, additional light fields are needed. Double Bragg diffraction promises to create coherent splitting in opposite directions with the

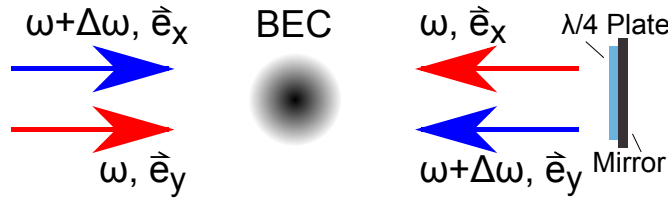


**Figure 3.3:** Two light beams with frequency difference  $\Delta\omega$  and orthogonal polarization are aligned on top of each other. After passing the atoms they are retro-reflected on a mirror. A  $\lambda/4$  waveplate in front of the mirror turns the polarization axis by  $90^\circ$ . This results in a combination of two optical lattices with orthogonal polarisation.

use of a single optical beam line. By combining two beams with orthogonal polarization and by utilizing the polarization as a selection criterion, two optical lattices can be realised that feature opposite acceleration directions.

This section will introduce double Bragg diffraction as a tool for atom optics by describing the time evolution of atoms in a double Bragg lattice (see Sec. 3.2.1). Next the influences of the momentum distribution of an atomic cloud will be shown (Sec. 3.2.2) as well as the influence of lattice depth (Sec. 3.2.3). The section ends with the description of typical pulse times used with double Bragg diffraction and will focus on the differences of the definition in respect to standard Bragg diffraction.

---

### 3.2.1 Rabi oscillations induced by Double Bragg diffraction

---

The theoretical analysis of double Bragg diffraction follows the method of averaging (Sec. 3.1.2) and the discussion on Bragg diffraction (Sec. 3.1).

The optical system used for double Bragg diffraction is depicted in Fig. 3.3. Two light beams are orthogonally linear polarized with respect to each other. The frequency difference of the two beams is  $\Delta\omega$ . After passing the atomic cloud for the first time they are retro-reflected by a mirror. In front of the mirror is a  $\lambda/4$  waveplate that rotates the polarization of each of the beams by  $90^\circ$ . The retro-reflected beams cross the atoms a second time and a combination of two optical lattices is produced. Each of the beams interferes with the only counter-propagating beam of the same polarization and the resulting two Bragg lattices feature different directions of momentum transfer. Instead of using linearly polarized light an identical system can be built using a pair of circular polarized beams. As long as the two lattices feature orthogonally polarization to suppress cross-talk, both systems are viable options that yield the same theoretical rep-

resentation.

The Hamiltonian describing the outlined system is given by [81]:

$$\begin{aligned}\hat{H} = & \frac{p^2}{2m} + \hbar\omega_{eg} (|e_+\rangle\langle e_+| + |e_-\rangle\langle e_-|) \\ & + \hbar\Omega_+ \left( e^{i(kz-\omega t)} + e^{i(-kz-(\omega+\Delta\omega)t)} \right) |e_+\rangle\langle g| \\ & + \hbar\Omega_- \left( e^{i(-kz-\omega t)} + e^{i(kz-(\omega+\Delta\omega)t)} \right) |e_-\rangle\langle g| + \text{h.c.},\end{aligned}$$

where  $\Omega_+$  and  $\Omega_-$  are the single photon Rabi frequencies. In the same way as single Bragg diffraction was applied to an arbitrary state to create a system of coupled differential equations the Hamiltonian  $\hat{H}$  is now applied to  $|\phi\rangle$ :

$$|\phi\rangle = \int dp \left( g(p) |g,p\rangle + e_+(p) |e_+,p\rangle + e_-(p) |e_-,p\rangle \right). \quad (3.23)$$

The result is a system of coupled differential equations. This system of differential equations is reduced with the method of averaging to the following equation:

$$\dot{\gamma}^{(1)} = i\Omega \begin{pmatrix} 0 & 1 & 0 \\ 1 & 0 & 1 \\ 0 & 1 & 0 \end{pmatrix} \gamma^{(1)}, \quad (3.24)$$

which can be solved algebraically. The solution for  $\gamma^{(1)}(t)$  is:

$$\begin{aligned}\gamma(t) = & \left[ \frac{1}{2} \begin{pmatrix} 1 & 0 & -1 \\ 0 & 0 & 0 \\ -1 & 0 & 1 \end{pmatrix} \right. \\ & + \frac{1}{2} \cos(\sqrt{2}\Omega t) \begin{pmatrix} 1 & 0 & 1 \\ 0 & 2 & 0 \\ 1 & 0 & 1 \end{pmatrix} \\ & \left. + \frac{i}{\sqrt{2}} \sin(\sqrt{2}\Omega t) \begin{pmatrix} 0 & 1 & 0 \\ 1 & 0 & 1 \\ 0 & 1 & 0 \end{pmatrix} \right] \gamma(0),\end{aligned} \quad (3.25)$$

where  $\gamma(0)$  is the initial state of the the system expressed by the state vector  $(\gamma_{-1}(0), \gamma_0(0), \gamma_1(0))^T$ . Eq. (3.25) describes the time evolution of momentum states in a double Bragg diffraction system. The population of each state is given by the state vector  $\gamma(t) = (\gamma_{-1}(t), \gamma_0(t), \gamma_1(t))^T$ :

$$|\gamma(t)|^2 = (P_{-2\hbar k}(t), P_{0\hbar k}(t), P_{2\hbar k}(t))^T. \quad (3.26)$$

The following sections discuss special additions in regards of double Bragg diffraction. In addition to this shortened discussion an in depth discussion of double Bragg diffraction can be found in [81].

---

### 3.2.2 Influences of a finite momentum distribution on double Bragg diffraction

---

In an experimental realisation all atomic ensembles feature a finite momentum distribution and in the case of BECs this momentum distribution evolves according to its mean-field energy [58]. An initial momentum, as introduced by the mean-field energy, will modify the time evolution of double Bragg diffraction as well as standard Bragg diffraction [77, 91]. This is especially relevant for high precision spectroscopy and matter wave interferometers [92].

Due to the momentum distribution of an atomic cloud each atom experiences a Doppler shift  $\omega_D$ . The Doppler shift  $\omega_D$  is given by:

$$\omega_D = \frac{p_D}{\hbar k} \times 2\omega_r, \quad (3.27)$$

where  $p_D$  is the momentum of the atom. For  $|p_D| \ll 2\hbar k$  or  $|\omega_D| \ll \omega_r$  Eq. (3.10) is still valid, the temporal change of  $H_i$  is small compared to the resonant excitation. For higher deviations this is no longer valid. The Doppler shift  $\omega_D$  introduces two additional terms on the diagonal of Eq. (3.24) [93]:

$$\dot{\gamma}^{(1)} = i \begin{pmatrix} \omega_D & \Omega & 0 \\ \Omega & 0 & \Omega \\ 0 & \Omega & \omega_D \end{pmatrix} \gamma^{(1)} \quad (3.28)$$

The solution for this differential equation is given by [81]:

$$\begin{aligned} \gamma(t, \omega_D) = & \left[ \frac{1}{\Omega_{\text{eff}}^2} \begin{pmatrix} \Omega^2 & -\omega_D \Omega & -\Omega^2 \\ -\omega_D \Omega & \omega_D^2 & \omega_D \Omega \\ -\Omega^2 & \omega_D \Omega & \Omega^2 \end{pmatrix} \right. \\ & + \frac{\cos(\Omega_{\text{eff}} t)}{\Omega_{\text{eff}}^2} \begin{pmatrix} \omega_D^2 + \Omega^2 & \omega_D \Omega & \Omega^2 \\ \omega_D \Omega & 2\Omega^2 & -\omega_D \Omega \\ \Omega^2 & -\omega_D \Omega & \omega_D^2 + \Omega^2 \end{pmatrix} \\ & \left. + \frac{i \sin(\Omega_{\text{eff}} t)}{\Omega_{\text{eff}}} \begin{pmatrix} \omega_D & \Omega & 0 \\ \Omega & 0 & \Omega \\ 0 & \Omega & -\omega_D \end{pmatrix} \right] \gamma(0), \end{aligned} \quad (3.29)$$

where  $\Omega_{\text{eff}}$  is defined as:

$$\Omega_{\text{eff}} = \sqrt{2\Omega^2 + \omega_D^2}. \quad (3.30)$$

Fig. 3.4 shows the solution of Eq. (3.29) for different Doppler shifts  $\omega_D$ . The

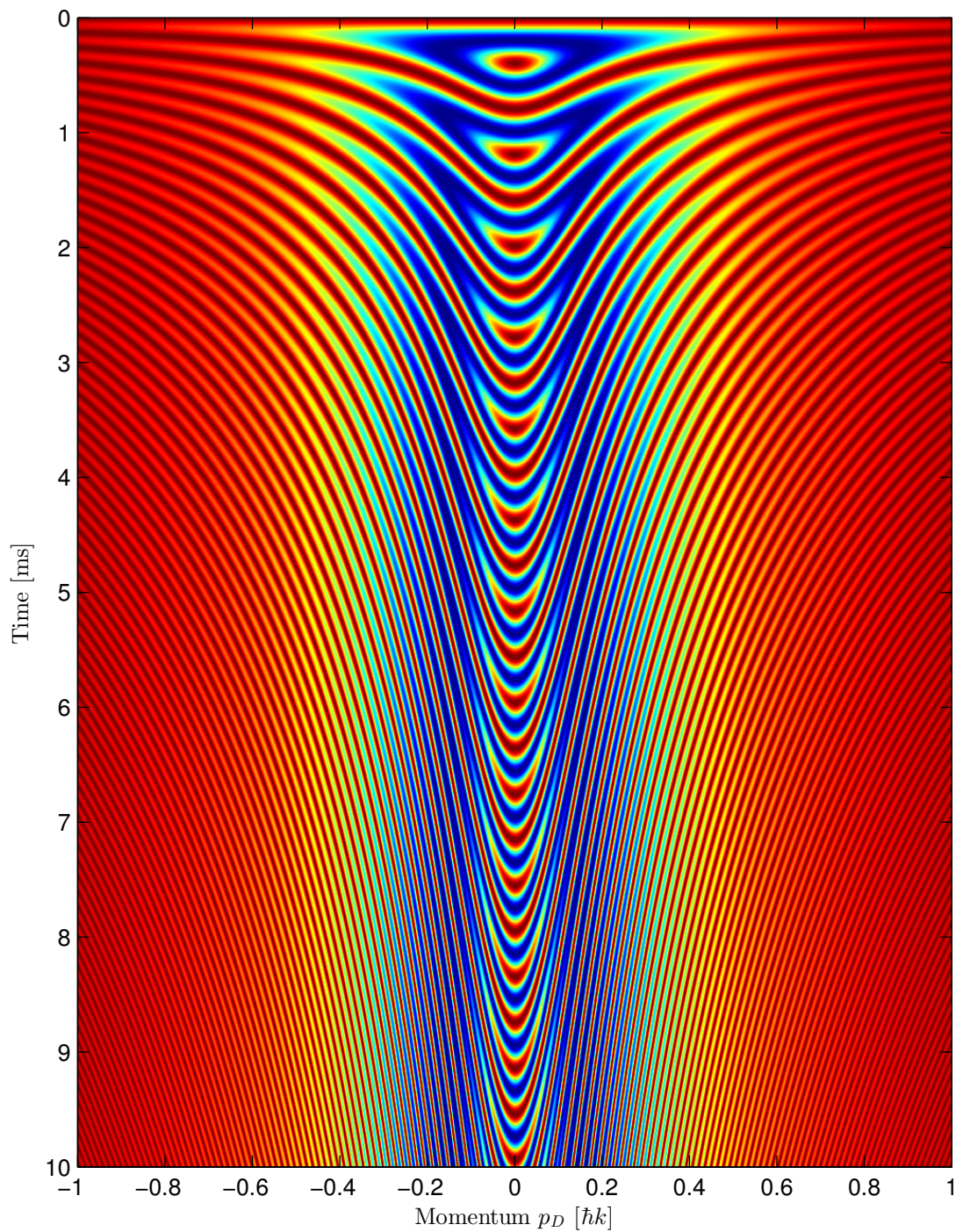


**Figure 3.4:** Population  $P_{0\hbar k}(t)$  of  $\gamma_0(t)$  according to Eq. (3.29). The initial state is  $\gamma(0, \omega_D) = (0, 1, 0)^T$  for all  $\omega_D$ . High population is shown in red, low population in blue.

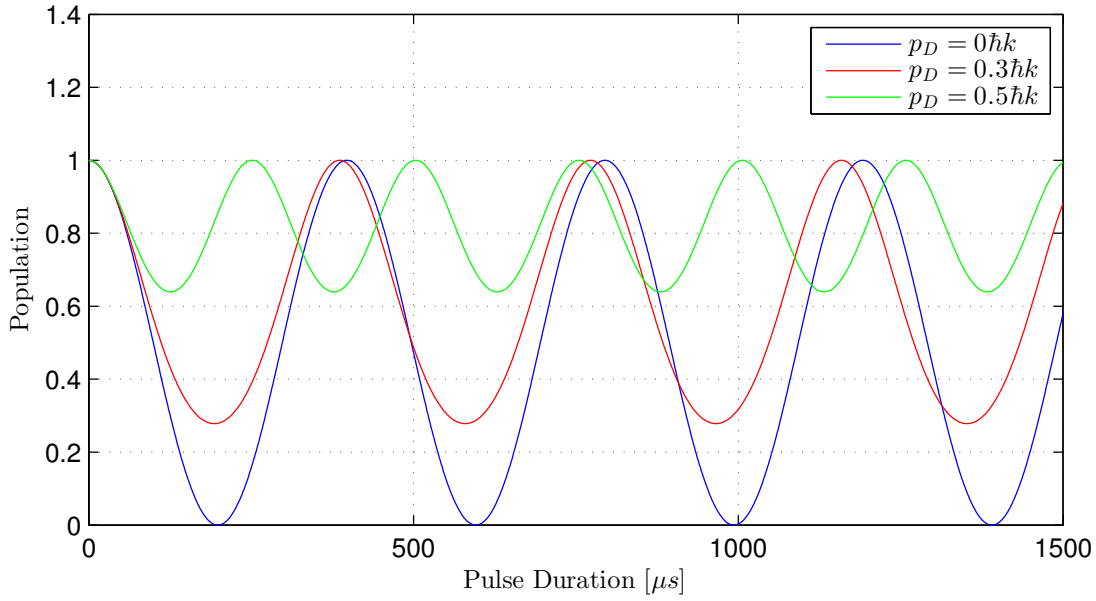


**Figure 3.5:** Oscillations of the momentum state  $|0\hbar k\rangle$  in a double Bragg lattice (Eq. (3.29)). For momenta  $p_D \neq 0$  an increased oscillation frequency is observed. In addition the transfer efficiency is reduced for higher initial momenta. The behaviour is analogue to Rabi oscillations of two state systems.

Doppler shift is presented as the momentum of a  $^{87}\text{Rb}$  atom in orders of  $\hbar k$ . For  $p_D = 0$  the system follows the same evolution of Eq. (3.25). For increasing values of  $p_D$  the oscillation frequency  $\Omega_{\text{eff}}$  changes according to Eq. (3.30). The more initial momentum is present the faster the oscillations occur. This behaviour is shown in Fig. 3.5 for three momentum  $p_D$ . According to their effective oscillation frequency atoms oscillate between the momentum states  $|0\hbar k\rangle$ ,  $|2\hbar k\rangle$ , and  $|-2\hbar k\rangle$ . Deviations from  $p_D = 0$  yield an increased oscillation frequency. Increasing the momentum further reduces the maximum population transfer and dampens the oscillation. This process is analogous to laser induced Rabi oscillations in two-level systems [88]. The dampening of the oscillations is increased the more initial momentum an atom has. The momentum distribution of an atomic ensemble yields a multitude of different initial momenta, which oscillate at different  $\Omega_{\text{eff}}$ . The population of a momentum state is then given by the sum over all  $p_D$ . The broader the momentum distribution gets the faster the dampening effects are observed and the more the mean oscillation period shifts towards higher frequencies. The resulting oscillation frequency  $\bar{\Omega}_{\text{Doppler}}$  can be determined by the weighted average of the Doppler shifted frequency  $\Omega_{\text{eff}}$ :

$$\bar{\Omega}_{\text{Doppler}}(\omega_D) = \frac{\int_{-\infty}^{\infty} \Omega_{\text{eff}}(\omega_D) \times N_{\text{BEC}}(\omega_D) d\omega_D}{\int_{-\infty}^{\infty} N_{\text{BEC}}(\omega_D) d\omega_D}, \quad (3.31)$$

where  $N_{\text{BEC}}(\omega_D)$  gives the amount of atoms with a given Doppler shift of  $\omega_D$  (see Sec. 3.5).

---

### 3.2.3 Influences of the lattice depth on double Bragg diffraction

---

Eq. (3.17) has shown that the adiabaticity is directly dependent on the potential depth of the optical lattice. Up until now the influences of a non-adiabatic excitation have been neglected. For  $\epsilon < 0.05$  the change in population is below 2.5%, which equates the experimental resolution of population states. For higher values of  $\epsilon$  the effects of faster oscillations are non-negligible. To accommodate for deeper lattices, and therefore working in the quasi-Bragg regime, rapidly oscillating correction have to be taken into account. Following Eq. (3.13) a solution is found for:

$$g(t) = \gamma(t) + \frac{\epsilon}{2} \begin{pmatrix} 0 & e^{i8\omega_r t} & 0 \\ -e^{-i8\omega_r t} & 0 & -e^{-i8\omega_r t} \\ 0 & e^{i8\omega_r t} & 0 \end{pmatrix} \gamma(t). \quad (3.32)$$

The modified solution of Eq. (3.25) introduces higher order fluctuations on top of the initial solution. The fluctuations occur with a frequency of  $8\omega_r$  and are suppressed by a factor of  $\epsilon/2$ . Fig. 3.6 depicts the sum of  $\gamma_{-1}$  and  $\gamma_1$  and the influence of  $\epsilon$  on the smoothness of the population oscillations. The larger the adiabaticity factor  $\epsilon$  gets, the higher the fluctuations become. It is important to notice, that fluctuations do not occur between the two states  $| -2\hbar k \rangle$  and  $| 2\hbar k \rangle$  but between  $| 0\hbar k \rangle$  and both accelerated momentum states. The dashed line shows the solution of Eq. (3.32) for  $\gamma_1$  and  $\gamma_{-1}$ . The introduced corrections are applicable to Eq. (3.25) and Eq. (3.29), thus describing population oscillations including the Doppler shift. Standard Bragg diffraction does not show this behaviour once the quasi Bragg regime is reached. Instead leaving the Bragg regime in standard Bragg diffraction shows excitation of non-resonant momentum states [94].

---

### 3.2.4 Beamsplitter and mirror for atoms

---

As with Bragg diffraction double Bragg diffraction is being used for atom interferometry. In the same manner specific pulse durations are defined, which are basic utilities for matter wave interferometry.  $\pi/2$ - and  $\pi$ -pulses are defined in the same manner as before: the duration  $\tau_{\pi/2}$  of a pulse is  $\pi/2 = \Omega_{\text{eff}} \tau_{\pi/2}$ . The duration of a  $\pi$ -pulse as  $\pi = \Omega_{\text{eff}} \tau_{\pi}$ . In contrast to Bragg diffraction, a  $\pi/2$ -pulse does not create an equally distributed population superposition. Instead the application of a  $\pi/2$ -pulse on the initial state  $\gamma(0) = (0, 1, 0)^T$  produces a depopulated ground state with zero momentum and two equally populated accelerated states:  $\gamma(\pi/2) = 1/\sqrt{2}(1, 0, 1)^T$  (see Fig. 3.7a). Applying the same

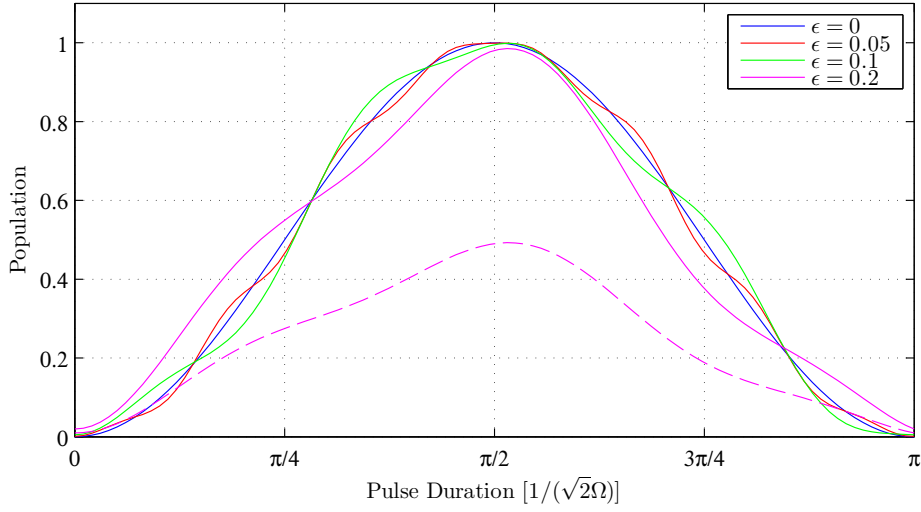


**Figure 3.6:** Dependence of the population oscillation of the sum of the accelerated states  $\gamma_{-1}$  and  $\gamma_1$  on  $\epsilon$ . Higher order fluctuations occur with the frequency of  $\omega_R/2$ . It is important to notice that  $\Omega$  and  $\epsilon$  cannot be chosen separately. For  $\epsilon = 0.2$  the dashed line represents the solution for  $\gamma_{-1}$  and  $\gamma_1$ . The fluctuations do not occur between the states  $|2\hbar k\rangle$  and  $|-2\hbar k\rangle$  but between the accelerated momentum states  $|\pm 2\hbar k\rangle$  and the initial state  $|0\hbar k\rangle$ .

pulse on a different initial state produces a completely different result. For example, the application of a  $\pi/2$  on the initial state  $\gamma'(0) = (1, 0, 0)^T$  (Fig. 3.7(a)) produces the state  $\gamma'(\pi/2) = 2(1/4, 1/2, 1/4)^T$ . This is of importance since each of these states is a possible exit of an interferometer (see Sec. 3.7). The behaviour holds true for the application of a  $\pi$ -pulse with double Bragg diffraction. Fig. 3.7 shows that a  $\pi$ -pulse creates an unexpected superposition of momentum states if the definitions of standard Bragg diffraction are applied. An initial state  $\gamma(0) = (0, 1, 0)^T$  (Fig. 3.7(b)) is transferred into the state  $\gamma(\pi) = (0, 1, 0)^T$  and represents the same population distribution. Applying a  $\pi$ -pulse on the state  $\gamma'(0) = (1, 0, 0)^T$  yields a different outcome: the state  $\gamma'(\pi) = (0, 0, 1)^T$ . This differs from the previously encountered two level systems such as standard Bragg diffraction but is a well known difference in multi-level system [95].

---

### 3.3 Experimental realization of double Bragg diffraction

---

To show that double Bragg diffraction is a versatile tool for controlled manipulation and matter wave interferometry an experimental implementation of double Bragg diffraction was performed. The experimental setup will be shown in Sec. 3.3.1 and the experimental procedure as well as the experimental results will be

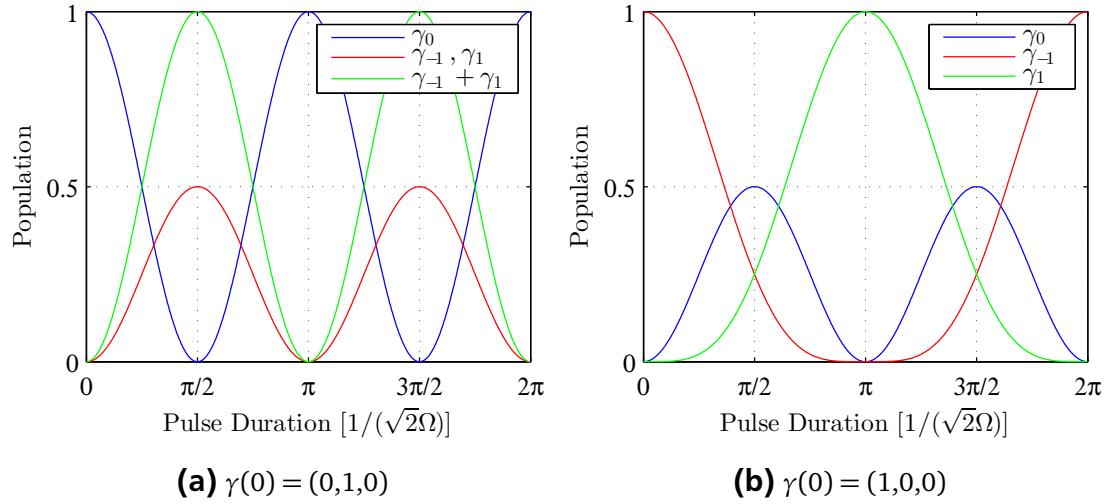


**Figure 3.7:** Population oscillation in a double Bragg system normalized to give defined pulse length in the range of 0 to  $2\pi$ . Depending on the initial state  $\gamma(0) = (\gamma_{-1}, \gamma_0, \gamma_1)$  the oscillation evolves differently according to Eq. (3.25)

discussed in Sec. 3.3.2. Additional experimental observations will be discussed in the following sections.

### 3.3.1 Experimental setup

The experimental implementation of an one-dimensional optical lattice consists of two steps. First the appropriate beams with their respective frequencies have to be produced. Afterwards they have to be aligned to create an optical lattice at the place of the atoms. An optical fibre is used to decouple these to parts experimentally.

The experimental setup is depicted in Fig. 3.8. An interference filter stabilized external-cavity diode laser [96] is used to produce light at  $\lambda = 780$  nm. The laser has a maximum output power of 40 mW. The light is guided through a Faraday isolator and a pick-up is used to guide a fraction of the light to a photodiode<sup>1</sup>. The light is spatially overlapped with a reference beam in order to create a beat signal which is used for offset stabilization [97]. The reference beam is stabilized to the  $D_2 F = 2 \rightarrow F' = 2$  transition of  $^{87}\text{Rb}$ . The lattice laser is stabilized to a frequency 750 MHz above ('blue') this transition.

The main fraction of the light is guided through is mechanical shutter and a  $\lambda/2$  waveplate. The  $\lambda/2$  waveplate is used to adjust the splitting of the light beam by the following polarizing beamsplitter cube with a ratio of 50/50. Each of the light beams is then guided through an AOM which imprints a frequency

<sup>1</sup> Ultrafast MSM Photodetector

---

shift  $\Delta\omega$  between the two beams. After the AOMs the two beams are aligned on top of each other with an additional polarizing beamsplitter cube. The light is then guided to the experiment by an optical fibre. The  $\lambda/2$  waveplate in front of the fibre is used to set to polarization axis for the polarization maintaining optical fibre.

At the experiment table, the light is collimated to a beam waist of  $w_0 = 1.7$  mm and guided to the experimental vacuum chamber. The lattice beam is aligned on top of leg 2 of the crossed optical dipole trap via a dichroic mirror. The mirror features a high transmittivity for  $\lambda = 1070$  nm, the wavelength of the dipole trap, and a high reflectivity for  $\lambda = 780$  nm. The light passes through the vacuum chamber and is decoupled from the dipole trap beam with an additional dichroic mirror. The light is reflected by a mirror and passes through a  $\lambda/4$  waveplate twice. The induced polarization rotation creates the desired combination of lattice beams for double Bragg diffraction. To optimize the spatial overlap of both lattice beams, the retro-reflected beam is again guided into the optical fibre. The spatial overlap is ideal once the maximum transmission of the retro reflected beam is achieved.

To create the desired frequency difference  $\Delta\omega$  between the two lattices, two AOMs are operated by a pair of synthesizers<sup>2</sup>. Each synthesizer offers a synchronization out-/input to synchronize the synthesizers with respect to each other. The frequency error of each synthesizers is 10 Hz. Each output of the synthesizers is connected to a power splitter-combiner<sup>3</sup> separately to offer a fast and reliable way of controlling the pulse form. The control input of the power splitter-combiners is connected to programmable waveform generators<sup>4</sup>. Depending on the input signal at the control port, the synthesizer signal can pass through the output port to the AOM amplifiers. Since the suppression of the power splitter-combiner is not sufficient to eliminate spontaneous scattering completely a mechanical shutter is installed to block the light completely. The home-built amplifiers increase the power to the needed level to drive the AOMs.

The experimental control of the optical lattice is covered by three independent LabView Vis [98], each having a discrete function to program and trigger the desired pulse shape for the optical lattice. The desired pulse shape for each waveform generator is programmed with a LabView Vi via GPIB. The Vi offers a programming interface in which arbitrary pulse shapes can be configured and joined to complex pulse trains. Each part of the pulse train can be adjusted independently. The Vi disassembles the pulse train to discrete time steps and converts them to the appropriate format for the waveform generators. Because GPIB offers parallel programming of multiple devices at once the pulse needs to be sent only one time. This step only defines the shape of the programmed pulse

---

<sup>2</sup> Hewlett-Packard, 8657A

<sup>3</sup> Mini-Circuits ZSC-2-1+

<sup>4</sup> Agilent 33120A

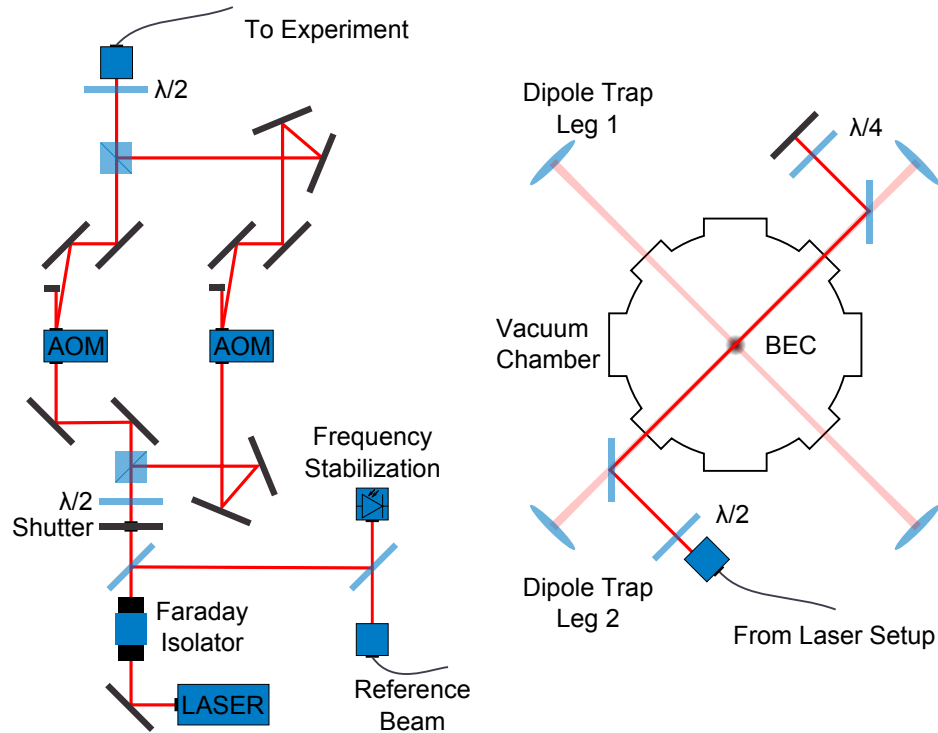


**Figure 3.8:** Optical setup for a one-dimensional optical lattice. The light is provided by an interference filter stabilized diode laser that is offset stabilized to a reference beam. The light is split and guided through two AOMs in order to imprint a frequency shift  $\Delta\omega$ . After recombining the two light beams the light is guided to the experiment with an optical fibre. The light is then aligned on top of leg 2 of the crossed optical dipole trap and later retro-reflected. The  $\lambda/4$  waveplate creates the polarization rotation of  $\pi$  required for a double Bragg lattice.

but no information on frequency or amplitude is given to the devices. Instead a second  $V_i$  is used to set these parameters. This has the advantage that they can be changed quickly. The initialization procedure ensures that the pulse is only triggered once for each external trigger pulse. After this procedure the system is ready to be used. The trigger mechanism is embedded in the main laboratory  $V_i$  via a digital output channel of a National instrument control card. This enables a seamless usage of the lattice in the normal experiment procedure. Once the trigger pulse is sent from the experimental control to the waveform generator the generator releases the pre-programmed waveform. To ensure that the light pulse reaches the atoms as desired the mechanical shutter in front of the AOMs is opened 2 ms in advance to impede influences of jitters during the opening procedure of the shutter.

This setup enables a maximum control of the lattice light pulses and ensures that each cycle performs the same. In principle this setup is able to implement pulse times as short as  $5 \mu\text{s}$ . Following Eq. (3.5) the used pulse time  $\tau$  did not fall below  $21 \mu\text{s}$  in the experiment. The programmable waveform generators offer a simple way to alter the pulse shape to the requirements of the experiment. As an addition an intensity stabilization for the lattice beams would reduce day-to-day fluctuations of laser power and thus accompanying fluctuations of lattice pulses. Without stabilization the pulses have to be adjusted every day to operate as desired, which is especially important for interferometric measurements (see Sec. 3.7).

---

### 3.3.2 Observing double Bragg diffraction experimentally

---

To observe double Bragg oscillations a cloud of condensed atoms was formed in the crossed optical dipole trap (see Sec. 2.3.2). After condensation, the trapping potential was switched off immediately and the trigger is sent to the pulse generator for double Bragg pulses. All the atoms are in the momentum state  $|0\hbar k\rangle$ . The atoms then interact with the optical lattice for variable times  $\tau$ . The lattice beams were adjusted to a power of  $230 \mu\text{W}$  each and the frequency difference is  $\Delta\omega = 2\pi \times 15.08 \text{ kHz}$ . Eq. (3.18) this yields a oscillation frequency of  $\Omega_{\text{eff}} = 2\pi \times (1.09 \pm 0.06) \text{ kHz}$  for  $\omega_D = 0$ . To further minimize non-adiabatic oscillations a Gaussian pulse shape was chosen. After the application of the lattice pulse an additional waiting period of 18 ms was applied. During this time the momentum distribution causes a visible separation of the atomic clouds. According to their position each cloud can be attributed to the appropriate state. The population of each momentum state can be determined by fitting a Gaussian distribution to each cloud. The relative population is determined by dividing the population of a cloud by the accumulated population of all clouds.

Fig. 3.9 shows the population oscillation caused by the application of a double Bragg pulse of the length  $\tau$ . On top of the figure are the absorption images

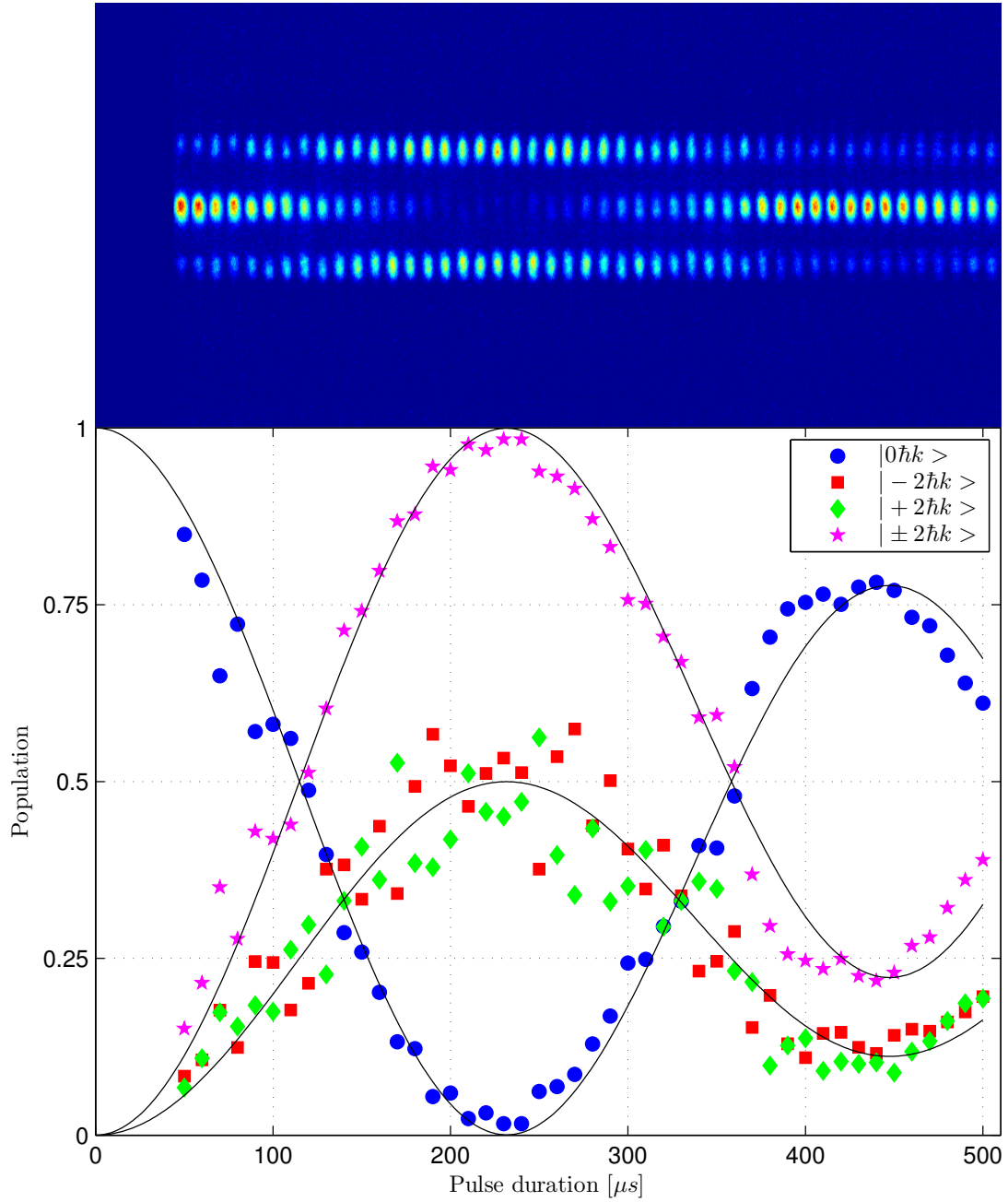


**Figure 3.9:** Double Bragg oscillations: A double Bragg pulse with  $n = 1$  was applied for the duration  $\tau$ . The population for  $|0\hbar k\rangle$ ,  $|-2\hbar k\rangle$ , and  $|+2\hbar k\rangle$  are shown as well as the combined population of  $|\pm 2\hbar k\rangle$ . Underlying the solution of Eq. (3.29) for each momentum state with  $\Omega_{\text{eff}} = 2\pi \times (1.09 \pm 0.06)$  kHz for  $\omega_D = 0$ . Each data set is accompanied by the correspondent absorption image and the time between each measurement is  $10 \mu\text{s}$ .

acquired in the measurements, taken in steps of  $10\ \mu\text{s}$ . Starting with  $50\ \mu\text{s}$  a transfer of atom population towards  $|\pm 2\hbar k\rangle$  begins. After  $230\ \mu\text{s}$  a full population transfer to  $|\pm 2\hbar k\rangle$  is achieved. Due to the special definition of the double Bragg pulses this pulse is defined as a  $\pi/2$ -pulse. This pulse demonstrates a beam-splitter of very high fidelity that can be utilized for matter wave interferometry (see Sec. 3.7). Due to the definition of the oscillation frequency  $\Omega$  for double Bragg diffraction this time is, by a factor of  $\sqrt{2}$ , longer than a  $\pi/2$  pulse for standard Bragg diffraction. For twice the time we would expect to reverse the momentum distribution, thus applying a  $\pi$  pulse. Instead of a full population of  $|0\hbar k\rangle$  we observe that 25% remain in the respective states  $|\pm 2\hbar k\rangle$ . This situation can be explained by the momentum distribution of the BEC itself. The velocity selectivity of Bragg diffraction causes a dephasing in the oscillation between the three momentum states. In addition the calculated oscillation frequency  $\Omega_{\text{eff}}$  falls short behind the measured oscillation period. The dephasing not only inhibits an effective population transfer but also changes the mean frequency to higher frequencies. Following Eq. (3.31) and with a momentum width of  $\sigma_p = 0.1\hbar k$  this yields a Doppler shifted frequency of  $\Omega_{\text{Doppler}} = 2\pi \times 1146\text{Hz}$ . This effect is well understood and will be covered in detail in Sec. 3.5.

Also more than 99% of the total number of atoms is transferred to the anticipated state, a clear variation in population transfer to the single states  $|-2\hbar k\rangle$  and  $|+2\hbar k\rangle$  can be seen. This can be attributed to intensity fluctuations and fluctuations of the polarization during the transport of the light to the experiment. For Fig. 3.9 two measurements were performed for each data point. To further suppress intensity fluctuations an active intensity stabilization would significantly improve the stability of the system. Also day-to-day variations, and therefore changing oscillation periods, would diminish. Because of the special setup for double Bragg diffraction an intensity stabilization, as normally used in the group [61], would be hard to implement. Because two perpendicularly linear polarized beams are guided through one optical fibre a polarizing beamsplitter would be of no use. One possible solution would be to use a polarization independent pick-up which could be used to branch a fixed laser intensity of the main lattice beam line. One of these non-polarizing beamsplitters is already used for the creation of ring potentials (see Chapter 5) but features an unusable division ratio of 50/50. This light could then be used to stabilize each polarization independently with an additional polarizing beamsplitter. Additional fluctuations of the population oscillation are introduced by polarization modifications imprinted by mechanical stress in the optical fibre. An polarizing beamsplitter after the optical fibre in conjunction with a  $\lambda/2$  waveplate is generally used to purify the polarization after an optical fibre. This is not possible with two perpendicular polarized light fields travelling through the fibre. The lack of an additional polarization selective element yields could increase cross-talk between the two optical lattices of double Bragg diffraction.

---

### 3.4 Higher-order double Bragg diffraction

---

Higher-order Bragg diffraction offers the possibility to accelerate atoms to multiple momenta of  $2\hbar k$ . The maximum momentum transfer achieved at the ATOMICS experiment has been  $12\hbar k$  [83] and is equivalent to a velocity of 140 mm/s. Higher momentum transfer is advantageous for atom optics since shorter transfer times can be realised. For guided matter waves this reduces interaction times and thus limits losses due to spontaneous scattering or collisions with the background gas. Higher-order Bragg diffraction is achieved by choosing  $\Delta\omega$  according to Eq. 3.1. The higher frequency difference yields a faster oscillation of the standing wave formed by the lattice beams and therefore reduces the minimum lattice pulse duration. To generate  $\pi/2$  and  $\pi$  pulses the lattice depth has to be chosen appropriately.

This section will demonstrate the implementation of double Bragg pulses of the order  $n = 2$  and  $n = 3$ . For  $n = 3$ , the atoms are accelerated to a velocity of 23.53 mm/s. Additionally Table A.2 features a compilation of experimental values to help find the appropriate settings for future experiments.

---

#### 3.4.1 Second-order double Bragg diffraction

---

Second-order Bragg diffraction is achieved by choosing a frequency difference of  $\Delta\omega = 8 \times \omega_R = 2\pi \times 30.17\text{kHz}$ . The experiment was performed in a similar fashion to previous double Bragg experiments. After Bose-Einstein condensation the atoms were released from the trap by switching the trap off completely. A lattice pulse of variable time  $\tau$  was applied. An additional waiting time of 18 ms after this ensured a macroscopic spatial separation of the ensembles according to the momentum difference. The population of each cloud was determined by fitting a Gaussian distribution to each of the evolving clouds separately. The relative population was calculated by taking into account all atoms for normalisation. In contrast to first-order double Bragg diffraction more than the expected ensembles of atoms with a momentum of  $4\hbar k$  and  $-4\hbar k$  develop. Additionally ensembles with  $+2\hbar k$  and  $-2\hbar k$  show a not negligible population. In previous experiments, non-desired momentum states were populated if too deep lattices were used. This behaviour showed population of  $|\pm 4\hbar k\rangle$  for Bragg diffraction even when the resonance has been set to excite  $|\pm 2\hbar k\rangle$ . By choosing a shallower lattice these excitation can be suppressed. For second-order Bragg diffraction, the observed excitation of lower momentum states hints a too shallow lattice, even if these states are not in resonance. Changing the offset lock detuning of the lattice to  $\Delta\omega_L = 500\text{MHz}$  yields a deeper lattice and therefore higher oscillation frequencies. Even though an increasing scattering rate limits the maximum pulse duration, the efficiency for short pulses could be increased. For future experiments with higher-order Bragg diffraction an increased overall laser power of the lattice could be favourable.

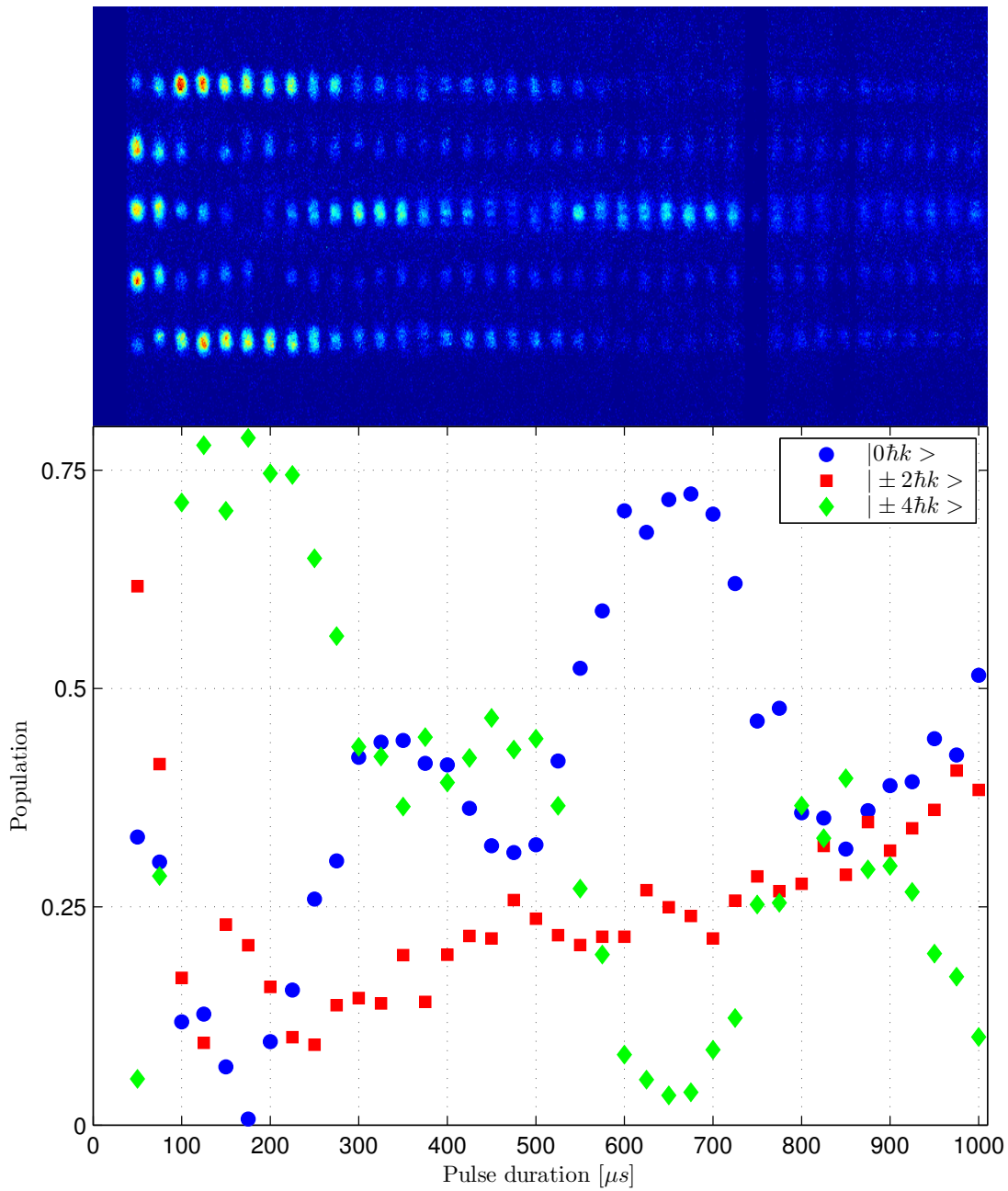


**Figure 3.10:** Population oscillation of atom momentum states after second-order double Bragg diffraction pulses of varying duration. A maximum of 77% of atoms are transferred into  $|\pm 4\hbar k\rangle$ .  $|\pm 2\hbar k\rangle$  is suppressed for short pulse durations but after 900 μs each momentum state is populated nearly equally. Measurements are taken every 25 μs.

Alternatively the width of the lattice beams could be reduced to increase the intensity at the position of the atoms.

Fig. 3.10 shows the population oscillation of second-order double Bragg diffraction. On top of the plotted population oscillation are the corresponding density distributions after 18 ms waiting time. Each data point is an average over two independent measurements. The shortest pulse duration used was  $50 \mu\text{s}$ . After  $180 \mu\text{s}$  77% of the atoms were transferred from  $|0\hbar k\rangle$  to  $|\pm 4\hbar k\rangle$ . This is the maximum efficiency achievable in the experiment. The rest of the atoms populate  $|2\hbar k\rangle$ . State  $|0\hbar k\rangle$  is completely depopulated. The pulse length of  $180 \mu\text{s}$  would be equivalent to a  $\pi/2$  pulse in this system. Due to the lack of laser intensity stabilization for the lattice beam this value has to be adjusted for each experimental measurement series to guarantee the best splitting efficiency. The high population of  $|2\hbar k\rangle$  indicates that the laser power, and consequently the lattice depth, are not sufficient to couple the momentum states. This has also been observed in previous experiments with Bragg diffraction [65]. Changing the detuning  $\Delta\omega_L$  of the frequency stabilization even closer to the resonance elevates scattering processes even more and makes observing double Bragg diffraction impossible.

According to the pulse duration of  $180 \mu\text{s}$  for a  $\pi/2$  pulse the duration of  $360 \mu\text{s}$  should be equivalent to a  $\pi$  pulse and create a complete oscillation of all of the atoms back to  $|0\hbar k\rangle$ . Fig. 3.10 shows that this is not the case. Instead only 40% of the atoms populate  $|0\hbar k\rangle$  and the remaining atoms occupy  $|\pm 2\hbar k\rangle$  and  $|\pm 4\hbar k\rangle$ . Roughly 40% of the atoms occupy  $|0\hbar k\rangle$  and 20% of the atoms occupy  $|\pm 2\hbar k\rangle$ . This behaviour originates from the velocity selectivity of double Bragg diffraction and is discussed in Sec. 3.4. The momentum distribution of the cloud yields a different  $\Omega_{\text{eff}}$  for each of the momenta present in the cloud. Additionally the population of  $|\pm 2\hbar k\rangle$  rises steadily and reduces the quality of the oscillation between  $|0\hbar k\rangle$  and  $|\pm 4\hbar k\rangle$ . After 1 ms the amount of atoms in  $|\pm 2\hbar k\rangle$  matches the population of  $|0\hbar k\rangle$  whereas the population of  $|\pm 4\hbar k\rangle$  shows oscillations with a reduced amplitude. The dampening effect can also be explained by the Fourier width of the lattice beam pulse (see Sec. 3.5). On top of these effects, spontaneous scattering through the Bragg beams reduces the total atom number and longer pulse durations cannot be evaluated.

---

### 3.4.2 Third-order double Bragg diffraction

---

As described in Sec. 3.4.1 higher-order Bragg diffraction is possible. In addition to second-order Bragg diffraction third-order Bragg diffraction has been successfully implemented. Similar to second-order Bragg diffraction, the key point limiting longer population oscillations is spontaneous scattering of photons. Due to the shallow lattice potential the coupling strength decreases for higher-order double Bragg diffraction. This is also the case for Bragg diffrac-

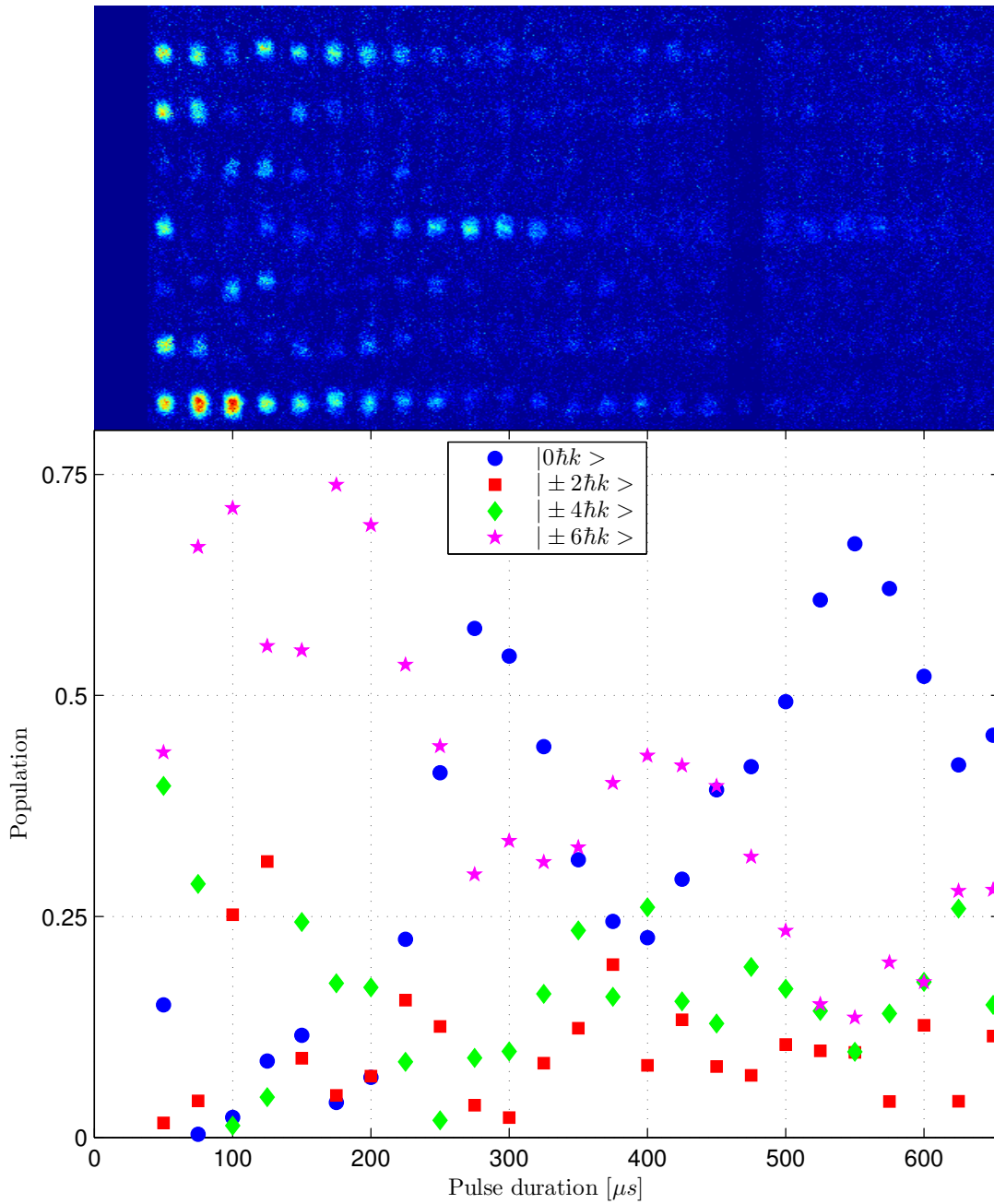


**Figure 3.11:** Double Bragg diffraction of the order  $n = 3$ . The population of  $|\pm 6\hbar k\rangle$  reaches a maximum after  $\tau = 170 \mu\text{s}$ . Longer pulses show an increasing amount of non-desired momentum states and a loss of contrast due to a decreasing atom number. Measurements are taken every  $25 \mu\text{s}$ .

tion [77]. First experiments were carried out with a stabilized lattice laser with  $\Delta\omega_L = 250$  MHz. The increased lattice depth should make efficient oscillations possible but no oscillation measurements could be performed. Decreased contrast and loss of atoms due high scattering rates could not be compensated. As a consequence, the measurements presented in this section were carried out with  $\Delta\omega_L = 500$  MHz.

To achieve resonant momentum transfer to  $|\pm 6\hbar k\rangle$  the detuning of the lattice beams was chosen to be  $\Delta\omega = 12 \cdot \omega_R = 2\pi \times 45.3$  kHz. After the BEC generation and release from the crossed optical dipole trap the lattice pulse was applied for variable duration. The density distribution was detected after an additional time of 18 ms of free expansion.

---

### 3.4.3 Quality of Bragg diffraction beamsplitters

---

Fig. 3.11 shows the population of each momentum state after varying pulse durations  $\tau$ . On top, the density profiles of the atoms after the application of the lattice pulse and the following free expansion time are shown. Each data point is averaged over two measurements. Similar to Sec. 3.4.1 the atoms are not only occupying  $|0\hbar k\rangle$  and  $|\pm 6\hbar k\rangle$  after the light pulse, but  $|\pm 2\hbar k\rangle$  and  $|\pm 4\hbar k\rangle$  are populated as well. Already after  $50 \mu\text{s}$ , the shortest lattice pulse duration, 85% of the atoms are occupying other states than  $|0\hbar k\rangle$ . After  $170 \mu\text{s}$  74% of the atoms populate  $|\pm 6\hbar k\rangle$  and a low population of all other states can be observed. After the maximum population transfer to  $|\pm 6\hbar k\rangle$ , and therefore a  $\pi/2$  pulse, the population reoccupies  $|0\hbar k\rangle$  after  $180 \mu\text{s}$  with a maximum of 75%. The overall population of the non-desired momentum states is increasing as the pulse duration increases. As before the lack of laser power and the probability of non-resonant excitation of unwanted transitions cause towards this behaviour. The oscillations of  $|\pm 6\hbar k\rangle$  shows an increased dampening effect in regard to lower-order double Bragg diffraction. The total atom number decreases steadily and after  $650 \mu\text{s}$  the remaining atoms do not give a sufficient signal for further analysis. In conclusion symmetric splitting of ultra-cold atoms clouds is possible with higher-order double Bragg diffraction. Up to 77% and 75% are transferred into the accelerated momentum states  $|\pm 4\hbar k\rangle$  and  $|\pm 6\hbar k\rangle$  respectively. The loss in efficiency is explainable by the frequency width of the laser, the lack of laser power provided by the laser used for the optical lattice, and the large beam waists of the lattice beams.

Fig. 3.12 shows a compilation of beamsplitters obtained with double Bragg diffraction. The top image shows the BEC after its creation in the crossed optical dipole trap and an additional free expansion time of 18 ms. The following images show the density distribution after the application of a  $\pi/2$  lattice pulse and an additional waiting time of 18 ms. From top to bottom the order of Bragg diffraction increases from one to three. First-order Bragg diffraction achieves

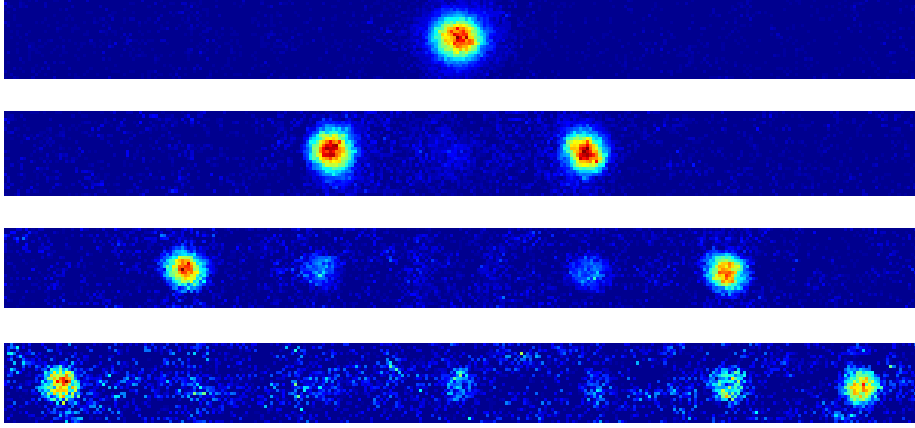


**Figure 3.12:** Experimental images demonstrating the quality of double Bragg diffraction as a matter wave beamsplitter. The initial resting BEC after the evaporation process is shown at the top. The following pictures show a  $\pi/2$  pulse for beamsplitters of  $n = 1, 2, 3$  respectively. The maximum efficiency for  $n = 1$  is 99%, for  $n = 2$  it is 77%, and for  $n = 3$  it is 75%.

creates a symmetric splitting in the momentum states  $|\pm 2\hbar k\rangle$ . For  $\tau = 230 \mu s$  a  $\pi/2$  pulse with an efficiency of 99%. Second-order Bragg diffraction splits the atomic ensembles into the momentum states  $|\pm 4\hbar k\rangle$  with an efficiency of 77%. The pulse duration is  $\tau = 180 \mu s$ . Third-order Bragg diffraction shows a symmetric splitting after  $\tau = 170 \mu s$ . The  $\pi/2$  pulse creates a symmetric momentum distribution of the states  $|\pm 6\hbar k\rangle$  with an efficiency of 75%.

The absolute efficiency of double Bragg diffraction is also limited absolute atom count after the application of the lattice pulse. Fig. 3.13 shows the relative atom count after the application of a double Bragg pulse. The atom count is normalized to the initial atom count of the experiment. Higher-order Bragg diffraction shows faster decay in atom number. Even though the momentum transfer to the desired momentum state is still highly efficient the total atom number decreases and reduces the applicability of double Bragg diffraction as an experimental tool for matter wave manipulation. This is especially relevant for momentum transfer to  $|\pm 6\hbar k\rangle$ , where less than 20% of the atoms are present after a pulse duration of  $600 \mu s$ . The main experimental difference between first-order and higher-order Bragg diffraction has been the reduced detuning of the lattice beams in respect to the  $D_2 F = 2 \rightarrow F' = 2$  transition of  $^{87}\text{Rb}$ . As displayed in Eq. (2.1) the scattering rate increases for a decreased detuning. The detuning for higher-order lattice beams has been reduced from 750 MHz to 500 MHz which increases the scattering rate significantly. Also the beam intensity has been adjusted to higher values, which further increases the scattering rate and therefore reduces the atom count. The underlying solid curves represent exponential fits giving the exponential decay rate  $\lambda$  (see Eq. (2.1)).

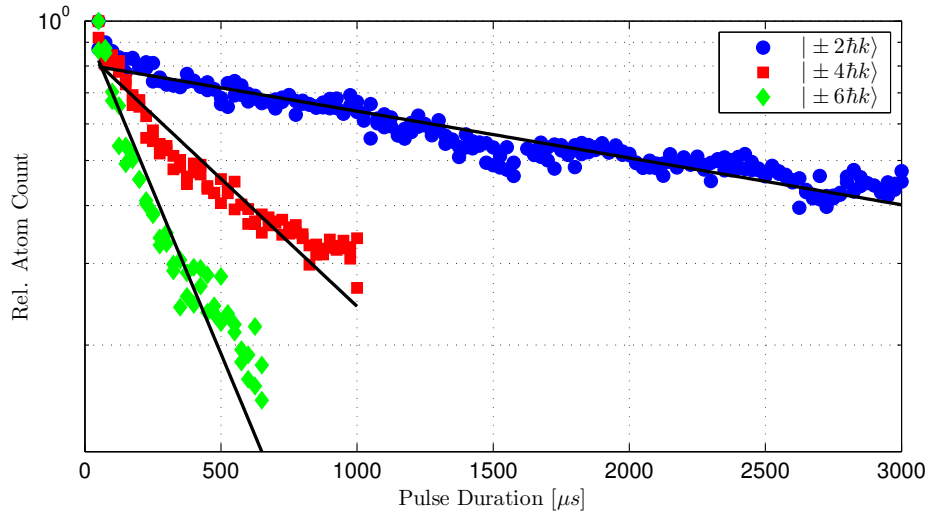


**Figure 3.13:** Atomcount after the application of a double Bragg lattice pulse for varying duration. Different orders of double Bragg diffraction are shown. The detuning of the lattice beams in respect to the  $D_2$   $F = 2 \rightarrow F' = 2$  transition of  $^{87}\text{Rb}$  has been reduced from 750 MHz to 500 MHz for momentum transfer to  $|4\hbar k\rangle$  and  $|6\hbar k\rangle$ .

3.1 shows the compiled experimentally obtained and calculated values. The decay rate  $\lambda$  is by a factor of at least two smaller than the calculated scattering rate. Thus the scattered atom does not immediately yield atom losses, but multiple scattered photons induce heating of the cloud and accelerate expansion and dilution of the ensemble. The experimental procedure of fitting Gaussian distributions to the imaged density distribution also neglects very shallow densities at the edge of each atomic ensemble, the location where heated atoms would be positioned. For future applications of double Bragg diffraction these atoms would be less desirable to use because the overall momentum width of the ensemble increases. A small momentum width of an atomic ensemble is favourable for transport and interferometric measurements. In addition exponential fits of first-order do not take into account losses due to many-body interactions, the fits do not fully describe the behaviour of the system. Due to the low detuning in the order of 750 MHz far-off resonant heating of atoms can be excluded as a reason for increased atom losses [99]. Instead  $\lambda$  gives an upper bound for the atom losses in the system and show that the loss rate scales with increasing intensity and decreasing detuning. Both parameters can be accommodated experimentally to reduce losses due to spontaneous scattering.

Order n	Detuning [MHz]	Optical Power P [ $\mu W$ ]	Scattering Rate (calculated) $\Gamma_{SC}$ [ $s^{-1}$ ]	Decay Rate $\lambda$ [ $s^{-1}$ ]
1	750	230	1467	$232 \pm 9$
2	500	300	4300	$1268 \pm 113$
3	500	500	7160	$3240 \pm 298$

**Table 3.1:** Compilation of experimentally obtained decay rates  $\lambda$  of the atom number after a double Bragg pulse. Additionally the calculated scattering rate  $\Gamma_{SC}$  (see Eq. (2.1)) is given. The scattering rate was calculated for the maximum intensity of a Gaussian beam.

### 3.5 Influences of the BEC momentum distribution on double Bragg diffraction

The experimental realisation of double Bragg diffraction as described in Sec. 3.3.2 showed that a beamsplitter with 99% efficiency has been implemented successfully. A mirror for atoms was implemented but showed a decrease in efficiency and part of the atoms reside in the accelerated state instead of completely populating state  $|0\hbar k\rangle$ . This section discusses the influence of the pulse length of the lattice beams as well as the momentum distribution of the atomic cloud in the experiment and shows that they contribute to the decreased efficiency of a double Bragg mirror.

#### 3.5.1 Fourier width of a Gaussian lattice pulse

The spectral composition of a pulse is determined by the length  $\tau$  and the shape of the pulse itself [100]. On one hand, the longer a pulse is the narrower its spectral distribution becomes. On the other hand, the shorter a pulse is the broader its spectral width becomes. The frequency distribution of the pulse can enter a regime in which it is smaller than the width of the spectral response of an atomic ensemble. The distribution of spectral response in the atomic clouds originates from the mean-field expansion where each momentum component can be assigned to a specific frequency  $\omega_D$  due to its doppler shift (see Eq. (3.27)).

Fig. 3.14 shows the two examples for different pulse durations. At top, two Gaussian envelopes for lattice pulses are shown. The red pulse symbolizes a short pulse, whereas the blue one symbolizes a long pulse. Each of the pulses is applied to a BEC with a fixed momentum distribution, that are symmetric around zero momentum. Depending on the pulse length the width of the pulse in the frequency domain changes. The longer a pulse gets, the smaller the frequency width gets. In the picture of Bragg diffraction, a non-zero momen-

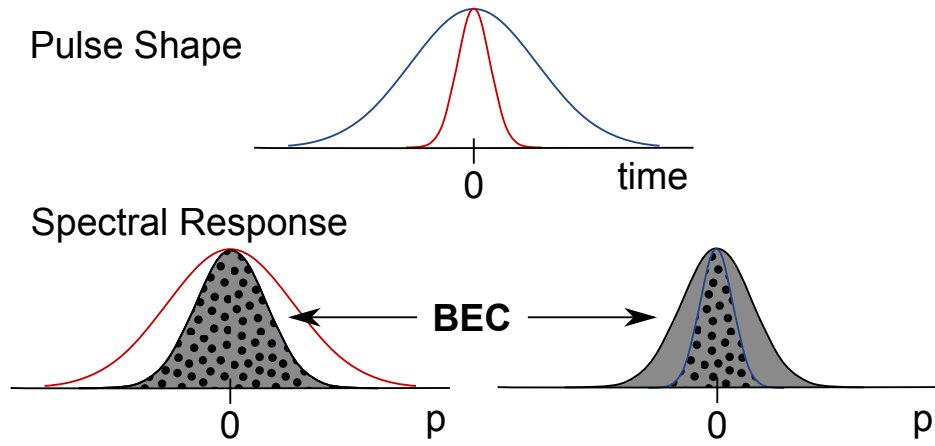


**Figure 3.14:** Schematic drawing of double Bragg diffraction and the influences of pulse length on the selectivity of a lattice pulse. A short (red) lattice pulse features a broad frequency spectrum and therefore covers the complete BEC frequency distribution. A long (blue) lattice pulse has a narrow frequency distribution and only part of the BEC is accelerated by the lattice pulse. The grey area shows the atomic ensembles whereas the dotted area depicts the fraction of atoms influenced by the lattice pulse.

tum corresponds to a frequency shift  $\omega_D$ , due to the Doppler effect, and can be calculated via Eq. (3.27). The red pulse is short and therefore the pulse in the momentum domain is wide enough to interact with the complete BEC momentum distribution. The blue Gaussian envelope on the other hand has a momentum width smaller than the BEC and selects the centre piece of the Bose-Einstein condensate. The remainder of the atoms is not affected by the pulse. If we consider a standard Bragg or double Bragg diffraction experiment this results in a fraction of the atoms being accelerated and part of the atoms remaining at rest.

To describe the momentum distribution it is approximated with a Gaussian distribution:

$$N_{\text{BEC}}(\omega) = N_0 e^{-\frac{1}{2} \left( \frac{\hbar k \omega}{2\omega_R \sigma_p} \right)^2} \quad (3.33)$$

$N_{\text{BEC}}$  gives the fraction of the total number of atoms  $N_0$  with a given initial momentum of  $\hbar k \omega_D / 2\omega_R$ . The momentum width of the distribution is described by the parameter  $\sigma_p$ . Because the momentum profile of a BEC is quadratic a Gaussian approximation introduces errors. These errors depend on the interaction strength of the species and are not significant for future discussion [61]. To limit non-adiabatic excitation of momentum states in optical lattices Gaussian envelopes are used for light pulses [83]. The width of a Gaussian distribution is given by the width  $\sigma_t$ . The relation to the pulse duration to the width of the

pulse in the momentum domain is called time-bandwidth product and given by [100]:

$$\text{FWHM}_t \times \text{FWHM}_\nu \approx 0.44. \quad (3.34)$$

The product of the full width half maximum (FWHM) in the time domain ( $t$ ) or frequency domain ( $\nu$ ) shows to be constant. In order to calculate the fraction of atoms interacting with a light pulse of length  $\tau$ , the width of the pulse in the momentum domain  $\text{FWHM}_p$  has to be calculated. The pulse width in the momentum domain defines the bounds  $\chi$  for the integration over the momentum distribution:

$$\chi = 3 \times \frac{\text{FWHM}_p}{2\sqrt{2 \ln 2}} = 3 \times \frac{0.44/\text{FWHM}_t}{2\sqrt{2 \ln 2}}. \quad (3.35)$$

It is assumed that every atom inside the  $3\sigma$  environment of the momentum distribution is interacting with the light pulse. The relation of the full width at half maximum is  $\text{FWHM} = 2\sqrt{2 \ln 2}\sigma$ . The fraction of atoms can now be calculated using:

$$N_F(t) = \frac{\int_{-\chi}^{\chi} N_{BEC}(\omega) d\omega}{\int_{-\infty}^{\infty} N_{BEC}(\omega) d\omega}. \quad (3.36)$$

The fraction of atoms manipulated by the pulse is given by  $N_F$  whereas the remainder is not interacting. For Bragg diffraction this means that the atoms are accelerated or stay in place without achieving a momentum transfer. Fig. 3.15 shows numerical evaluation of Eq. (3.36). Depending on the momentum width  $\sigma_p$  and the pulse duration  $\tau$ , the maximum efficiency of a pulse is modified. For typical momentum width of a BEC in the ATOMICS experiment of  $\sigma_p = 0.2 \hbar k$  a pulse duration of less than  $\tau = 500 \mu s$  has to be used to achieve a complete momentum transfer with respect to the Fourier width of the pulse. Using longer pulse durations yields a decrease in efficiency.

This effect does not only inhibit the usage of Bragg diffraction but also gives the possibility to examine specific parts of the BEC by applying long pulses on purpose. This method is called Bragg spectroscopy [79] and is discussed in the next section.

---

### 3.5.2 Bragg spectroscopy of a Bose-Einstein condensate

---

The calculated maximum efficiency of a lattice pulse calculated in 3.5.1 not only limits the applicability of Bragg diffraction and double Bragg diffraction. The limited efficiency can also be used to get detailed information on the momentum distribution of the BEC. Given a fixed detuning of  $\Delta\omega = 4 \times \omega_R$  and a pulse length of at least 1 ms only the central part of the momentum distribution of a BEC is taking part in Bragg diffraction. After waiting an appropriate amount of time the atomic clouds separate according to their mean momenta.

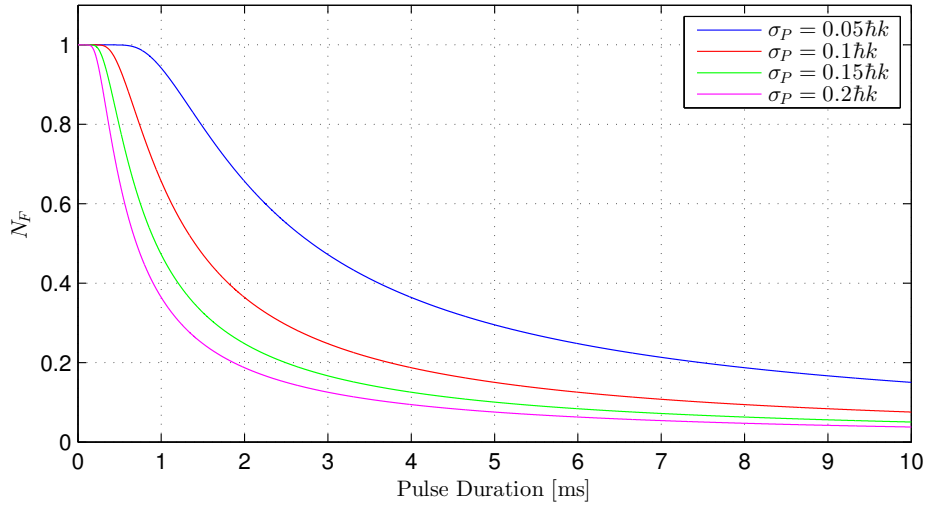


**Figure 3.15:** Fraction of atoms  $N_F$  being accelerated by a lattice pulse depending on the momentum width  $\sigma_P$  of the BEC distribution (see Eq. (3.36)). Increasing the momentum width of a BEC shows that the maximum efficiency decreases faster and shorter pulses have to be used in order to guarantee 100 % efficiency.

By imaging the density distribution the fraction of atoms accelerated by Bragg diffraction can be determined. By choosing a  $\pi$ -pulse it is guaranteed that all of the atoms affected by the lattice pulse are accelerated. Due to the velocity selectivity of a Bragg pulse (see Sec. 3.2) it is possible to shift the average momentum of the part of the BEC that is cut out. Atoms with an initial momentum unequal to zero are resonant to different  $\Delta\omega$ . By tuning  $\Delta\omega$  it is possible to image the population of atoms occupying different momenta of the momentum distribution in ultra-cold atom clouds and BECs. Previous experiments (see Sec. 3.3) have shown that the momentum distribution has to be smaller than  $2\hbar k$ . Otherwise ensembles would not separate completely because their width would increase faster than their distance with respect to each other.

The experimental realisation of Bragg spectroscopy was performed in a standard Bragg configuration. In principal double Bragg diffraction would also be viable but increases the difficulty of the analysis due to the splitting in multiple accelerated clouds. After the preparation of a BEC the trapping potential of the crossed dipole trap was switched off immediately. After 2 ms free expansion a lattice pulse of fixed length  $\tau_{BS}$  was applied. The time of 2 ms was chosen to make sure that mean-field expansion has stopped completely and a quadratic phase profile has evolved (see Sec. 2.2.3). Subsequently an additional time of 14 ms passed before detection of the atoms. The pulse duration was chosen to be  $\tau_{BS} = 1.45$  ms, which yields a sufficiently small Fourier width of the lattice pulse to accelerate only a fraction of atoms. Fig. 3.15 shows that the pulse is well in the regime where a reduced efficiency is expected. The pulse intensity

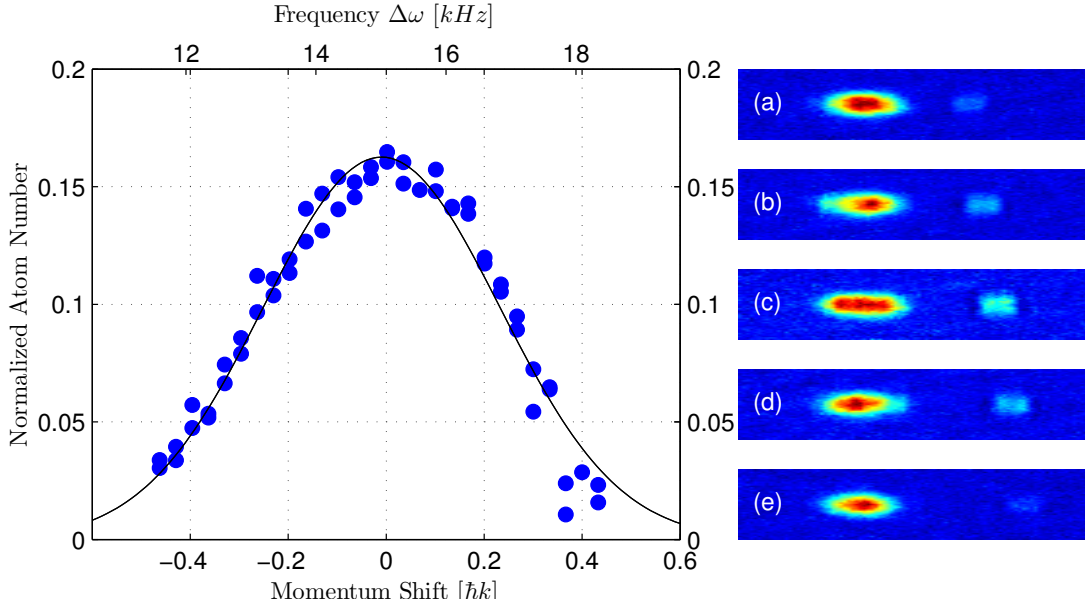


**Figure 3.16:** Experimental realisation of Bragg spectroscopy. A fraction of atoms is accelerated with a lattice pulse of duration  $\tau_{BS} = 1.45$  ms depending on the detuning  $\Delta\omega$  of the lattice beams. The atom count has been normalized to the total atom count in each experimental realisation. The x axis shows the shift relative to a momentum of  $2\hbar k$ . On the right are five experimental images for different values of  $\Delta\omega$ . The accelerated atoms move to the right with a momentum of  $2\hbar k$ . From top to bottom  $\Delta\omega = 2\pi \times (10.61 \text{ kHz}, 13.11 \text{ kHz}, 15.11 \text{ kHz}, 17.61 \text{ kHz}, 20.11 \text{ kHz})$ .

was chosen that the pulse forms an ideal  $\pi$  pulse by maximizing the intensity of the lattice and measuring the fraction of accelerated atoms. To spectroscopically analyse the condensate, the detuning between the lattice beams was modified. Fig. 3.16 shows the fraction of atoms accelerated after by the lattice pulse with  $\tau_{BS}$  depending on the detuning  $\Delta\omega$  of the two lattice beams used for Bragg diffraction. The distribution shows that the maximum section is generated at  $\Delta\omega = 2\pi \times 15.08 \text{ kHz} = 4 \times \omega_R$ , corresponding to atoms at rest. This is the expected behaviour because all the atoms are at rest after evaporation and the mean-field expansion is isotropic (see Sec. 2.2.2). Therefore a maximum fraction of atoms is accelerated and the population of the accelerated ensemble is maximum. The frequency shifted lattice pulse selects a different part of the BEC out of the density distribution. The reduced density causes a reduced signal. The right part of Fig. 3.16 shows a set of experimental images showing the density distribution after the  $\pi$ -pulse the additional waiting time.

Additionally the position of the accelerated ensemble can be associated with the position in the resting ensemble. Lower detuning cuts out a part of the cloud that is more to the right. Since the atoms to the left of the centre have

a negative momentum with respect to the acceleration direction the Doppler shift adds to a total frequency of  $\Delta\omega = 4 \times \omega_R$  giving a perfectly resonant lattice pulse. In the laboratory frame, this part of the cloud has a lower velocity compared to a section of the central part of the distribution. The momentum difference yields a displaced position of the accelerated ensemble.

Fig. 3.16 shows the population  $N_0$  of atoms coupled out of the atomic cloud. The distribution is centred at a momentum of  $2\hbar k$  and the  $x$  axis shows the momentum shift relative to  $2\hbar k$ . The fitted Gaussian (Eq. (3.33)) distribution in Fig. 3.16 features a momentum width of  $\sigma_p = (0.24 \pm 0.03) \hbar k$ . This value shows that we are well under the momentum of  $2\hbar k$  that is imprinted on the atoms by Bragg diffraction and double Bragg diffraction. Depending on the evaporation depth of the crossed dipole trap the momentum width can be tuned. Colder atomic ensembles feature a narrower momentum distribution. In the BEC regime, the population of the ground state and the atom number in general have to be taken into account and the momentum width cannot be chosen independently.

To further calculate the impact of velocity selectivity, the momentum width  $\sigma_p$  is used in Sec. 3.5 to show that the effectiveness of double Bragg diffraction is not limited by the experimental implementation but by the momentum distribution of the Bose-Einstein condensate produced in the experiment. To investigate broader momentum distributions a switch to higher orders of Bragg diffraction can be made in order to create a macroscopic separation of the two atomic ensembles.

---

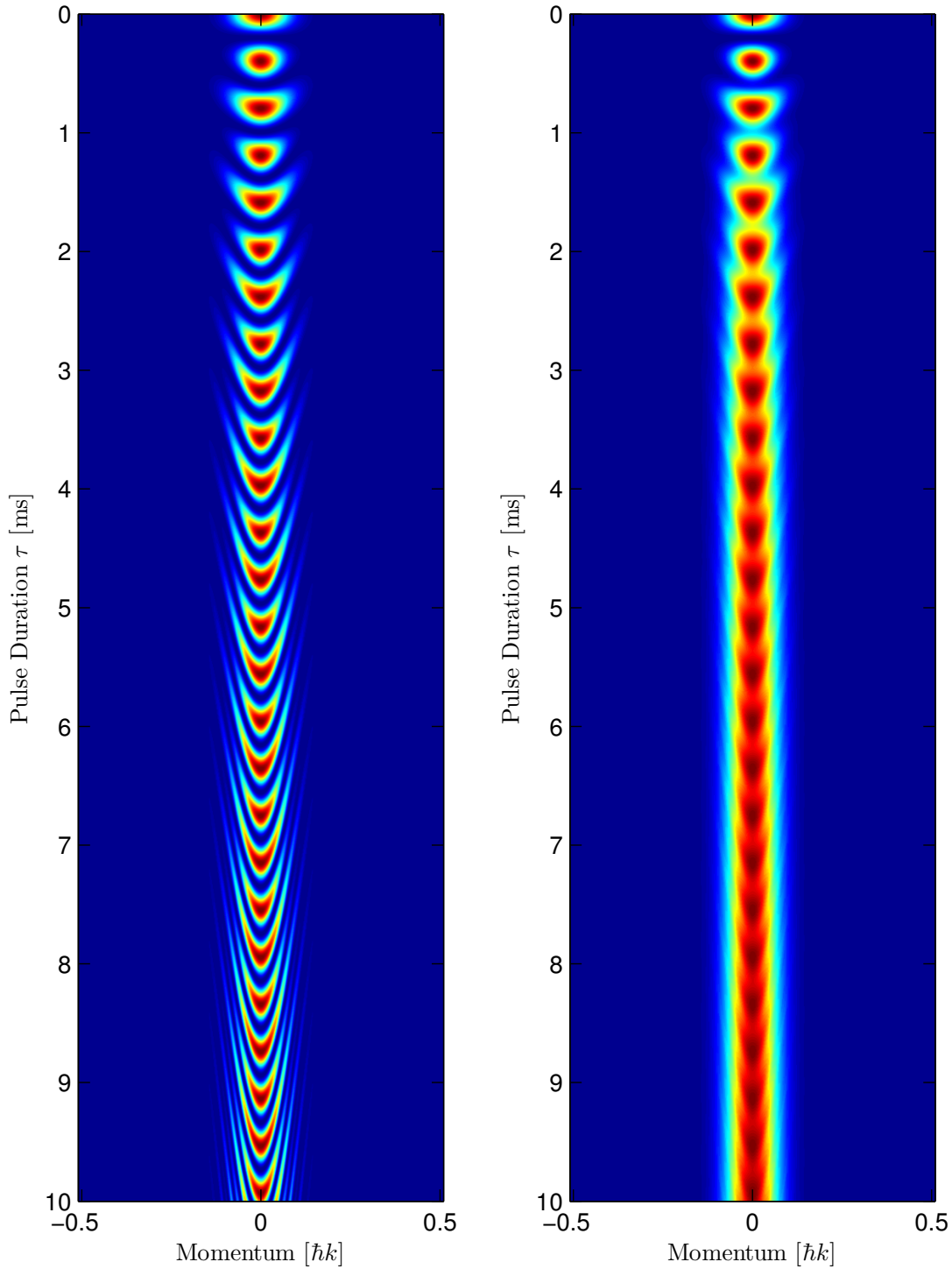
### 3.5.3 Experimental realisation of long-pulse double Bragg diffraction

---

As previously described in Eq. (3.29) the momentum distribution of the atomic cloud is important for the achievable efficiency of double Bragg diffraction. Fig. 3.17 shows the solution of Eq. (3.29) for the state  $|0\hbar k\rangle$  for different momentum shifts weighted by the number of atoms in the BEC with this momentum (see Sec. 3.5.2). It is given as the product of Eq. (3.29) and Eq. (3.33):

$$N_0(t, \omega_D) = \gamma_0(t, \omega_D) \times N_{\text{BEC}}(\omega_D) \quad (3.37)$$

The centre of the distribution of  $\omega_D = 0$  follows the simple solution of Eq. (3.25) and does not experience a modified Rabi frequency, thus  $\Omega_{\text{eff}} = \Omega$ . Depending on the initial momentum the Rabi frequency  $\Omega_{\text{eff}}$  gets shifted towards faster oscillations. Each part of the atomic cloud executes a complete momentum transfer between full population and depopulation and no loss in efficiency is happening. The width is sufficiently narrow. Since a real atomic cloud shows a multitude of different initial momenta the sum over all population oscillations has to be considered. Fig. 3.17(a) shows the time evolution of the population of  $|0\hbar k\rangle$ , which are Rabi oscillations of  $|0\hbar k\rangle$  weighted by the relative occupation



(a) Solution of Eq. (3.37)

(b) Solution of Eq. (3.38)

**Figure 3.17:** Population of state  $|0\hbar k\rangle$  depending on the initial momentum width  $\sigma_p = 0.1 \hbar k$  of the atoms and the Fourier width of the lattice pulse. (a) shows the solution of Eq. (3.37) and (b) the solution of Eq. (3.38) for the same input parameters. Colour Coding: High population (red) and no population (blue).

of a fixed momentum distribution width  $\sigma_p = 0.1 \hbar k$ . The value of  $\sigma_p$  has been derived by a numerical fit of Eq. (3.29) to the experimentally obtained double Bragg induced oscillations. It is a factor of two smaller than the momentum width of the BEC measured with Bragg spectroscopy in the previous section. For the calculations a Gaussian momentum distribution was assumed, which is an acceptable approximation to a real bimodal distribution (see Sec. 2.2.2). The momentum distribution is symmetric about zero representing a resting BEC after evaporation. To acquire the fraction of atoms populating  $|0\hbar k\rangle$  the integral over the full momentum distribution has to be carried out. For the first 2 ms a complete momentum transfer to  $|2\hbar k\rangle$  can be observed, thus  $|0\hbar k\rangle$  is depleted for all momenta present. Beginning at 1 ms a deformation of the population profile occurs. Atoms with higher initial momentum populate the state  $|0\hbar k\rangle$  whereas atoms with  $\omega_D = 0$  are still occupying  $|\pm 2\hbar k\rangle$ . Because of the momentum profile of the atomic cloud atoms with higher momentum are less common and their impact is small at the beginning. After 2 ms a non-negligible amount of atoms occupies  $|0\hbar k\rangle$  whereas the central part of the atomic cloud is still populating  $|\pm 2\hbar k\rangle$ . This yields a loss of efficiency in momentum transfer if the complete cloud is taken into account. For sufficiently small momenta, double Bragg oscillations show now decreasing efficiency. For increasing times this effect damps the oscillations even more. Broader momentum distributions of a cloud will amplify this effect. To observe perfect momentum oscillations the momentum distribution has to be small. To create a perfect beamsplitter with a  $\pi/2$  pulse the width has to be smaller than  $0.125 \hbar k$ . To create a perfect mirror the momentum distribution has to be even narrower. Broader momentum distributions can exploit an additional feature of double Bragg diffraction. Every even multiple of  $\pi$  creates a slightly more efficient mirror pulse.

After about 1 ms the effects of the finite momentum width inhibit the full population transfer to  $|\pm 2\hbar k\rangle$  and the oscillations are damped and completely vanish for longer durations.

The experimental observation of long pulses is carried out in the same way as already described in Sec. 3.3.2. After the preparation of the BEC the dipole trap is switched off instantaneously and a lattice pulse of up to 3 ms is provided. A waiting time of 18 ms was applied before imaging to guarantee a spatial separation of the ensembles according to their momentum. In order to be able observe more oscillation periods the lattice depth was increased thus the Rabi frequency was enhanced to  $\Omega_{\text{eff}} = 2\pi \times 1.26 \text{ kHz}$ .

Fig. 3.18 shows the population of atoms in  $|0\hbar k\rangle$  after the application of a double Bragg pulse of  $\tau$ . The solid black line takes into account the Fourier width of the applied pulse as well as the momentum distribution of the BEC. It can be calculated by integrating over complete momentum distribution of the atomic cloud for each time step. The oscillation shows a complete transfer of population from  $|0\hbar k\rangle$  to  $|\pm 2\hbar k\rangle$  after  $230 \mu\text{s}$ , which can be associated with a  $\pi/2$  pulse. After a pulse of twice this duration a maximum population of  $|0\hbar k\rangle$  is

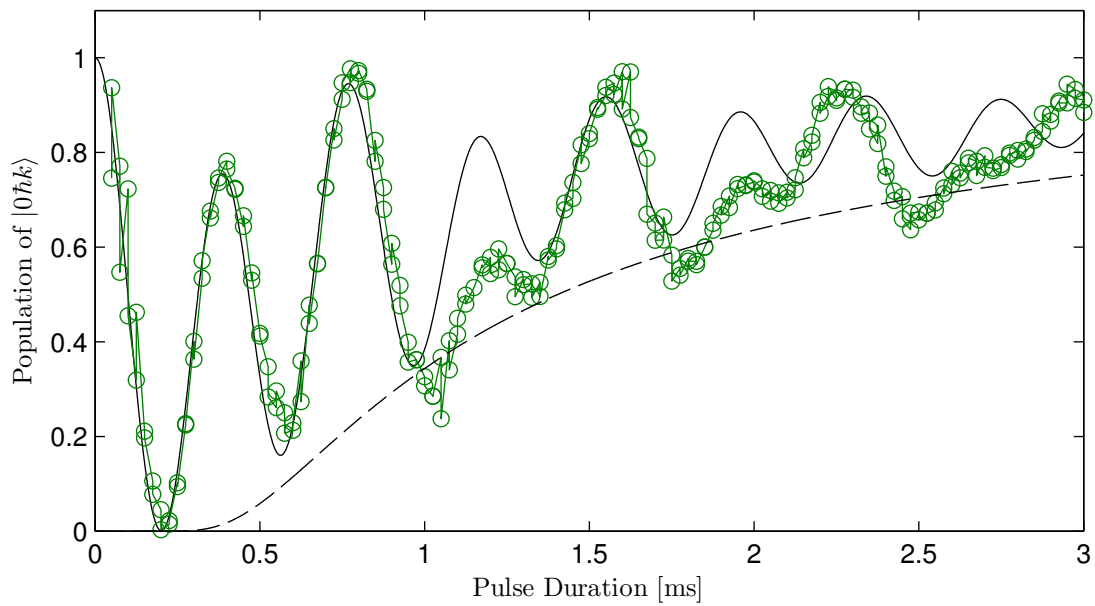


**Figure 3.18:** Population of state  $|0\hbar k\rangle$  after the application of a double Bragg pulse of variable duration. The solid black line represents a solution of Eq. (3.38) taking the momentum distribution of the atomic cloud into account as well as the Fourier limit of the lattice pulse. The dashed line shows the maximum efficiency expected due to the Fourier width of the pulse (Eq. (3.36)).

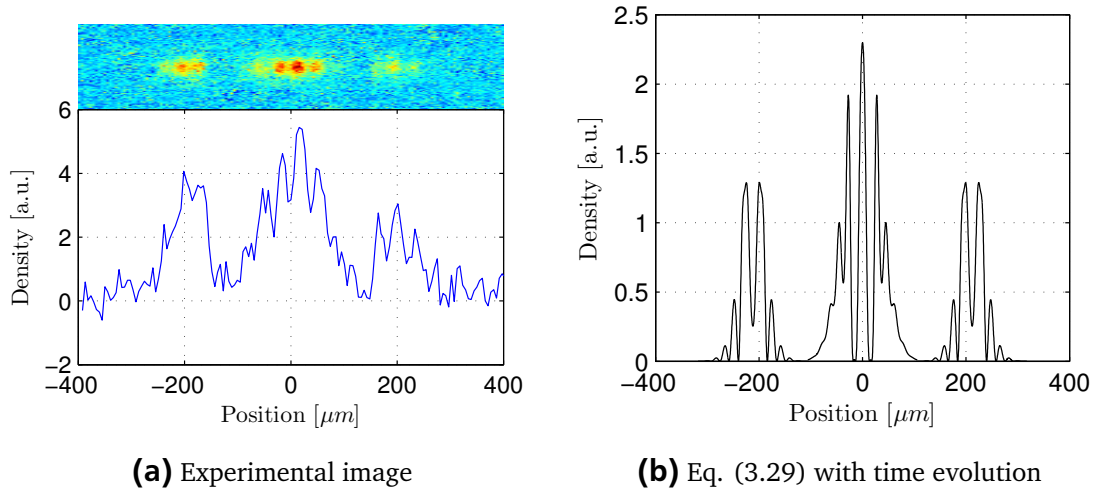
observed, with 80 % of the population returning to the  $|0\hbar k\rangle$  and the rest of the atoms occupying  $|\pm 2\hbar k\rangle$ . In a simple damped oscillating system the efficiency of population transfer would constantly decline. In a double Bragg diffraction setup the revival of the population can appear. This is the case after  $840\ \mu\text{s}$  - a  $2\pi$  pulse. 100 % of the atoms return to  $|0\hbar k\rangle$  and no population of  $|\pm 2\hbar k\rangle$  is measurable.

Fig. 3.18 shows that a  $\pi$ -pulse reaches an efficiency of 80 %. A  $2\pi$ -pulse is applied with an efficiency of 98 %. For interferometric applications the shortest pulse time that achieves the desired splitting will be chosen to reduce spontaneous excitation. As discussed in Sec. 3.5.1, the length of a lattice pulses also limits the amount of atoms that are influenced by double Bragg diffraction. The calculation depicted in Fig. 3.17(b) takes into account the Fourier width of an applied pulse in the momentum domain. This is done by multiplying the maximum fraction of atoms taking part in oscillations derived from Eq. (3.36) with the population oscillation (Eq. (3.37)):

$$N_{0,F}(t, \omega_D) = N_0(t, \omega_D) \times N_F(t). \quad (3.38)$$

For pulse durations larger than 1 ms the increase of the lower limit for the population in state  $|0\hbar k\rangle$  can be explained by the Fourier limited efficiency of double Bragg diffraction. Instead of converging towards a mean value of  $N_0/N = 0.5$  all of the atoms stay at rest in  $|0\hbar k\rangle$ . The oscillation period for higher times is getting shorter as well. The increased Rabi frequency can be explained by the free movement of the BEC. Since the lattice is not strong enough to hold atoms against gravity the atoms can escape the initial interaction region. It could be possible, that they fall in a range of higher lattice depth, which would yield higher oscillation frequencies. Also mean-field expansion is occurring during the interaction of the atoms with the lattice (see Sec. 2.2.2). Mean field interaction creates a broadened momentum distribution until its energy is depleted and a fixed momentum distribution is established. Due to the quadratic contribution of  $\omega_D$  in Eq. (3.31), a broader momentum distribution yields a higher effective Rabi frequency averaged over the whole atom cloud. The increasing momentum width can therefore increase the effective Rabi frequency which explains why the oscillation for large pulse durations are faster in the experimental data. These effects are not taken into account in the underlying calculations represented by the solid line in Fig. 3.18.

As discussed earlier in this section the Doppler shift introduces a momentum selective frequency modulation. Different fractions of the atomic ensemble oscillate with different frequencies. This behaviour introduces patterns in the atomic clouds. Fig. 3.19 shows a comparison between an experimental image obtained with a double Bragg diffraction pulse and the solution of Eq. (3.29) with an additional time of free expansion of 18 ms to account for the spatial spreading of the atoms. Fig. 3.19(a) shows a density distribution after a lattice pulse of length  $\tau = 800\ \mu\text{s}$ . The density distribution shows a modulation along



**Figure 3.19:** Measuring the population in  $| -2\hbar k \rangle$ ,  $| 0\hbar k \rangle$ , and  $| 2\hbar k \rangle$  of a double Bragg pulse for a long double Bragg pulse with  $\tau = 800 \mu\text{s}$ . depending on the expansion for the duration  $t_w$  in free space.

the separation direction in the accelerated and the non accelerated states. Fig. 3.19(b) shows the solution of Eq. (3.29) multiplied with a BEC density distribution after 18 ms obtained by the scaling law (see Sec. 2.2.3). The clouds at  $-220 \mu\text{m}$  and  $220 \mu\text{m}$  were positioned according to momenta  $-2\hbar k$  and  $2\hbar k$  after a time-of-flight of 18 ms. The obtained density distribution features the same periodic structures as the experimentally obtained density distributions of Fig. 3.19(a). The Doppler shift induced frequency change  $\Omega_{\text{eff}}(\omega_D)$  yields periodic population of each of the momentum states. The spatial separation for  $\tau = 800 \mu\text{s}$  is chosen in a way that the spacing is visible.

The width of the density distribution in the  $x$  and the  $y$  direction is shown to be different. By minding the time of free expansion of 18 ms the initial momentum width of the cloud is  $\sigma_{p,x} = (0.28 \pm 0.05) \hbar k$  in the  $x$  direction and  $\sigma_{p,y} = (0.09 \pm 0.03) \hbar k$  in the  $y$  direction. The  $y$  direction features the momentum width that has been calculated by the fit of Eq. (3.29) to the oscillations of momentum states caused by double Bragg diffraction. The  $x$  direction gives a higher momentum width by a factor of three. The  $x$  direction is the direction in which both lattice beams are aligned. The broadening of the atomic ensemble may be caused by the illumination of near resonant of the double bragg lattice for  $\tau = 800 \mu\text{s}$ .

This section shows that double Bragg diffraction of broad momentum distributions faces a reduced efficiency. This behaviour can be used to examine fundamental properties of atomic clouds via Bragg spectroscopy (see Sec. 3.5.4). For pulse durations larger than 3 ms the inhibiting effects dominate and the oscillation amplitudes are reduced to a point where less than 20 % of the atoms can

be manipulated.

---

### 3.5.4 Measuring the mean-field expansion of a BEC with double Bragg diffraction

---

As discussed in Sec. 3.5.3, the efficiency of double Bragg diffraction depends on the momentum width of the BEC. This behaviour can be exploited to measure the momentum width by fitting  $N_{0,F}$  to the population oscillation. Since the mean-field expansion alters the momentum distribution according to Eq. (2.36), introducing a waiting time before the application of double Bragg pulse makes the process observable. Because the main contribution of the mean-field expansion happens during the first 3 ms, the times were selected accordingly to map this parameter area.

The experiment was carried out in the same way as described in Sec. 3.5.3. In addition a variable waiting time  $t_w$  was introduced before the application of the double bragg pulse. The waiting time  $t_w$  was then modified from 0 ms to 5 ms in steps of 1 ms. The density distribution was measured 18 ms after the application of the lattice pulse in order to let the atoms separate according to their momentum.

Fig. 3.20 shows the population of  $|0\hbar k\rangle$  for different waiting times  $t_w$ . After  $\tau \approx 200 \mu s$  a  $\pi$  pulse is achieved for all depicted  $t_w$ , but its efficiency is dependent on the momentum width of the BEC. For increasing waiting times before the pulse application the efficiency decreases. For pulse durations of  $\tau < 500 \mu s$  all atoms are accelerated by the double Bragg pulse and therefore Eq. (3.37) was fitted to the population oscillation. The momentum width  $\sigma_p$  of the BEC was a fit parameter. The solid line in each of the plots shows the fitted population oscillation. Plotting the obtained width  $\sigma_p$  as a function of the initial waiting time  $t_w$  enables the direct observation of the evolution of the momentum width. Fig. 3.21 shows the fitted momentum width  $\sigma_p$  for over the waiting time  $t_w$ . Because the pulse duration of several  $100 \mu s$  is in the same order as the observed mean-field conversion time the momentum distribution itself changes significantly during the pulse. Therefore a mean pulse duration of  $200 \mu s$  was assumed and was added to the initial waiting time:  $t_{\text{exp}} = t_w + 200 \mu s$ . The solid black line is a numerical solution for  $R_{\text{TF}} \times \dot{\lambda}_x$  of Eq. (2.36) for the initial parameters  $\omega_x(0) = \omega_y(0) = 2\pi \times 115 \text{ Hz}$ ,  $\omega_z(0) = \sqrt{\omega_x^2 + \omega_y^2}$ ,  $\omega_x(t) = \omega_y(t) = \omega_z(t) = 0 \text{ Hz}$ , and  $R_{\text{TF}} = 3.7 \mu \text{ m}$ . All but the first data point corresponds to the theoretical description of the expansion. The initial data point is in a regime where the change in momentum is caused by the mean-field interaction. The mean pulse duration used for  $t_w = 0$  obviously underrates the expansion time. The remaining data points follow the theoretical prediction and lie within the error margin. The mean-field expansion is mostly happening during the first 1.5 ms after the atoms have been

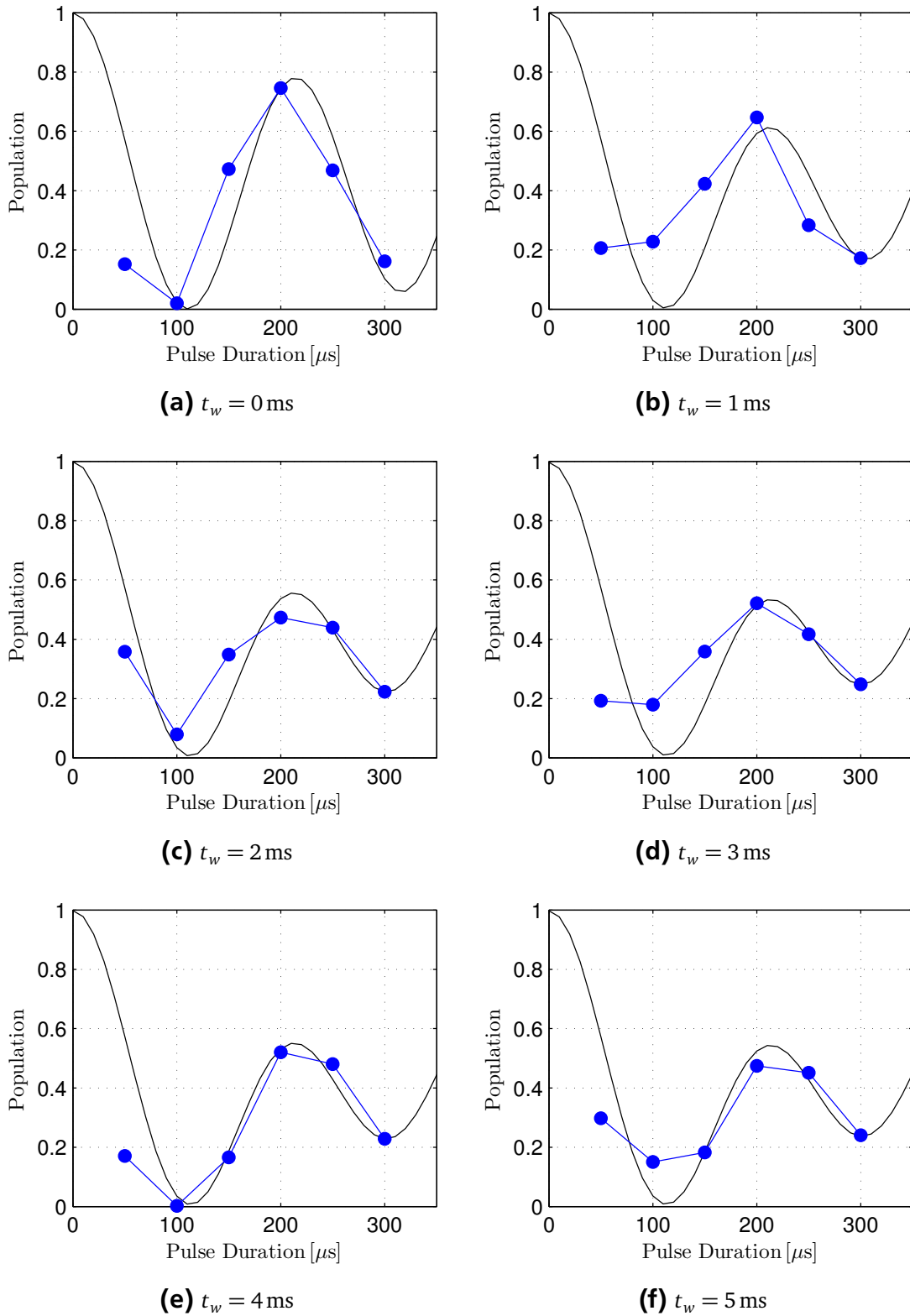


**Figure 3.20:** Measurement of the population in  $|0\hbar k\rangle$  of a double Bragg pulse depending on the free expansion of a BEC for the duration  $t_w$  in free space before double Bragg diffraction.

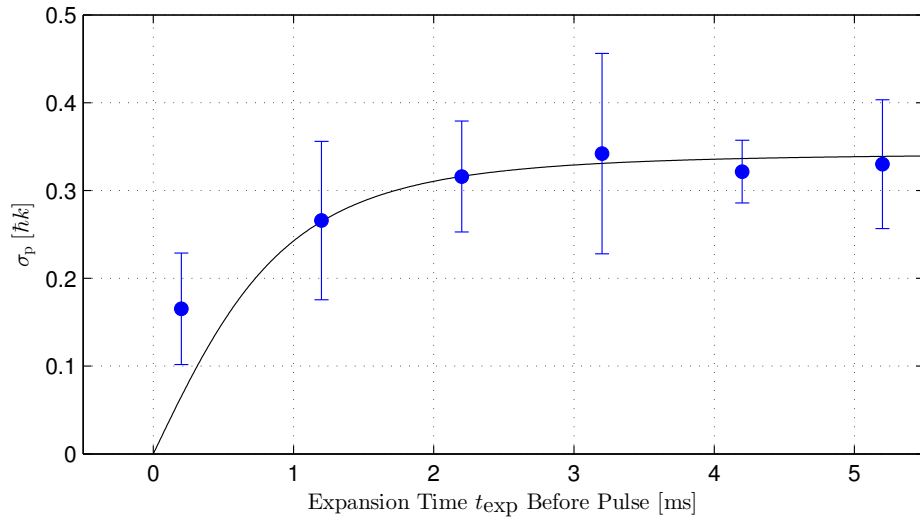


**Figure 3.21:** Momentum width  $\sigma_p$  of a BEC after variable times  $t_w$ . The solid black line is the numerical solution of Eq. (2.36) with no free parameters. The waiting time before the experiment is defined as  $t_{\text{exp}} = t_w + 200 \mu\text{s}$ , where  $200 \mu\text{s}$  is the mean duration of the double Bragg pulse.

released from the trap with a full expansion achieved after 3 ms. This approves the first estimation that mean-field expansion is happening in the first 5 ms after the release (see Sec. 2.2.3).

---

## 3.6 Other methods of coherent Beam splitting

---

In addition to double Bragg diffraction, two other methods were used to create a symmetric and coherent superposition of matter waves. Three-frequency Bragg diffraction, first described in [65], and the so called 'Pendellösung' in a non-moving optical lattice are shown [101]. Both methods feature a simple and reliable way to implement beamsplitters and mirrors for matter wave optics. This section compares the different methods and shows their experimental implementation. The experimental results are compared to double Bragg diffraction and a in depth discussion on applications for each of the methods is given.

---

### 3.6.1 Three-frequency Bragg diffraction

---

Three frequency Bragg diffraction is first described in [65]. Instead of having one frequency in each of the lattice beams, one of the beams features an additional second frequency. The frequencies are distributed in a way that one of the lattice beams is driven with the centre frequency of  $\omega$ . The second AOM features two frequencies  $\omega + \Delta\omega$  and  $\omega - \Delta\omega$ . The experimental setup described in Fig. 3.22 can be used without further modifications. One of the

AOMs used for Bragg diffraction was used without any modification. In order to achieve a second frequency in one of the lattice beams two frequencies derived from two synthesizers<sup>5</sup> were combined with a power splitter/combiner<sup>6</sup> [65]. A third synthesizer is used to drive the remaining AOM at the frequency of  $\omega = 80$  MHz. The detuning  $\Delta\omega$  was chosen to be  $4 \times \omega_R$ . Fig. 3.23 (b) shows the configuration at the point of the atoms. Atoms in the cross section of the lattice experience a spatial overlap of two optical lattices that each fulfil the Bragg condition. Because the two lattices have an opposing detuning, the acceleration direction is opposite and a splitting in different atom clouds with opposite direction is achieved.

---

### 3.6.2 'Pendellösung' in a non-moving optical lattice

---

In the previous sections, Bragg diffraction and double Bragg diffraction were observed in moving optical lattices, i.e. lattices in which a frequency shift was introduced between counter propagating beams ( $\Delta\omega \neq 0$ ). Without frequency shift double Bragg diffraction can no longer be observed, but depending on interaction time and lattice depth two different regimes for Bragg diffraction emerge: For short interaction times of the lattice  $\tau$ , the Kapitza-Dirac regime dominates [102]. For longer interaction times and shallow optical lattices the Bragg regime is reached [101, 103]. The so called 'Pendellösung' describes the limit of excitation of only  $|0\hbar k\rangle$  and  $|\pm 2\hbar k\rangle$  momentum states [104]. For deeper potentials a in depth discussion can be found in [38]. The upper bound of the interaction time in which the Kapitza-Dirac regime dominates is the inverse of the recoil frequency  $\omega_R$  [105]:

$$\tau \leq \frac{1}{\omega_R}. \quad (3.39)$$

To observe the Kapitza-Dirac regime with  $^{87}\text{Rb}$  the interaction time has to be less than  $26 \mu\text{s}$  [106]. This has been studied in detail at the ATOMICS experiment in previous works [61, 83].

When using longer interaction times, well in the Bragg regime, stimulation of higher momentum orders can be observed. The highest momentum order can be estimated by [85]:

$$n_{\max} \approx \sqrt{\frac{|U_{1D}(0)|}{4\hbar\omega_R}}, \quad (3.40)$$

where  $U_{1D}(0)$  is the amplitude of the modulation in the potential depth. The resulting oscillation frequency is given by  $\Omega_p = U_0/2\hbar$  [89]. To describe the

---

<sup>5</sup> Hewlett-Packard, 8657A

<sup>6</sup> Mini-Circuits Power Splitter/Combiner ZSC-2-1+

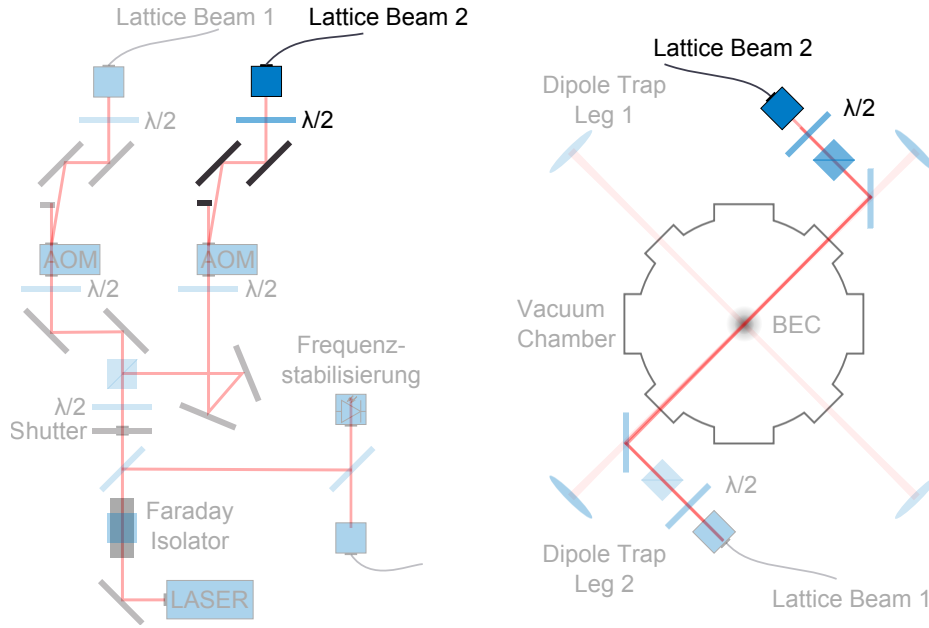


**Figure 3.22:** Modification of the double Bragg experimental setup (see Fig. 3.8) for the implementation of standard and three-frequency Bragg diffraction. Instead of a retro-reflecting mirror and a quarter wave-plate an additional fibre coupler is used to guide the light of lattice beam 1 and lattice beam 2 in two different optical fibres to the experimental setup.

time evolution of the atom momentum state in an optical lattice the resulting time-dependent Schrödinger equation can be solved using a trial solution. The in depth discussion on the solution to the system can be found in [107]. The 'Pendellösung' is a solution of the resulting differential equation:

$$\begin{aligned} N_0 &= \cos^2(U_0 t / 4\hbar) \\ N_2 &= \sin^2(U_0 t / 4\hbar) . \end{aligned} \quad (3.41)$$

$N_0$  gives the population in the momentum state  $|0\hbar k\rangle$  and  $N_2$  the sum of the population of the momentum states  $|\pm 2\hbar k\rangle$ . The population of  $|2\hbar k\rangle$  and  $| - 2\hbar k\rangle$  is distributed equally.

To achieve a symmetric splitting with a non-moving optical lattice, the appropriate lattice depth has to be used in order to provide a perfect beamsplitter. To increase the fidelity of the beamsplitter and to avoid unnecessary fluctuations an intensity stabilized lattice is favourable.

---

### 3.6.3 Modifications to the experimental setup

---

The initial setup described in Sec. 3.3.1 for double Bragg diffraction could be used with only slight modifications. Fig. 3.22 shows the modified setup of

Fig. 3.8 with the highlighted modifications. Instead of recombining the light beams after the two AOMs and guiding them to the experimental setup with only one optical fibre, a second optical fibre was installed. Each of the beams' polarization was carefully adjusted to be linear in parallel to each other. Polarizing beam-splitter cubes and  $\lambda/2$  waveplates after each optical fibre ensured a matching linear polarization. The alignment on top of one of the optical dipole trap legs was performed in the same way as for the double Bragg lattice alignment. To align the now counter-propagating second lattice beam, the rearward transfer efficiency of one beam through the other fibre can be used. A perfect alignment is achieved if the transfer efficiency is maximized. The electronic control of the modified optical lattice could be used without major modifications. Only the appropriate frequency setting needs to be adjusted for each lattice type used.

It is important to notice that due to the limited space available the experimental setup, for double Bragg diffraction is easier to accomplish but lacks the opportunity to use a single double Bragg lattice. The modified setup enables the usage of non-moving optical lattices (see Sec. 3.6.2) and also two simultaneous moving lattices (see Sec. 3.6.1) for beam splitting. On top of that, the acceleration of an atom cloud into a single momentum state can be accomplished. A single accelerated momentum component enables easier characterization measurements and is therefore used in Chapter 5 and Chapter 6 to characterize the potentials.

---

### 3.6.4 Comparison of different beam splitting configurations

---

Fig. 3.23 shows a compilation of the three different lattice configurations discussed earlier. Fig. 3.23 (a) shows the configuration of double Bragg diffraction where two perpendicular polarized beams are retro-reflected. Due to the  $\pi/2$ -waveplate the polarization is turned and a combination of two Bragg diffraction lattices interacts with the atoms. Fig. 3.23 (b) shows the three-frequency Bragg implementation. A single beam is joined with two counter-propagating beams that feature a detuning  $\pm\Delta\omega$ . All beams are linear polarized in the same direction  $\vec{e}_x$ . Fig. 3.23 (c) shows the setup for the 'Pendellösung' beamsplitter in a non-moving optical lattice.

To compare the three matter wave beamsplitters, three sets of measurements were performed in a comparable fashion. After a BEC was produced in the crossed optical dipole trap the trap was switched off and the Bragg pulse was applied. All three lattices were optimized in a way that excitation of the  $|-2\hbar k\rangle$  and  $|2\hbar k\rangle$  was achieved. The interaction time of the lattice and the atoms  $\tau$  was varied up to a duration of a  $\pi$ -pulse. After an additional waiting time of 18 ms, during which the atom clouds separate, the density distribution was measured. The double Bragg diffraction implementation follows the discussion in Sec. 3.3.2. The atoms are split with an efficiency of 99% by a  $\pi/2$ -pulse and

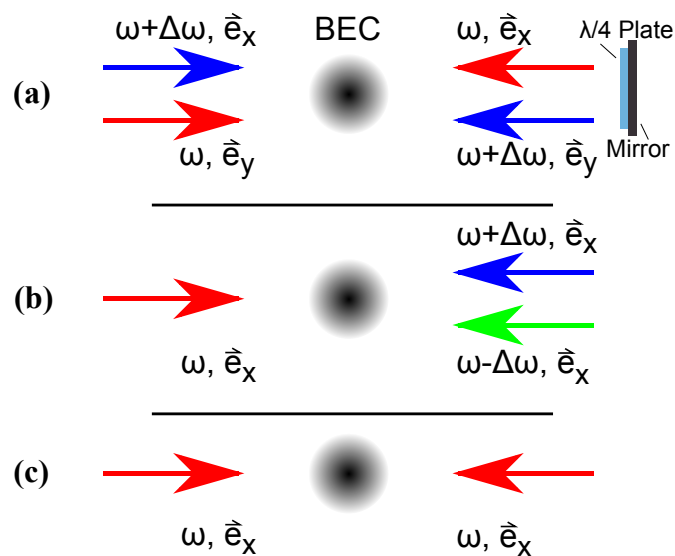


**Figure 3.23:** Beam configuration for different Bragg beamsplitters. (a) Double Bragg diffraction uses linear polarized light and creates a pair of one-dimensional optical lattices. (b) Three-frequency Bragg diffraction uses one beam with the centre frequency  $\omega$  and two counter propagating beams with the same polarization but different frequencies  $\omega - \Delta\omega$  and  $\omega + \Delta\omega$ . (c) The 'Pendellösung' beamsplitter utilizes non-moving optical lattices. By varying interaction times and lattice depth a beamsplitter is realized in all three configurations.

---

show a reduced efficiency of a  $\pi$ -pulse of 75 % due to the momentum width of the cloud, as discussed in Sec. 3.5.

The three-frequency Bragg lattice shows a splitting efficiency of 82 % for a  $\pi/2$ -pulse. The lattice depth and therefore the pulse time of three frequency Bragg were chosen to be in the same order as double Bragg diffraction. Additional damping effects cannot be explained by the pulse duration and a  $\pi$ -pulse already shows that only 50 % of the atoms return into the state  $|0\hbar k\rangle$ . Working with a focussed optical lattice, the same as used for the 'Pendellösung' configuration, also shows the dampening effect experienced with three-frequency Bragg diffraction [65]. The experimental parameters used with standard Bragg diffraction did not show this behaviour and it is unclear if the special combination of light pulses in this setup introduces additional resonant excitation of momentum states or if higher order fluctuations inhibit the population oscillations. Because all of the three lattice beams are linearly polarized in the same direction, cross-talk and unwanted interference processes can be a possible explanation.

For a standing optical lattice, the lattice depth was not sufficient to excite a high population of  $|\pm 2\hbar k\rangle$ . Therefore an additional lens was used to focus the light. The achieved waist was  $w_0 \approx 80 \mu\text{m}$ , which is twice the size of the crossed optical dipole trap beams, and the lattice depth was  $U_{1D}(0) = 19 E_R$  [83], which equates to  $n_{\text{max}} \approx 2$ . According to Eq. (3.40) the achievable maximum order is way above  $n = 1$  and a symmetric splitting into the states  $|\pm 2\hbar k\rangle$  was achieved. In order to create a good  $|\pm 2\hbar k\rangle$  beamsplitter the lattice depth has to be chosen following Eq. (3.40). The chosen lattice depth results in a pulse duration of  $\tau = 9 \mu\text{s}$  for a  $\pi/2$  pulse. This time is well within the region where Kapitza-Dirac diffraction may occur. Fig. 3.24 shows that the resulting efficiency of a  $\pi/2$ -pulse is 88 %. Because of the short pulse time, the frequency width is sufficiently long to guarantee a full momentum transfer of all atoms. The remaining 12 % of the atoms are either excited to  $|\pm 4\hbar k\rangle$  or reside in  $|0\hbar k\rangle$ , which could be first effects of the Kapitza-Dirac regime.

All three methods show that splitting of an atomic cloud is possible with high efficiency. The reduced efficiency of each of the methods has been discussed. In the case of the 'Pendellösung' an active intensity stabilization would increase the stability and is essential for a reliable usage. Three-frequency Bragg and Bragg diffraction show that the resonant excitation of momentum transfer is more robust with respect to intensity fluctuations. Three-frequency Bragg diffraction also offers the possibility to have different detuning for each of the lattice beams opening up the opportunity to have asymmetric splittings in different momentum states. This could be a useful technique for future applications. The large pulse durations originate from the decision to use a large beam. With additional laser power the oscillation frequencies could be increased. The advantage of a collimated large beam is the insensitivity in regards of day to day beam position drifts. Double Bragg diffraction has shown to be the most efficient way to split

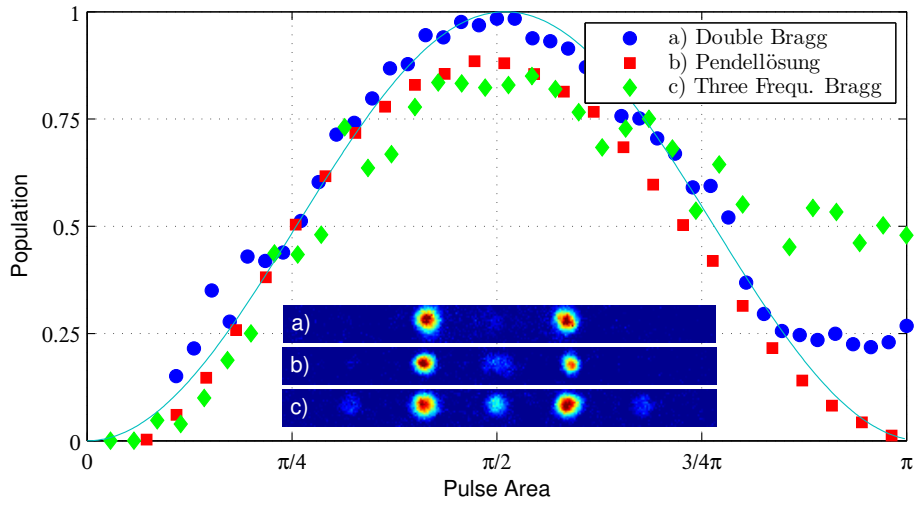


**Figure 3.24:** A full  $\pi$  period of the three different methods of Bragg based beam splitting of atomic clouds. The efficiency of each process is above 80 %. The insets show an absorption image obtained at the time of maximum splitting, which is therefore defined as a  $\pi/2$  -pulse. a) Double Bragg diffraction b) 'Pendellösung' diffraction c) Three-frequency Bragg diffraction.

atoms symmetrically in the momentum states  $|\pm 2\hbar k\rangle$ .

In addition to the shown methods of beam splitting additional methods exist and have been demonstrated experimentally. By using a combination of two standing wave lattice pulses a coherent splitting with high fidelity can be achieved [108]. This method uses the relative phase of the two clouds to create a beamsplitter into the states  $|\pm 2\hbar k\rangle$ . It was already used to implement an interferometer [109] but is limited to a coherent splitting to the order  $n = 1$ .

### 3.7 Matter wave interferometry with double Bragg diffraction

To demonstrate that double Bragg diffraction is an efficient tool for atom interferometry a Ramsey-type interferometer was realized by using double Bragg diffraction pulses. The method of Ramsey-type interferometry with matter waves has been investigated before [110, 111] and serves as a well known method for auto-correlation measurements on BECs [65].

This section shows the initial idea behind Ramsey-type interferometry and the applied method in this work (see Sec. 3.7.1). Next a discussion with a theoretical description of the expected density modulation in a BEC after the interferometer sequence is given (see Sec. 3.7.2). The algorithm used to experimentally determine the fringe spacing is explained in Sec. 3.7.3. Afterwards the experimental use of double Bragg diffraction interferometry is shown and discussed. In particular the differences to standard Bragg diffraction interfer-

---

ometry are shown (see Sec. 3.7.4). The section closes with the experimental realization of a second-order Bragg diffraction interferometer showing that the developed method is also applicable to other velocity regimes (see Sec. 3.7.5).

---

### 3.7.1 Experimental procedure of a Ramsey-type interferometer

---

Initially Ramsey interferometry was developed to measure the frequency of atomic resonances in atom beams [112]. To measure the frequency of an atomic resonance, atoms are guided through two interaction regions. These regions are spatially separated. In the first interaction region, a superposition of internal states is imprinted on the atoms. During the transfer from one interaction region to the other, these superpositions oscillate with a specific frequency. The phase difference of the internal frequency and the stimulating frequency is used to determine the internal oscillation frequency of the atoms [113]. The accuracy of this method is directly proportional to the time between the two interaction areas.

Today this method is used to determine the SI unit of time as  $1\text{ s} = 9,192,631,770$  revolutions of  $^{133}\text{Cs}$  [114]. In addition Ramsey method has been extended to an Ramsey-Bordé interferometer which uses four interactions regions [115, 116]. In a Ramsey-Bordé interferometer rotation or acceleration can be applied to shift the Ramsey fringes. These shifts can be measured with high precision [117].

Matter wave interferometry can in addition apply the Ramsey interferometer for auto-correlation measurements of an atomic ensemble. Instead of two spatially separated interaction regions, two temporally displaced interactions are used. Fig. 3.25 shows the experimental procedure of a Ramsey-type matter wave interferometer. First a coherent matter wave is generated in the crossed optical dipole trap via Bose-Einstein condensation. The long experimental procedure of over 60 ms to follow arises the need to hold the atoms against gravity. Otherwise they would leave the field of view of the detection camera. The atoms are therefore loaded into one of the crossed optical dipole trap legs. Theoretically it would be sufficient to switch off one of the legs. Experimentally the trapping force of one dipole trap leg is not sufficient to hold atoms against gravity. To compensate, the intensity of dipole trap leg 2 is increased before leg 1 is disabled. The trapping frequency in the radial direction of leg 2 is approximately  $\omega_t = 2\pi \times 150\text{ Hz}$  after the ramping process (see 2.13). The longitudinal trapping frequency is  $\omega_r < 2\pi \times 1\text{ Hz}$  because of the large Rayleigh range of the focussed Gaussian beams generating the dipole trap.

The waiting time  $t_1$  ensures that the mean-field energy is depleted and that ballistic expansion is the dominant process. After the waiting time  $t_1$  the first  $\pi/2$ -pulse is applied. This process has to be done before each experimental run to ensure a full beamsplitter. The time between the two pulses  $\tau_i$  gives the two atom clouds the time to displace from each other. The time  $\tau_i$  is short

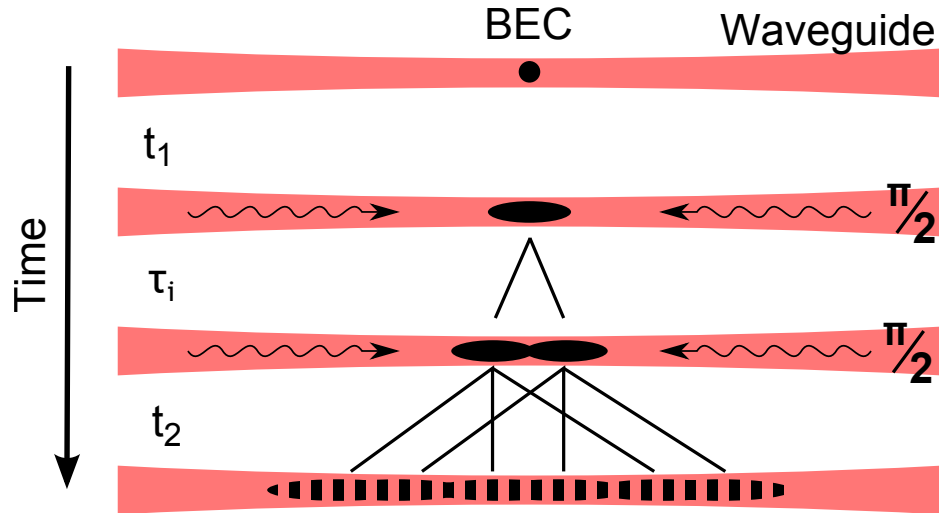


**Figure 3.25:** Experimental sequence of a Ramsey-type interferometer. After a waiting time  $t_1$  a  $\pi/2$  pulse is applied to create coherent superposition of the momentum states  $|\pm \hbar k\rangle$ . After a time  $\tau$  a second  $\pi/2$  pulse is applied. After an additional waiting time  $t_2$  the resulting density distribution is imaged via absorption imaging.

enough so that the clouds never separate completely and partly overlap all the time. After the time  $\tau_i$  has passed the second  $\pi/2$ -pulse is applied. The final pulse creates a total three wave packets. The three clouds have a momentum of  $-2\hbar k$ ,  $0\hbar k$ , and  $2\hbar k$ . This process happens to both of the ensembles created by the first  $\pi/2$ -pulse. The separation between the two clouds imprinted during the time  $\tau_i$  between the two interferometer pulses determines the displacement  $\Delta x$  between the clouds of same momentum (see Fig. 3.25). The spatial overlap present in all three pairs of ensembles yields a density modulation. This density modulation is imaged after an additional waiting time of  $t_2$ .

In contrast to standard Bragg diffraction not a single but two spatial frequencies can arise. Due to inequalities in the beam splitting process part of the atoms reside in  $|0\hbar k\rangle$ . This creates a second effective displacement which yields a second spatial frequency. This has been shown in the experiment and is discussed in Sec. 3.7.4.

---

### 3.7.2 Fringe period of interferometric measurements

---

The interference pattern after a Ramsey-type interferometer sequence is dependent on two parameters: First the observed density modulation originates from the interference of two wave packets with quadratic phase profile. Second the relative velocity of the wave packets  $\Delta v$  introduces density modulations as well. By choosing the interferometer sequence appropriately  $\Delta v = 0$  can be accomplished.

Applying a Ramsey-type interferometer sequence with double Bragg diffraction results in the creation of three interferometer exit ports. For simplicity, the discussion continues for one of the possible interferometer outputs where all of the outputs feature the same behaviour. In addition due to the separability of the wave function in the radial and axial parts, the discussion can be done for axial part only. Each experiment is oriented in way that displacements occur only in one direction.

A wave function  $\psi(x)$  can be written as

$$\psi(x) = f(x) e^{i\phi(x)}, \quad (3.42)$$

where  $\phi(x)$  describes the phase profile and  $f(x)$  the density profile of the wave packet. In the Thomas-Fermi approximation the phase  $\phi(x)$  of a wave function is defined as

$$\phi(x) = \frac{\alpha}{2}x^2 + \beta x, \quad (3.43)$$

where  $\alpha$  gives the phase gradient as defined in Sec. 2.2.3 and  $\beta$  gives a linear phase profile, the constant motion of an atomic ensemble. During the interferometer process two wave packets are separated spatially by  $\Delta x$ . The density distribution of two interfering wave packets with spatial overlap centred at the positions  $x$  and  $x + \Delta x$  is given by:

$$|\psi(x) + \psi(x + \Delta x)|^2 = \left| f(x) e^{i\left(\frac{\alpha}{2}x^2 + \beta x\right)} + f(x + \Delta x) e^{i\left(\frac{\alpha}{2}(x + \Delta x)^2 + \beta(x + \Delta x)\right)} \right|^2. \quad (3.44)$$

Considering the relevant cross term  $F(x)$  of the absolute value yields:

$$\begin{aligned} F(x) &= f(x)f(x + \Delta x) e^{-i\left(\frac{\alpha}{2}x^2 + \beta x\right) + i\left(\frac{\alpha}{2}(x + \Delta x)^2 + \beta(x + \Delta x)\right)} \\ &\quad + f(x)f(x + \Delta x) e^{i\left(\frac{\alpha}{2}x^2 + \beta x\right) - i\left(\frac{\alpha}{2}(x + \Delta x)^2 + \beta(x + \Delta x)\right)} \\ &\text{with } N(x) = f(x)f(x + \Delta x) \\ &= 2N(x) \cos\left(\frac{\alpha}{2}(x^2 - 2\Delta x - \Delta x^2) - \beta(x - \Delta x) - \frac{\alpha}{2}x^2 - \beta x\right) \\ &= 2N(x) \cos\left(-(\alpha\Delta x + 2\beta)x + C\right). \end{aligned} \quad (3.45)$$

The constant factor  $C$  introduces a constant phase that is defined as:

$$C = \beta\Delta x - \Delta x^2 \frac{\alpha}{2}. \quad (3.46)$$

The cross term of Eq. (3.45) describes a density modulation with a spatial frequency of

$$\kappa = \alpha\Delta x + 2\beta. \quad (3.47)$$

$\beta$  is proportional to the relative velocity  $\Delta v$  between the interfering wave packets after the second beamsplitter and is given by [118]:

$$\beta = \frac{m\Delta v}{\hbar}. \quad (3.48)$$

The relative velocity  $\Delta v$  introduces additional interference patterns as long as different packets of the cloud overlap spatially. The large relative velocity of at least  $\Delta v = 2\hbar k/m = 11 \text{ mm/s}$  makes a detection of the resulting narrow structure in the current experimental set up not possible. The second pulse ensures that the relative velocity of the pair of wave packets interfering within each exit port is  $\Delta v = \beta = 0$ . Given the definition of  $\alpha$  (see Eq. (2.40)) the fringe spacing  $d$  of the low frequency component is given by:

$$d = \frac{2\pi}{\kappa} = \frac{2\pi}{\alpha\Delta x} = \frac{\lambda h}{\lambda m\Delta x} \quad (3.49)$$

The density modulation of two interfering atom clouds is controllable by the separation  $\Delta x$  in the experiment. In general  $\alpha$  is dependent on the time (see Sec. 2.2.3). After the initial mean-field driven expansion (typically 3 ms after release), ballistic expansion of the BEC is dominant  $\alpha$  is considered to be constant.

---

### 3.7.3 Analyses of spatially periodic density profiles

---

The absorption image of an interferometric measurement shows a modulated density profile with one or more spatial frequencies present.

As discussed before the expected density profile consists of three interferometer exit ports with two distinct spatial frequencies. The resulting density modulation is described by the following function  $D(x)$ :

$$\begin{aligned} D(x) = & A_1 e^{-\frac{1}{2}\left(\frac{x-x_0-x_2\hbar k}{\sigma_x}\right)^2} \cdot \left(1 + B_{1,a} \sin(\kappa_a \cdot x + \phi_{1,a}) + B_{1,b} \sin(\kappa_b \cdot x + \phi_{1,b})\right) \\ & + A_2 e^{-\frac{1}{2}\left(\frac{x-x_0}{\sigma_x}\right)^2} \cdot \left(1 + B_{2,a} \sin(\kappa_a \cdot x + \phi_{2,a}) + B_{2,b} \sin(\kappa_b \cdot x + \phi_{2,b})\right) \\ & + A_3 e^{-\frac{1}{2}\left(\frac{x-x_0+x_2\hbar k}{\sigma_x}\right)^2} \cdot \left(1 + B_{3,a} \sin(\kappa_a \cdot x + \phi_{3,a}) + B_{3,b} \sin(\kappa_b \cdot x + \phi_{3,b})\right). \end{aligned} \quad (3.50)$$

The density distribution  $D(x)$  features three distinct atom clouds, each one representing an interferometer exit port. Each cloud consists of a Gaussian distribution with amplitude  $A_1$ ,  $A_2$ , and  $A_3$  and the same width  $\sigma_x$ . The displacement of the clouds is determined by the time of flight after the interferometer and can be calculated by  $x_{2\hbar k} = 2\hbar k/m \times t$  for first-order double Bragg

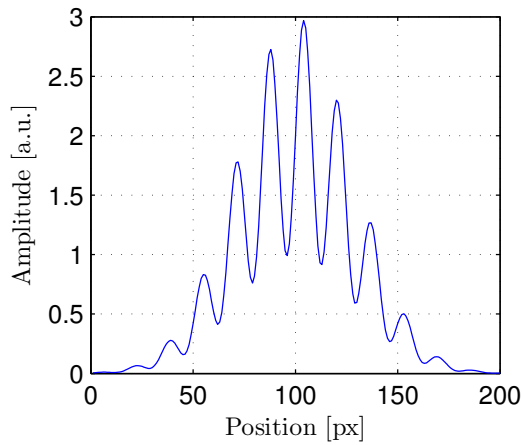
diffraction. Higher orders have to consider the changed velocity. Each Gaussian distribution is a sum of an unmodulated background and two contributions with sinusoidal density modulations with frequency  $\omega_a$  and  $\omega_b$ . Each of these feature a distinct phase  $\phi_{1,a}$ ,  $\phi_{1,b}$ ,  $\phi_{2,a}$ ,  $\phi_{2,b}$ ,  $\phi_{3,a}$ , and  $\phi_{3,b}$ . The amplitude of the modulation is given by the product of  $A_{1,2,3}$  and  $B_{1,2,3;a,b}$  respectively. This yields the possibility to determine the contrast of each of the modulations separately.

Eq. (3.50) has a total of fifteen independent variables and a fitting routine considering all parameters appropriately could not be found. To compensate for the lack of fitting the complete distribution the problem was divided into two steps. First all spatial frequencies are extracted with the use of discrete Fourier transformation (DFT). Afterwards the remaining parameters are fitted to the density distribution using the determined frequencies  $\kappa_a$  and  $\kappa_b$  as fixed values. The Fourier transformed distribution  $F(\kappa)$  is given by:

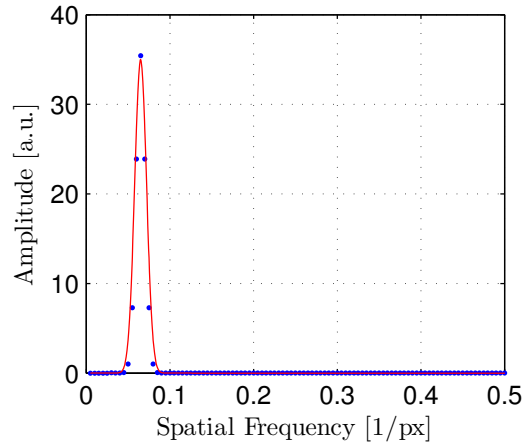
$$F(\kappa) = \sum_{x=1}^N D(x) e^{\left(\frac{-2\pi i}{N}\right)^{(x-1)(\kappa-1)}. \quad (3.51)$$

A DFT offers a fast and reliable way to determine the frequency spectrum of a temporal and spatial series of data. The initial two-dimensional density distribution is summed perpendicular to the Bragg beam direction to create a one-dimensional vector. The width of the one-dimensional waveguide was chosen as boundaries for the summation. The sampling frequency equates to the pixel count of the image. According to Eq. (3.51) the density distribution was converted to a spatial frequency distribution. The scaling of the  $x$  axis has to be chosen carefully and is determined by one over the sample length  $N$ . Fig. 3.26 shows a compilation of images depicting two density distribution before the application of an DFT and the calculated spectrum for each of the distributions. Fig. 3.26(a) and Fig. 3.26(c) feature an example density modulation on top of a Gaussian background. This is a simplification of Eq. (3.50) to help demonstrate the advantage of DFT. Fig. 3.26(c) adds additional noise to the same density distribution. White noise was chosen to demonstrate random errors that accumulate across the experimental procedure. The amplitude of the noise was set to 1, the same amplitude as used for the sinusoidal density modulation.

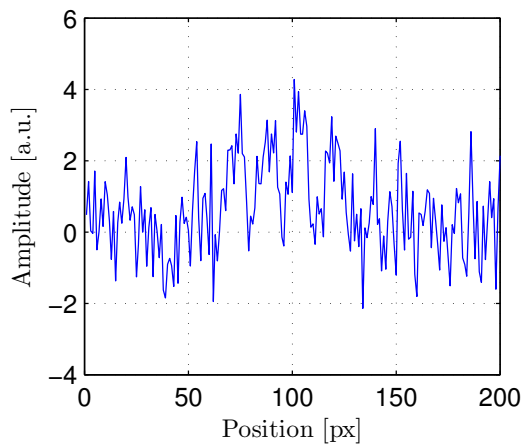
Each of the two distributions were analysed using DFT. The resulting distributions in the frequency domain are shown in Fig. 3.26(b) and Fig. Fig. 3.26(d). Fig. Fig. 3.26(b) shows a distinct peak at  $\kappa = 0.06$  1/px which matches the initial example value of the modulation perfectly. The frequency is determined by fitting a Gaussian at the highest frequency available in the spectrum. The centre of the Gaussian distribution yields the spatial frequency. Fig. 3.26(b) shows the influences of noise. The expected peak at  $\kappa = 0.06$  1/px is still visible and is a maximum for the spectrum. The weight of other frequencies has



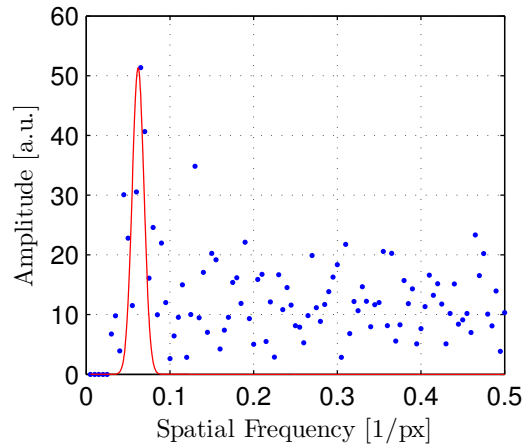
(a) Noiseless density profile



(b) Fourier spectrum of density profile



(c) Density profile with noise



(d) Fourier spectrum of density profile with noise

**Figure 3.26:** A comparison of density profiles and their respective Fourier spectra with and without noise.  $\kappa$  is determined by a fit of a Gaussian distribution to the maximum value of the Fourier spectrum. The error in the determination of  $\kappa$  is increased by noise. The visible noise is not sufficient to introduce a significant error and shows the robustness of DFT.

increased significantly. Still it is possible to determine the frequency with the method of fitting a Gaussian to the maximum of the distribution. If multiple frequencies are present in a distribution the procedure has to be executed multiple times. Each time the Gaussian distribution is subtracted and the next highest frequency can be fitted with another Gaussian.

After the modulation frequencies are determined  $D(x)$  can be fitted more easily to the density distribution. Fig. 3.27 shows two example density distributions of a Ramsey-type interferometer and the resulting fits of Eq. (3.50).

---

### 3.7.4 Matter wave interferometry with double Bragg diffraction

---

Matter wave interferometry with double Bragg diffraction has been performed according to the sequence explained in Sec. 3.7.1. The experiment started by with loading a BEC of 25000  $^{87}\text{Rb}$  atoms into the one-dimensional waveguide. The waiting time before the interferometer was chosen to be  $t_1 = 30$  ms. The pulse duration of the optical lattice was set to create a  $\pi/2$ -pulse. This was determined experimentally beforehand and instead of Gaussian pulses Blackman pulses [119] were used to achieve smaller values for  $\tau_i$ .  $\tau_i$  is defined as the time span between the maxima of the two pulses. Blackman pulses feature a steeper without altering the pulse area and can therefore be positioned closer with respect to each other.

Fig. 3.27 shows two density profiles of a double Bragg interferometer. Fig. 3.27(a) features a pulse separation of  $\tau = 105 \mu\text{m}$  and a waiting time of  $t_1 = 30$  ms and  $t_2 = 30$  ms. The black solid lines depict the position of the Gaussian distribution after the experiment and show that the displacement from the centre  $x_{2\hbar k} = (352 \pm 21) \mu\text{m}$  due to the different momentums matches perfectly the calculated position of a cloud with a momentum of  $2\hbar k$  that moves for  $t_2 = 30$  ms, which is  $x_{2\hbar k, \text{calc}} = 353.1 \mu\text{m}$ . As expected, there are three distinct Gaussian distributions that describe the three different exit ports of the interferometer. For two perfect pulses each of the outer Gaussian distributions should have the same amplitude whereas the centre Gaussian distribution features a amplitude twice as large. In contrast all three Gaussian distributions feature nearly the same amplitude. This can be explained by the variation of the beamsplitter efficiency for the  $|2\hbar k\rangle$  and  $| -2\hbar k\rangle$  splitting. Also the second  $\pi/2$ -pulse can add to this inequality. These variations in splitting efficiency have been shown in Sec. 3.3.2. Fig. 3.27(b) features the same experimental conditions but  $\tau = 210 \mu\text{s}$ . The position of the two outer Gaussian distributions again matches the calculated position  $x_{2\hbar k} = (352 \pm 21) \mu\text{m}$ . Also the width of the distribution  $\sigma_x = (298 \pm 38) \mu\text{m}$  is in the order of the calculated width derived of Eq. (2.36), which is  $\sigma_{x, \text{calc}} = 271 \mu\text{m}$ . Both distributions show that two spatial frequencies are present. Because the fringe spacings are wider in Fig. 3.27(a) the effect is more visible. Between the maxima of the larger fringe spacing smaller peaks arise and show that two spatial frequencies modulate the

density distribution. Fig. 3.28 shows the measured fringe spacing for different pulse separations  $\tau_i$ . The expected fringe spacing is plotted with black lines for the two different spatial frequencies separately. Following Eq. (3.49) each of the two curves follows the product of  $\tau$  and the relative velocity  $\Delta v$  according to the relative momentum  $\Delta p$ . Two velocities separated by a factor of two should therefore show the behaviour of two separate fringe spacings with  $\Delta p = 2\hbar k$  and  $\Delta p = 4\hbar k$ .

In order to achieve a higher fringe spacing it would be possible to switch to a Mach-Zehnder interferometer sequence [120]. It features a  $\pi/2$ - $\pi$ - $\pi/2$ -pulse sequence with two separate waiting times between the pulses. By tuning the two waiting times accordingly even smaller effective pulse separations are realizable. This offers the flexibility to choose  $\tau$  without experimental limitations of the actual pulse duration and the closeness in which the pulses can be positioned temporarily. The experimental implementation of a Bragg mirror with double Bragg diffraction has been shown in Sec. 3.3.2.

---

### 3.7.5 Interferometry with higher order double Bragg diffraction

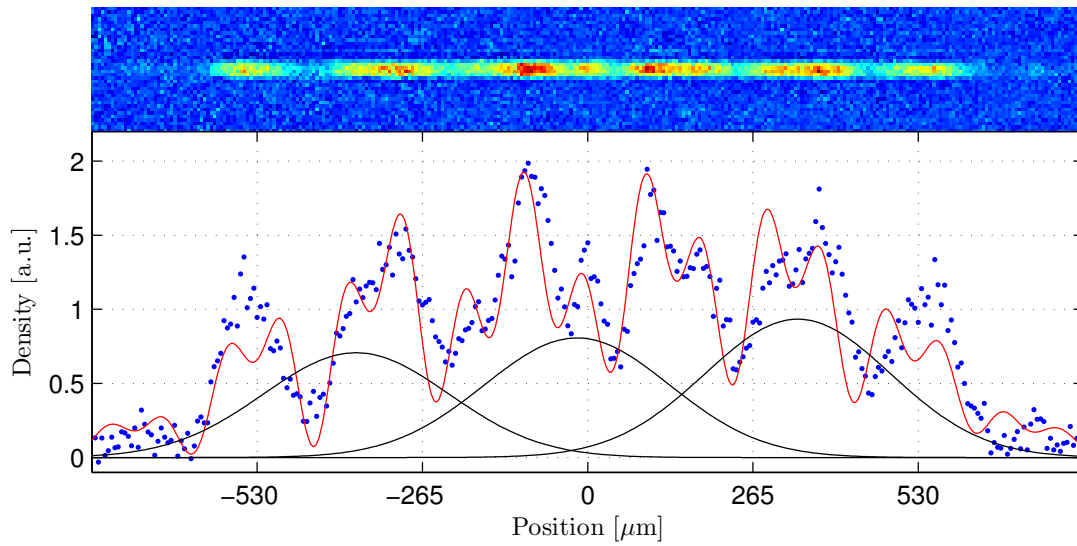
---

In order to further investigate the properties of interference effects with double Bragg diffraction an interferometer sequence with second-order Bragg diffraction was performed. The interferometer follows the the Ramsey-type interferometer sequence described in Sec. 3.7.1.

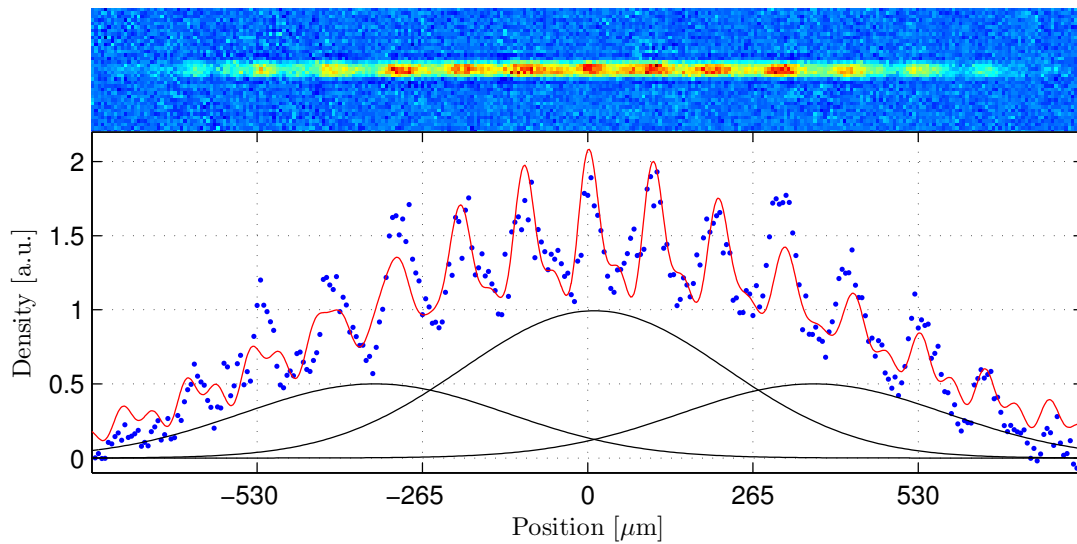
As Sec. 3.7.2 discusses the expected fringe period depends on the relative velocity of the wave packets as well as the time between the two interferometer pulses. Second-order double Bragg diffraction features acceleration of wave-packets to a momentum of  $\pm 4\hbar k$  that doubles the relative velocity that wave packets have in regards to first-order Bragg diffraction. The expected fringe period for the same time  $\tau$  between the interferometer pulses should therefore decrease by a factor of two. To investigate this behaviour three different sets of parameters were investigated. First second-order Bragg diffraction was performed with two different values of  $\tau$ :  $60\ \mu\text{s}$  and  $120\ \mu\text{s}$ . Additionally a second-order Bragg diffraction interferometer with  $\tau = 60\ \mu\text{s}$  was performed.

The main concern of second-order Bragg diffraction is the increased momentum that yields a faster decrease in fringe spacing which could reduce the spacing under the detectable resolution. To make sure that the fringe spacing is detectable  $\tau$  was chosen to be  $60\ \mu\text{s}$ . The expected fringe period with a relative momentum of  $8\hbar k$  is  $d_{8\hbar k, \text{calc}} = 97\ \mu\text{m}$ . The fringe period should be half the size of first-order Bragg diffraction with the same value of  $\tau$ , because the displacement of the cloud is twice as large. A value of  $\tau = 120\ \mu\text{s}$  should result in the same fringe period because the cloud displacement is the same.

Fig. 3.29 shows the density distribution after a Ramsey-type interferometer for first-order (see Fig. 3.29(a)) and second-order (see Fig. 3.29(b)) double Bragg pulses. Fig. 3.29(b) shows the density distribution for a second-order



**(a)**  $\tau_i = 105 \mu s$



**(b)**  $\tau_i = 210 \mu s$

**Figure 3.27:** Density distributions of a Ramsey-type interferometer based on double Bragg diffraction with different  $\tau_i$  between the two  $\pi/2$ -pulses. The three Gaussian distributions depict the different exit ports of the interferometer and are part of the fitting routine of Eq. (3.50). The observed density distributions of each figure are summed over the radial direction which gives the one-dimensional density profile. The position of the outer Gaussian distributions is  $x_{2\hbar k} = (352 \pm 21) \mu m$  and the width is  $\sigma_x = (298 \pm 38) \mu m$ . The solid red line shows the fitted density distribution of Eq. (3.50).

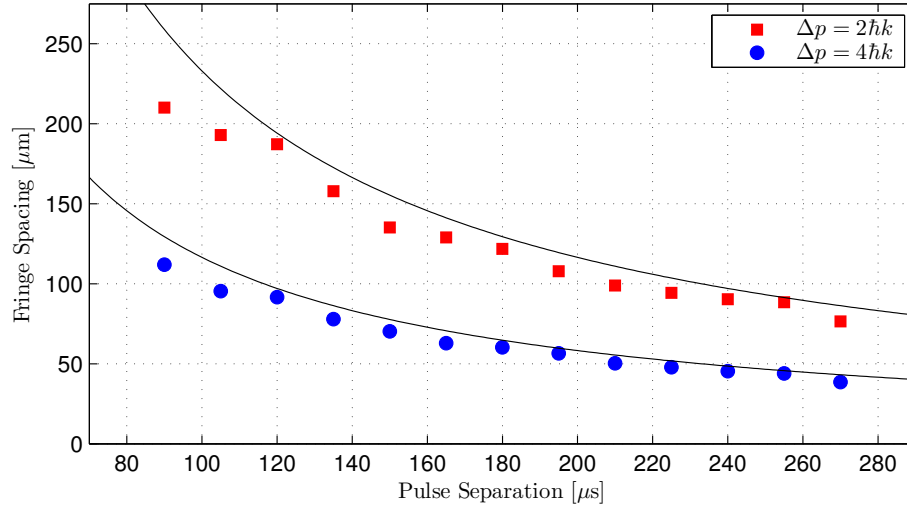


**Figure 3.28:** Fringe period of the density modulation after a Ramsey-type interferometer. The fringe period is dependent on the waiting time  $\tau_i$  between the two  $\pi/2$  pulses of the interferometer pulse sequence. The solid lines depict the solution of Eq. (3.49) for two different relative momenta of  $\Delta p = 2\hbar k$  and  $\Delta p = 4\hbar k$ .

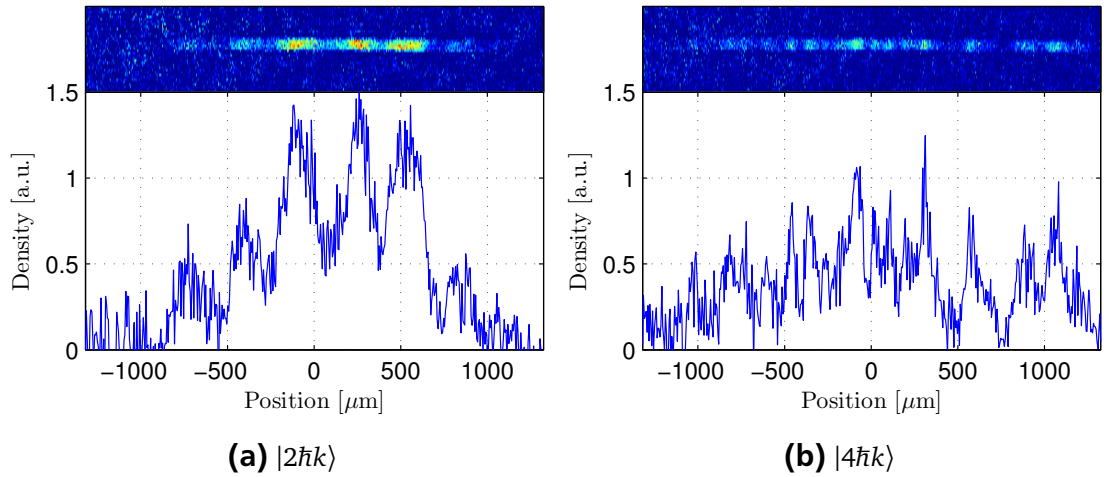


**Figure 3.29:** Realization of a double Bragg interferometer with different orders of diffraction. Fig. (a) shows a first-order ( $n = 1$ ) double Bragg interferometer and Fig. (b) shows a second-order ( $n = 2$ ) double Bragg diffraction interferometer. Both sequences featured a waiting time before the interferometer sequence of  $t_1 = 30$  ms and a time after the interferometer sequence of  $t_2 = 30$  ms. The separation of the two  $\pi/2$ -pulses was chosen to be  $\tau = 60$   $\mu$ s in both cases.

double Bragg diffraction interferometer. The lattice depth had to be increased in order to achieve a sufficient splitting into the momentum state  $|\pm 4\hbar k\rangle$ . The increased lattice depth on the other hand also increases losses due to spontaneous scattering. The density distribution shows a complex distribution of peaks and features a small fringe spacing. As shown in Eq. (3.49) the factor determining the fringe spacing is the separation of the clouds  $\Delta x = \Delta p/m \times \tau$ . The same separation can be achieved either by altering  $\Delta p$  or  $\tau$ . The parameter for  $\tau_i = 120 \mu s$  for first and  $\tau_i = 60 \mu s$  for second-order Bragg diffraction has been chosen in order to achieve identical values of  $\Delta x$ . Table 3.2 shows the compiled measured fringe spacing values for the chosen parameters. In Sec. 3.7.4 it has already been shown experimentally that double Bragg diffraction interferometers feature two distinct frequencies. First-order double Bragg diffraction with  $\tau = 60 \mu s$  shows a good agreement with the calculated values for  $\Delta p = 4\hbar k$  and  $\Delta p = 2\hbar k$ . The largest spatial frequency should be twice the size of the largest spatial frequency of the other implementations of the interferometers. Both other experiments show a good agreement with the calculated fringe spacing as well. First-order double Bragg diffraction and second-order Bragg diffraction have equal values for  $\Delta x$  by choosing  $\tau$  accordingly. This should yield identical spatial frequencies for all interferometer sequences featuring the same displacement  $\Delta x$ . All values match the calculated fringe spacing within the error margin and show an overall agreement with showing two distinct frequencies. For second-order double Bragg diffraction and with a spatial displacement of  $\Delta x = 2.82 \mu m$  the fringe spacing shows a huge uncertainty. The uncertainty is derived from the Gaussian fit to the Fourier spectrum of the one-dimensional density distribution. This error could originate from the increased noise in comparison to the other measurements, due to an increased lattice depth. The low fringe spacing introduces a large uncertainty for the determined period yielding an overall unreliable value. In addition the spacing of  $\Delta x = 2.82 \mu m$  lies in the regime of the coherence length of the condensate, which has been determined in previous experiments [65]. The coherence length of a BEC in a one-dimensional waveguide has been determined to be  $L_C = (2.42 \pm 0.3) \mu m$ . Since the coherence length gives the value where the observable contrast is reduced to  $1/e$  of the maximum observable contrast the large error can be explained.

As an additional difference to a first-order double Bragg diffraction interferometer the second-order interferometer shows that the moving exit ports after the interferometer have higher momentum. Because the time  $t_2 = 30 ms$  is the same for both orders the higher momentum yields a twice as large spatial separation of the exit ports. For second-order Bragg diffraction this yields a complete spatial separation of the two clouds. One of the clouds is visible in Fig. 3.29(b) at the position of  $1000 \mu m$ . On the opposite side at  $-1000 \mu m$  a similar density distribution is expected. The observation of a significantly reduced density distribution hints inequalities of the lattice pulses. In addition to

$\Delta x$ [ $\mu m$ ]	Fringe Period [ $\mu m$ ]			
	Calc	1st order DB		2nd order DB
$\Delta p/m \times \tau$	value	$\tau = 60 \mu s$	$\tau = 120 \mu s$	$\tau = 60 \mu s$
0.71	386	$342 \pm 52$	*	*
1.41	193	$164 \pm 36$	$186 \pm 18$	$220 \pm 24$
2.82	97	*	$93 \pm 8$	$66 \pm 41$

**Table 3.2:** Compilation of experimental values of measured fringe spacings after a Ramsey-type interferometer sequence for first-order and second-order double Bragg diffraction. Cells marked with \* are not measurable due to  $\Delta p/m \times \tau$  do not match  $\Delta x$  for the experimental configuration.

the already reduced density, due to additional losses due to spontaneous scattering, this increases the difficulty of detecting the interference distribution. An advantage of second-order double Bragg diffraction pulses is, that the resulting interferometer exit ports can be measured independently due to their larger relative velocity.

An additional disturbance is the reduced efficiency of  $\pi/2$  -pulses of second-order double Bragg diffraction. Sec. 3.4 shows that the maximum beamsplitter efficiency is 77% and that the remainder of the atoms either stays in  $|0\hbar k\rangle$  or populates  $|\pm 2\hbar k\rangle$ . This yields an additional interference pattern between all of the clouds travelling with different momentums present. This not only reduces the visibility of the main interference patterns but also reduces the maximum efficiency. At least there are four different combinations of interferences possible characterized by their relative momentum:  $\Delta p = 8\hbar k$ ,  $\Delta p = 6\hbar k$ ,  $\Delta p = 4\hbar k$ ,  $\Delta p = 2\hbar k$ . Each of them is a combination of the momentum states present:  $|0\hbar k\rangle$ ,  $|\pm 2\hbar k\rangle$ , and  $|\pm 4\hbar k\rangle$ . A reduction in visibility of the expected momentum states could be due to these unwanted additional spatial frequencies. Even if the spatial frequency analysis could not determine a significant excitation of unwanted density modulations.

Second-order double Bragg diffraction has shown to also be a valuable tool for matter wave interferometry. The reduced visibility and the overall loss of contrast can be explained by inaccurate  $\pi/2$  -pulses and a reduced spatial density. The expected decrease of fringe spacing by a factor of two could be shown.



---

## 4 Conical Refraction

Conical refraction is an optical phenomenon that occurs when light passes through a bi-axial crystal along one of its optical axis. From a first description in the early years of the 1830 to its application as a trap for atoms, as demonstrated in this work, conical refraction has shown to give unique opportunities to shape light beams with unique properties.

This chapter will give a brief introduction in birefringence in general (Sec. 4.1) and the properties of birefringence in bi-axial birefringent crystals (Sec. 4.2). The occurrence of conical refraction in these crystals will be discussed in Sec. 4.3 and a description of the introduced formalism is given. The chapter continues with the description of two basic regimes of conical refraction: the Poggendorff dark ring in Sec. 4.4.1 and the three-dimensional dark focus in Sec. 4.4.2. Both regimes will receive a detailed discussion as they are both implemented as trapping geometries for ultra-cold atoms and BECs, as discussed in Chapter 5 and Chapter 6.

---

### 4.1 Birefringence

---

Light in an optical medium experiences a change in the propagation velocity due to a modified refraction index  $n$ . Depending on the direction of the beam, the permeability  $\mu$ , and the dielectric constant  $\epsilon = (\epsilon_x, \epsilon_y, \epsilon_z)$ , the velocity of the beam can be derived from the following definition [121]:

$$v_x = \frac{c}{\sqrt{\mu\epsilon_x}}, \quad v_y = \frac{c}{\sqrt{\mu\epsilon_y}}, \quad v_z = \frac{c}{\sqrt{\mu\epsilon_z}}. \quad (4.1)$$

Derived from Maxwell's equations, the electromagnetic wave has to fulfil the following equation [121]:

$$E_k = \frac{n^2 s_k (\vec{E} \cdot \vec{s})}{n^2 - \mu\epsilon_k}, \quad \text{where } k = x, y, z, \quad (4.2)$$

the electric field  $\vec{E} = (E_x, E_y, E_z)$ , and the index of refraction  $n$  are introduced. Vector  $\vec{s} = (s_x, s_y, s_z)$  gives the normalized propagation direction of the incident wave, hence  $s_x^2 + s_y^2 + s_z^2 = 1$ . The non-zero solution of the system yields the Fresnel equation, which is given in one of its possible forms:

$$\frac{s_x^2}{v_p^2 - v_x^2} + \frac{s_y^2}{v_p^2 - v_y^2} + \frac{s_z^2}{v_p^2 - v_z^2} = 0, \quad (4.3)$$

where  $v_p = c/n$  is the phase velocity of the incident beam and  $n = \sqrt{\mu_r \epsilon_r}$  the index of refraction.

For uni-axial crystals the velocity in two dimensions is equal, hence  $v_x = v_y = v_o$ . The third dimension is defined as  $v_z = v_e$  where the indices  $o$  and  $e$  stand for ordinary and extra-ordinary. Eq. (4.3) can now be written as:

$$(v_p^2 - v_o^2) \left[ (s_x^2 + s_y^2) (v_p^2 - v_e^2) + s_z^2 (v_p^2 - v_o^2) \right] = 0. \quad (4.4)$$

The equation has two solutions with  $s_x^2 + s_y^2 = \sin^2 \theta$  and  $s_z^2 = \sin^2 s_z^2$  respectively, given

$$v_p^2 = v_o^2 \quad (4.5)$$

$$v_p^2 = v_o^2 \cos^2 \theta v_e^2 + \sin^2 \theta, \quad (4.6)$$

with  $\theta$  being the angle between the  $z$  axis and the normalized vector  $\vec{s}$ . The propagation of light in uni-axial crystals is given by the direction of the incident light and its intersection points with the ordinary and the extra-ordinary wave surfaces. The resulting direction of the beams inside the crystal is given by the normal vector of the tangent plane of this intersections points. In general there will be two different directions of propagation, corresponding to each of the two intersection points. However where the two wave surfaces intersect the two tangent planes of the wave surfaces coincide and only one beam can be observed. This direction defines the optical axis of the crystal.

A beam propagating through an optical medium with length  $d$  an index of refraction  $n \neq 1$  experiences a changed optical path length  $d_{OP}$  which is given by [122]:

$$d_{OP} = dn. \quad (4.7)$$

The modified optical path is important for the alignment of the focal plane of a conical refraction setup and will be considered in Chapter 5 and Chapter 6.

---

## 4.2 Birefringence in bi-axial crystals

---

In contrast to uni-axial crystals, bi-axial crystals feature three different indices of refraction. For simplicity it is assumed that:

$$v_x > v_y > v_z \text{ thus } \epsilon_x < \epsilon_y < \epsilon_z. \quad (4.8)$$

The solution of Eq. (4.3) for the given system is shown in Fig. 4.1. Each plot shows a cut through the wavefront of the crystal [121]. A three-dimensional system would span a sphere, whereas the shown plots depict cuts along each of the planes of the coordinate system. The cuts are obtained by settings the

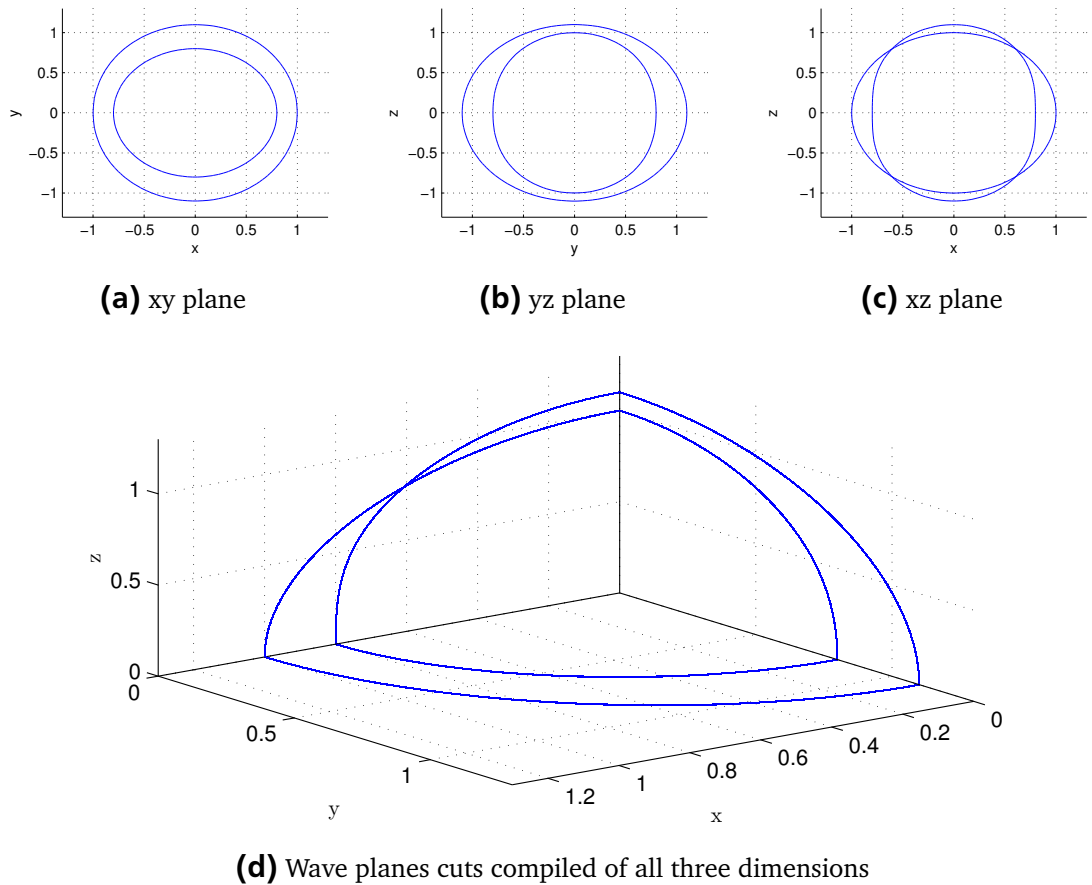


**Figure 4.1:** Wavefronts obtained by solving Eq. (4.3). (a-c) Each picture shows a cut through the three-dimensional double sphere of wavefronts giving the different velocities in each propagation direction. (d) gives a combination of all three directions dimensions and only shows one quadrant of the three-dimensional spheres of wavefronts.

---

remaining direction  $s_k = 0$  and solving Eq. (4.3). The calculated wavefronts are compiled in Fig. 4.1(d). Fig. 4.1(d) shows only a section of the obtained wavefronts which are symmetric along the planes of the coordinate system. Fig. 4.1(a) and Fig. 4.1(b) show that the wavefronts in these directions share no points regardless of the orientation of the incident beam. In the relevant direction for uni-axial crystals two surfaces intersect in two points, but with bi-axial crystals four intersection points are given (see Fig. 4.1(c)). Analogously to uni-axial crystals, the two lines connecting the opposite touching points of the wave surfaces in bi-axial crystals define the optical axis. It can be shown that no more than these four touching points exist [121]. Light propagating along any direction inside the crystal follows the behaviour described in uni-axial crystals. In contrast, along any of the optical axis, the intersection between the two wave surfaces has no well defined tangent plane, giving rise to an optical singularity known as conical refraction.

---

### 4.3 Conical refraction

---

As explained in the previous section, conical refraction occurs when the incident beam is aligned along one of the optical axis of the bi-axial crystal. The two crossing points of the wave surfaces do not define a single tangent plane, instead an infinite amount of tangent planes, forming a cone, exist. The normal vectors of these planes, giving the propagation direction of the incident beam, also form a cone. Therefore the incident beam will refract conically inside the crystal. Due to its unexpected behaviour this point has also been named 'Hamilton's diabolical point' [123]. Upon leaving the conical refraction crystal, a hollow cylinder emerges and propagates along the propagation direction. An important property of the produced cylinder is, that it is shifted laterally with respect to the input beam (see Fig. 4.3). The discussed properties are valid for ideally collimated beams, which are not possible to produce experimentally. Physically correct analysis takes into account diffractive optics as well as a Gaussian beam shape of the incident light. Focussed Gaussian beams have been considered for the re-formulation of a complete theory of conical refraction used in this thesis [31, 124, 125].

The most relevant properties of conical refraction beams is the occurrence of a pair of bright rings separated by the Poggendorff dark ring [126] in the focal plane of the focussed incident Gaussian beam. Also the Raman spot that appears symmetrically on both sides of the focal plane is a signature phenomenon of conical refraction. Without taking into account diffractive optics the occurrence of these very specific planes cannot be described.

In order to observe conical refraction experimentally, the incident axis of the light has to be aligned along one of the optical axis. This is only possible if the crystal has been cut and polished orthogonal with respect to one of the axis.

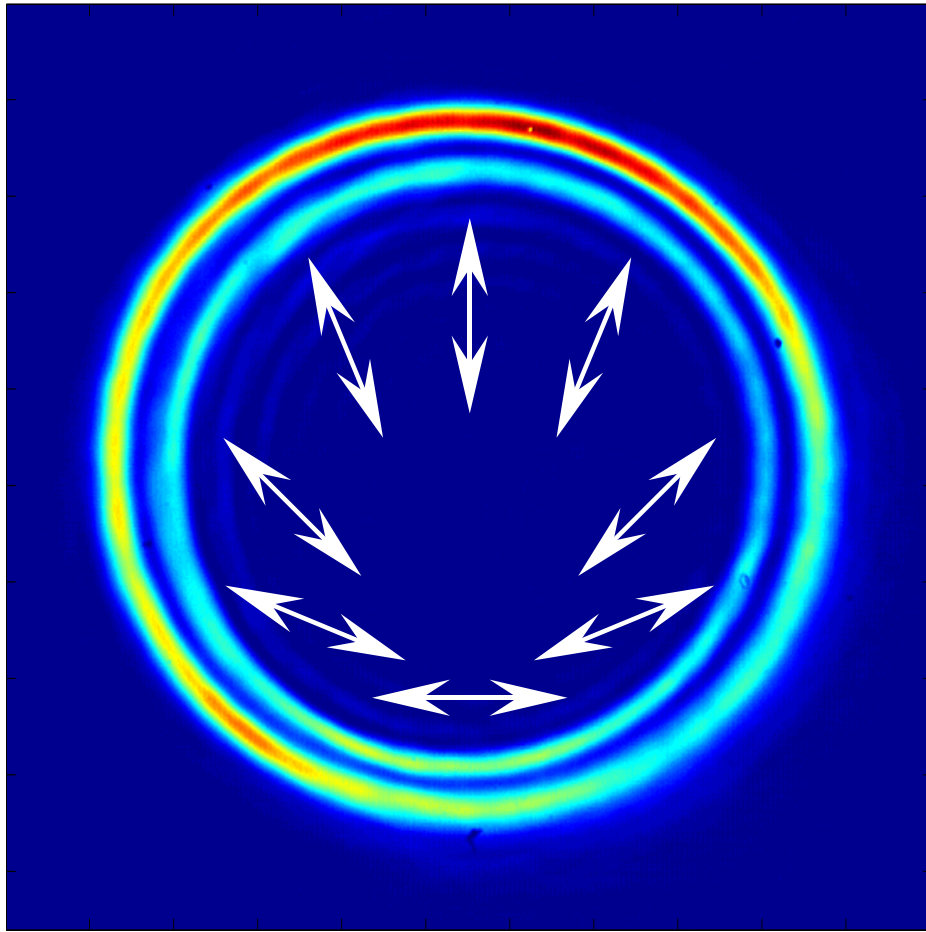


**Figure 4.2:** Experimental intensity distribution along the focal plane of a conical refraction structure. The ratio of beam waist  $w_0$  and ring radius  $R_0$  is  $\rho_0 = 14$ . Each point of the intensity is linear polarized and the polarization turns according to the azimuthal shift along the ring.

---

#### 4.3.1 Polarisation dependence of conical refraction light field

---

As described before, conical refraction structures are created at Hamilton's diabolical point. The first ever observation of conical refraction has been done with completely unpolarized light and yields the same intensity distribution as circular polarized light. Due to the polarization selectivity of the refraction angle on the conical refraction cone, each point of the conical refraction intensity distribution can be associated a distinct linear polarization axis. The axis evolves along the azimuthal angle of the intensity distribution. This behaviour is depicted in Fig. 4.2. The figure shows an experimentally obtained intensity distribution of the conical refraction beam at the focal plane. The arrows indicate the polarization vector of the electric field, which depends on the orientation of the crystal. The colour code of the experimental data already hints that the incident light features a non-desired elliptical polarization, where cer-

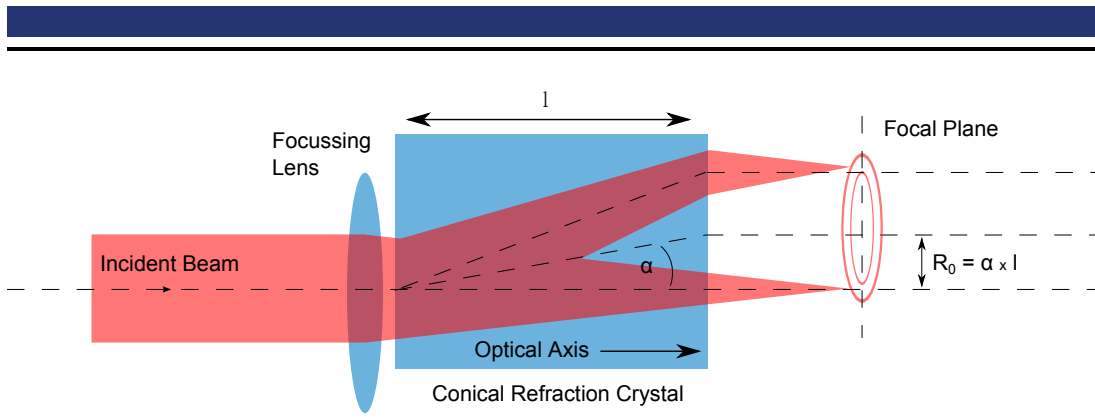


**Figure 4.3:** Scheme of the creation of conical refraction structures. The depicted scheme shows the creation of a Poggendorff dark ring in the focal plane of the focussing lens. The beam is aligned along one of the optical axis of the crystal. The half-opening angle  $\alpha$  determines the opening angle of the cone of light emerging from the conical refraction crystal.

tain polarization vectors are more dominant. This effect can be observed by the varying intensity along the azimuthal distribution of the ring.

By polarizing the light field linearly on purpose part of the structure can be selected. This has been shown for the three-dimensional dark focus as well as for the double ring structure and the Poggendorff dark ring. The achieved intensity distribution will be shown in the following sections.

It is important to notice that a homogeneous intensity distribution is key to achieve versatile trapping geometries for ultra-cold atoms. Varying intensities along the structure yield varying trapping potentials and could introduce non-desired effects. To avoid these, selected optical elements like a non-polarizing beamsplitter have been used in order to guarantee the best possible circular polarization for the experimental realization optical dipole potentials created with conical refraction crystals.

---

### 4.3.2 Important parameters of conical refraction setups

---

Fig. 4.3 shows a scheme of the beam propagation and introduces important parameters where applicable. The half-opening angle  $\alpha$  of the conical refraction cone is defined as [122]:

$$\alpha = \sqrt{(n_2^2 - n_1^2)(n_3^2 - n_2^2)}/n_2, \quad (4.9)$$

where  $n_1 < n_2 < n_3$  are the indices of refraction of the used conical refraction crystal. This equation is a paraxial approximation and valid for  $\text{KGd}(\text{WO}_4)_2$ , the used material of the conical refraction crystal in this work. The length of

the crystal  $l$  determines the diameter of the cone after the crystal and therefore the radius  $R_0$  of the created structure in the focal plane:

$$R_0 = l\alpha. \quad (4.10)$$

By choosing the length of the crystal and the focus size of the incident beam the shape and the nature of the intensity distribution can be altered significantly. This is discussed in Chapter 5 and Chapter 6, where two different structures are created with conical refraction. The criterion used to distinguish between the different regimes of conical refraction is defined as:

$$\rho_0 = \frac{R_0}{w_0}, \quad (4.11)$$

where  $w_0$  is the waist of the incident beam in the focal plane. This is also the waist of the radial symmetric ring structure created in the focal plane. The introduction of  $\rho_0$  also simplifies the discussion of the obtained structure since their shape is only defined by  $\rho_0$ . For values of  $\rho_0 > 5$  a double-ring structure is observed in the focal plane with a dark ring in the middle, the Poggendorff dark ring [123]. The Poggendorff dark ring is discussed in detail in Sec. 4.4.1. For  $\rho_0 = 0.92$  a single ring is created with an intensity minimum of zero in its centre [127].

In propagation direction, the  $z$  direction, the normalized parameter  $Z$  is used:

$$Z = \frac{z}{z_R}, \quad (4.12)$$

which gives the position  $z$  in orders of the Rayleigh range  $z_R$ .

Each regime of  $\rho_0$  features the occurrence of the Raman spot [128] at the location  $z_{\text{Raman}}$  of [126]:

$$z_{\text{Raman}} = \pm \sqrt{\frac{4}{3}} \rho_0 z_R. \quad (4.13)$$

Due to normalization issues, the definition used in this work differs from the original. Eq. (4.13) has been confirmed experimentally and numerically [127]. Given the definitions above, a full set of parameters used to describe conical refraction structures in different regimes is present that will be used to calculate the intensity distribution of the beam.

---

### 4.3.3 Intensity distribution of conical refraction

---

By the introduction of wave optics, an analytical solution for the description of par-axial conical refraction could be found [32, 124]. The analytical solution

was reformulated and the intensity distribution of a focussed Gaussian beam after it passed a conical refraction crystal along one of the optical axis is given by [123]:

$$I_{CP}(\rho, Z) = P_{in} \left( \left| B_C(\rho, Z) \right|^2 + \left| B_S(\rho, Z) \right|^2 \right), \quad (4.14)$$

$$I_{LP}(\rho, Z) = I_{CP} + 2\text{Re} \left( B_C(\rho, Z) B_S^*(\rho, Z) \right) \cos \left( 2\Phi - (\phi - \phi_0) \right). \quad (4.15)$$

$I_{CP}(\rho, Z)$  gives the normalized intensity distribution of a circular polarized Gaussian beam passing a conical refraction crystal.  $I_{LP}(\rho, Z)$  describes the intensity distribution for a linear polarized light beam. The linear polarization direction of the incident beam is given by  $\phi_0$  and  $\phi$  denotes the azimuthal angle in cylindrical coordinates.  $\rho$  is the radial coordinate in cylindrical coordinates.  $\Phi$  denotes the orientation of the plane of the optical axis of the crystal.  $B_C(\rho, Z)$  and  $B_S(\rho, Z)$  are defined as:

$$B_C(\rho, Z) = \frac{1}{2\pi} \int_0^\infty \eta a(\eta) e^{-i\frac{Z}{4}\eta^2} \cos(\eta\rho_0) J_0(\eta\rho) d\eta, \quad (4.16)$$

$$B_S(\rho, Z) = \frac{1}{2\pi} \int_0^\infty \eta a(\eta) e^{-i\frac{Z}{4}\eta^2} \sin(\eta\rho_0) J_1(\eta\rho) d\eta, \quad (4.17)$$

where  $a(\eta)$  is:

$$a(\eta) = \sqrt{\frac{2\pi P}{w_0^2}} e^{-\frac{\eta^2}{4}}, \quad (4.18)$$

for Gaussian input beams [127], and  $\eta$  is:

$$\eta = k w_0, \quad (4.19)$$

the normalized wave vector with  $k = 2\pi/\lambda$ .  $J_0$  and  $J_1$  denote Bessel functions of zero and first-order. A full discussion can be found in [123] and the discussion of beam profiles along the propagation direction follows for selected values of  $\rho_0$  in subsequent sections.

---

#### 4.4 Intensity distribution for varying $\rho_0$

---

The solution of Eq. (4.15) is investigated for various values of  $\rho_0$  in order to gain additional insight on the structures of achievable with conical refraction. Since the distribution of conical refracted light beams is rotationally symmetric the discussion continuous to be in cylindrical coordinates as already hinted with the choice of  $\rho$  as the parameter. Fig. 4.4 shows cuts through the focal plane

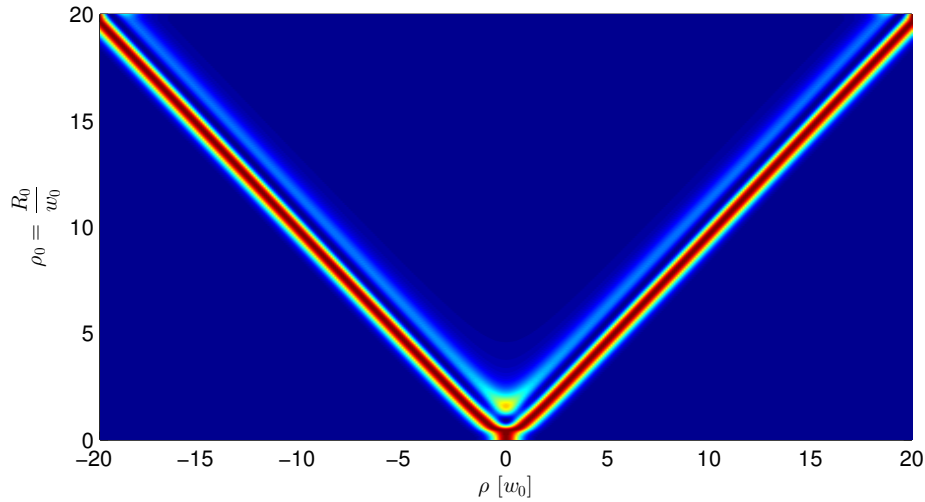


**Figure 4.4:** Intensity distributions in the focal plane for different values of  $\rho_0$ . Three different regimes emerge, which will be discussed separately. For  $\rho_0 \approx 0.92$  a dark focus trap is created (see Chapter 6). A double ring structure emerges for  $\rho_0 > 2$  and in between  $\rho_0 \approx 1.5$  a dark ring potential is created in the focal plane (see Sec. 4.5.2). Each column has been rescaled to give a maximum value of one.

at  $z = 0$  for varying values of  $\rho_0$ . Each column has been rescaled to increase the contrast. A normalized optical power would show a decreasing contrast for higher values of  $\rho_0$ .

As already mentioned four distinct regimes can be identified whereas three of them feature unique properties. For values of  $\rho_0 < 0.5$  a distribution similar to a Gaussian beam can be observed. In principle it can be seen as a regime where the radius  $R_0$  of the produced intensity distribution is smaller than the width of the produced ring.

For values of  $\rho_0 \approx 0.92$  a ring structure emerges. Fig. 4.4 shows that the intensity around the centre of the radial symmetric trap is near zero. To further investigate this behaviour, Fig. 4.5 shows the intensity for different values of  $\rho_0$  at  $z = 0$  and  $\rho = 0$ . As already mentioned the intensity is zero for  $\rho_0 = 0$ . The obtained intensity distribution is of interest for a new set of experiments and therefore investigated in more detail in Sec. 4.4.2 as well as experimentally implemented in Chapter 6.

In particular the creation of a double ring structure and the Poggendorff dark ring have been investigated. Since it has been the first structure observed showing conical refraction experimentally it is a well known structure for nearly 200 years. It emerges once  $\rho_0$  is larger than 5. The structure has been used at the ATOMICS experiment before to trap atoms and implement matter wave interferometers. In the mean-time its properties have been investigated further and additional insight on the achievable parameters will be given in Sec. 4.4.1.

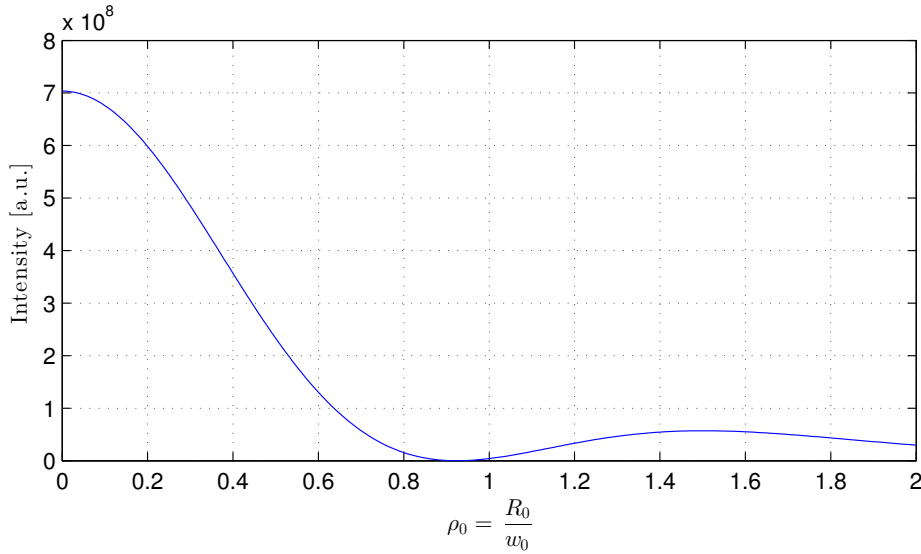


**Figure 4.5:** Intensity at  $\rho = 0$  and  $z = 0$  for varying values of  $\rho_0$ . The values are derived from Eq. (4.14) and show a local minimum at  $\rho_0 = 0.92$  where the intensity of the structure is zero.

It has been implemented experimentally, which will be discussed in detail in Chapter 5. By altering the parameter  $\rho_0$  between the values of 0.92 and 5 an additional distinct regime occurs: the focal plane features a ring shaped potential with a single focus in the centre. The distribution has not been investigated experimentally yet but for a value of  $\rho_0 = 1.5$  a brief discussion can be found in Sec. 4.5.2.

---

#### 4.4.1 Creation of a double ring structure with conical refraction

---

The double ring structure created with conical refraction was one of the first structures observed experimentally in an aragonite crystal in the early 1830th [30]. The dark ring between the double ring structure could not be explained theoretically up until 1978 [31, 124, 125]. Recent discussion has shown that the emerging Poggendorff dark ring can also be interpreted as the interference of counter-propagating cones of light [129]. Each of the cones originates from one of the Raman spots propagating in the direction of the focal plane. Due to the symmetric spacing of the Raman spot around the focal plane the created interference pattern of the two cones is also symmetric around the focal plane. The intensity distribution of the double ring structure in the focal plane is shown in Fig. 4.6 for circular and linear polarized light. Fig. 4.6(a) shows the resulting intensity distribution for circular polarized light. The intensity is divided into two rings. The inner and the outer ring, which are separated by the Poggendorff dark ring. The radius of the Poggendorff dark ring is not  $R_0$ , but smaller

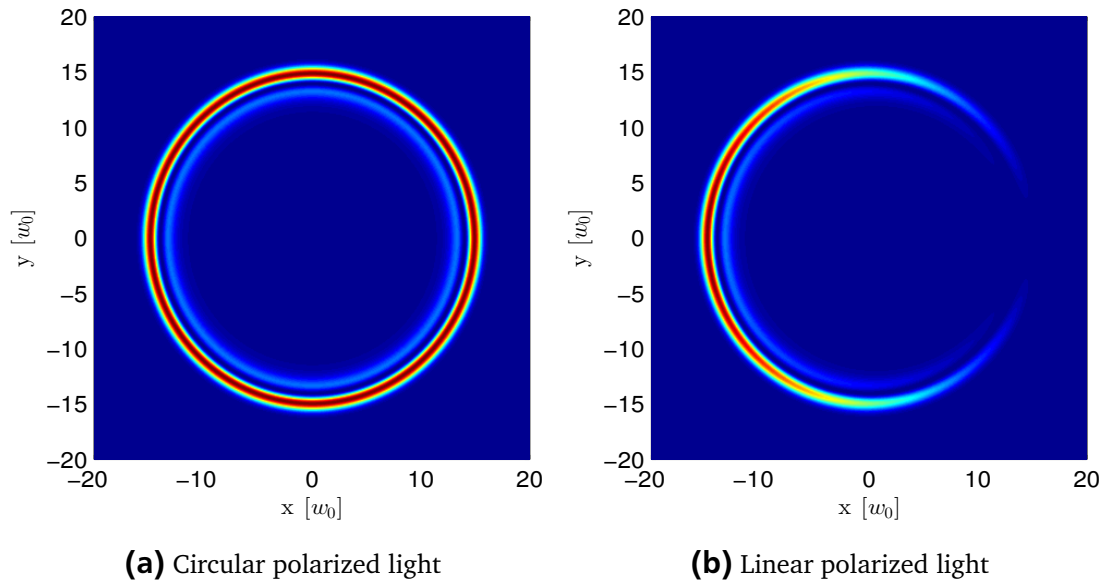


**Figure 4.6:** Solution of Eq. (4.14) for circular polarized light and Eq. (4.15) for linear polarized light. Shown is the focal plane of the intensity distribution, hence  $z = 0$ . The value of  $\rho_0 = 14.3$  is taken from the experimental implementation chosen for Chapter 5.

by  $w_0/2$  [130]. The intensity of the Poggendorff dark ring is zero and its radial waist is  $w_0$ . In radial direction the Poggendorff dark ring is confined by two maxima given by the double ring structure. The depth of the potential is determined by the lowest, the inner ring potential. In the focal plane, the intensity ratio between the outer and the inner ring is 4.7 [65].

Fig. 4.6(b) shows the intensity distribution of the identical setup but with linear polarized light. Due to the azimuthal polarization dependence of the intensity distribution linear light creates a gap in the ring. The intensity distribution shows a  $\cos^2$ -dependence along twice the azimuthal angle.

On increasing the distance  $z$ , the intensity in the Poggendorff dark ring increases. Fig. 4.7 shows the intensity distribution of three different positions in  $z$  direction. The increase is symmetric around  $z = 0$  and additionally the intensity ratio between the inner and the outer ring structure changes. The outer ring amplitude is decreased whereas the inner ring amplitude is increased. In the longitudinal direction, the intensity of the Poggendorff dark ring rises up until  $z = \pm 1.52z_R$  [130], giving a confinement in the beam propagation direction. In addition the spatial separation of the two rings increases. At the Raman plane  $z = z_{\text{Raman}}$  the intensity of the outer ring has completely vanished and the remaining inner ring has collapsed to the Raman spot. The complete contour of the intensity distribution of the conical refraction structure is shown in Fig. 4.8. This allows to understand an additional remarkable Ansatz for the description of conical refraction: By defining the focal plane as the interference pattern

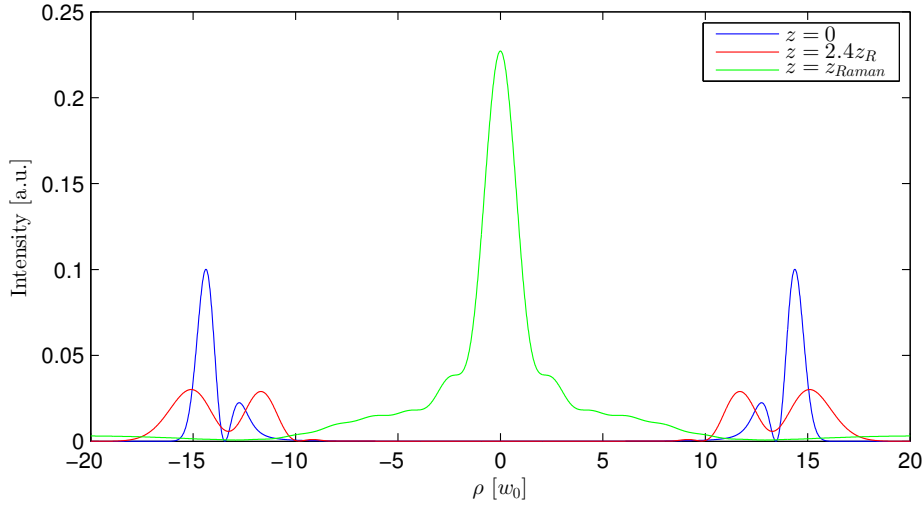


**Figure 4.7:** Solution of Eq. (4.14) for circular polarized light. Shown is the focal plane of the intensity distribution, and two additional positions. The value of  $\rho_0$  is chosen to be 14.3 which yields a intensity of zero for  $z = 0$  in the centre between the two rings, the Poggendorff dark ring.

of two cones of light originating from the Raman spots  $\pm z_{\text{Raman}}$  a complete description of the pattern is obtained [129]. This approach is used to demonstrate the creation of a single ring structure with conical refraction in Sec. 4.5.3.

The potential depth of the Poggendorff dark ring can be approximated by an harmonic potential and the derived potential depth can be found analytically [130]. In the focal plane at the position of the Poggendorff dark ring  $\rho_{\text{PDR}} = R_0 - 0.5w_0$  the potential in radial direction is:

$$U_{\pm}(\rho_{\text{PDR}}) = C_{\pm} \hat{U}_{\text{Rb}} \frac{P}{4\pi^2 w_0^2 \rho_0}, \quad (4.20)$$

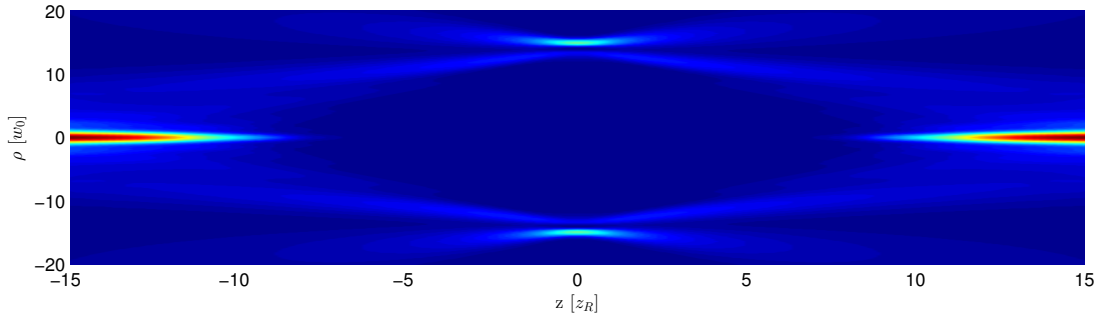


**Figure 4.8:** Intensity distribution of the conical refraction structure created for  $\rho_0 = 14.3$ . The shown contour plot is derived from the numerical solution of Eq. (4.14).

where  $\hat{U}_{\text{Rb}}$  is given by Eq. (2.3),  $C_+ = 2.54$  for the outer ring and  $C_- = 0.54$  for the inner ring. Since the atoms will leave the potential at the weakest point  $U_-$  will determine the potential depth. The trap depth in longitudinal direction is given by:

$$U_z(\rho_{\text{PDR}}) = 0.17\hat{U}_{\text{Rb}} \frac{P}{4\pi^2 w_0^2 \rho_0}. \quad (4.21)$$

With the approximation of an harmonic potential the trapping frequencies of the Poggendorff dark ring in the focal plane can be given as [130]:

$$\omega_{\text{radial}} = \sqrt{\frac{A_{\text{radial}}(0) \times \hat{U}_{\text{Rb}} P}{\pi^2 m w_0^2 \rho_0}}, \quad (4.22)$$

$$\omega_z = \sqrt{\frac{0.34 \times \hat{U}_{\text{Rb}} P}{\pi^2 m w_0^2 \rho_0}}. \quad (4.23)$$

With  $A_{\text{radial}}(0) = 4.64$ . The equations show that the trapping potential in the radial direction is far more intense than in the longitudinal direction. The radial trapping frequency in distance  $Z$  from the focal plane is derived with the modified value of  $A_{\text{radial}}(Z)$ :

$$A_{\text{radial}}(Z) = -0.05 + \frac{8.82}{1.87 + 2.31Z^2}. \quad (4.24)$$

---

#### 4.4.2 Creation of a three-dimensional dark focus with conical refraction

---

The three-dimensional dark focus has been first predicted by [127]. As shown in the previous section, it features a radial confinement with a diameter of  $2 \times w_0$  and zero intensity in its centre. Fig. 4.9 shows the normalized solution of Eq. (4.14) for circular polarized light (see Fig. 4.9(a)) and linear polarized light (see Fig. 4.9(b)). Both density distribution show a radius of  $1.1 \times w_0$  in the focal plane and a waist of  $w_0$  [127, 131]. For circular polarized light a perfectly radially symmetric intensity distribution can be found in the radial direction. In principle completely unpolarized light can also be used to create said structure. Linear polarized light on the other hand shows that only part of the ring potential is created. The linear polarization follows a  $\cos^2$  dependence with half the azimuthal angle as argument. The experimental creation is easily done by using a polarizing beamsplitter.

Fig. 4.10 shows the evolution of the radial intensity for four different positions of  $z$ . The focal plane at  $z = 0$  shows a confinement in the radial direction around  $\rho = 0$  where the intensity is zero. Moving away from the focal plane yields a rising intensity in at  $\rho = 0$  and a decreasing maximum intensity. Also

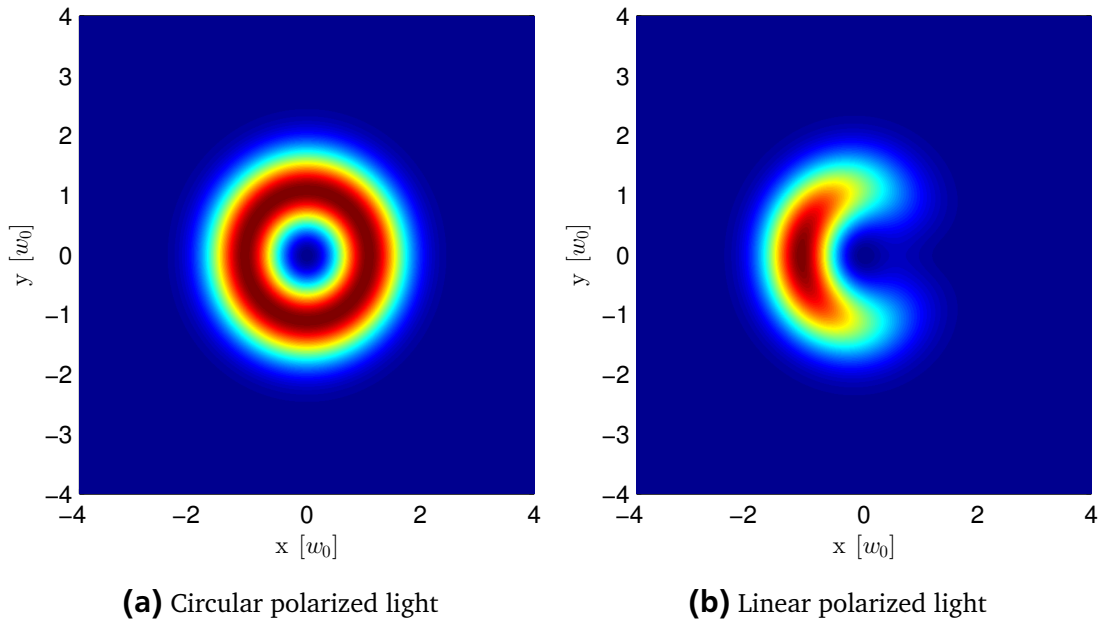


**Figure 4.9:** Solution of Eq. (4.14) for circular polarized light and Eq. (4.15) for linear polarized light. Shown is the focal plane of the intensity distribution, hence  $z = 0$ . The value of  $\rho_0$  is chosen to be 0.92 which yields a intensity of zero in the centre of the ring shaped intensity distribution.

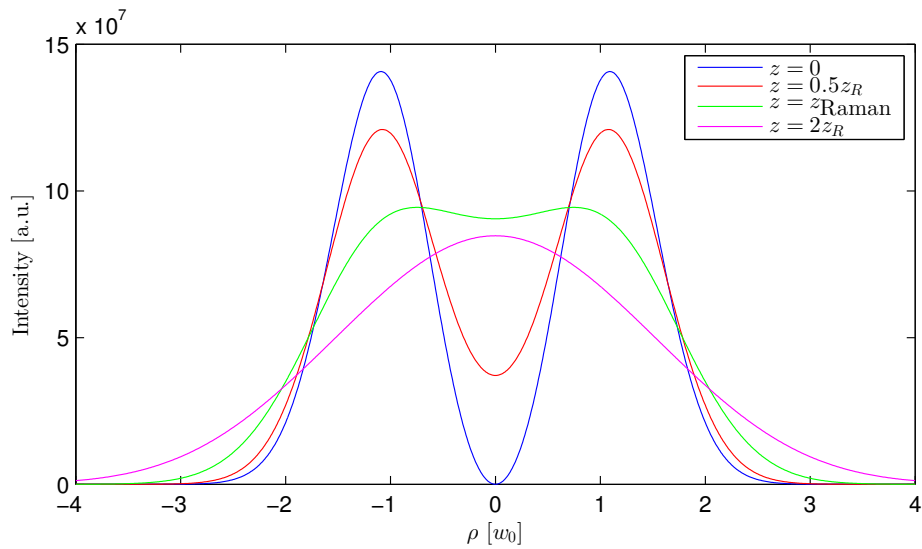


**Figure 4.10:** Calculated intensity distribution in four different planes. Shown is the solution of Eq. (4.14) for  $\rho_0 = 0.92$ . The intensity distribution is symmetric around the focal plane.

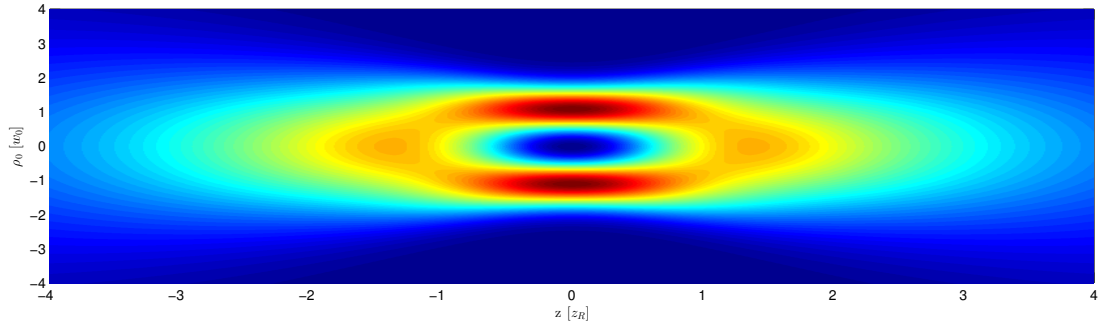


**Figure 4.11:** Intensity distribution along the beam propagation in the longitudinal and radial direction. The beam is rotationally symmetric around the  $z$ -axis and symmetric with respect to the focal plane. The shown intensity distribution is obtained with Eq. (4.14) for  $\rho_0 = 0.92$ .

the position of the maximum shifts towards smaller  $\rho$ . Up until the Raman spot ( $z = z_{\text{Raman}}$ ), two separate intensity maxima are distinguishable. After the Raman spot, for  $z > z_{\text{Raman}}$  only a single intensity peak is visible. The evolution of the intensity is also depicted in the contour plot in Fig. 4.11. The contour plot shows that the intensity distribution creates a closed area around  $\rho = 0$  and  $z = 0$ . In the centre of the distribution zero intensity is present creating a truly dark focus. The radial extension of the beam is determined solely by the waist  $w_0$  of the incident focussed beam whereas the radius  $R_0$  has to be chosen appropriately for the desired application. The elongation in propagation direction is determined by the Rayleigh range of the beam (see Eq. (2.5)). Depending on the optical setup, a full three-dimensional trap for atoms can be produced: for blue detuned light, high intensity yields a strong repulsive force on the atoms that pushed the atoms to regions of low intensity, e.g. the centre of the intensity distribution.

In order to trap atoms, multiple parameters are of interest and have been theoretically predicted in [131]. Even though the normalized solution of Eq. (4.14) can be used to calculate the trapping potential depth, an analytical solution has been found for both, the trapping potential depth in the radial and the longitudinal direction, and the trapping frequencies in both directions.

The trap depth of the created potential is estimated by a Taylor series around  $\rho \approx 0$  and in the axial direction for  $\rho = 0$ . Both calculations can be found in [131]. The trap depth in radial direction is given by

$$U_\rho = \hat{U}_{\text{Rb}} \frac{2P}{\pi w_0^2} \times 0.8, \quad (4.25)$$

and in longitudinal direction by

$$U_z = \hat{U}_{\text{Rb}} \frac{2P}{\pi w_0^2 (1 + Z^2)} \times 0.54. \quad (4.26)$$

$\hat{U}_{\text{Rb}}$  is given by Eq. (2.3),  $P$  is the optical power of the incident beam. With the approximation of a harmonic trap, the trapping frequencies have been determined by [131]:

$$\omega_\rho = \sqrt{\frac{13.66\hat{U}_{\text{Rb}}P}{\pi m w_0^4} \left| \frac{F_1\left(2; \frac{3}{2}; \frac{-0.854}{1+iZ}\right)}{(1+iZ)^2} \right|}, \quad (4.27)$$

and

$$\omega_z = \sqrt{\frac{\hat{U}_{\text{Rb}}P}{\pi m w_0^2 z_R^2}}. \quad (4.28)$$

$F_1$  denotes the Kummer confluent hyper-geometric function of the order of one.

---

## 4.5 Additional intensity distributions created with conical refraction

---

This section will briefly introduce additional intensity distributions that can be achieved by using conical refraction crystals. First a new way to create light-sheet potentials will be shown by using conical refraction with an elliptical focussed Gaussian beam. Next, a two dimensional ring potential with an additional focus in the centre of the ring will be introduced. Finally an additional way to create single ring structures for values of  $\rho_0$  greater than five is discussed.

---

### 4.5.1 Lightsheet potential with conical refraction

---

In addition to circular symmetric beams addition geometries can be implemented that use the advantageous of conical refraction. The ATOMICS experiment uses a two dimensional sheet of light to support ultra-cold atoms and BECs against gravity and to perform measurements (see Sec. 5.1.2). The implemented lightsheet uses light at  $\lambda = 782.5$  nm which is only 2.5 nm detuned in respect to the  $D_2$  transition of  $^{87}\text{Rb}$ . The resulting scattering rate is  $\approx 2.4 \text{ s}^{-1}$  and limits the achievable coherence and trapping times inside the potential.

The lightsheet potential is produced with an cylindrical Gaussian beam that is focussed by a cylindrical lens. This setup can be mimicked with conical refraction by guiding the same light through an additional conical refraction crystal behind the focussing cylindrical lens [132]. If aligned along one of the optical axes of the conical refraction crystal, the circular polarized beam creates a combination of two lightsheets separated by  $2 \times R_0$ . The elongation along the  $y$  axis is the unfocussed beam whereas the focussed beam in  $x$  direction features a focus of  $w_0 = 20 \mu\text{m}$ . The applied crystal has a half-opening angle of  $\alpha = 1^\circ$  and length of  $2.2 \mu\text{m}$ . Fig. 4.12 shows the experimentally obtained image of a

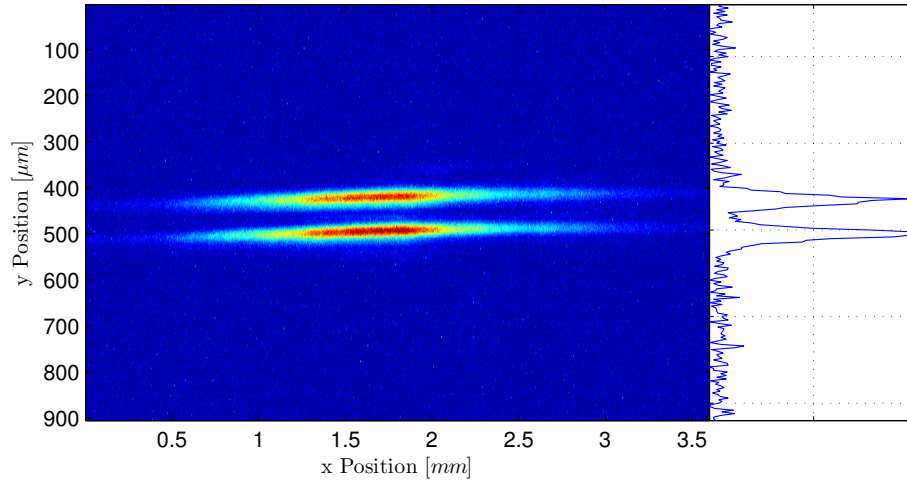


**Figure 4.12:** Experimental image of two lightsheets created with a elliptical Gaussian beam and conical refraction.

CCD camera [133].

Due to the polarization selectivity of conical refraction the two beams can feature a orthogonal polarization. With the help of a  $\lambda/2$  waveplate these intensity distribution of the two beams can be controlled. This is shown for two different positions of an additional  $\lambda/2$  waveplate in front of the conical refraction crystal in Fig. 4.13. Fig. 4.13(a) shows the beam polarized in  $\vec{e}_x$  direction. Over 90% is of the optical power is in the top of the two beams where as Fig. 4.13(b) shows the opposite behaviour for light linearly polarized in  $\vec{e}_y$  direction. The optical power is now completely in the bottom sheet of light

The lightsheet created with conical refraction offers the possibility to create a combination of two repulsive beams that trap atoms in the area between the lightsheets or a single red detuned lightsheet that supports atoms against gravity with its attractive potential. By using conical refraction to create these lightsheet potential a fast and reliable way is implemented to switch between these regimes. Additionally the intensity ratio between the two lightsheets can be chosen freely with the help of a  $\lambda/2$  waveplate.

---

#### 4.5.2 Single ring with central barrier

---

The transition from the three dimensional dark focus regime to the double ring regime yields an intermediate state. The intermediate state is given for a value of  $\rho_0 \approx 1.5$  and features a ring potential with additional intensity in the centre of the ring. Fig. 4.14 shows the intensity distribution in the focal plane calculated with Eq. (4.14) for  $\rho_0 = 1.5$ .

The diameter of the inner spot is in the order of  $w_0$  and can be compared to the focal spot of a focussed Gaussian beam. The outer ring has a radius of  $R_0 = 1.5 \times w_0$ , which is the expected position for  $\rho_0 = 1.5$ . The inner focus in

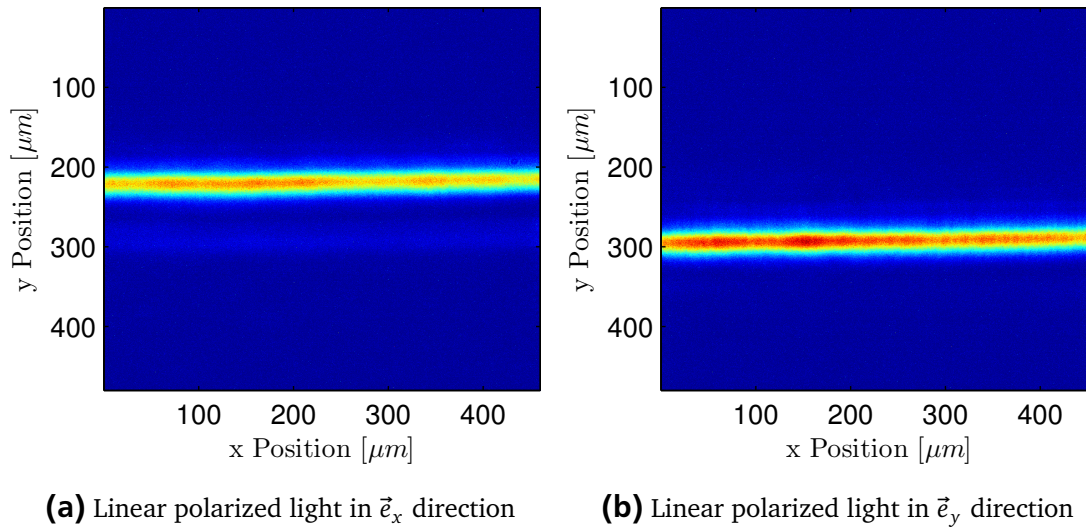


**Figure 4.13:** Experimentally obtained intensity distribution of a Gaussian beam focussed by a cylindrical lens. Fig. (a) shows the intensity distribution for linear polarisation in  $\vec{e}_x$  direction whereas Fig. (b) shows incident light with linear polarisation in  $\vec{e}_y$  direction.

the centre of the ring has a waist of  $w_0$  and by changing  $\rho_0$  the ratio between the inner focus and the outer ring can be tuned.

Other experimental implementations of similar potentials feature the use of two or more optical potentials [134], or involve the use of time orbiting potentials [135] in conjunction with magnetic coils. These setup could be replaced with the introduced potential created with conical refraction and show that conical refraction offers a multitude of novel trapping geometries for ultra-cold matter wave optics.

---

### 4.5.3 Single ring in a double ring configuration

---

In addition to the interpretation of the beam propagation discussed in Sec. 4.3, an additional way of describing conical refraction is introduced in [129]. The propagation of the light after it passed through a conical refraction crystal can be described by two cones with slightly shifted vertices. The polarization of the cones is orthogonal but matched in the region of the vertices and interference occurs.

By blocking one of the two cones spatially a single ring potential can be created [129]. The single ring potential is similar to the ring potential created with  $\rho_0 = 0.92$  in Sec. 4.4.2 but offers a main advantage: The diameter of the ring and the width of the ring structure can be chosen independently. Because the non-desired light is blocked completely the process is inefficient. Instead of blocking the light spatially a sectorized linear polarization plates can

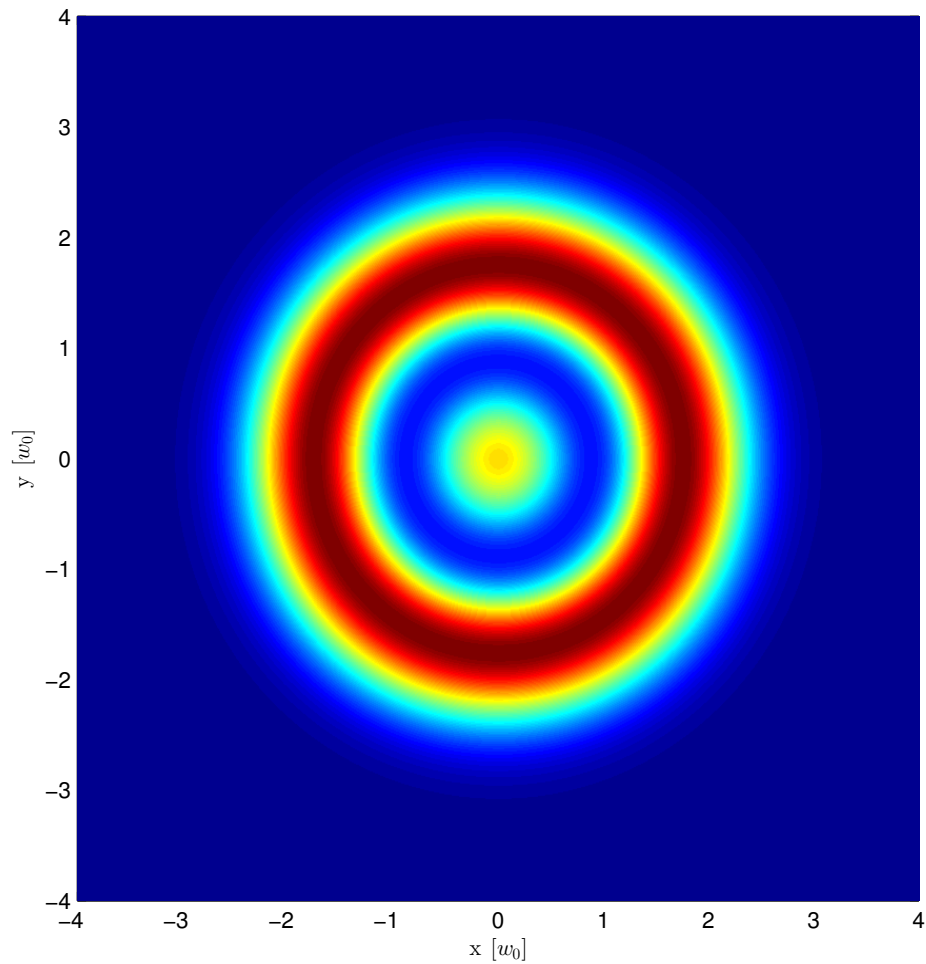


**Figure 4.14:** Intensity distribution in the focal plane for  $\rho = 1.5$ . The intensity distribution features a ring shaped outer structure and an additional intensity maximum in its centre. Using blue-detuned light creates a single dark ring with central barrier that can be used to trap atoms if an additional confinement in the third dimension is provided.

---

be used [136]. The polarization plate features a starburst pattern and opposite sectors give orthogonal polarization filtering. By positioning the pattern in front of the focal plane a single ring in the focal plane is observed.

A single red or blue detuned ring potential that is scalable and created with a single focussed beam offers a huge advantage over current strategies to create said structure. Since the setup consists of small and static components without electronic or mechanical additions it surpasses other setups such as time-averaged adiabatic potentials [135]. A possible application for the potential is the creation of a planar disc shaped potential with circular shaped bounds and [61, 65, 137].

---

## 5 Toroidal waveguide for ultra-cold atoms and BECs

Ring shaped trapping geometries are used to investigate basic properties of matter waves and are of interest for the creation of complex guiding structures for atoms or molecules [138]. Ideally, a guided matter wave interferometer like a Sagnac interferometer can be implemented in toroidal wave guides. Sagnac interferometers have already been demonstrated experimentally with ultra-cold atoms [139–141]. The possibility to create periodic boundary conditions or periodic disturbances are main advantageous of ring potentials [142]. The experimental creation of these potentials is a demanding task and a multitude of approaches exist. Complex combinations of coils [143] or atom chips [144] can be used to create magnetic trapping potentials. Time-averaged adiabatic potentials (TAAP) work with fast oscillating magnetic fields to create toroidal trapping structures [135]. Additionally time-averaged dipole potentials can be used to create time-averaged optical toroidal potentials [145]. Also Gauss-Laguerre beams have been used to guide atoms in rings [146]. Two polished optical fibres can also be used to create attractive dipole potentials to store atoms [147].

This section introduces a new technique to produce ring shaped trapping geometries with far-detuned light. Conical refraction is used to create a pair of repulsive light tubes nested inside each other. The tubes are aligned to propagate along the direction of gravity. To compensate gravity and to define a working plane, a thin lightsheet potential is used. Sec. 5.1 shows the experimental implementation and discusses the process of alignment of said potential. To further investigate ring shaped density distributions a conversion is characterized which creates one dimensional density profiles (see Sec. 5.2). Sec. 5.3 discusses the potential parameters and characteristics of atoms inside the guiding potential. In Sec. 5.4 properties of travelling atoms inside a ring shaped dipole potential are shown. Sec. 5.5 demonstrates the dynamic loading procedure of the ring potential to load BECs created outside into the toroidal guiding structure. This chapter concludes with the discussion on guided matter wave interferometry inside a ring shaped trap (see Sec. 5.6).

---

### 5.1 Experimental realisation of ring potential

---

To accomplish a toroidal waveguide for ultra-cold atoms and BECs conical refraction is used. The atoms are trapped inside the Poggendorff dark ring be-

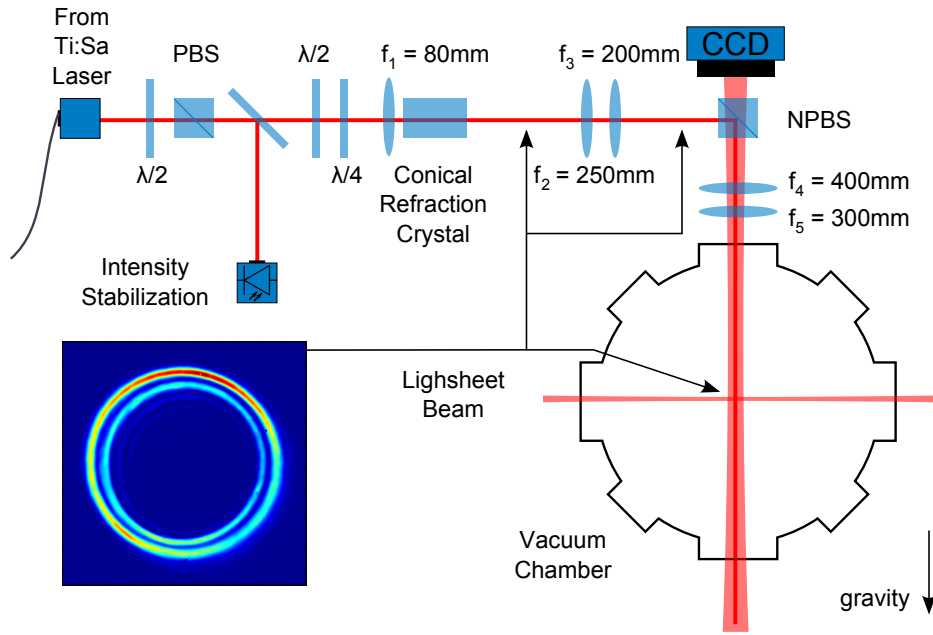


**Figure 5.1:** Optical setup for the creation of a toroidal trap. The ring structure is created outside the vacuum chamber and transferred into the vacuum chamber with two additional telescopes. The inset image is an image of the focal plane taken with a CCD camera.

tween two blue detuned ring shaped potentials. The setup does not provide a trapping force against gravity and therefore an additional lightsheet potential was implemented. The next section discusses the experimental realisation of the ring shaped trapping potential (see Sec. 5.1.1). Next Sec. 5.1.2 shows the construction and alignment of the lightsheet potential.

---

### 5.1.1 Optical setup for the ring shaped potential

---

Fig. 5.1 depicts the experimental setup used to create the double ring structure and to guide it into the experimental vacuum chamber. The light is guided from a Ti-sapphire laser<sup>1</sup> (Ti:Sa) to the experimental setup with an optical fibre [67]. The laser offers a large tunable wavelength between 750 nm and 850 nm which is used to either create repulsive or attractive dipole potentials for <sup>87</sup>Rb. The Ti:Sa laser is pumped by a solid state laser<sup>2</sup> at a wavelength of 532 nm with a maximum output power of 18 W. In addition an AOM and a mechanical shutter are used to control the light intensity.

On the experimental table, the laser light is aligned through a  $\lambda/2$  waveplate and a polarizing beamsplitter to purify the polarization. Afterwards a fraction

<sup>1</sup> Tekhno-Scan TIS-SF-07

<sup>2</sup> Coherent Verdi V18

of light is guided to an intensity stabilization [61]. As discussed in Sec. 4, perfectly circular polarized light is needed for the creation of a homogeneous illuminated double ring structure. This is ensured by a combination of a  $\lambda/2$  and a  $\lambda/4$  waveplate. The use of a single  $\lambda/4$  waveplate has been shown to create elliptical polarized light. The additional  $\lambda/2$  waveplate compensates polarization drifts on surfaces of optical elements and aids with the creation of a homogeneous ring created by circular polarized light.

The lens in front of the conical refraction crystal has a focal length of  $f_1 = 80$  mm. The spot size in the focal plane for the incident beam is  $w_0 = 20.4 \mu\text{m}$ . The conical refraction crystal is positioned between the lens and its focal point. The  $\text{KGd}(\text{WO}_4)_2$  crystal has a length of  $l = 16.55$  mm and an opening angle of the conical refraction cone of  $\alpha = 1.0^\circ$ . Its indices of refraction are compiled in Table C.1 as well as the values for other biaxial crystals. The crystal is cut and polished in a way that one of the optical axis is oriented parallel to the incident beam direction. This simplifies the alignment of the light beam in the crystal. In general the back scattered light of the crystal can be used to adjust perpendicular incidence.

Following Eq. (4.10) the radius of the Poggendorff dark ring created by the optical setup is  $R_0 = 290 \mu\text{m}$  in the focal plane. The resulting ratio between the width of the two rings and the radius of the ring is given by  $\rho_0 = R_0/w_0 = 14.3$  and therefore well in the regime to produce a Poggendorff dark ring. The focal plane is then re-imaged and demagnified by the combination of lens  $f_2$  and  $f_3$ . The diameter of the crystal is reduced by a factor of 0.8 and is  $232 \mu\text{m}$  in the re-imaged plane. The beam path is then aligned on top of the detection beam of the horizontal detection system (see Sec. 2.3.3). Since the polarization of the beam is a key element for its homogeneity a non-polarizing beamsplitter with a ratio of 50/50 is used. The beamsplitter features a reflectivity of 50% for p-polarized light and 52% for s-polarized light at a wavelength of  $\lambda = 792.5$  nm. This means that 50% of the optical power of the ring light and 50% of the detection light are lost already.

The focal plane of the conical refraction ring is then re-imaged a second time into the vacuum chamber at the place of the atoms. The lens system  $f_4$  and  $f_5$  demagnify the focal plane by a factor of 0.75. This yields a calculated ring radius of  $174 \mu\text{m}$ . The waist  $w_0$  is demagnified to  $12.2 \mu\text{m}$ . The light is guided through the optical chamber and disperses on the inner walls of the vacuum chamber.

To trap atoms in all three dimensions gravity has to be compensated. As shown in Fig. 4.8 the conical refraction potential used to create blue detuned walls offers no trapping force against gravity. Instead a focussed elliptical Gaussian beam is used as a second trapping potential to support atoms against gravity (see Sec. 5.1.2).

The total optical power provided by the Ti:Sa laser and usable for the creation of the double ring structure is 200 mW. The used intensity stabilization is posi-

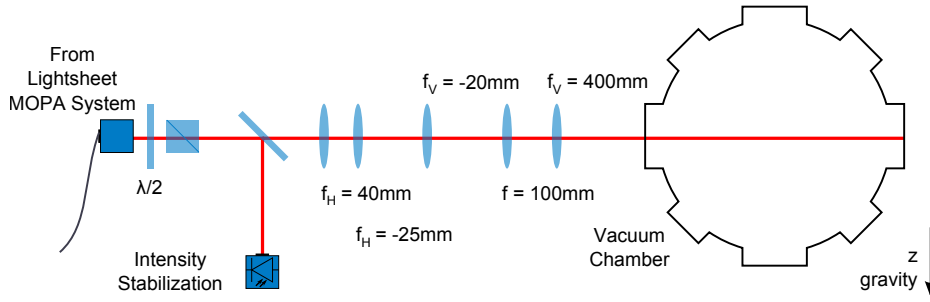


**Figure 5.2:** Schematic drawing of the lightsheet potential used to hold ultra-cold atoms and BECs against gravity. Two telescopes with cylindrical lenses shape the beam to create a highly anisotropic beam profile. The beam is focussed with the last cylindrical lens to provide a tight confinement in the  $z$  direction and to hold atoms against gravity.

tioned behind the polarizing beamsplitter in order to compensate polarization drifts that occur in the optical fibre. The optical power is controlled by an analogue voltage output of the experimental control that is connected to the AOM via its driver. The intensity stabilization offers a linear relation between the input voltage of the electronic stabilization system and the optical power available in the experiment. The optical power  $P_{\text{Ti:Sa}}$  corresponding to the voltage  $V_{\text{PD}}$  on the photo diode is given by:

$$P_{\text{Ti:Sa}} = V_{\text{PD}} \times 24.25 \frac{\text{mW}}{\text{V}}. \quad (5.1)$$

### 5.1.2 Lightsheet potential

A lightsheet potential is an elliptical Gaussian beam focussed by a cylindrical lens. The system is designed to support the atoms against gravity and forms a homogeneous trapping potential in the plane perpendicular to gravity. It is possible to trap atoms in the lightsheet potential and use the Poggendorff dark ring as a radial confinement to create an toroidal trap in three dimensions. The construction and the characterization of the lightsheet potential was performed by Martin Hasch during his masters thesis [148]. This section will focus on a short overview of the lightsheet potential and its experimental parameters crucial for the experiment.

The light for the lightsheet potential is provided by a master oscillator power amplifier (MOPA) system. The master oscillator is a self-built external cavity diode laser with an maximum output power of up to 70 mW. The wavelength is tunable with an external grating and laser operation is possible at wavelengths from 778 nm to 785 nm. The beam is coupled into a commercial tapered amplifier<sup>3</sup> and amplified to a maximum power of 500 mW. The resonant spontaneous

<sup>3</sup> Toptica TA 100

emission background of the tapered amplifier is rejected by two bandpass interference filters<sup>4</sup>. By tilting the filters the central wavelength of transmission is shifted to the desired value. The combination of two filters guarantees cancellation of unwanted light by a factor of 1000. The laser is guided through a mechanical shutter and an AOM to be then transported to the experimental table with an optical fibre. The AOM is used for intensity stabilization via the optical diode on the experimental table and the corresponding electronics [61]. The mechanical shutter is used to block the light completely.

On the experimental table, the beam exits the optical fibre and is collimated by a collimation lens. The light then travels through two telescopes built with cylindrical lenses in order to generate an elliptical Gaussian beam sufficient to form the lightsheet potential. The beam is then focussed into the vacuum chamber with a cylindrical lens. The produced lightsheet has a vertical waist of  $w_z = (26.2 \pm 0.5) \mu\text{m}$  and a vertical waist of  $w_z = (2752 \pm 42) \mu\text{m}$ . The wavelength of the MOPA system has been chosen to be 783.55 nm which fits well the compromise between trap depth and losses due to spontaneous scattering. The lifetime of atoms in this trap is 1 s [148]. The trap depth, reduced due to gravity [44], in the vertical direction is  $U_{LS}/k_B = 1.24 \mu\text{K}$ .

The alignment of the lightsheet potential is done with the help of absorption imaging. Ideally an influence of the potential is already visible when the lightsheet is roughly pointed at the atomic ensemble confined by the MOT. By choosing the detuning of the lightsheet to be near a resonance of  $^{87}\text{Rb}$  this effect can be amplified. Once an influence of the lightsheet potential can be observed the positioning in the vertical direction is trivial. With the help of the side-detection system the lightsheet potential is aligned at the place of the crossed optical dipole trap. Ideally the focus of the lightsheet is positioned on top of the cross section of the crossed optical dipole trap. The horizontal alignment is done by loading atoms into the trapping potential and applying a waiting time. During the waiting time, the drift of the atoms inside the lightsheet potential is observed. In the region of the focal point an isotopic expansion is visible. The lightsheet has been modified in a way that the final cylindrical lens is tillable on a mechanical translation stage. By tilting the lens previously observed inequalities of the potential could be compensated.

The vertical trapping frequency of the lightsheet potential has been measured experimentally by loading atoms into the lightsheet and exciting vertical oscillations [65]. This is done by switching the lightsheet off for a short period of time. After switching the lightsheet on again the potential energy deposited in the system results in a vertical oscillation of the atoms. This has to be done carefully so that atoms do not leave the potential. The measured trapping frequency is  $\omega_z = 2\pi \times (169 \pm 1.5) \text{Hz}$  [65].

<sup>4</sup> Semrock Maxline LL01-785

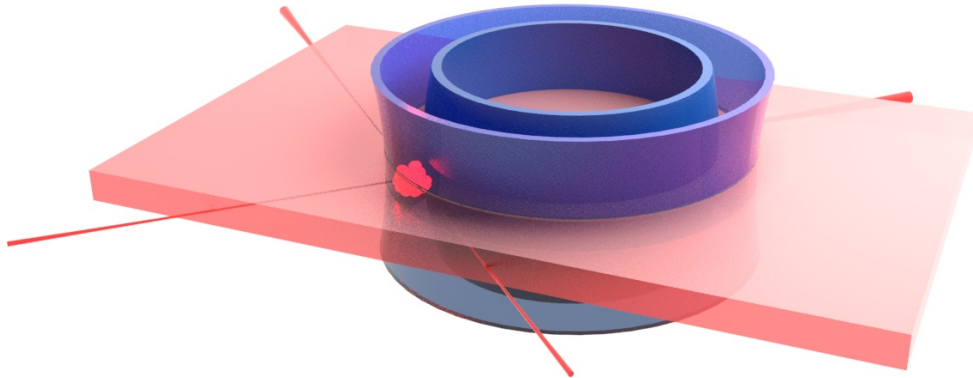


**Figure 5.3:** Three dimensional scheme of the complex combination of trapping potentials. The crossed optical dipole trap (red) creates the BEC in the cross-section. The atoms are then trapped in the three dimensional wave guide created by the attractive lightsheet and the repulsive double ring structure.

Fig. 5.3 shows a three dimensional drawing of the combined optical configuration of trapping beams. The tightly focussed crossed optical dipole trap creates a cloud of ultra-cold atoms. The blue double ring structure is aligned along the  $z$  and provides a tight confinement in the plane of the crossed optical dipole trap. In order to trap the atoms in all three dimensions the lightsheet provides a tight and homogeneous attractive potentials that holds the atoms against gravity.

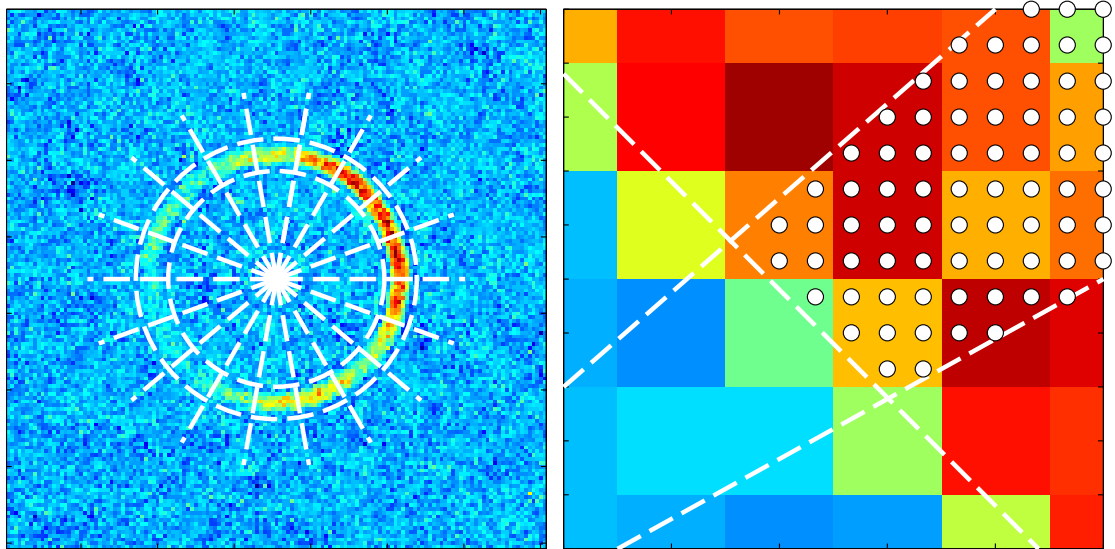
---

## 5.2 Analysis of ring shaped density profiles

---

To investigate the properties of atoms inside a ring shaped trapping geometry additional image processing is necessary. The tight confinement of the atoms in the radial direction reduces the motion of the atoms to a one-dimensional problem with periodic boundary conditions. This greatly simplifies curve fitting and is favourable for additional analysis. To decompose the image into a one-dimensional representation a grid of sections is superimposed on top of the image. Each section covering a distinct area of the ring shaped density profile. The density inside each section is binned together and represents the value of the section. This accuracy of this method is largely dependant on the parameters used.

The most important benchmark is the total atom number that has to be con-



(a) Grid of superimposed sections

(b) Subpixels aligned in one of the sections

**Figure 5.4:** Illustration of the transformation process. Fig. (a) shows the superimposed sections on top of the ring structure. Each section represents a data point in the one-dimensional density distribution. Fig. (b) shows the process of creating subpixels for an increased transformation and binning quality. Depending on the position of each subpixel an original pixel gets divided into different sections.

stant after the transformation. Using radial cuts to determine the density along the azimuthal direction could consider single pixels multiple times which is prevented by applying the following algorithm. This section will discuss the process of transforming a ring shaped density profile into a one-dimensional representation. A discussion on possible errors and the influence of several parameters is given. A set of parameters used for image transformation is elaborated. With the one-dimensional representation of the density distributions additional data examination is simplified.

The creation of a one dimensional density profile is done by dividing the ring shaped density distribution into equally shaped sections. Each sector covers a fixed angular part of the ring. Inside each sector, the sum of all pixels is binned together to determine the cumulated density. The atom count is calculated with Eq. 2.41. To determine the affiliation of each pixel to a section, two properties have to be matched: At first the distance of the pixel to the central point of the ring shaped distribution has to be between the inner ( $r_i$ ) and the outer radius ( $r_o$ ) of the ring. Fig. 5.4(a) depicts the inner and outer ring as dashed circles which enclose the density distribution. The second property is the angle in respect to an arbitrarily chosen starting point on the ring. To determine the angle, a line is drawn from the centre of the ring to each pixel. The angle is

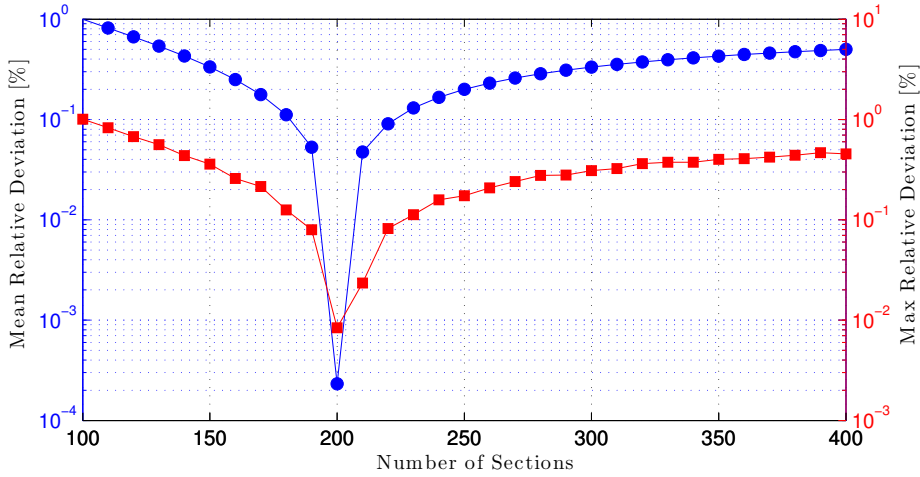


**Figure 5.5:** Mean and maximum deviation of the transformation depending on the section count. The mean deviation as well as the maximum deviation have a minimum at  $n_s = 200$ . The obtained resolution is identical to the optical resolution of the detection system. Changing the ring diameter implies that a new section count has to be chosen to match the resolution of the imaging system.

obtainable by the spanned rectangular triangle. Depending on the angle, each pixel is sorted into one of the sectors spanning the according angular section (see Fig. 5.4(a)). The more sectors are used the smaller each section becomes. Fig. 5.5 shows dependence of the section count ( $n_s$ ) to the error made when applying the binning algorithm. The obtained values of the density distribution are compared to the analytical solution of the area  $A$  of a section of the ring potential:

$$A = \frac{\pi(r_o^2 - r_i^2)}{n_s}. \quad (5.2)$$

Each pixel of the benchmark image has a value of one, which normalizes the distribution for testing purposes. The mean deviation shown in Fig. 5.5 reaches a minimum for a section count of  $n_s = 200$ . Given a radius of the conical refraction guiding structure of  $r_{Ring} = 173 \mu\text{m}$  (see Sec. 5.3.4) each of the 200 sections can be attributed to a span of  $5.4 \mu\text{m}$ . The resolution of the experimental imaging system in vertical direction is  $5.33 \mu\text{m}$  (see Sec. 2.3.3). The benchmark shows that the least deviation is achieved when the resolution of the transformation is the same as the resolution of the used image. In this section all future image processing will be done with a section count of  $n_s = 200$ , if not stated otherwise. For different diameters of ring shaped structures the section count has to be adjusted to match the detection resolution.

The position of the first sector can be chosen in a way that the resulting density profile is positioned optimal for additional analysis. Atoms occupying

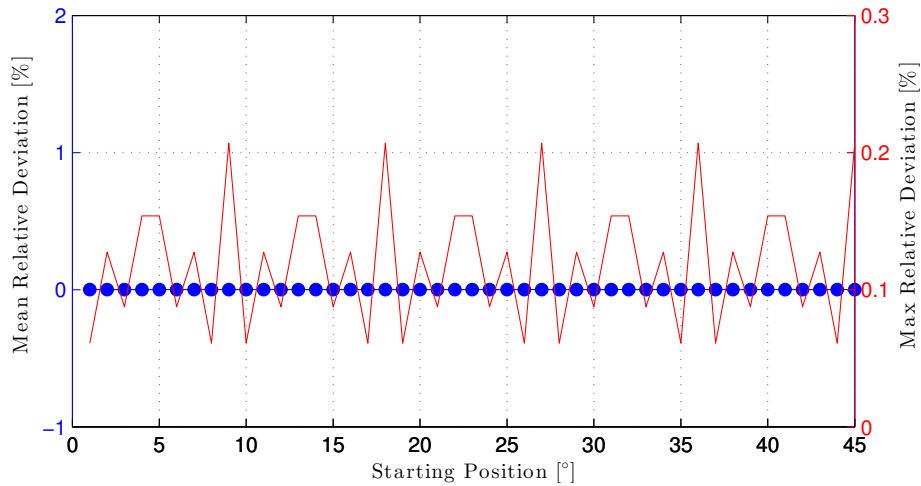


**Figure 5.6:** Mean and maximum deviation of the image transformation depending on the starting angle. The mean deviation is zero for all starting angles and a section count of  $n_s = 200$ . The maximum deviation has a periodicity of about  $9^\circ$ .

only a certain part of the ring should be positioned in the centre of the one-dimensional representation to give an easy graphic representation. Since the density distribution is periodic no fixed starting point is defined and can be chosen separately for each image. This is done by applying a simple angular offset to shift the density distribution accordingly. Depending on the exact value an increased maximum deviation can occur. To further investigate the impact of the starting position a comparison of different starting angles was done (see Fig. 5.6). The deviation shows a periodic behaviour with a period of about  $9^\circ$ . The mean deviation on the complete circle is zero for a section count of  $n_s = 200$ . The maximum deviation on the other hand changes with the starting position. It peaks at 0.2%. Choosing an offset of  $0^\circ$  gives a minimum deviation and is favourable. The position of the section on the ring is then given by the algorithm and is originated to the right of the ring structure (see Fig. 5.8(a)). Additionally the one-dimensional representation of the density distribution can be shifted. This can be done without losing accuracy just by shifting the data values accordingly. Therefore it is favourable to use a value of zero for the starting angle to reduce errors. In order to further improve the resolution of the transformation process, an additional method is introduced. Because the pixels of the camera are quadratic an easy scheme can be applied to create a set of subpixels. Each pixel is divided into smaller quadratic subpixels of equal size and weighted according to the covered area. Fig. 5.4 shows an example area of a density distribution acquired during absorption imaging (see Fig. 5.4(a)). The ring shaped trapping potential is magnified to show the alignment of subpixel in place of a normal pixel (see Fig. 5.4(b)). Each pixel is divided into nine equally sized subpixels with a new weight of one ninth of the

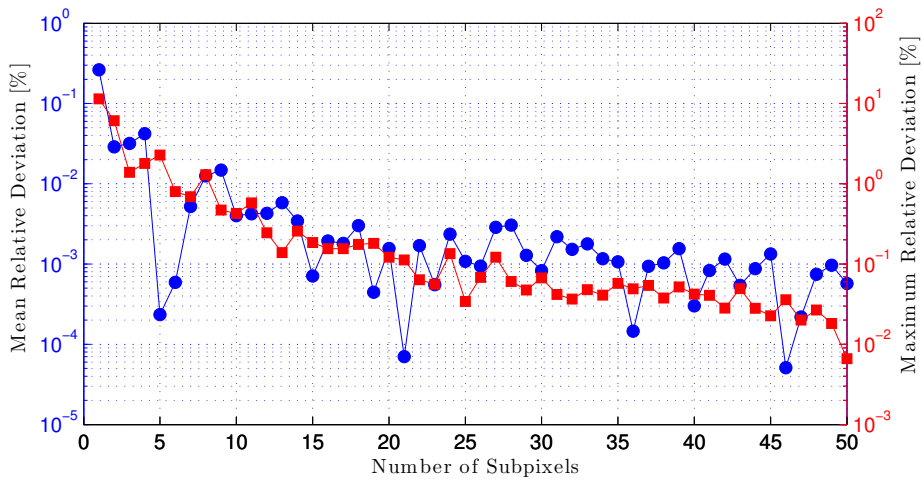


**Figure 5.7:** Mean and maximum deviation of the image transformation depending on the subpixel count. The more subpixels are used, the smaller the mean and maximum deviation are. The drawback is an increased computation time since this problem scales with  $O(n^2)$ .

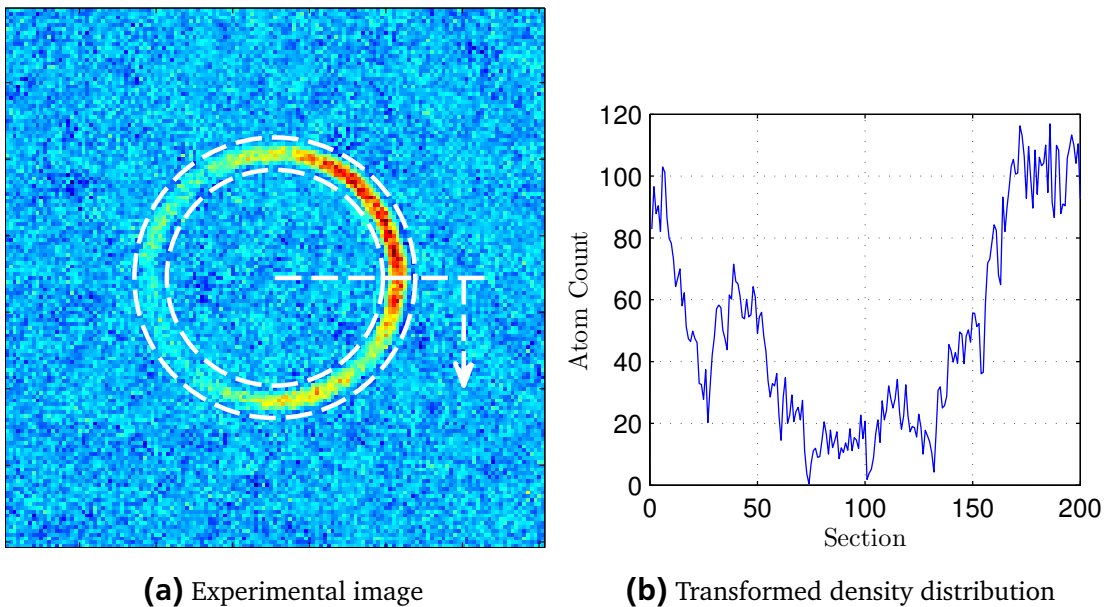


**Figure 5.8:** Example image of atoms trapped in a ring shaped geometry. (a) The inner and the outer boundary of the ring shaped guiding structure limit the radius and the initial position of the first section is shown. 200 sections are distributed over the full circumference of the ring. (b) Density distribution obtained after the transformation to a one-dimensional profile.

previous pixel value. The newly created pixels receive a new position according to their centre. Afterwards they are sorted into sections of the ring to create an one-dimensional representation of the ring shaped potential. Fig. 5.7 describes the influence of the subpixel count according to the error made by binning the pixels in discrete sections. As before the error made by this method is calculated towards a perfect binning of an artificial density distribution where every pixel has a value of one. According to the outer and the inner radius of the interesting section of the density distribution an analytical solution of the density can be given by Eq. (5.2). The binning algorithm was evaluated on the same artificial image and the deviation of the total section value to the analytical solution was calculated. The mean deviation of all sections is plotted as a function of the number of subpixels. As previously observed some of the sections show, according to the position of the intersecting section boundaries, different deviations. The maximum deviation is also given as a function of subpixels used per real pixel. The maximum deviation as well as the mean deviation decrease for an increasing subpixel count. On the one hand an increasing subpixel count is favourable to achieve an increased accuracy of the one dimensional profile. On the other hand the time needed to calculate the one dimensional profile increases due to the increased computer power needed. A viable subpixel count which gives a good accuracy and a short processing time is found for 25 subpixels. In this work all transformations will be performed with a subpixel count of 25, if not stated otherwise.

Fig. 5.8 shows an example for the application of the algorithm. Fig. 5.8(a) depicts an experimental image with atoms trapped inside a ring shaped wave guide. Between the boundaries of the inner and the outer ring, shown by dashed circles, the density distribution is transformed to a one-dimensional representation. As discussed the section count, initial angle, and the subpixel count have to be chosen appropriately. The transformation was done with a section count of  $n_s = 200$ , a starting angle of  $0.1^\circ$  and a subpixel count of 25. The calculated density distribution is shown in Fig. 5.8(b). Each sector represents a part of the ring geometry containing between zero and  $120 \text{ }^{87}\text{Rb}$  atoms.

---

### 5.3 Loading and expansion of a Bose-Einstein condensate

---

The Poggendorff dark ring presented in Sec. 4.4.1 will serve as an atom guide for ultra-cold atoms and coherent matter waves. The flatness and additional properties as well as the loading process will be discussed in this section. It starts with the horizontal alignment of the potential in Sec. 5.3.1, which is the key to loading atoms in the toroidal wave guide (see Sec. 5.3.2). Once atoms are trapped, a fine tuning of the vertical position can be done (see Sec. 5.3.3) to find the focal plane and to adjust it on top of the crossed optical dipole trap. Next, Sec. 5.3.4 discusses properties of the focal plane and the section is completed with a discussion on the expansion of atoms inside the toroidal

---

wave guide (see Sec. 5.3.5) and the lifetime of atoms stored in the trap (see Sec. 5.3.6).

---

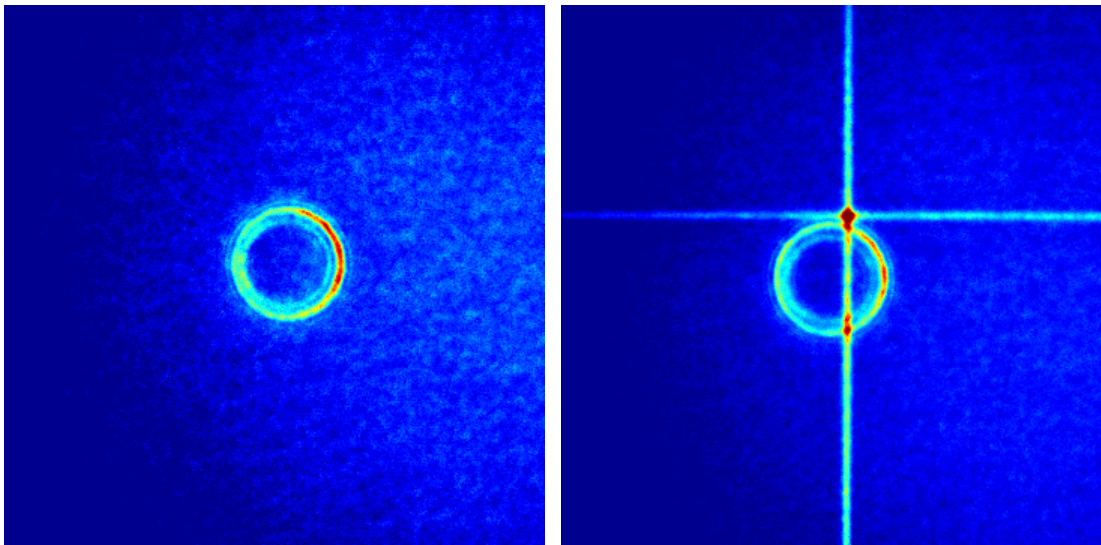
### 5.3.1 Horizontal alignment of the conical refraction potential

---

The horizontal alignment of the trapping potential is a two-step process. First the focussed Gaussian beam is aligned to run through the MOT and its focal point is determined to be in the atomic cloud. In a second stage, the conical refraction crystal is placed after the focussing lens (see Sec. 5.1).

To align the focussed Gaussian beam into the cloud of atoms of the MOT multiple aids are available. To make interactions between the atoms and the incident light beam more visible the detuning should be reduced to a minimum in respect to a transition of  $^{87}\text{Rb}$ . Because the ring light is aligned on the same optical axis as the vertical detection light it can be used to pre-align the beam before it enters the vacuum chamber. The detection light also has to pass the non-polarizing beamsplitter in front of the detection camera (see Fig. 5.1) and half of its intensity is reflected into the beam line of the conical refraction ring potential. Once the alignment has been performed outside the vacuum chamber, the light should already be visible inside the MOT. Depending on the alignment it could be useful to work with an attractive rather than a repulsive potential. Red-detuned light will produce an area of increased intensity, a blue-detuned light beam will create a hole in the MOT. To pre-align the  $z$  position of the beam, the waist of the created hole is used. The focal plane is reached once its diameter is minimal. The focussing lens is positioned on a translation stage to help with the positioning.

After the focal point of the focussing Gaussian beam is positioned in the MOT the conical refraction crystal should be placed in front of the lens. The crystal should be positioned to create the desired double ring structure and the waveplates in front of the focussing lens can be used to optimize the polarisation and therefore the intensity distribution in the focal plane. Ideally, this happens with a well aligned Poggendorff dark ring after the non-polarizing beamsplitter in order to compensate its inequalities. Due to the crystals refraction index, the distance of the focal plane after the focussing lens will be increased by 8.5 mm (see Eq. (4.7)). Due to the large Rayleigh range of  $z_R = 592\ \mu\text{m}$  the beam the Poggendorff dark ring should still be visible in the MOT. In Fig. 5.9(a) a red-detuned beam is aligned in the MOT. The background shows the atom distribution achieved by the MOT. The attractive double-ring structure is aligned with the maximum optical power available from the Ti:Sa laser system. The double ring structure is clearly visible and can be used to position the potential. This configuration can also be used to determine, whether the ring potential has a tilt with regards to the optical axis of the detection beam. If the ring potential is tilted, its image will show a deformed double ring structure. If the tilting angle is large enough, the separation between the inner and the outer ring van-



(a) Ring potential

(b) Ring potential and crossed optical dipole trap

**Figure 5.9:** Experimental images of the alignment process of the Poggendorff dark ring. For a small detuning with respect to the  $D_1$  transition of  $^{87}\text{Rb}$  the double ring structure can be observed in the MOT. With the addition of the crossed optical dipole trap, fine positioning in the horizontal plane is possible.

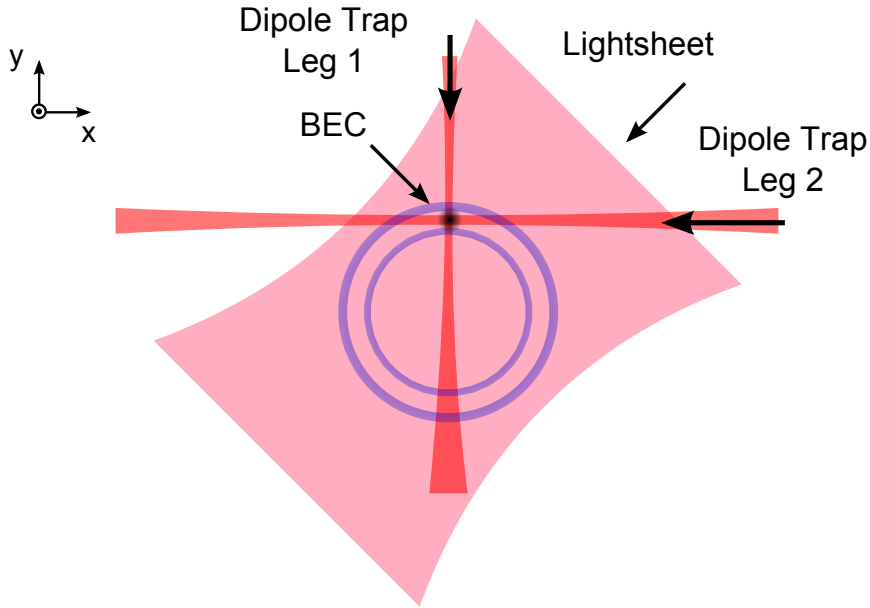


**Figure 5.10:** The Poggendorff dark ring is aligned on top of the intersection of the crossed optical dipole trap. The lightsheet supports the atoms against gravity and an efficient loading configuration for the toroidal trap is accomplished.

ishes on the absorption image. This effect appears due to the large elongation of the MOT along the detection axis. If the ring potential is perfectly aligned with the absorption light, a clear distinction between both rings is visible. In order to load atoms into the Poggendorff dark ring it is aligned on top of the intersection of the crossed optical dipole trap. Fig. 5.10 shows the alignment in a schematic drawing. The crossed optical dipole trap is positioned between the double ring structure and the lightsheet supports the atoms against gravity. Fig. 5.9(b) shows an absorption image taken during the alignment process. The double ring structure and the crossed optical dipole trap are slightly misaligned and a clear separation between the four light fields is visible. The ring can be positioned via a beam walk in front of the non-polarizing beamsplitter.

---

### 5.3.2 Adiabatic loading of the toroidal trapping potential

---

The experimental usability of the ring potential depends on the coherent loading efficiency of ring potential. A non-adiabatic loading transfer of atoms from one trapping geometry to another yields the risk of losing coherence and increasing the heat in the atomic ensemble. The coherent loading of the potential was demonstrated in [65] and a brief overview on the experimental details will be given. Afterwards a characterization of the loading scheme will be shown.

Adiabatic loading of an harmonic potential is possible if the change in trapping frequency is smaller as its squared value [70]:

$$\frac{d\omega}{dt} \ll \omega^2. \quad (5.3)$$

The total change of trapping frequency in the experiment is determined by the crossed optical dipole trap as well as the combined ring and lightsheet potential. The trapping frequency  $\omega_{DT}$  of the crossed optical dipole trap at the end of the evaporation process is in the order of  $\omega_{DT} = 2\pi \times 100$  Hz. The trapping frequency of the toroidal trap can be determined by Eq. (4.22). With an optical power of 200 mW and a wavelength of  $\lambda = 792.5$  nm a trapping frequency of the ring of  $\omega = 2\pi \times 400$  Hz is never exceeded. For a linear ramping time  $t_{ramp}$  of the combined optical potentials a lower bound for the ramping time is given by [65]:

$$t_{ramp} \gg \frac{(2\pi \times 400 \text{ Hz})^2}{2 \times (2\pi \times 100 \text{ Hz})^3} = 12.7 \text{ ms}. \quad (5.4)$$

The loading process of the toroidal potential with linear intensity ramps has therefore a minimum ramp time of  $t_{ramp, \min} = 12.7$  ms. The choice of an experimental ramping time of 40 ms for all experiments carried out in this work gives a sufficient separation from the lower boundary and should provide adiabatic loading of atoms into guiding structures.

---

### 5.3.3 Vertical alignment of the conical refraction beam

---

The large Rayleigh length of  $z_R = 592 \mu\text{m}$  (see Sec. 5.1) makes a vertical alignment of the trapping potential difficult. In previous implementations the potential was aligned so that atoms could be trapped [65] but the  $z$  position of the ring potential could only be calculated afterwards. The experimental procedure started by positioning the focal plane of the focussing lense in front of the crystal and adding the crystal at a later stage. Due to the crystals index of refraction the optical beam path shortens and the focussing lense can be positioned appropriately. Due to the large Rayleigh range the positioning process is prone to uncertainties and a more reliable way was developed.

The goal of the alignment process is to position the focal plane at the same vertical position as the intersection of the crossed optical dipole trap. This offers multiple advantages. In the focal plane the Poggendorff dark ring features a minimum intensity of zero. This should reduce effects of the ring potential towards the trapped atoms. Additionally, the slope of the trapping potentials is the steepest at the focal plane yielding a tight radial confinement.

The fine-tuning of the vertical position  $z$  of the ring potential can begin once atoms are trapped inside the guiding structure. The ring potential is positioned

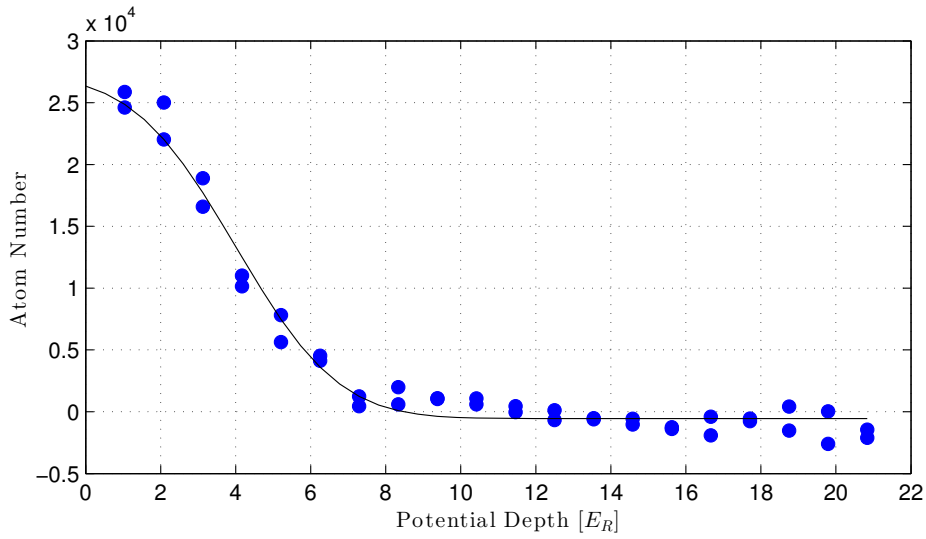


**Figure 5.11:** Fraction of atoms leaving the ring shaped guiding potential after an acceleration perpendicularly towards the outer repulsive ring. On top of the fitted data points an error function is used to determine the point where half of the atoms stay trapped inside the potential. The measurement was taken for  $z = 0$  (i.e.  $z = z_0$  as determined according to Fig. 5.12) of the conical refraction potential. The potential depth axis was scaled according to Eq. (5.5).

in such a way that Bose condensed  $^{87}\text{Rb}$  atoms are loaded into the Poggendorff dark ring area. After the loading procedure of the potential, a Bragg diffraction  $\pi$ -pulse is applied. The potential is aligned such that the atoms move perpendicularly towards the outer ring potential. Depending on the laser intensity a fraction of the atoms is able to travel over the repulsive potential of the blue detuned light. The higher the kinetic energy of the atoms, the higher the potential barrier must be to successfully reflect the atoms. Since the laser intensity for the outer ring is the highest in the focal plane the power needed should be at a minimum.

An accelerated atom cloud with a momentum of  $4\hbar k$  was chosen which has a kinetic energy of  $E_{kin} = 4E_R$ . After accelerating the atoms an additional waiting time of 18 ms was applied so that the atoms leaving the trapping geometry are separated spatially. Fig. 5.11 shows a representative measurement where the laser intensity was slowly increased until all of the atoms stayed inside the trapping potential. At the beginning nearly all of the initial 25000  $^{87}\text{Rb}$  atoms are accelerated outside of the potential. The number of atoms decreases as the intensity rises and the repulsive force of the ring potential increases. The data is rescaled to match  $4E_R$  at the point where 50% of the atoms are trapped and 50% can leave the potential. By moving the ring potential along the vertical direction an intensity evolution along the double ring guiding structure is measured. The smaller the needed optical power, the closer the  $z$ -position is to the

focal plane.

Fig. 5.12 shows the resulting data for multiple iterations of the potential height measurement. Depicted is the optical power needed to create a  $4E_R$  steep potential barrier as a function of the vertical position  $z$  of the ring potential. Since the translation stage on which the focussing lens in front of the conical refraction crystal is mounted offers a scale a reliable calibration of the position can be done. The values used for the position are only viable for the experimental setup realised in this experiment and have to be rescaled for different Rayleigh ranges or after the repositioning of the focussing lens. Each of the data points represents a full measurement of the fraction of atoms trapped in the ring potential for varying optical power. The needed optical power to create a  $4E_R$  high barrier has a minimum at  $z_0 = (14.36 \pm 0.06)$  mm giving the position of the focal plane of the conical refraction crystal. The value of  $z_0$  is taken in respect to the translation stage used to position the lens and has to be re-evaluated once changes to the beam path have been applied.

As described in Sec. 4.4.1, each vertical position shows a different set of attributes in regards of potential height, potential width, intensity ratio between the inner and the outer ring, and the intensity of the Poggendorff dark ring. Fig. 5.12 gives a map to find the desired position for future experiments.

In addition this measurement is used to calibrate the laser intensity of the Ti:Sa laser and the corresponding trap depth of the ring potential. In this way losses of the optical power can be determined and the efficiency of the whole laser setup is determined. The intensity distribution of the Ti:Sa laser is given by Eq. (4.14) and the total optical power  $P$  is determined by Eq. (5.1). Without knowing the losses of the optical beam path, the trap depth determined by Eq. (2.3) is only an upper bound for the intensity. Due to losses at the non-polarizing beamsplitter and additional optical elements, the potential height of the blue detuned walls will be smaller. As shown in Fig. 5.11, the optical power needed to create a trap depth of  $4E_R$  is well known. This value is used to calculate the losses. The optical power needed for a  $4E_R$  high potential wall is  $P_{\text{in}} = 70.8$  mW as measured in front of the conical refraction crystal. This yields a usable optical power  $P_{\text{ring}}$  at the place of the atoms of:

$$P_{\text{ring}} = 0.3379 \times P_{\text{in}}. \quad (5.5)$$

The calculated optical efficiency of the complete setup is 33.79%. Due to the non-polarizing beamsplitter, 50% of the optical power is lost already at this element. The remaining optical elements and account for the remaining losses of 16.21% showing that the conical refraction system used to create an optical storage ring is very efficient in regards to the optical power.

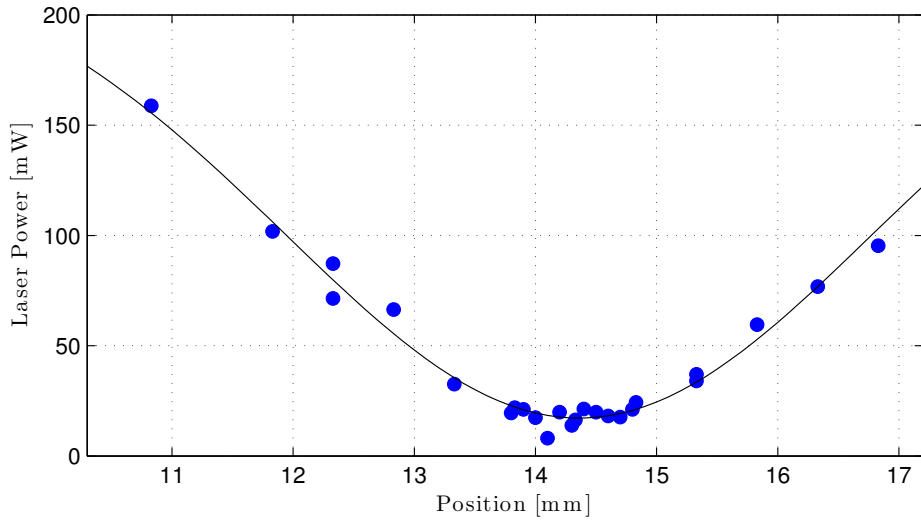


**Figure 5.12:** Optical power needed to create a  $4 E_R$  repulsive potential with the outer ring of the conical refraction double-ring structure. Optical power needed has a minimum at  $z = (14.36 \pm 0.06)$  mm indicating the focal plane.

---

### 5.3.4 Properties of the potential in the focal plane

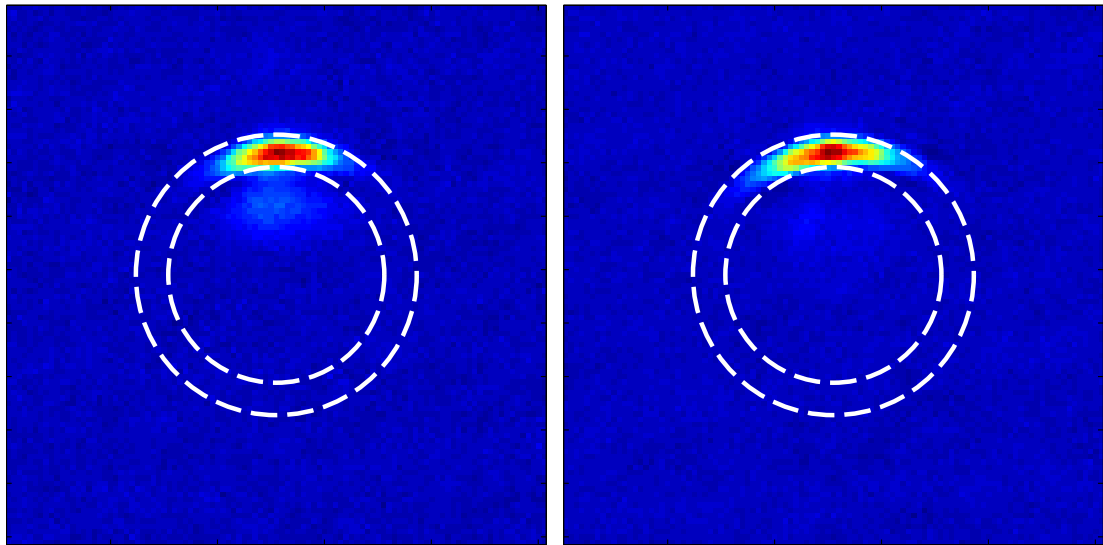
---

#### Loading efficiency

---

After the positioning in the  $z$ -direction of the ring potential has been performed according to Sec. 5.3.3 the loading efficiency of the ring potential was investigated. Following Eq. (5.4) the linear ramping time was chosen to be  $t_{\text{ramp}} = 40$  ms. The alignment of the potential is shown in Fig. 5.10. The intensity of the Ti:Sa laser was varied in order to create different trap depth of the ring guiding structure whereas the lightsheet was kept at a constant depth. After the loading procedure an additional waiting time of 10 ms was applied. Fig. 5.13 shows two example images taken 10 ms after the loading process. Fig. 5.13(a) was taken with a potential depth of  $U_R = 1.37 E_R$ . The atoms are loaded into the ring potential at the top of the guiding structure in a way that losses are minimized. This is done by slightly adjusting the position of the ring and measuring the losses. The losses can be seen as atoms floating around the actual trapping region depicted by the two dashed circles showing the guiding structure of the ring.

After the alignment process, the loading efficiency of the potential was measured by comparing the atom number inside the ring geometry with the total atom number. Atoms not trapped in the ring geometry occupy the disc shaped potential created by the lightsheet and the inner ring potential. No atoms could be observed on the outside of the outer ring potential and the optical power



(a)  $U_R = 1.37E_R$

(b)  $U_R = 8.22E_R$

**Figure 5.13:** Absorption images taken 10 ms after the loading of the toroidal wave guide has been completed. Fig. (a) shows a low potential depth of  $U_R = 1.37E_R$  whereas Fig. (b) shows a deep potential of  $U_R = 8.22 E_R$ .

available allows to alter the trap depth between  $0E_R$  and  $8.22E_R$ .

Fig. 5.14 shows the loading efficiency of the trap for varying potential depth. For shallow potentials 24% of the atoms are loaded into the inner part of the ring geometry were the remainder of the atoms is positioned in the desired ring structure. The more the depth of the potential increases the more atoms are loaded into the guiding ring structure. For trap depth above  $5 E_R$  the trap depth is sufficient to load over 90% of the atoms into the guiding potential. The increased trap depth yields an additional effect on the atoms loaded into it. Due to the increased radial trapping frequency the expansion in the azimuthal direction is increased following Eq. (2.36). This can be observed by the two absorption images shown in Fig. 5.13. The lower trapping frequency in the radial direction show corresponds to a smaller azimuthal spread of the condensate (see Fig. 5.13(a)). Fig. 5.13(b) shows an increased azimuthal width by a factor of 1.3 whereas the trap depth is increased by a factor of five. For interferometric measurements, such as shown in Sec. 5.6, this effect could be exploitable to tune the spreading of the travelling wave packets.

---

#### Ratio between the inner and the outer repulsive ring potential

---

The ratio of the inner and the outer wall in the focal plane according to Eq. (4.14) is 4.7. By using the method already introduced to find the focal plane

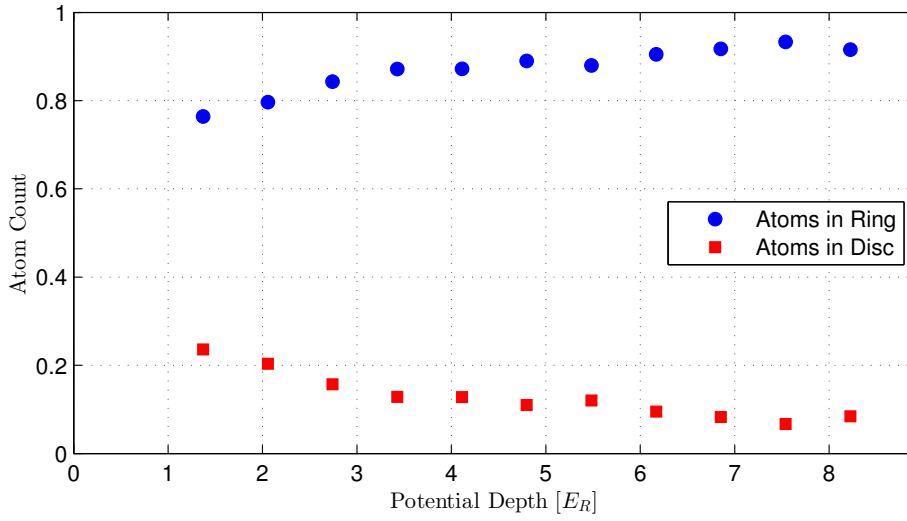


**Figure 5.14:** Fraction of atoms loaded into the ring shaped trapping potential depending on the optical power. The Potential depth is calculated according to Eq. (5.5). Initially a BEC of 25000  $^{87}\text{Rb}$  atoms is created in the crossed optical dipole trap.

(see Sec. 5.3.3) it is now possible to investigate the potential height of the inner and the outer wall of the potential separately. The crossed optical dipole trap is therefore aligned to the left or to the right of the ring potential to accelerate atoms orthogonally into either the inner or the outer potential barrier. A standard Bragg lattice is used to accelerate the atoms to momenta of  $2\hbar k$  or  $-2\hbar k$  depending on the aimed ring wall and side.

Depending on the optical power, the fraction of atoms remaining in the potential changes. The higher the repulsive potential gets, the more atoms are trapped in the ring guiding structure. Once 50% of the atoms are trapped in the guiding potential the potential barrier has reached a height of  $4E_R$ . Ideally, both sides would act in the same manner showing that the double ring structure is rotationally symmetric.

Fig. 5.15 shows a schematic of the measured optical power needed to create a repulsive potential of  $4E_R$  height. The inner potential on the right side needs an optical power of  $(70.0 \pm 11)$  mW to create said barrier. The outer ring needs a factor of 3.8 less optical power:  $(18.1 \pm 1.9)$  mW. On the left side of the pattern, the inner ring needs an optical power of  $(56.4 \pm 12.1)$  mW of optical power and the outer ring needs  $(21.7 \pm 1.9)$  mW, which yields a factor of 2.6 less power.

Both sides are below the expected ration of 4.7 and show a distinct difference of nearly 30%. Multiple reasons for this discrepancy with regards to the expected ratio can be found. On the one hand, the circular polarization of the potential has to be determined outside of the potential and was adjusted with the help of a CCD camera. This approach does not include out additional optical elements as lenses and mirrors that guide the light into the vacuum chamber.

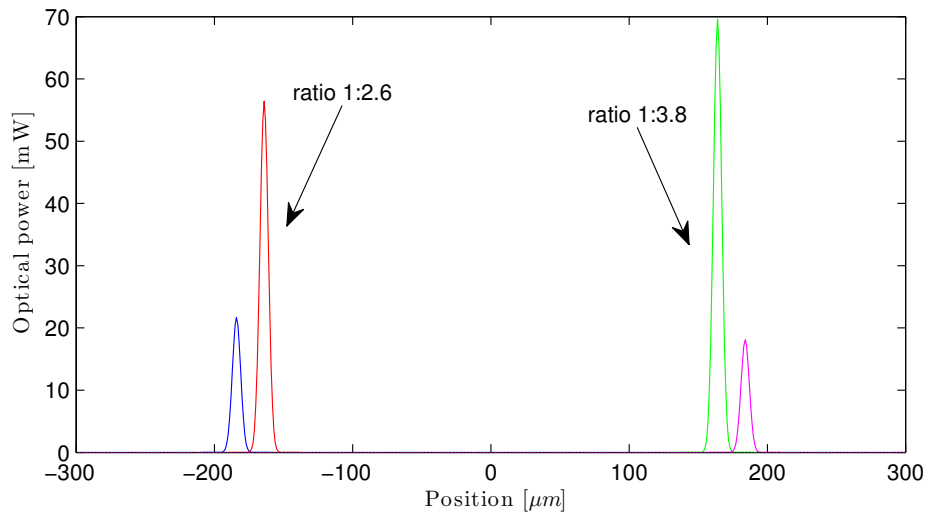


**Figure 5.15:** Optical power needed to create a  $4E_R$  repulsive potential. To demonstrate the position and the shape of the potential Gaussian distributions were chosen and their width was chosen arbitrarily. The plot does not give an representation of the actual potential shape.

On the other hand, the ring potential and the optical beam path is prone to diffraction and interference. Additionally an elliptic beam profile would create a modulation along the radial intensity distribution in the focal plane.

---

### Radius of the Poggendorff dark ring in the focal plane

---

The diameter of the Poggendorff dark ring has been observed experimentally with an CCD camera outside of the experimental vacuum chamber. The additional optical elements used to guide the light into the chamber introduce possible errors that would change the ring diameter. To eliminate uncertainties and to verify the calculated ring diameter of  $174\ \mu\text{m}$  at the place of the atoms, an additional characterization measurement of the ring radius was performed. The atoms were loaded into the trapping potential and part of the atoms was accelerated to travel along the guiding ring structure. A standard Bragg lattice was used in order to accelerate the atoms. Its experimental implementation and additional discussion can be found in Sec. 5.4. After the atoms have travelled half the circumference of the ring, an absorption image was taken. A one-dimensional cut through the density profile and through the center of the ring was made. The peaks from the density distribution of the atoms were used to calculate the distance and therefore the diameter of the Poggendorff dark ring. Fig. 5.16 shows the absorption image in addition to the one-dimensional cut

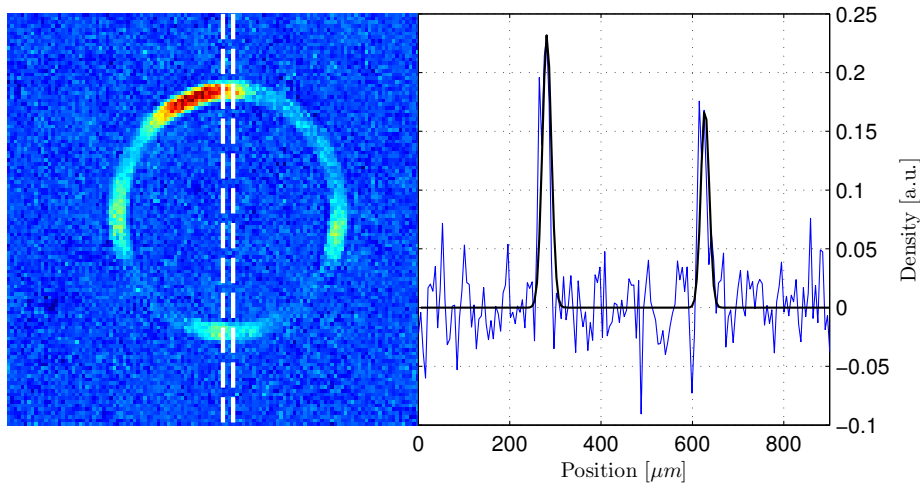


**Figure 5.16:** Experimental image used to determine the diameter of the Poggendorff dark ring. The density distribution of guided atoms allows to use a cut through the potential as seen on the right to determine the distance of the peaks. Two Gaussian distributions were fitted in order to obtain the distance. The resulting measured radius of the Poggendorff dark in the focal plane is  $\rho_{\text{PDR}} = (173 \pm 2) \mu\text{m}$ .

used to determine the diameter. The calculated diameter of the Poggendorff dark ring is:

$$\rho_{\text{PDR}} = (173 \pm 2) \mu\text{m}, \quad (5.6)$$

which is close to the expected radius of the Poggendorff dark ring in the focal plane.

---

### 5.3.5 Expansion of atomic ensembles in the ring potential

---

The free expansion of an ensemble of trapped atoms in the ring guide is a benchmark for the flatness of the potential. Previous work has shown that free expansion is not always possible in ring geometries created with light [61, 65]. Due to the radial trapping frequency created by the repulsive ring walls, the azimuthal expansion should be different compared to the expansion in free space. Depending on the azimuthal trapping frequency a free ballistic expansion should be observable. If the azimuthal trapping frequency is non-negligible, the combination of light fields would not provide a flat toroidal trap.

Fig. 5.17 shows the azimuthal width  $\sigma$  of the BEC after variable expansion times. Underlying is the solution of Eq. (2.36) (solid line) for  $\omega_r(0) = \omega_\phi(0) = 2\pi \times 150 \text{ Hz}$  and  $\omega_z(0) = 2\pi \times 212 \text{ Hz}$ , which are the initial trapping frequencies of the crossed optical dipole trap. The initial width of the condensate was set to the Thomas-Fermi radius of  $R_{TF} = 3.02 \mu\text{m}$ . The loading process of the toroidal trapping potential was not modelled in the numerical solution. Instead

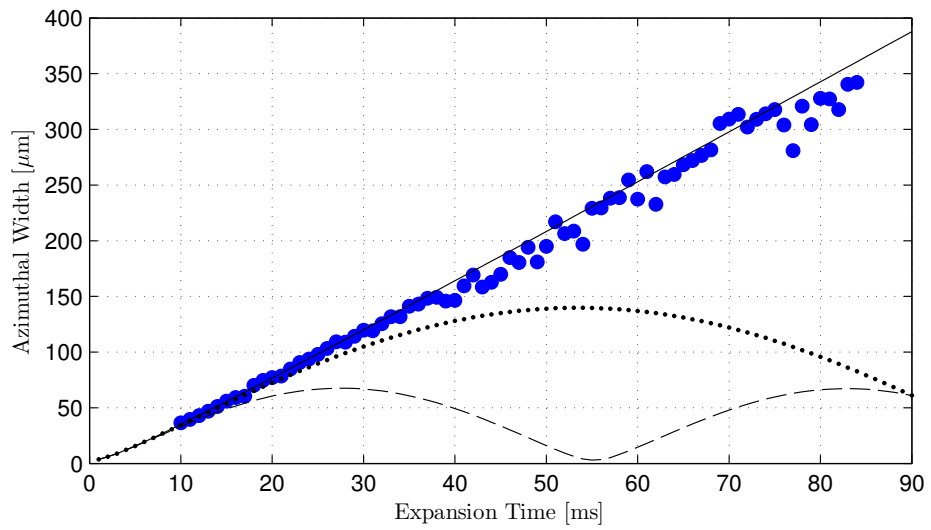


**Figure 5.17:** Azimuthal expansion of a BEC loaded into the toroidal trapping potential. The underlying solid line is a solution of Eq. (2.36) for the initial parameters  $\omega_r(0) = \omega_\phi(0) = 2\pi \times 150$  Hz and  $\omega_z(0) = 2\pi \times 168$  Hz and  $\omega_r(t) = 2\pi \times 250$  Hz,  $\omega_\phi(t) = 0$  Hz and  $\omega_z(t) = 2\pi \times 168$  Hz. The initial width of the atomic ensemble was set to  $R_{TF} = 3.02 \mu\text{m}$ . The dotted line shows Eq. (2.36) with a modified trapping frequency of  $\omega_\phi(t) = 2\pi \times 5$  Hz and the dashed line features  $\omega_\phi(t) = 10$  Hz

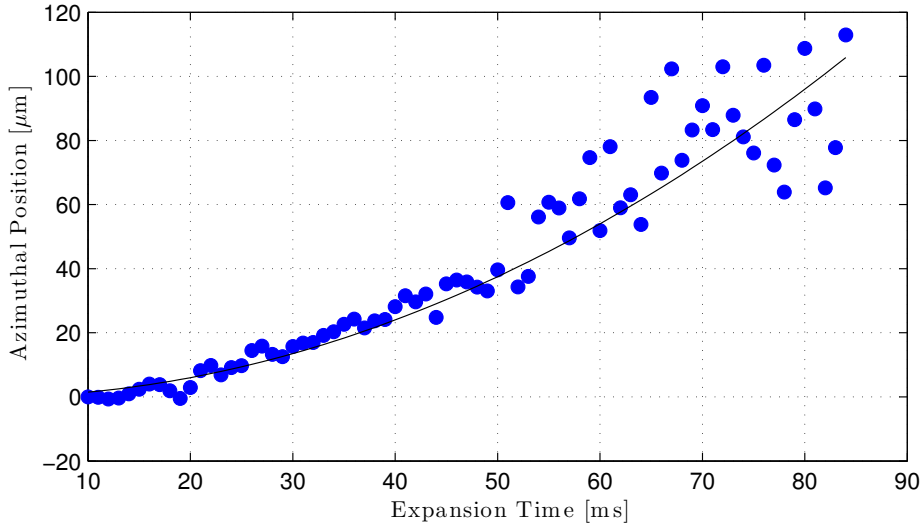


**Figure 5.18:** Position of the centre of mass of the atomic cloud as a function of the expansion time in the trapping geometry. The solid line depicts an accelerated motion with an acceleration of  $a = (15 \pm 1) \text{ mm/s}^2$ .

the trapping frequency in the radial direction is set to  $\omega_r(t) = 2\pi \times 250 \text{ Hz}$ , the frequency of the radial confinement. The trapping frequency in  $z$  direction was set to  $\omega_z(t) = 2\pi \times 168 \text{ Hz}$ , the trapping frequency of the lightsheet potential. In the azimuthal direction the frequency was set to  $\omega_\phi(t) = 0 \text{ Hz}$ . Fig. 5.17 depicts that the measured azimuthal expansion follows the theoretical predictions, showing that the trapping frequency in the azimuthal direction is indeed zero. After 80 ms the ensemble width is nearly  $500 \mu\text{m}$ , which means that the condensate nearly covers the full circumference of the ring. In addition, two values of  $\omega_\phi(t)$  were plotted in conjunction with  $\omega_\phi(t) = 0 \text{ Hz}$ .  $\omega_\phi(t) = 5 \text{ Hz}$  (dotted line) decline of ensemble width after 55 ms already showing that higher trapping frequencies in azimuthal direction produce oscillations of the ensemble width  $\sigma$ . This effect is even more pronounced for a trapping frequency of  $\omega_\phi(t) = 10 \text{ Hz}$  (dashed line). Comparing the experimental results with the numerical solutions shows that the flatness of the ring potential is given. The highest trapping frequency in azimuthal direction describing the measured expansion of the ensemble is  $\omega_\phi(t) \approx 1 \text{ Hz}$ .

If the coherence of the atomic ensemble is not destroyed during the expansion inside the potential, it should be possible to observe interference fringes on the opposite side of the loading point [149, 150]. Because of the relative velocity of the ensemble parts these density modulations are smaller than the resolution of the imaging system.

In addition to the expansion of the ensemble the drift of the centre of mass of the atomic distribution is shown in Fig. 5.18. The ensemble is loaded into the trap at the azimuthal position zero. During the free expansion the centre of mass moves clockwise along the ring potential. The drift is described with an

---

accelerated motion with an acceleration of  $a = (15 \pm 1) \text{ mm/s}^2$ . The cause for the drift are due to the misalignment of the lightsheet potential or residual light from the ring potential in the Poggendorff dark ring. To estimate the impact of each of these factors, the movement of the atoms in the lightsheet without the ring potential was observed. It shows that the movement of the centre of mass of a cloud inside the lightsheet potential is the same as the drift direction in the ring direction. Assuming a tilt of the lightsheet potential resulting in an accelerated motion of the atoms, the measured acceleration can be used to determine the tilt angle. For an acceleration of  $a = (15 \pm 1) \text{ mm/s}^2$  the calculated tilt is less than  $0.1^\circ$  which is the maximum precision achievable experimentally. After 50 ms, the ensemble shows a distinct increase of the variation of the centre of mass of the atomic ensemble.

Future interferometric measurements aim to split BECs into two distinct wave packets where one of the wave packet travels a full circumference in the ring structure while the other stays in place (see Sec. 5.6). After a full round-trip the matter waves should interfere and therefore long storage times of the atoms are important. The round-trip time of a travelling wave packet depends on its momentum but can be as short as 30 ms in the current experimental configuration (see Sec. 5.4). The sequence time of an interferometric measurement is therefore well below 50 ms and the measurements of the potentials shows that a well defined positioning of atomic clouds is possible.

---

### 5.3.6 Lifetime of trapped atomic ensembles in the toroidal trap

---

The lifetime of the atoms is a crucial parameter for all applications of the wave guide structure. Applications like atomic clocks or guided matter wave interferometers rely on small losses and large storage times of up to several seconds [16]. Disturbance in all optical traps often comes from spontaneous scattering. These losses also yield a decrease in coherence destroying the possibility to perform interferometric measurements [151].

Therefore, as discussed in Sec. 2.1, large detuning of the beams with respect to atomic transitions are favourable. In the experiments with the ring guiding structure detuning of trapping potentials are in the order of 3 nm in respect to the  $D_1$  or  $D_2$  transition of  $^{87}\text{Rb}$ . The chosen detuning is used to achieve sufficient trap depth with the laser power available. This yields the problem that spontaneous scattering is non-negligible. The lightsheet potential features a detuning of  $\Delta\lambda_{LS} = 2.5 \text{ nm}$  to the red with respect to the  $D_2$ -transition of  $^{87}\text{Rb}$ , which results in a scattering rate of  $\approx 2.4 \text{ s}^{-1}$  (see Sec. 5.1.2). The ring potential created by conical refraction was chosen to have a wavelength of  $\lambda = 792.5 \text{ nm}$ , which is blue detuned in respect to the  $D_1$ -transition of  $^{87}\text{Rb}$ . The advantage of the double ring structure is that atoms are trapped in the Poggendorff dark ring, which has no intensity in the focal plane and therefore spontaneous scattering is suppressed. Even if the alignment is off by a margin the intensity is bellow

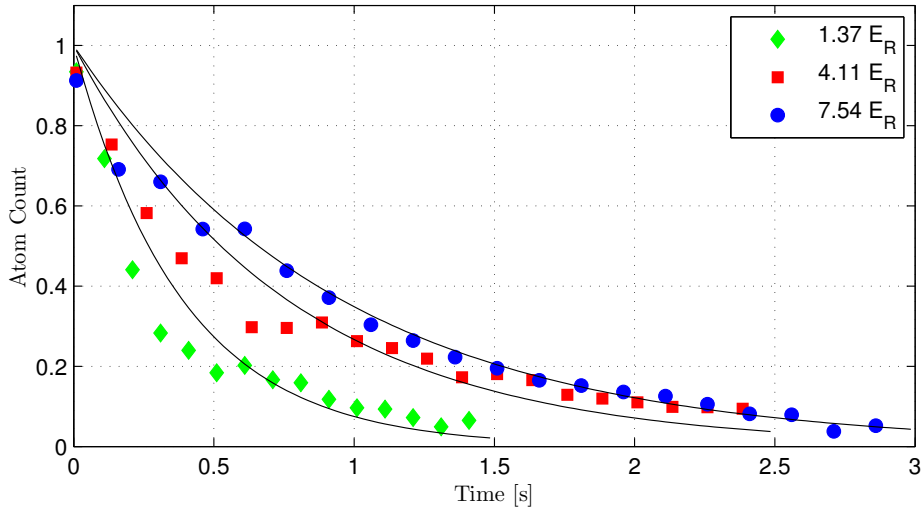
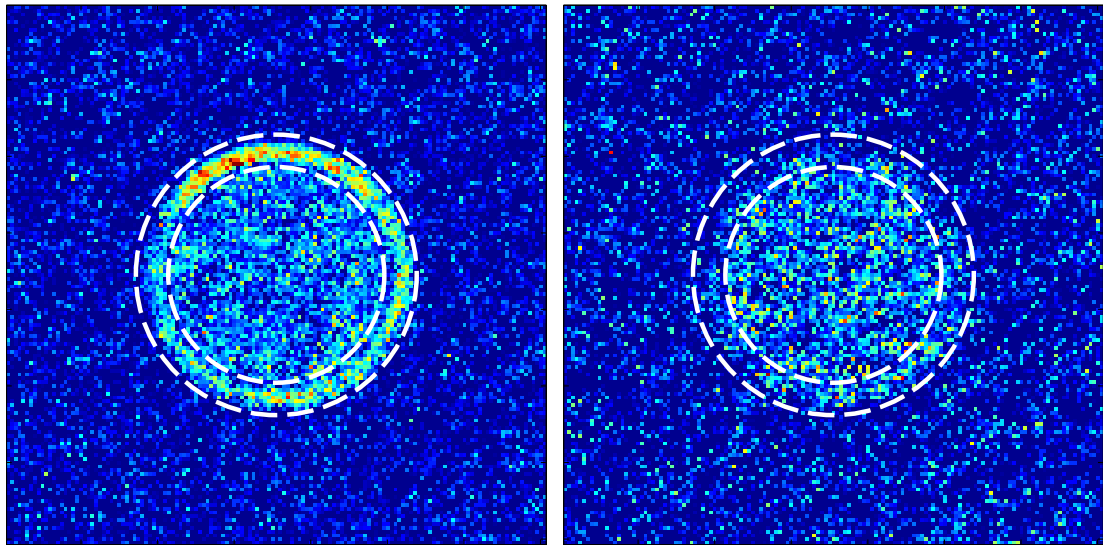


**Figure 5.19:** Lifetime of atoms in the ring potential as a function of potential depth of the ring potential. Each dataset has been scaled to the initial atom number of each measurement.

the scattering rate of the lightsheet potential.

To observe the lifetime of atoms in the ring guiding structure the condensed atoms were loaded into the Poggendorff dark ring and supported by the light-sheet against gravitational force. The lifetime is determined by observing the atom number in the trapping area after variable times. Fig. 5.19 shows the atom number after different times inside the ring potential. Three different trap depth were chosen:  $1.37 E_R$ ,  $4.11 E_R$ , and  $7.54 E_R$ . Depending on the trap depth a lifetime change of the atoms inside the ring structure can be observed. The deeper the trapping potential is, the longer the atoms stay inside the ring structure. In the focal plane the ratio of the outer ring potential depth to the inner ring potential depth is 4.7 (see Sec. 4.4.1) making it more likely to lose atoms in the direction of the smaller barrier, the inner ring potential. The solid lines in Fig. 5.19 are fitted exponential decays to determine the loss rate of the potentials. Even if the trap depth increases it cannot account for all of the losses. Fig. 5.20 shows experimental images obtained at a trap depth of  $U_{CR} = 4.11 E_R$ . The left image (Fig. 5.20a) shows the atom distribution in the ring after 685 ms. The ring potential is marked with two dashed rings showing the position of the inner and the outer guiding rings. From the initial atom count only 32% of the atoms are still in the ring structure. The lost atoms are either lost completely or occupy the inner part of the ring potential. This behaviour intensifies the longer the atoms reside in the trapping geometry. After 2.34 s only 10% of the atoms reside in the ring shaped trapping geometry whereas more atoms are now trapped in the centre of the ring structure (see Fig. 5.20b). In addition to the inner ring potential limiting the free expansion of the atoms in the inside, the light-sheet potential supports the atoms against gravity. Thus the structure



(a) 685ms

(b) 2335ms

**Figure 5.20:** Experimental images of the density distribution of atoms loaded into the toroidal trapping geometry. Fig. (a) shows the distribution after 685 ms where most of the atoms reside inside the ring wave guide. (b) After 2335 ms more atoms occupy the inner part of the trapping geometry.

can be seen as a disc like potential that features a homogeneous trapping region and offers the possibility to perform matter wave resonator experiments [65]. Sec. 5.3.4 already discussed the initial loss of atoms due to the loading procedure.

All of the measurement show that the decrease of atom number in the trapping region follows an exponential decay which is typical for atoms trapped in an optical dipole trap [152]. This is also true for combinations of multiple traps where each light field introduces additional heating mechanics. For dipole traps the most important parameter is the scattering rate of the trapping light which is dependent on the intensity and the detuning of the light field with respect to resonant transitions of  $^{87}\text{Rb}$ . Due to the rather small detuning, compared to other optical dipole trap potentials, the lifetime of the atoms inside the light-sheet potential are expected to be short. Previous measurement have shown that the lifetime does not exceed 1 ms for a detuning of  $\Delta\lambda_{LS} = 2.5 \text{ nm}$  (see Sec. 5.1.2). Depending on the potential depth the atom number in the toroidal trapping geometry varies. The lifetime of the atoms inside the ring shaped trapping region is higher for a deeper ring potential and is shown in detail in Fig. 5.21 for varying trap depth  $U_R$ . The values are compiled in Table 5.1. Deeper optical traps yield a stronger force that keeps atoms in place. In the case of the ring shaped potential the ring structure imposes a repulsive force that pushes

atoms into the Poggendorff dark ring. The time evolution of the system can be described by a set of first-order coupled differential equations:

$$\begin{aligned}\dot{N}_R &= -\alpha_R N_R - \alpha_{\text{spont}} N_R, \\ \dot{N}_D &= +\alpha_R N_R - \alpha_{\text{spont}} N_D.\end{aligned}\tag{5.7}$$

The variables  $N_R$  and  $N_D$  give the atomic number in the ring and the disc potential respectively. The parameter  $\alpha_R$  is the loss coefficient describing atoms moving from the ring potential into the disc potential.  $\alpha_{\text{spont}}$  stands for losses due to spontaneous effects, such as collisions with the background gas or spontaneous scattering off the light either from the lightsheet potential or the ring potential. The inverse of the loss coefficients gives the lifetime of the atoms in the trap. The analytical solution of Eq. (5.7) yields a coupled system describing the decay of the atom number in the ring and the decay of the atom number in the disc potential. To evaluate the appropriate values to describe the decay a combined fit on both, the atoms in the ring and the atoms in the disc potential, was performed. The values for each of the measurements are compiled in Table 5.1. Depending on the depth of the ring potential a change of  $\alpha_R$  occurs. The deeper the potential of the ring gets, the longer atoms remain in the trapping region of the ring. This can be seen by an increased lifetime of atoms inside the toroidal potential. The main losses from the ring potential can be attributed towards the drift of the atoms from the ring into the disc structure. As the ring depth increases, the loss coefficient  $\alpha_R$  decreases showing that the possibility for atoms to move over the potential barrier of the inner ring is inhibited. In addition to the initial losses during the loading process (see Sec. 5.3.4) using a very shallow ring potential is not favourable.

The loss of atoms from spontaneous scattering and other loss processes is combined in parameter  $\alpha_{\text{spont}}$ . The lifetime in the lightsheet potential has been measured to be in the order of 0.5–1 s for a wavelength of  $\lambda_{LS} = 782.5$  nm (see Sec. 5.1.2). For a ring depth of  $1.37 E_R$  the lifetime of atoms in the disc potential is the same as the measured lifetime of atoms in the lightsheet. The lifetime is dominated by the lifetime of atoms in the lightsheet potential. Increasing ring depth an increase in the lifetime is observed. Atoms can be trapped significantly longer in the trap with the a deep ring potential present. The repulsive potential of the ring increases the force that holds atoms on the inside. Since the ring potential is trapped in the Poggendorff dark ring the additional laser intensity should not contribute to an increased spontaneous scattering rate. This increases the lifetime of the atoms in the trapping potential [153]. Additionally the increased trap depth diminishes the rate of atoms flowing from the ring into the disc potential. In combination with lower losses during the loading process a deep ring potential is favourable to trap atoms for large periods.

For a ring depth of  $1.37 E_R$  a combined lifetime of  $(\alpha_R + \alpha_{\text{spont}})^{-1} = 0.36$  s is calculated. Higher trapping depth of the ring potential achieve a longer lifetime of up to 0.95 s. This result shows that the lifetime in the ring potential

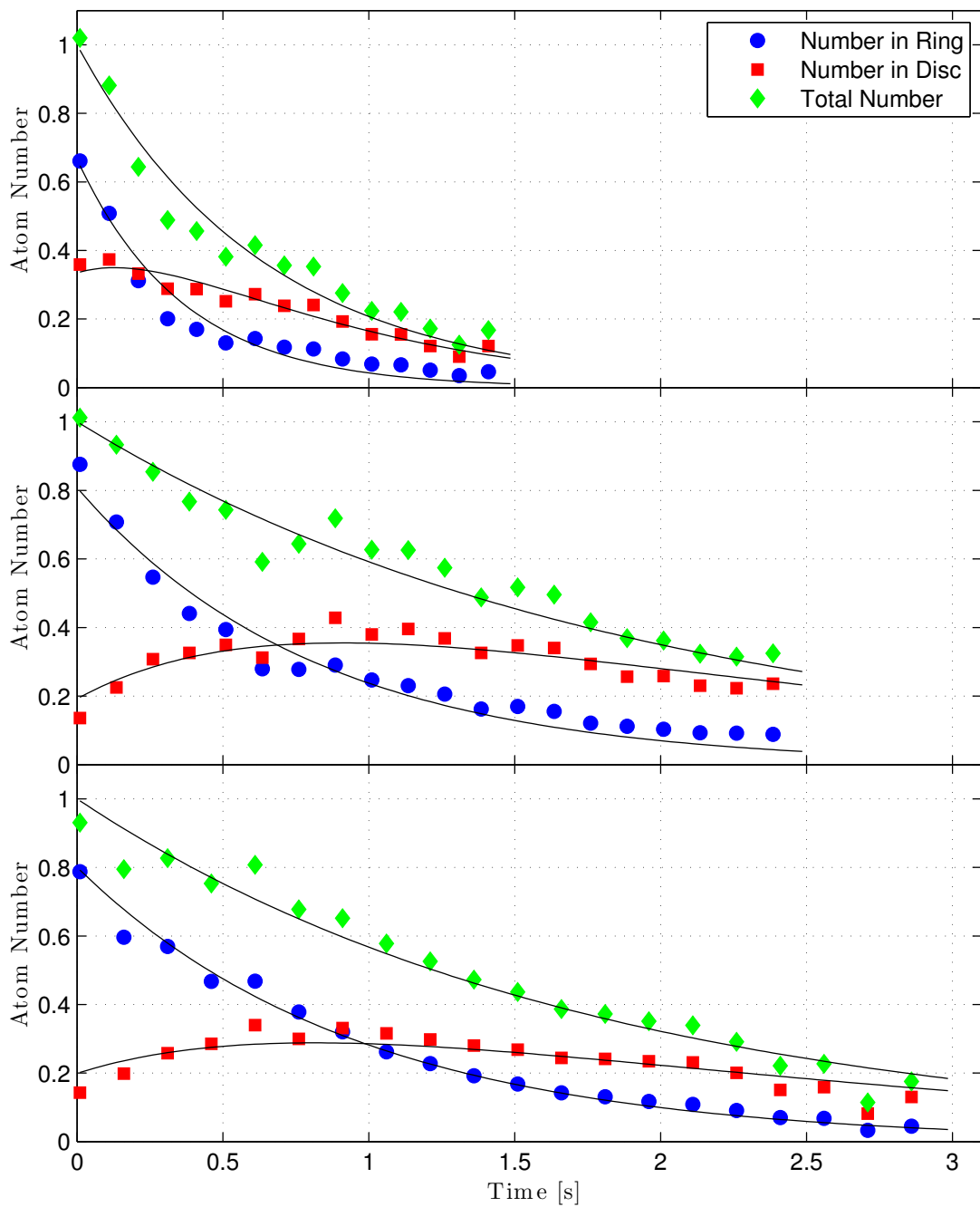


**Figure 5.21:** Atom number in different areas of the trapping geometry for different trapping depth of the ring potential. From top to bottom the trap depth increases; starting from  $U_R = 1.37 E_R$  going to  $U_R = 4.11 E_R$  and  $U_R = 7.54 E_R$ . Each

Potential Depth [ $E_R$ ]	$\alpha_R^{-1}$ [s]	$\alpha_{\text{spont}}^{-1}$ [s]	Combined Lifetime [s]
1.37	0.85	0.64	0.36
4.11	1.43	1.90	0.81
7.54	2.1	1.76	0.95

**Table 5.1:** Compilation of the lifetime of atoms inside the trapping geometry of the ring potential.  $\alpha_R^{-1}$  gives the lifetime of atoms in the ring potential lost to the disc potential.  $\alpha_{\text{spont}}^{-1}$  is the lifetime according to losses due to spontaneous scattering of light from either the light-sheet potential or the ring potential. The combined lifetime is given by  $(\alpha_R + \alpha_{\text{spont}})^{-1}$ .

is largely dominated by the losses due to the lower inner blue detuned wall in contrast to spontaneous scattering. The atoms occupying the disc potential show a much longer lifetime than atoms trapped in the toroidal wave guide for longer trapping times. The lifetime increases if the trap depth of the ring potential is increased. The spontaneous scattering rate of the lightsheet potential limits the lifetime, which is in the order of previously observed lifetimes in the lightsheet potential [148].

The lifetime of atoms in the ring guiding structure largely depends on the depth of the blue detuned double ring structure. Because the inner ring is less intense than the outer ring most atoms are lost into the inner region of the trapping geometry. The use of deep ring potentials is favourable in order to increase trapping times but the drawback is an increased localisation of atoms due to inequalities of the optical potentials (see Sec. 5.4).

## 5.4 Transport of BEC in ring shaped trapping potentials

Optical potentials and wave guides are widely used for a coherent matter wave transport or for atom storage. Especially ring potentials created with conical refraction offer a high grade of scalability [132]. The application of these potentials could also be useful for atomtronics [154]. In addition full interferometer procedures can be performed in ring shaped dipole potentials. The exact knowledge on the movement and adjustability of these potentials is needed in order to implement high precision experiments [155].

This section will discuss the application of a toroidal trapping geometry as a wave guide for accelerated atoms. The atoms velocity is adjustable in multiples on  $2\hbar k$  with the use of a one-dimensional optical lattice. Sec. 5.4.1 will discuss the experimental changes in order to accelerate atoms in the guiding potential. Sec. 5.4.2 shows the experimental work done with accelerated atom ensembles. Next Sec. 5.4.3 shows the symmetric splitting and guiding of wave packets in

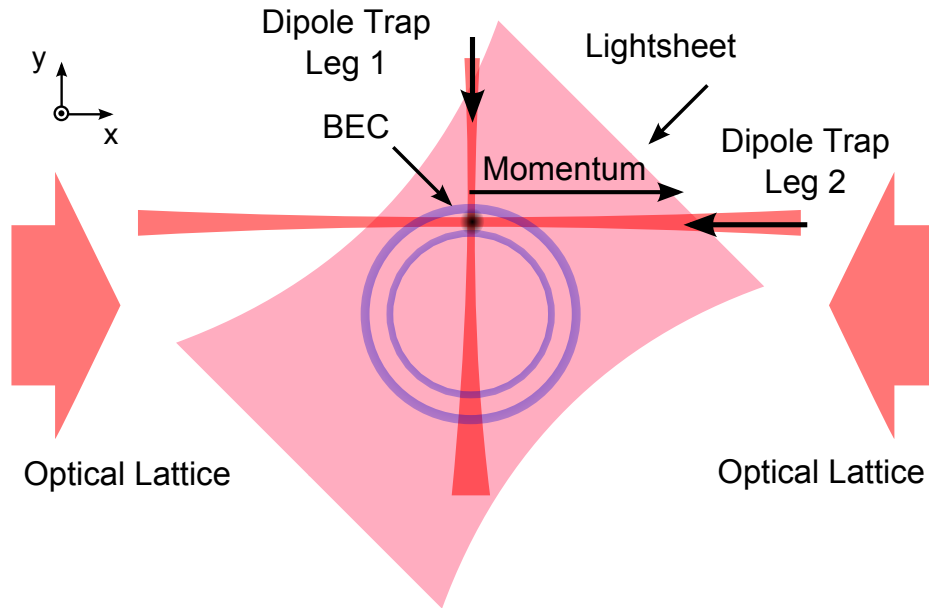


**Figure 5.22:** As an addition to Fig. 5.10 an optical lattice is aligned on top of dipole trap leg 2. This enables a tangential acceleration of the atoms.

the optical potential. This section ends with the discussion on large trapping times of up to 300 ms of accelerated atomic ensembles (see Sec. 5.4.4). The measurements are carried out at a position of  $Z \approx 1.3$ .

---

#### 5.4.1 Additions to the optical setup

---

In order to accelerate atoms in a toroidal wave guide, the experimental additions as depicted in Fig. 5.22 were implemented. The experimental configuration is an extension of the setup used to store atoms (see Sec. 5.3). An optical lattice was aligned on top of leg 2 of the optical dipole trap used to create the BEC. The toroidal potential is aligned with respect to the crossed optical dipole trap that allows a tangential acceleration of the atoms. Misalignment of the double ring guiding potential creates additional atom losses because atoms are accelerated directly into the repulsive potential barrier provided by the ring potential.

Experimentally the acceleration of the atoms is done after the loading of the BEC into the toroidal wave guide has finished. After the loading process is complete no additional waiting time is needed and the ensemble can be manipulated by the optical lattice. Typically the acceleration of the full condensate or the splitting of the condensate into 50/50 ratio is used. This yields either a complete BEC travelling inside the waveguide or half of the BEC travelling through the wave guide while the rest of the atoms stays in place at the point of loading.

---

## 5.4.2 Accelerated atoms in a toroidal trapping geometry

---

The experiments for matter wave guiding were all carried out in a similar manner. The BEC was loaded into the guiding toroidal structure and without an additional waiting time the atoms were accelerated to the desired momentum. The trap depth of the guiding structure was adjusted to create a sufficient confinement for the moving ensemble. All experiments were carried out using a standard Bragg lattice that provides acceleration in one direction only. Fig. 5.23 shows a compilation of all three different momenta used:  $2\hbar k$ ,  $4\hbar k$ , and  $6\hbar k$ . With standard Bragg diffraction momentum transfer is possible in two directions, depending on the choice of  $\Delta\omega$ . By using different values of  $\Delta\omega$  transport in both directions, clockwise and counter-clockwise, and with different momenta was investigated. The solid lines depict the theoretical position of the atomic ensemble after varying times for the appropriate momentum after a Bragg pulse.

---

### Momentum transfer to $|2\hbar k\rangle$

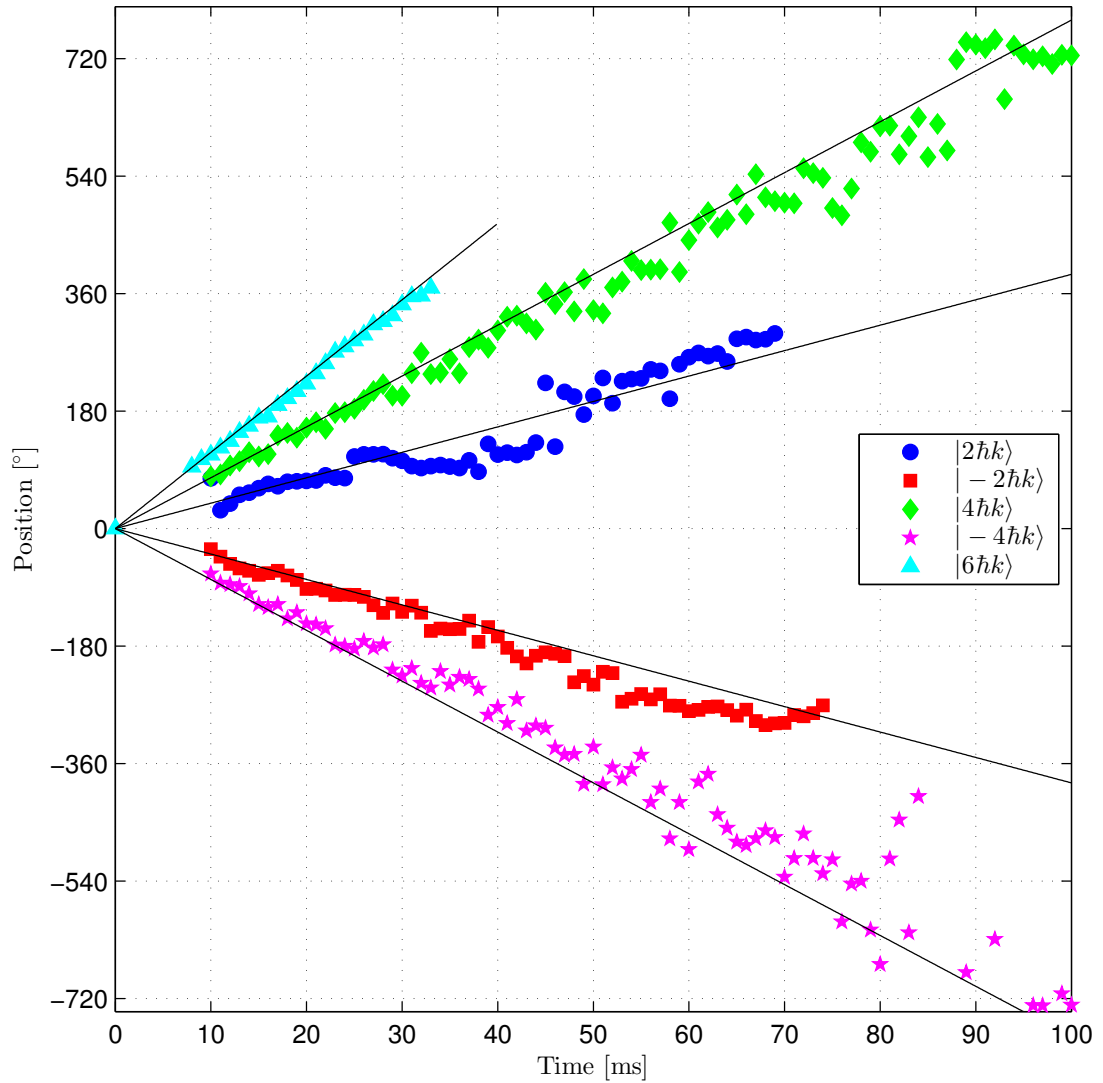
---

The position of the cloud in the toroidal wave guide has been determined with absorption imaging and is shown in Fig. 5.24(a). The acceleration direction was chosen to be clockwise but the measurements were also performed for counter-clockwise movement of the atomic ensemble (see Fig. 5.24(b)). The detuning between the two lattice beams was set to  $\Delta\omega = 15.08$  kHz and lattice pulse duration and amplitude were adjusted to accelerate all atoms.

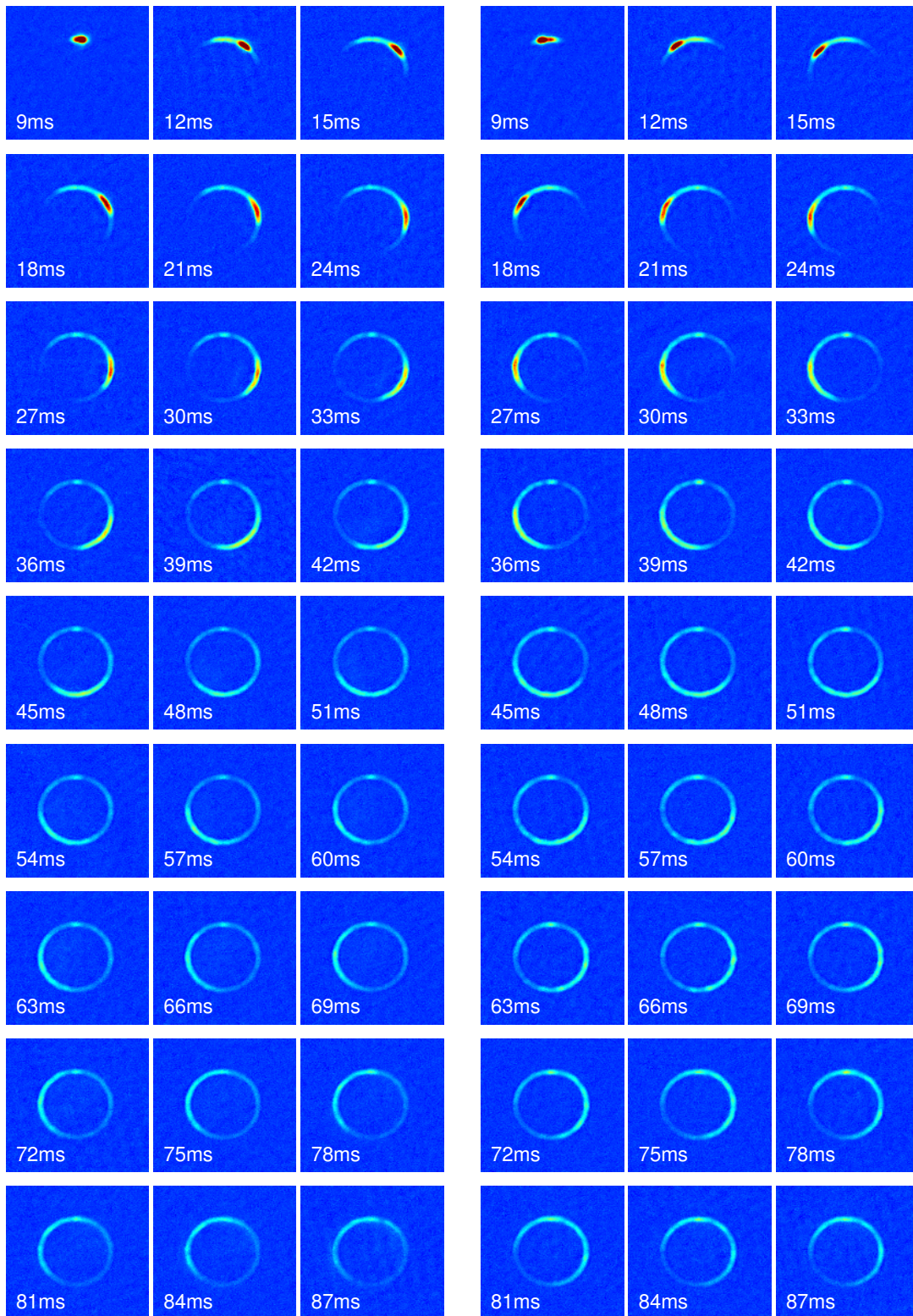
The acceleration of the wave packet was performed with a potential height of the outer ring of  $20.8E_R$ . The inner ring has a reduced height of a factor of 3.8 (see Sec. 5.3.4). The kinetic energy of a wave packet travelling with a momentum of  $2\hbar k$  is  $4E_R$ , therefore the potential is well suited to guide the atoms along its ring shape.

Fig. 5.24a depicts the time evolution of the atomic ensemble inside the trapping geometry after the lattice pulse. In contrast to the beforehand adjusted lattice pulse, without guiding potential, part of the atoms stay in place and are not accelerated. They are strongly localised at the initial loading point of the potential and stay in place without expanding. The accelerated fraction of the atoms travels along the guiding ring potential with a momentum of  $2\hbar k$ . The calculated round trip time of the atom cloud is  $t_{2\hbar k} = 93.0$  ms. Fig. 5.24 shows the time evolution until a free evolution time of 87 ms. Due to random shot-to-shot density variations in the ensemble for higher times the determination of the centre of mass is no longer possible. The movement up to this time shows a very good agreement of the experimental data with the underlying calculated position of the centre of mass (see Fig. 5.23).

In addition to the large centre of mass perturbation, another effect is increas-



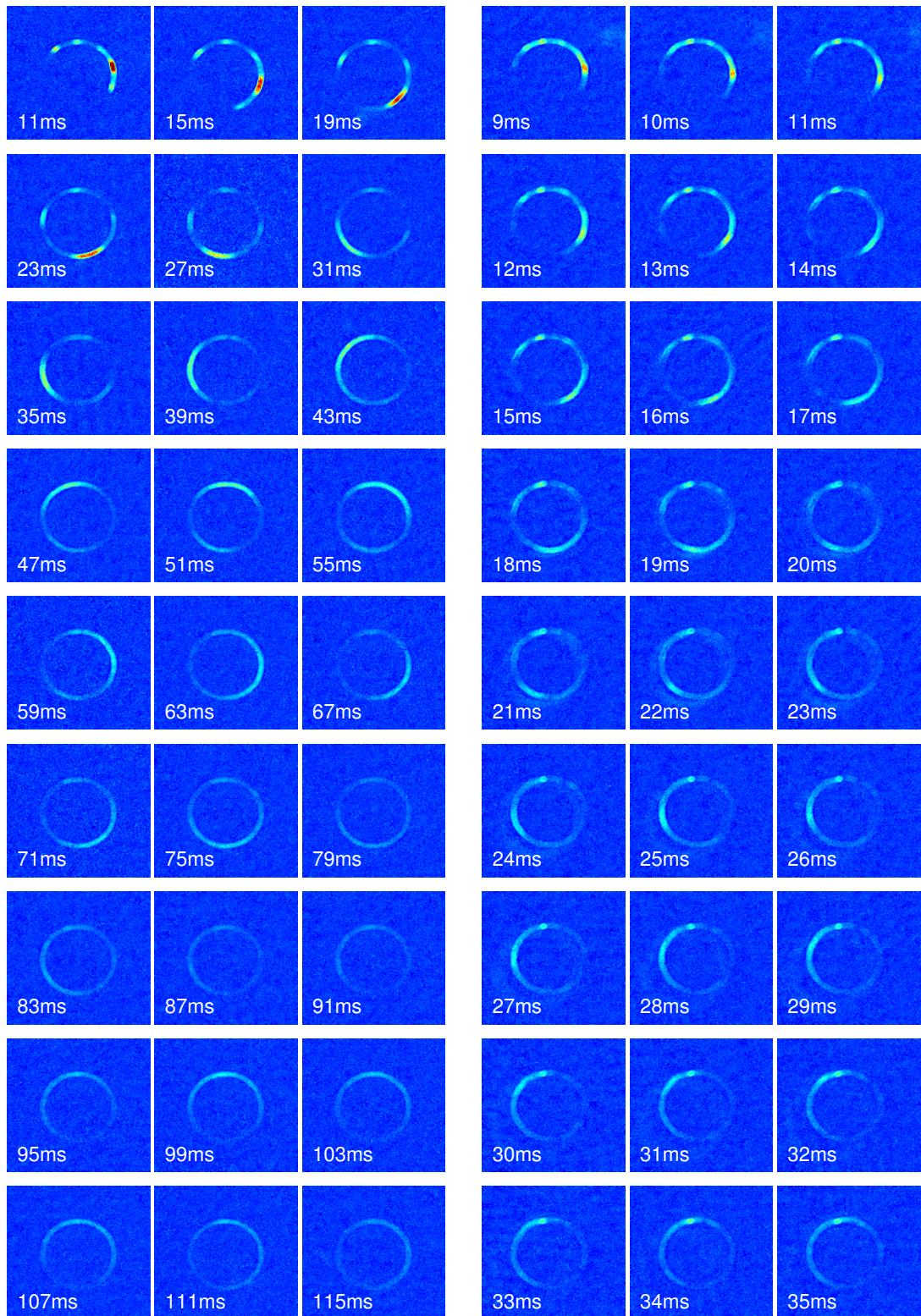
**Figure 5.23:** Position of atoms in the toroidal guiding potential after an acceleration pulse of the standard Bragg optical lattice. The lattice pulse has been adjusted to accelerate as many atoms as possible and by choosing an appropriate frequency difference  $\Delta\omega$  between the two lattice beams the momentum transfer has been selected. The atoms have been successfully transferred to the momentum states  $|2\hbar k\rangle$ ,  $|-2\hbar k\rangle$ ,  $|4\hbar k\rangle$ ,  $|-4\hbar k\rangle$ , and  $|6\hbar k\rangle$ . The solid lines show the theoretical position of atomic ensembles travelling with the equivalent momentum for each measurement series.



(a)  $|2\hbar k\rangle$

(b)  $|-2\hbar k\rangle$

**Figure 5.24:** Atoms with  $|2\hbar k\rangle$  and  $|-2\hbar k\rangle$  inside a toroidal wave guide.



(a)  $|4\hbar k\rangle$

(b)  $|6\hbar k\rangle$

**Figure 5.25:** Atoms with  $|4\hbar k\rangle$  and  $|6\hbar k\rangle$  inside a toroidal wave guide.

ing the difficulty to determine the centre of mass for large times. Due to the expansion of the cloud and the limited amount of atoms, the density decreases. The reduced density yields a reduction of the signal to noise ratio introducing additional uncertainties. For interferometric measurement, a change to higher order Bragg diffraction seems to be a good choice in order to reduce transport time and limit the uncertainties in the positioning of the cloud after transport.

---

#### Momentum transfer to $|4\hbar k\rangle$

---

The movement of atoms with a momentum of  $4\hbar k$  is shown in Fig. 5.25a between 11 ms and 115 ms after the lattice pulse. The lattice has been adjusted to a relative frequency of  $\Delta\omega = 30.17$  kHz and the lattice amplitude was chosen in order to accelerate a maximum fraction of the atoms. The depicted absorption images show a clockwise rotation of the atoms inside the toroidal guiding potential. Fig. 5.23 shows that the transport is also possible in counter-clockwise direction. The lattice depth has been chosen as before in order to be able to trap atoms with a momentum of  $4\hbar k$  or a kinetic energy  $16 E_R$ .

The atomic ensemble is loaded into the guiding structure and accelerated immediately. Over 90% of the atoms are accelerated to the desired state of  $|4\hbar k\rangle$  while the remaining atoms occupy the states  $|\pm 2\hbar k\rangle$  and  $|0\hbar k\rangle$ . As already observed before the remaining atoms stay at the loading point and do not show expansion. In addition atoms in state  $|\pm 2\hbar k\rangle$  move according to their momentum around the guiding structure. The atoms accelerated into the desired state  $|4\hbar k\rangle$  travel the full circumference of the guiding potential in 47 ms, which is 2 ms longer than anticipated but close to twice as fast as atoms accelerated to a momentum of  $2\hbar k$ . After 103 ms a second revolution of the atoms in the toroidal potential is observed, which is consistent with the first round trip time. The density of the atomic cloud allows the observation of slightly longer times but due to a loss of contrast no additional revolutions can be observed.

---

#### Momentum transfer to $|6\hbar k\rangle$

---

Fig. 5.25(b) shows the time evolution of a wave packet inside the toroidal wave guide travelling with a momentum of  $6\hbar k$ . The atoms are accelerated clockwise and a full circumference is shown. Due to the increased velocity additions on the trapping potentials had to be made. The kinetic energy of a  $^{87}\text{Rb}$  atom travelling with a momentum of  $6\hbar k$  is nine times the energy of a wave packet with  $2\hbar k$ :  $36 E_R$ . The repulsive ring potential depth was matched to hold atoms inside the outer ring. In order to achieve the needed potential depth the detuning of the Ti:Sa laser was changed to  $\lambda = 793.5$  nm. With an optical power of 97.0 mW the repulsive potential of the outer ring is  $45.4 E_R$  which is sufficient to guide atoms with a momentum of  $6\hbar k$ . The inner ring potential is reduced by a factor 3.8 as determined in Sec. 5.3.4. Due to imperfections the potential

height will vary along the full circumference of the potential which can induce unwanted losses. In addition the lattice depth had to be increased in order to achieve efficient excitation of the desired state  $|6\hbar k\rangle$ . This was achieved by setting the detuning of the lattice beam to 500 MHz in respect to the  $D_2$   $F = 2 \rightarrow F' = 2$  transition of  $^{87}\text{Rb}$ . The lattice depth was adjusted to result in a  $\pi$  pulse and the detuning between the two lattice beams was chosen to be  $\Delta\omega = 45.23$  kHz. About 75% of the atoms can be transferred to  $|6\hbar k\rangle$ .

The guiding of atoms with a momentum of  $6\hbar k$  gives a calculated round trip time of  $t_{6\hbar k} = 31.0$  ms. Fig. 5.25(b) shows the time evolution between 9 ms and 35 ms. The position of the centre of mass in the ring potential is also shown in Fig. 5.23. The initial loading position is corresponding to  $0^\circ$ . After 9 ms the atoms already traversed nearly a third of the full circumference. Additionally a cloud of atoms can be observed that leaves the guiding geometry after the initial acceleration and is now propagating straight right at 9 ms and 10 ms in to the right (see top of Fig. 5.25(b)). The position of the cloud indicates the acceleration direction and shows that a tangential acceleration was achieved. The resting atoms at the top of the ring geometry show that the acceleration up to  $6\hbar k$  lacks efficiency in respect to an acceleration to  $2\hbar k$ . In addition multiple wave packets are observable that move with lower momentum as  $6\hbar k$ . Clearly visible are wave packets of the momentum state  $|2\hbar k\rangle$  and  $|-2\hbar k\rangle$ . They originate from the off-resonant excitation of the undesired momentum states and are also travelling along the ring. Earlier experiments have shown that resting atoms could expand without azimuthal confinement cause of the very low trapping frequency in the azimuthal direction. This is no longer observed in a trapping potential sufficiently deep to guide atoms with  $6\hbar k$  momentum. Like earlier experiments have shown imperfections in the potential yield a localisation that prohibits expansion [61]. Non-desired momentum states like  $|2\hbar k\rangle$  or  $|-2\hbar k\rangle$  move along the guiding structure, therefore the potential depth of corrugations has to be less than  $4E_R$ .

The moving atomic ensemble with a momentum of  $6\hbar k$  traverses the full circumference of the ring after 33 ms, which is 3 ms more than anticipated before. This could originate from radial oscillations that inhibit azimuthal propagation but has not been investigated in detail. During the movement through the trapping potential an increased loss of atoms can be observed. Between 20 ms and 28 ms a second much less pronounced ring shaped cloud can be observed. Its shape follows the shape of the toroidal guiding potential. This effect is more pronounced in the lower left part of the ring potential on the absorption images. This indicates that the potential depth is modulated along the ring. From previous measurement it is known that the left and the right part of the potential feature an unequal ratio between the inner and the outer ring potential. The increased loss rate yields a shortened observability of the movement. After 35 ms the atomic cloud travelling with  $6\hbar k$  is no longer observable.

For future interferometric measurements the free expansion of a BEC is of interest. As discussed in Sec. 5.3 free expansion of a resting BEC has been observed. Since the phase  $\alpha$  of the BEC evolves according to its spatial evolution a free expansion of both interferometer legs is favoured. Differences of the phase gradient will create additional spatial modulations and degrade the interferometer measurements.

A possible interferometer sequence would create a resting and a moving cloud in the guiding structure and after a full round trip of the moving ensemble the interferometer would be closed once the clouds overlap spatially. To gain insight on the evolution of the phase profile the azimuthal width of the BEC was observed during its movement in the ring shaped wave guide. Fig. 5.24 shows the time evolution of two BECs with  $2\hbar k$  and  $-2\hbar k$  momentum travelling clockwise through the guiding structure. The accelerated cloud expands in azimuthal direction during its movement along the ring. A fitted Gaussian distribution yields the width of the ensemble and its time evolution is shown in Fig. 5.26. Underlying to the measurements of the width of atoms in the state  $|2\hbar k\rangle$  and  $|4\hbar k\rangle$  is the numerical solution of Eq. (2.36) with the starting parameters of the trap as follows:  $\omega_r(0) = \omega_\phi(0) = 2\pi \times 100\text{Hz}$  and  $\omega_z = 2\pi \times 150\text{Hz}$  and  $\omega_r(t) = 2\pi \times 300\text{Hz}$ ,  $\omega_\phi(t) = 0\text{Hz}$  and  $\omega_z = 2\pi \times 168\text{Hz}$ . The initial expansion of the ensemble was set to the Thomas-Fermi radius of the cloud  $R_{\text{TF}} = 3.02\ \mu\text{m}$ .

The expansion of atoms travelling with a momentum of  $2\hbar k$  (see Fig. 5.26) is as expected and follows the numerical solution for the first 50 ms. The time period in which mean-field interaction is dominant has already past and after 10 ms ballistic expansion is dominant. At 10 ms the measured width agrees perfectly with the numerical solution. Since mean-field energy is already depleted and ballistic expansion should be dominant a linear scaling of the width is expected for longer evolution times. This behaviour can be observed in Fig. 5.26 for expansion times of up to 40 ms. The azimuthal width of the atomic distribution is  $200\ \mu\text{m}$  after 40 ms which corresponds to approximately a fifth of the full circumference of the ring potential. After this time the width of the ensemble is not following the expected behaviour any more. Instead the expansion of the ensemble nearly stops and the width stays in the regime of  $200\ \mu\text{m}$ .

The expansion of atoms with a momentum of  $4\hbar k$  was investigated (see Fig. 5.26). The behaviour of the azimuthal width follows the expected behaviour and is identical to the expansion of the wave packet with a momentum of  $2\hbar k$  showing that the expansion is not dependent on the momentum. For times between 38 ms and 48 ms no reliable width could be determined. This originates from the resting atom cloud at the initial loading point. It broadens the measured width and yields an incalculable spread. After the cloud has passed the overlap region the width is determinable again. This width shows a distinct

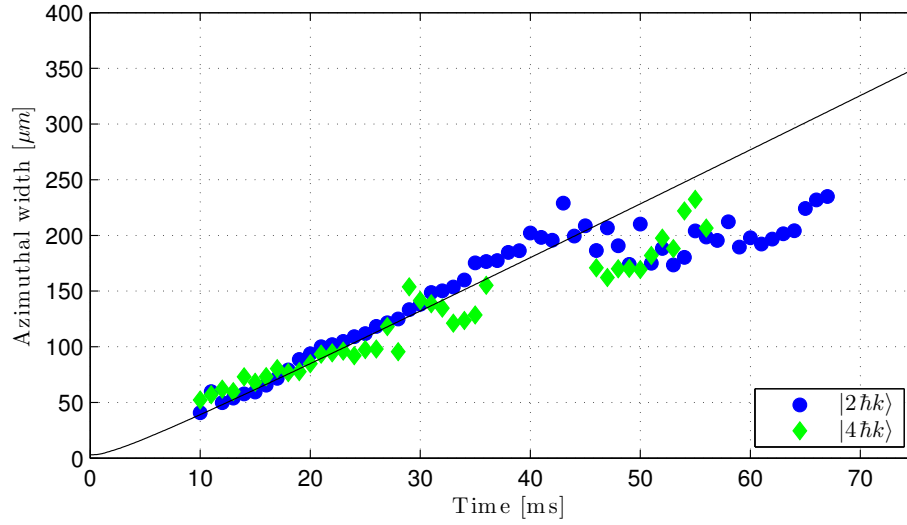


**Figure 5.26:** Azimuthal expansion of two BECs loaded and accelerated clockwise in the toroidal trapping potential. The underlying solid line is a solution of Eq. (2.36) for the initial parameters  $\omega_r(0) = \omega_\phi(0) = 2\pi \times 100$  Hz and  $\omega_z = 2\pi \times 150$  Hz and  $\omega_r(t) = 2\pi \times 300$  Hz,  $\omega_\phi(t) = 0$  Hz and  $\omega_z = 2\pi \times 168$  Hz. The initial width of the atomic ensemble was set to  $R_{TF} = 3.02 \mu\text{m}$ . For clarity reasons the width of counter-clockwise are not plotted but act in the same manner.

difference to the numerical solution: In contrast to atoms with  $2\hbar k$  momentum, ballistic expansion again is the dominant process. The azimuthal width of the condensate shows a distinct difference to the numerical solution but the overall ballistic behaviour is still present. This indicates that the measured trapping frequencies are not as high as assumed and the spreading of the ensemble happens slower. The measured behaviour indicates that the azimuthal width of the ensemble evolves ballistically for times between 38 ms and 48 ms, the time needed for a complete round-trip of the atoms in the toroidal potential. This would yield an identical behaviour to the measured azimuthal width of a resting BEC (see Sec. 5.3).

Because of the unpredictable behaviour of the spreading of atoms with  $2\hbar k$  momentum atoms with a momentum of  $4\hbar k$  should be used for interferometric measurements. Due to the expected behaviour they would feature a nearly identical phase gradient  $\alpha$  as resting atoms, which would be ideal for interferometric measurements. The demonstration of interferometric measurements will be discussed in Sec. 5.6.

---

---

## Cleaning of the ring with additional dipole trap kick pulses

---

In order to remove non-accelerated atoms it is possible to apply a short distortion to the trapping potential to increase losses on one side of the ring on purpose. This is done by switching leg 2 of the crossed optical dipole trap on for a limited amount of time after the lattice pulse has been applied. The intensity of leg 2 is increased for a maximum duration of 3 ms which induces enough disturbance and additional heating to fully remove all atoms remaining at the initial loading point of the trapping potential. Since all atoms in the overlap area of the ring guiding structure and the crossed optical dipole trap are affected by this process a waiting time has to be applied to make sure the desired atoms are on the other side of the ring potential. The time needed varies with the momentum state of the atoms and is typically half the time of one circulation. This procedure is useful for interferometric measurements as described in Sec. 5.6 to remove non-desired atoms in the interferometer area, if the interferometer sequence features an appropriate configuration.

---

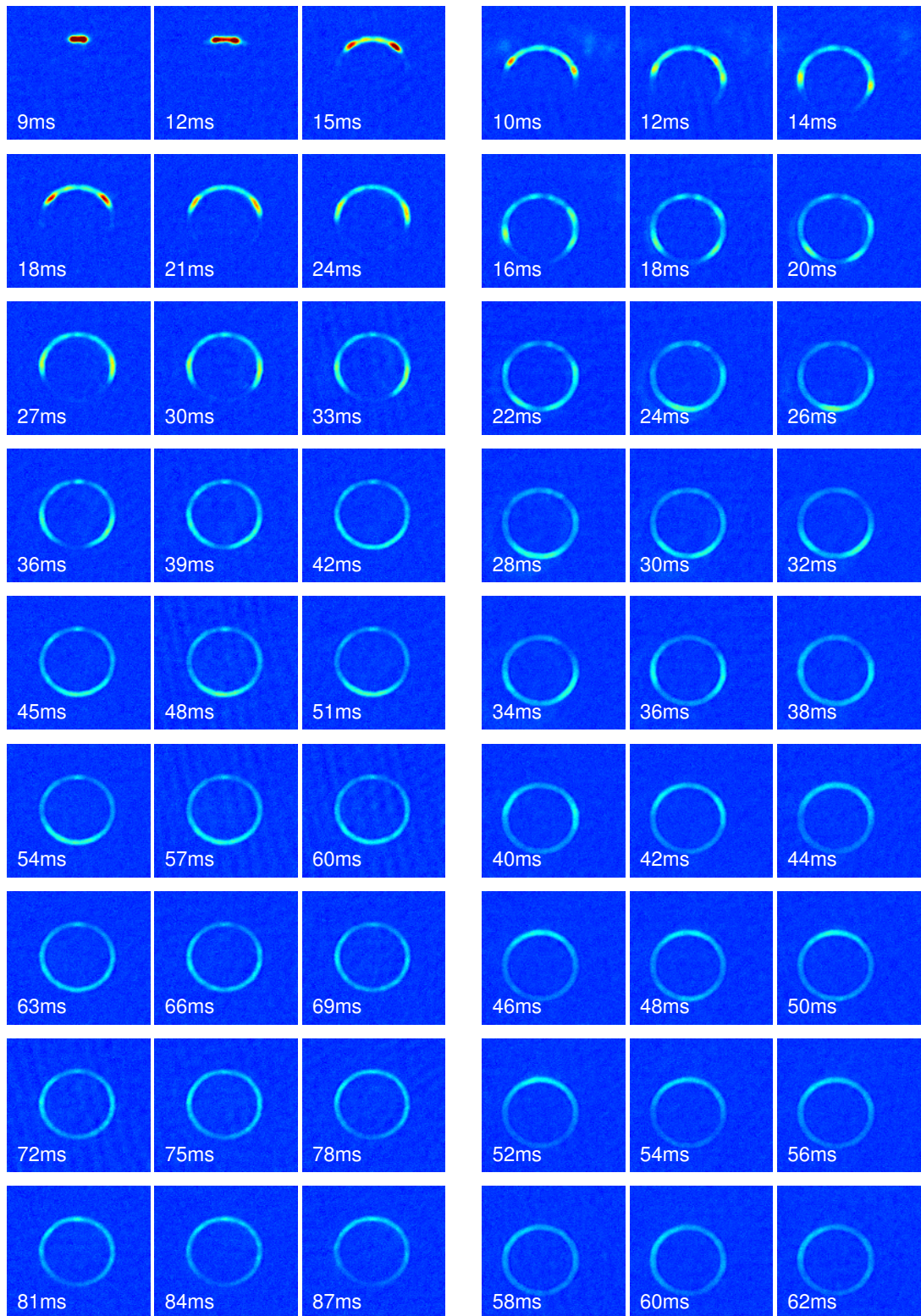
### 5.4.3 Symmetric splitting of wave packets inside the toroidal potential

---

In addition to the standard Bragg acceleration, two three-frequency Bragg experiments have been performed to accelerate atoms in the ring potential (see Sec. 3.6.1). The experimental configuration used for the acceleration in one direction stayed in place and an additional frequency shift is imprinted on one of the lattice beams. The experimental sequence was the same as described earlier and the lattice pulse is applied directly after loading of the toroidal ring trap has been finished.

The lattice depth and pulse duration have been adjusted to perform as a beam-splitter for atomic ensembles to the momentum states  $|\pm 2\hbar k\rangle$ . The detuning was chosen to be  $\Delta\omega = 15.08$  kHz to accelerate the atoms to a momentum of  $\pm 2\hbar k$ . The ring potential height was chosen to be  $20.8 E_R$  of the outer ring.

Fig. 5.27(a) shows the time evolution of the atoms in the toroidal trap after a lattice pulse was applied. The time is varied from 9 ms and 87 ms in steps of 3 ms. The efficient splitting of three-frequency Bragg diffraction is visible after 15 ms. After 30 ms each of the two atomic ensembles has already covered more than a quarter of the full circumference of the toroidal wave guide. As before the fraction of atoms staying in place of the initial loading area does not expand. The travelling atoms move with a momentum of  $\pm 2\hbar k$  and meet at the opposite side of the potential after 48 ms. Since the wave packets azimuthal size already covers a quarter of the ring a definitive meeting point is not defined. The clouds run through each other and after a total of 72 ms after the initial lattice pulse the ensembles have separated in the ring potential and move towards the loading area. The clouds do not show a decreased velocity after the passing at the bottom part of the ring. After 87 ms both clouds occupy the initial loading area



**(a)**  $|\pm 2\hbar k\rangle$

**(b)**  $|\pm 4\hbar k\rangle$

**Figure 5.27:** Atoms of  $|\pm 2\hbar k\rangle$  and  $|\pm 4\hbar k\rangle$  inside a toroidal wave guide.

---

in the ring. They have spread to cover half of the rings circumference and no distinction between the two clouds can be made any more. Due to the reduced density and losses longer observation times could not distinguish between two clouds.

In addition to the symmetric splitting of atoms to  $|\pm 2\hbar k\rangle$  symmetric splitting to the momentum states  $|\pm 4\hbar k\rangle$  has been demonstrated experimentally. The same experimental parameters as before were used in order to observe the splitting and guiding process. The relative detuning of the lattice beams was adjusted to  $\Delta\omega = 30.17$  kHz. Fig. 5.27(b) shows the experimentally obtained images. The splitting process shows the same diminished efficiency as already discussed for the single Bragg splitting. The additional components travelling with a momentum of  $\pm 2\hbar k$  are clearly visible. The efficiency of the splitting process varies greatly, which explains why some images show nearly no non-desired excitation, where other show significantly more atoms in the wrong momentum state. Atoms travelling with a momentum of  $4\hbar k$ , as desired, meet the first time after the splitting process after 24 ms which is slight above the expected duration of 23 ms. The atoms pass each other without measurable loss of velocity and meet again at the initial loading point after 48 ms. At the same time atoms with the non-desired momentum of  $\pm 2\hbar k$  meet at the opposite side of the toroidal potential.

---

#### 5.4.4 Behaviour for long storage times

---

The experiments with accelerated atom ensembles in the toroidal guiding structure have shown that after 100 ms no distinct position of an atomic ensemble is determinable. Even though the atoms are still in the ring they occupy nearly the complete circumference of the ring and the ring features an equal density distribution along its guiding path. Initially sharp density peaks could be monitored in order to obtain the position and the velocity of atoms in the ring. This is not possible once the atoms cover the complete circumference of the guiding potential.

To gain insight in the atom motion after large travel times the lightsheet and the double ring potentials are switched off to release the atoms from the waveguide. Fig. 5.28 shows a compilation of absorption images for times of 156 ms and 306 ms free evolution after a  $4\hbar k$  momentum transfer with a standard Bragg lattice. Fig. 5.28(a) (about 3.5 revolutions) and Fig. 5.28(c) (about 7 revolutions) show the density distribution in the ring after their given propagation times, whereas Fig. 5.28(b) and Fig. 5.28(d) show the same experimental sequence with an additional 6 ms TOF during which the lightsheet and the ring potential are switched off before detection.

After 156 ms (see Fig. 5.28(a)) the atom distribution has filled the full circumference of the ring and no movement of the atoms is visible. The density distribution shows a maximum at the top of the potential which might originate

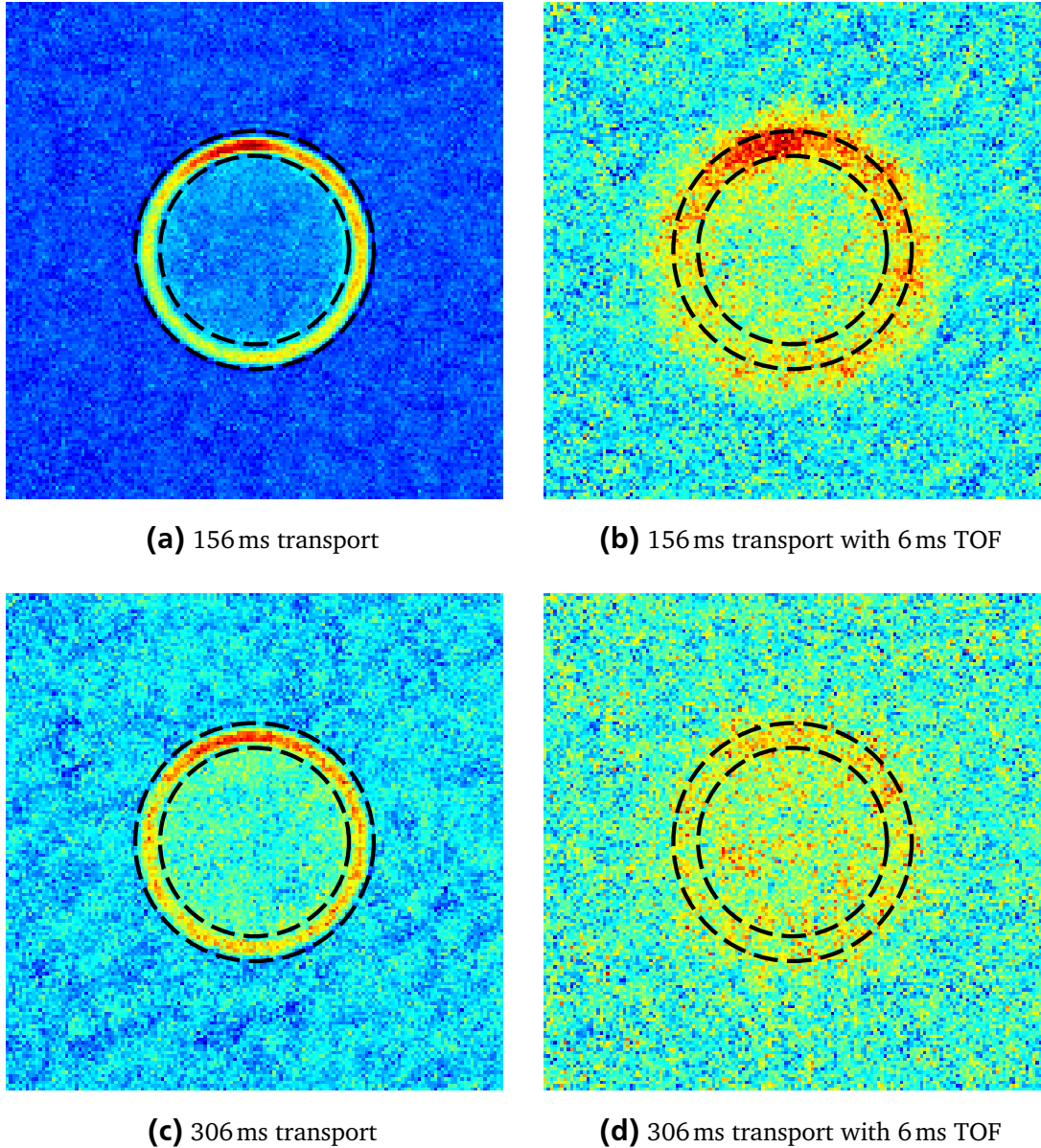


**Figure 5.28:** Compilation of atom distribution in the ring potential after a  $4\hbar k$  momentum transfer. Each image is an average over a total of 20 absorption images to increase the visibility of the atom distribution. Parts (a) and (c) show the density distribution after the given transport times. Parts (b) and (d) feature an additional 6 ms TOF to observe the velocity distribution of the atoms in the ensemble.

---

from a gradient in the trapping potential that pushes atoms in this direction. Fig. 5.28(b) features an additional TOF of 6 ms that yields a covered distance of  $141\ \mu\text{m}$  for  $^{87}\text{Rb}$  atoms with a momentum of  $4\hbar k$ . If atoms would travel with said momentum, after the release from the ring potential each of the atoms should move tangentially to its last point of occupation in the ring potential. The additional  $141\ \mu\text{m}$  would result in a new ring structure with an increased radius of  $222\ \mu\text{m}$ . The dashed guiding lines mark the inner and outer bounds of the trapping region of the atoms before and after the release and are originated at the same position in each image. This shows that the centre of the ring shaped density distribution is staying the same after the release from the potential. The increased radial width is explainable by isotropic expansion to the centre of the ring and away from the centre of ring structure. This implies that the motion of the atoms has stopped almost completely. The increase of ring radius is  $12\ \mu\text{m}$  which would equate to a velocity of  $10.08\ \text{mm/s}$ . Less than 50% of the anticipated velocity of  $23.43\ \text{mm/s}$ . The same behaviour can be observed for the increased transport time of 306 ms. The reason for the inhibited motion of the atoms for long times is unknown and should be investigated again in smaller toroidal trapping geometries, where the lifetime of the condensate in the trapping potential is much larger compared to the time it takes to expand over the full circumference. The decrease of contrast due to losses and the limited atom number in the beginning increases the difficulty in observing the atom distribution for long transport times. A smaller ring structure as presented in Sec. 4.5.2 should be viable to observe the effect. Due to its scalability it is also a promising system to observe persistent current dynamics, a system where the full circumference is covered by a moving coherent matter wave [156].

---

## 5.5 Dynamic loading and release of atoms in ring shaped guiding structure

---

Wave guides offer the possibility to guide and store atoms for long times. Long storage times offer the possibility to introduce complex systems for matter wave transport [157]. The advantages of optical wave guides are the high customizability, the easy combinability, and the easy and space-saving structure. Guided matter waves can be used for interferometer experiments and a ring shaped guiding structure can serve as a delay device. Additional functionality can extend these towards velocity selectivity [158].

This section demonstrates the external loading of a ring shaped guiding structure. A linear wave guide is aligned tangentially on-top of the ring potential. An accelerated cloud of atoms is sent towards the ring and loaded into the ring potential (see Sec. 5.5.1). Additionally the release of moving atoms from the potential is investigated (see Sec. 5.5.2).

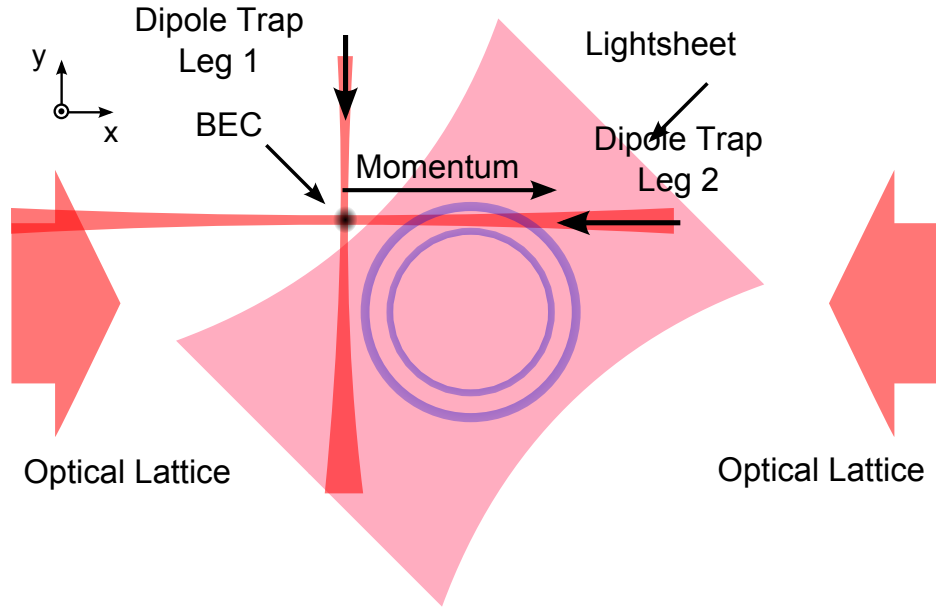


**Figure 5.29:** Experimental setup to dynamically load atoms into the toroidal ring potential. In contrast to Fig. 5.22 the ring guiding potential is aligned next to the overlap section of the crossed optical dipole trap. This allows the acceleration outside of the guiding structure to demonstrate a dynamic loading process of the toroidal wave guide.

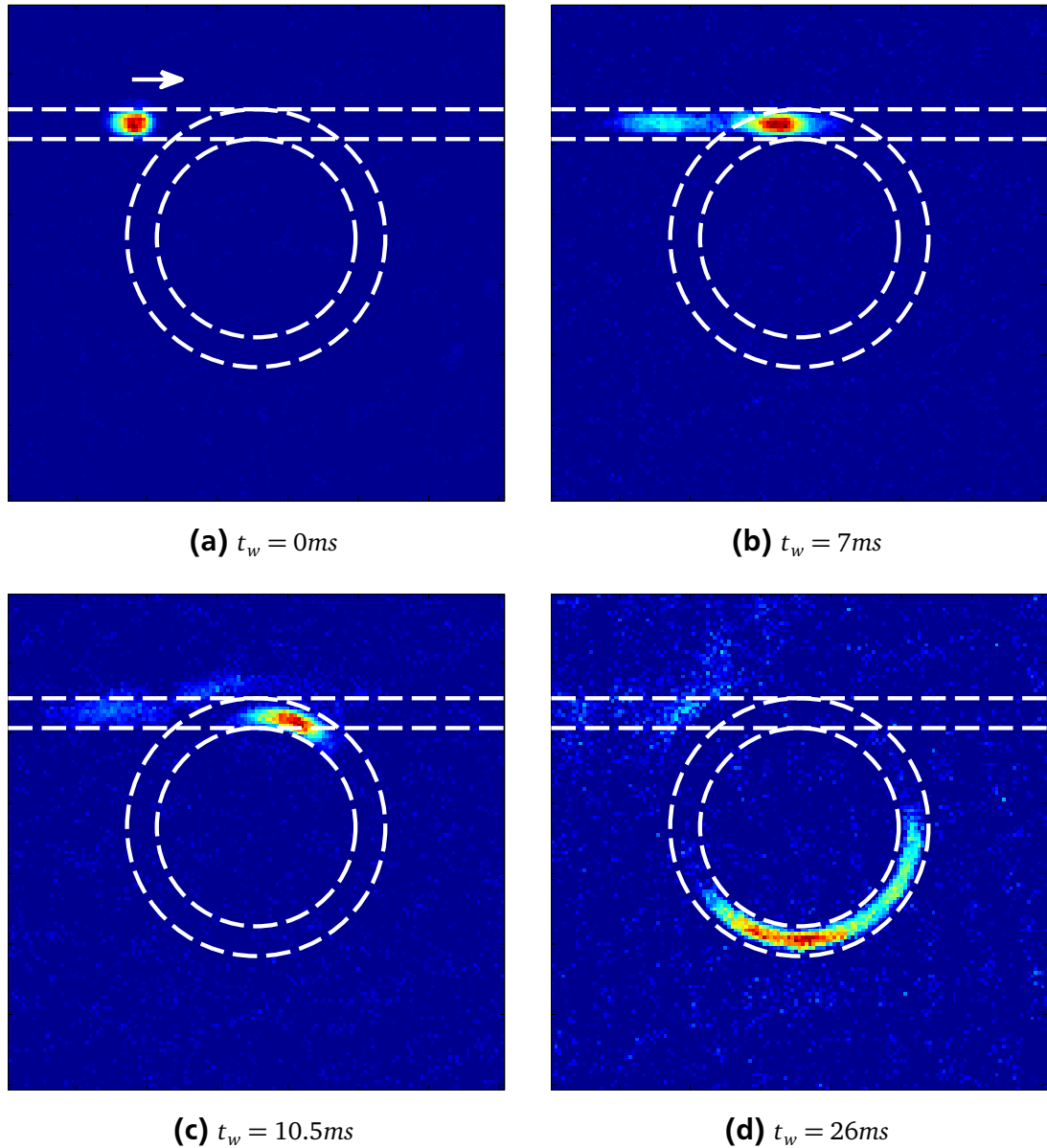
### 5.5.1 Loading a moving wave packet into the ring potential

In order to dynamically load the atoms into a guiding ring structure the setup of Sec. 5.1 has been modified. Fig. 5.29 shows the experimental alignment. Instead of placing the ring shaped trapping potential on top of the crossed optical dipole trap the overlap section of the trap is shifted to the left. The displacement of the cross section is  $x_D = 150 \mu\text{m}$ . Leg 2 of the crossed optical dipole trap is oriented tangentially on the ring guiding structure. The remaining setup is not changed. The experimental procedure starts with the creation of a Bose-Einstein condensate in the crossed optical dipole trap. During the creation of the BEC the ring shaped trapping geometry, including the lightsheet as well as the ring potential, are turned off. Instead of releasing the condensed atoms from the crossed optical dipole trap, leg 2 of the trap has its intensity increased. By lowering the intensity of leg 1 of the crossed dipole trap a quasi one-dimensional wave guide is created. The intensity of leg 1 is reduced linearly to zero. The depth of the potential produced by leg 2 of the dipole trap is chosen to be enough to hold atoms against gravity. The condensed atom cloud is then accelerated to a momentum of  $p = 4\hbar k$ . The atoms now travel in the trapping potential of leg 2 of the dipole trap. As the atoms reach the overlap region the intensity of the lightsheet potential as well as the ring potential is

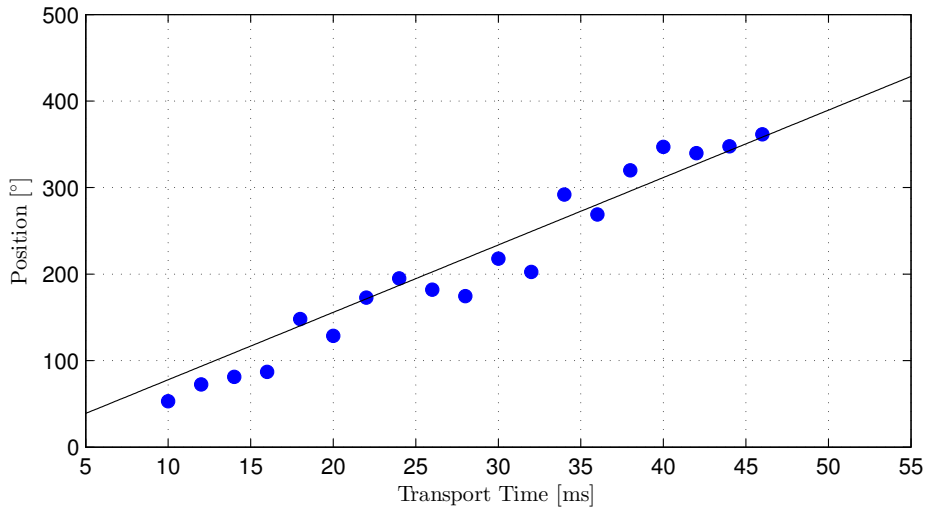
ramped up. In the same manner the intensity of leg 2 of the crossed dipole trap is ramped down until it is shut off completely. The lightsheet potential now fully supports the atoms against gravity and the blue detuned double ring structure forces the atoms to travel in the ring shaped guiding structure. The speed of the atoms yields that the distance  $x_D$  is covered in 6.5 ms. Eq. (5.4) shows that adiabatic loading is possible for small changes of the trapping frequencies. The trapping frequency of the lightsheet potential in the gravitational direction is in the same order of leg 2 of the dipole trap potential that serves as a guiding potential first. The radial trapping frequencies of the ring potential of  $\omega_{Ring} \approx 2\pi \times 300 \text{ Hz}$  is higher than the radial trapping frequency of the linear wave guide. The calculated ramp time should be larger than 12.7 ms. Experimentally these ramp times are too large. Due to their movement atoms will leave the overlap region before a sufficient confinement of the ring trap is achieved. Therefore the experimental ramp duration was chosen to be 2 ms. Losses introduced by longer waiting times due to the lack of confinement of the ring potential rose significantly for longer times. Ramping up the ring potential and the lightsheet separately also yielded additional losses. The 2 ms ramp was started after 5.5 ms so that atoms are well into the ring geometry before the repulsive potential shuts most of the atoms out.

Fig. 5.30 shows a compilation of experimental images showing crucial points of the loading procedure. Fig. 5.30(a) shows the initial point where the atoms are condensed in the cross section of the optical dipole trap. The momentum transfer accelerates the atoms towards the overlap region to the right on the experimental image. After the initial momentum transfer the atoms travel into the overlap region, which is shown in Fig. 5.30(b). Part of the atoms are not accelerated and stay at the initial point of creation. About 10 % of the atoms remain at rest. They are not to be mistaken for atoms not loaded into the ring shaped guiding structure. Instead they disperse after the linear waveguide has been shut off. In Fig. 5.30(c) the remainder of the resting atoms can be seen. The waveguide has been completely shut off for 3 ms. The ring shaped guiding potential and the lightsheet potential are the remaining guiding structures. 95 % of the accelerated atoms already follow the curvature of the ring potential and are fully trapped into the guiding structure. 5 % of the accelerated atoms are lost because they at the top left are repelled by the blue detuned ring wall. Fig. 5.30(d) shows the repulsed atoms dispersing away from the trapping geometry. The atoms which were successfully loaded into the trapping geometry are travelling inside of the ring with a momentum of  $4\hbar k$ . The process of loading the atoms into the trapping potential from the outside could also be accomplished by using atoms with a momentum of  $2\hbar k$ . Due to the decreased velocity the atomic cloud reached the overlap after 14 ms. The increased travelling time yields an increased cloud size and the loading procedure is less efficient.

Fig. 5.31 shows the position of the atomic cloud in the ring shaped guiding structure after loading from the one-dimensional wave guide. The centre-of-



**Figure 5.30:** Experimental images after different times of the experimental procedure. (a) The atoms are created outside of the ring potential and are accelerated towards the ring potential indicated by the arrow. (b) After 7 ms the atoms occupy the overlap region of the toroidal trap and the one-dimensional wave guide. (c) After the loading process the atoms travel inside the ring shaped wave guide. (d) The atoms travel in the waveguide after the loading process has been completed.



**Figure 5.31:** Position of the centre of mass of the atomic cloud inside the ring guiding structure. The black line represents the analytical solution of a wave packet of  $^{87}\text{Rb}$  atoms travelling with a momentum of  $4\hbar k$ . The motion of the centre of mass is not disturbed by the loading procedure.

mass position was taken after increasing evolution times. The solid line indicates the calculated position for a wave packet of  $^{87}\text{Rb}$  atoms moving with a momentum of  $4\hbar k$ . The loading procedure does not inhibit the velocity of the cloud. The angular position of the cloud at the overlap point is given as zero and after 45 ms a full circumference has been travelled by the atoms. Due to the limited time the atoms stay in the overlap region the intensity ramp for the three light fields was chosen to be 2 ms. Non-adiabatic loading is a common problem if the trapping frequencies change too quickly [70]. A non-adiabatic loading process shows excitation of higher energy states and can be detected by observing heating processes. Additionally non-adiabatic loading destroys coherence [159] and therefore an adiabatic loading procedure is desirable. The energy deposited due to heating should result in a faster spread of the atom cloud loaded into the guiding structure. Additionally an increased temperature should increase losses. Fig. 5.32 shows the width of the atomic cloud in the azimuthal direction for different transport times. The broadening of the atomic cloud can be described by the scaling parameters  $\lambda$  as discussed in Sec. 2.2.3. Next to the data points a solution of Eq. (2.36) is plotted for the parameters of the ring shaped trapping potential. The cloud is in the ballistic expansion regime and a linear increase of width is expected. The measured width of the ultra-cold atoms increases with a slightly lower slope indicating a slightly lower trapping frequency of the potential. This can be explained with day to day fluctuations of the experimental setup of the conical refraction double ring structure. No acceleration of the wave packet spreading can be ob-

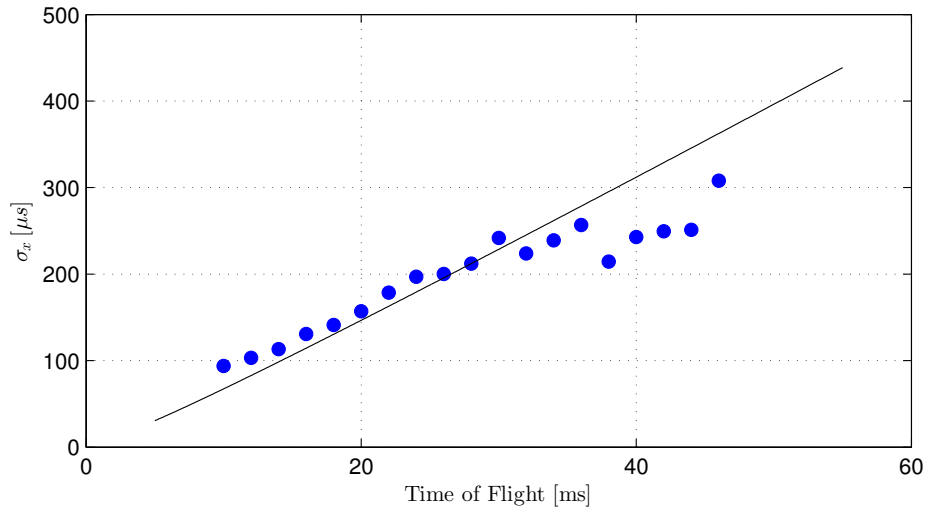


**Figure 5.32:** Width  $\sigma_x$  of the atomic cloud as a function of time in the trapping potential. The solid line describes the numerical solution of Eq. 2.36 with the parameters for the trapping ring geometry. The slope of the expansion is slightly lower than the theoretical prediction indicating that the loading procedure did not impose a heating process.

served showing that the loading procedure itself is working without increasing the temperature of the atom distribution.

---

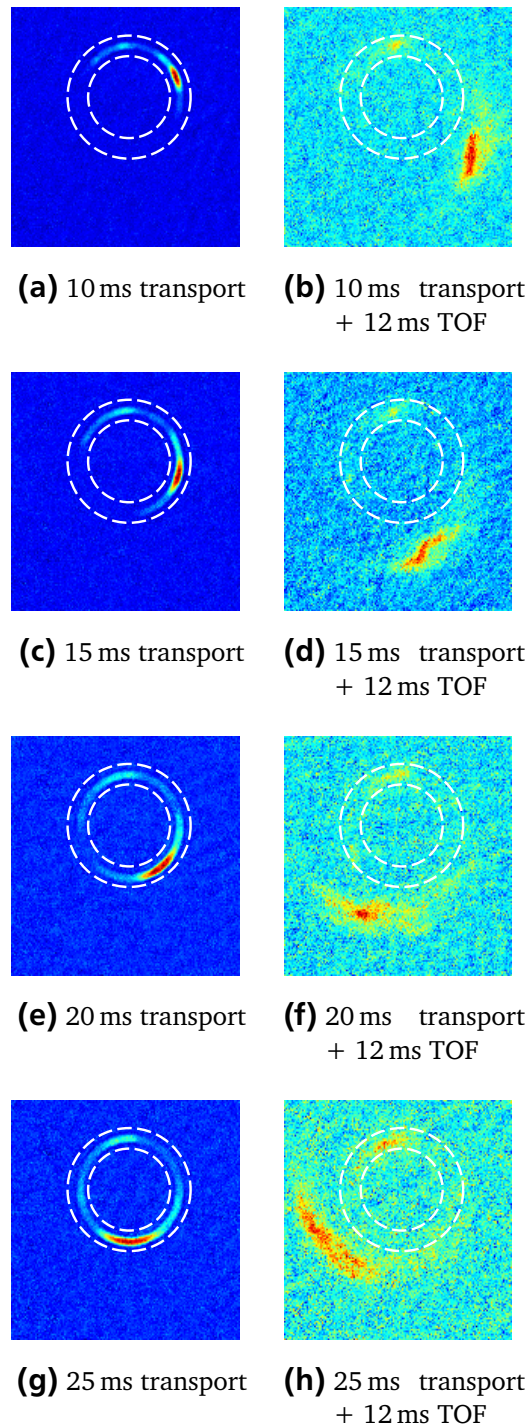
### 5.5.2 Releasing atoms from the ring potential

---

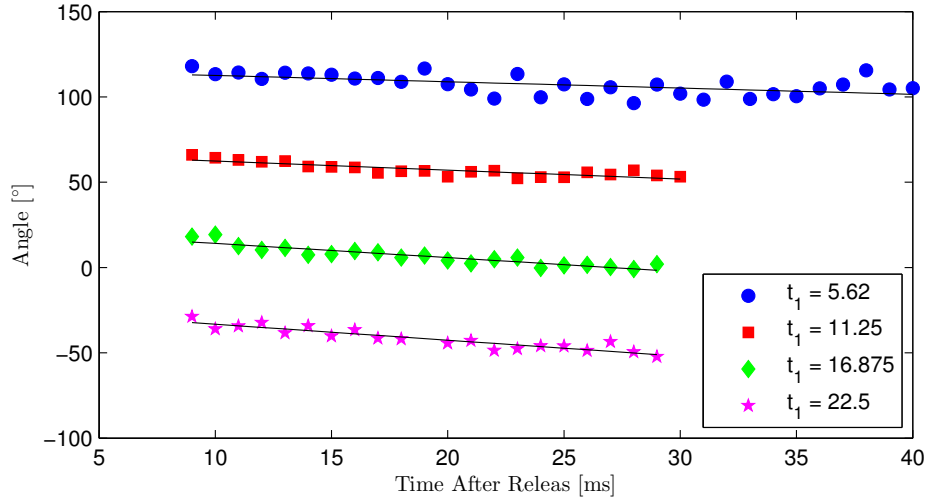
To gain insight in the movement of the atoms inside the trapping potential and to study the dynamics of moving atoms in a toroidal waveguide, atoms were released on purpose from the potential after they were accelerated. As a function of the transport time in the potential before the atoms were released different effects could be observed.

Fig. 5.33 shows four sets of images for different transport times. The atoms were accelerated to a momentum of  $4\hbar k$  after they were loaded into the toroidal wave guide. The accelerated atoms travel in clockwise direction along the trapping potential. The depth of the potential was chosen so that the atoms could be guided along the ring potential. After a varying transport time the atoms were released from the potential by switching off the Ti:Sa AOM as well as closing the mechanical shutter in front of the AOM. An additional time-of-flight in the lightsheet potential alone was applied and the density distribution was imaged by absorption detection.

Fig. 5.33(a) shows the position of the atomic cloud 10 ms after the lattice pulse. The atoms travelled  $230\mu\text{m}$  in the toroidal potential. Fig. 5.33(b) shows the corresponding image with additional 12 ms of free expansion in the lightsheet



**Figure 5.33:** Absorption images of the transport of atoms in the ring potential with a momentum of  $4\hbar k$ . On the left side the atoms reside in the trapping potential whereas on the right side the atoms were released after the transport in the ring potential and detected after an additional TOF of 12 ms. Depending on the azimuthal spreading a varying rotation of the atomic ensemble is observable.



**Figure 5.34:** Rotation of a released moving ultra-cold atomic ensemble from the toroidal wave guide for different travelling times  $t_1$ . The slope, giving the angular velocity  $\omega_{\text{twist}}$ , increases for longer transport times  $t_1$  as described in Eq. (5.8).

potential without the ring potential. The atoms leaving the trapping area of the ring tangentially and due to the azimuthal expansion of the ensemble different propagation directions emerge. The front part of the ensemble has a different tangential direction than the back side of the ensemble. This induces a twist of the atomic ensemble once it is released from the ring potential. The twisting of the ensemble is largely dependent on the initial azimuthal waist. The images of Fig. 5.33 show the evolution of the twist for different azimuthal widths. A higher azimuthal width was achieved by longer travelling times in the ring potential.

To observe the twist of the atomic ensemble its evolution was monitored for varying times after the release from the toroidal potential. The experimental results are shown in Fig. 5.34 for four different initial transport times  $t_1$  in the guiding ring structure. The angle is measured by fitting a two-dimensional Gaussian distribution, where a dependence of the orientation on an angle  $\alpha$  was introduced.  $\alpha$  gives the twist in respect to the vertical axis of the ring potential in the horizontal plane of the toroidal wave guide structure. The underlying solid lines are linear fits to determine the slope  $\omega_{\text{twist}}$  of the rotation of the ensemble. The twisting shows a distinct variation for increased travelling times and shows the following experimental correlation between the travelling time  $t_1$  and the angular velocity  $\omega_{\text{twist}}$  after the release of the guiding potential:

$$\omega_{\text{twist}} = -0.0356 \frac{\circ}{\text{ms}} \times t_1 - 0.165^\circ. \quad (5.8)$$

As shown in Fig. 5.34 the twisting of the atom distribution shows a linear behaviour. Since no angular momentum has been imprinted on the atomic

---

ensemble the twisting of the atoms should continue until a full  $180^\circ$  twist is completed. Due to the limited field of view of the detection system this process cannot be observed.

The experimental demonstration of free evolving ultra-cold ensembles previously trapped in a toroidal geometry could serve as an interesting starting point for the study of collisions of ultra-cold atoms and BECs [160]. By using double Bragg diffraction (see Chapter 3) a symmetric splitting of the condensate in the toroidal wave-guide can be achieved. The moving atoms in the wave guide can be released after they nearly travelled half of the rings circumference. Depending on their relative angle the collisions of clouds can be observed. By limiting the momentum width of the cloud an additional momentum selectivity of ensemble can be implemented. Depending on the exact release point of the atoms the relative angle can be adjusted under which the ensembles collide.

---

## 5.6 Matter wave interferometry in ring shaped dipole potentials

---

The common ground of all interferometers is the coherent splitting of an initial state, the subsequent evolution of the created superposition of the system, and finally the recombination the respective parts. A phase difference between the two or more parts of the interferometer yields an experimentally observable signature. For matter wave interferometry, the initial state is represented by the Bose-Einstein condensate of  $^{87}\text{Rb}$  atoms. In addition an optical lattice can be used to split and recombine the ensemble. This has been shown in Sec. 3.7 with a double Bragg lattice. The Ramsey type interferometer, consisting of two  $\pi/2$  pulses, serves as an auto-correlation measurement and the phase difference between the interfering ensembles is realized by a spatial offset of the two clouds.

By implementing a Mach-Zehnder like interferometer the phase accumulated along a path can be observed. The Mach-Zehnder interferometer were first created with light, where an initial optical beamsplitter creates two beams of light that each travel different beam path. They are, at a later stage, recombined with a second optical beamsplitter and depending on the phase difference the interferometric intensity modulation can be measured at the two exits of the interferometer. In combination with toroidal wave guides this scheme can be conferred easily to matter wave interferometry. A coherent ensemble is split in two parts with an optical lattice beamsplitter pulse. One of the two parts travels a full circumference along the rings guiding structure and upon reaching the resting part the interferometer sequence is completed. In this section the implementation of an Mach-Zehnder-type interferometer in toroidal guiding potentials will be demonstrated. In the following sections the experimental scheme for matter wave interferometers is shown and the experimental measurements will be discussed. The interferometer sequence was implemented by utilizing coherent splitting and recombination with Bragg diffraction (see Sec.

5.6.1). Possible influences prohibiting a successful implementation of the interferometer are discussed in Sec. 5.6.2. This section closes with a discussion on consequences for future interferometric measurements at the ATOMICS experiment to successfully implement a toroidal matter wave interferometer (see Sec. 5.6.3).

---

### 5.6.1 Experimental implementation of interferometric measurements with Bragg diffraction

---

The introduced toroidal wave guide helps with the implementation of a matter wave interferometer due to its periodic structure in azimuthal direction. Accelerated atoms periodically return to the exact same position after a full circumference in the ring potential. This eliminates the need to implement a  $\pi/2$ - $\pi$ - $\pi/2$  pulse sequence, which is normally used for Mach-Zehnder-type interferometer. Instead the  $\pi$  pulse is replaced with a sufficiently long waiting time to let the atoms travel a full circumference of the rings guiding structure. The interferometric pulse sequence therefore mimics the pulse sequence of a Ramsey type interferometer presented in Fig. 3.25.

Fig. 5.35 depicts the implemented interferometer sequence. A Bose-Einstein condensate of 25000  $^{87}\text{Rb}$  atoms is produced in the crossed optical dipole trap. The toroidal potential is positioned on top of the crossed optical dipole trap and the atoms are loaded into it adiabatically. As Fig. 5.35(a) depicts the atoms are then accelerated with standard Bragg  $\pi/2$  pulse. The coherent superposition between the momentum states  $|0\hbar k\rangle$  and  $|2\hbar k\rangle$  yields a separation of the two atomic ensembles. Fig. 5.35(b) shows the resting ensemble at the initial point of loading whereas the accelerated part travels along the guiding potential with its imprinted momentum of  $4\hbar k$ . After the atoms travelled a full circumference in the ring potential both clouds spatially overlap again (see Fig. 5.35(c)). A second  $\pi/2$  pulse is applied and the interferometer sequence is complete. In order to observe the imprinted density modulation due to the spatial separation  $\Delta x$  an additional waiting time is given until the density distribution is imaged (see Fig. 5.35(d)).

Analogously to the interferometric measurements with double Bragg diffraction in Sec. 3.7 the fringe period  $d$  is dependent on the spatial displacement  $\Delta x$  of the clouds. The spatial displacement can be tuned by altering the time  $\tau$  between the two  $\pi/2$  pulses.

The implementation of an interferometer with optical lattice pulses is not dependent on the choice of the order of the Bragg lattice. As discussed earlier the azimuthal width of the condensate follows the theoretical predictions up to a time of 50 ms (see Sec. 5.3.5 and Sec. 5.4) After that time the width of the condensate is not well defined and shows unpredictable behaviour. The phase gradient  $\alpha$ , determining the properties of the expected density modulations, therefore also is unpredictable, which makes interferometric measurements im-

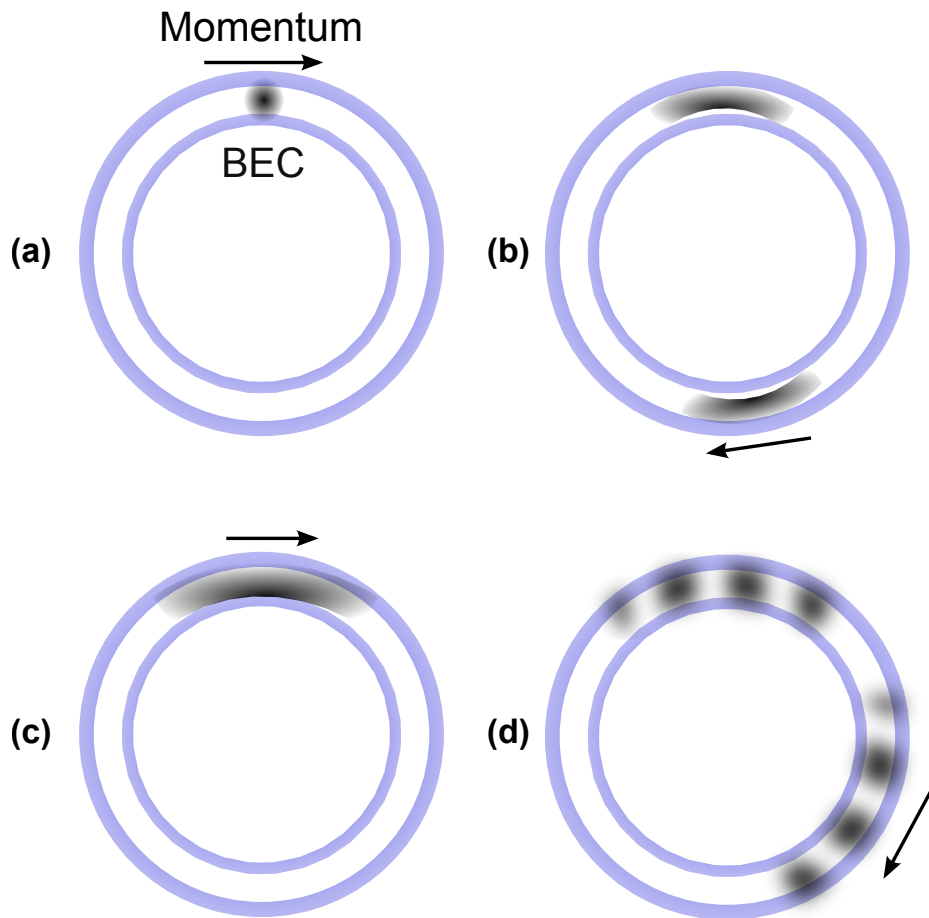


**Figure 5.35:** Schematic overview of the sequence used for matter wave interferometry in toroidal wave guides. (a) A Bose-Einstein condensate is loaded into the toroidal wave guide. (b) A  $\pi/2$  lattice pulse implements a matter wave beamsplitter. Half of the atoms move with a momentum of  $4\hbar k$  in azimuthal direction along the ring guiding structure. The other half of the initial atomic ensemble stays at rest. Both atomic ensembles spread according to the scaling law described in Sec. 2.2.3. (c) After a full round trip both ensembles overlap spatially. A second  $\pi/2$  pulse closes the interferometer and projects the coherent superposition of the two atomic clouds. Depending on the separation of the two  $\pi/2$  pulses the clouds are displaced by  $\Delta x$ . (d) After an additional waiting time the two exits of the interferometer are spatially separated. The density modulation is visible in both interferometer exits.

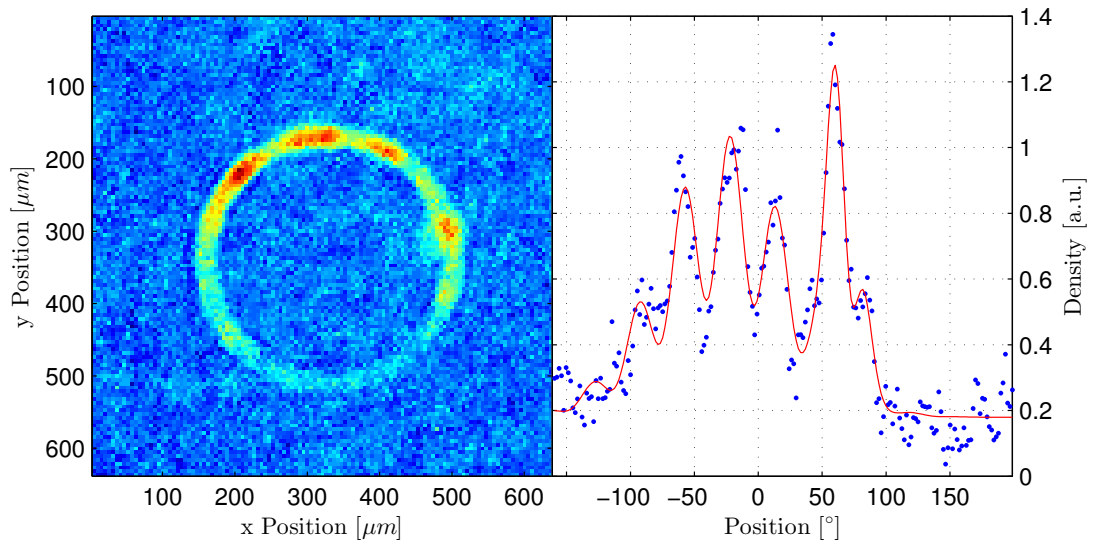


**Figure 5.36:** (left) Density distribution after a full Mach-Zehnder-type interferometer. The time between the two  $\pi/2$  pulses of the interferometer is 45.5 ms. After the second  $\pi/2$  pulse an additional waiting time of 18 ms passed before the absorption detection image is implemented. (right) After the transformation to a one-dimensional density profile a fit to the distribution was made (solid red line).

possible. Because the round trip time of a BEC with a momentum of  $2\hbar k$  is 92.3 ms, single order Bragg diffraction cannot be used. Second-order Bragg diffraction on the other hand features half the round trip time and is therefore used to implement a matter wave interferometer in toroidal guiding structures with standard Bragg diffraction.

Fig. 5.36 shows the obtained density distribution. The left side shows the observed two-dimensional density distribution whereas the right side gives the transformed density distribution to a one-dimensional profile (see Sec. 5.2). The time between the two  $\pi/2$  pulses was set to 45.5 ms which is 0.7 ms short of the time needed for a full circumference. The resulting displacement of the clouds is  $\Delta x = 0.7 \text{ ms} \times 23.5 \mu\text{m/ms} = 16.6 \mu\text{m}$ . The density profile shows a very distinct density modulation along its azimuthal direction. The density modulation is present in both interferometer exits. The moving exit (about  $0 - 100^\circ$ ) shows a very high density in its centre. Its centre of mass moved according to its velocity for additional 18 ms. The resting part of the density distribution is originated at angles between  $-100$  and  $0^\circ$ . Its azimuthal width is higher which yields more fringes to be visible. The distance of the fringes is the same as the distance of the fringes in the first interferometer exit. The fit used was derived from Eq. (3.50) but featured the following simplifications: instead of two spatial frequencies only one was implemented and instead of three Gaussian distributions only two were fitted.

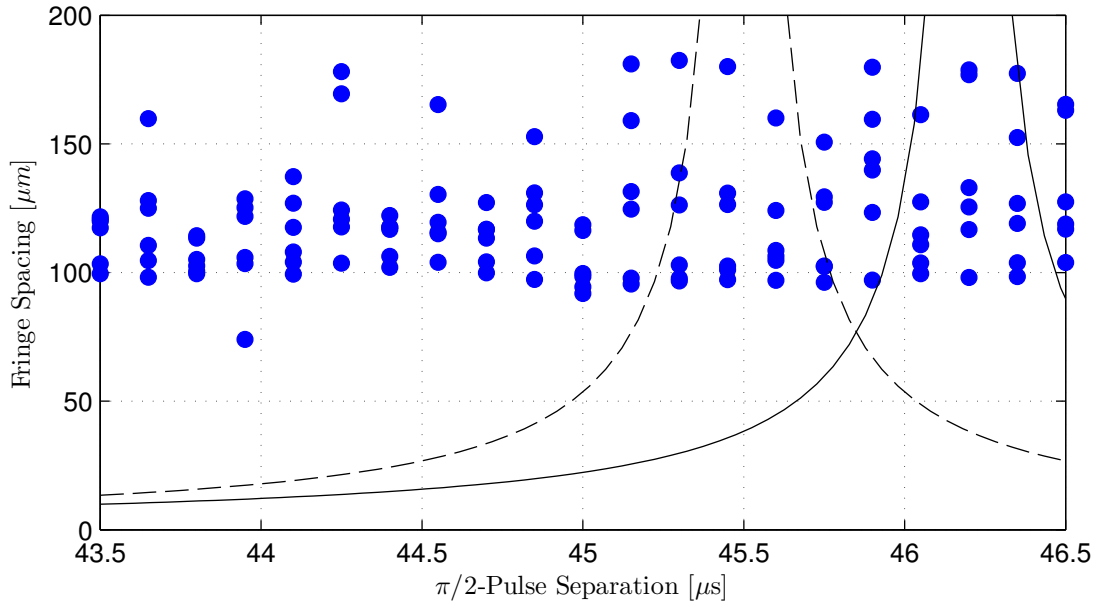


**Figure 5.37:** Fringe spacing obtained after a Mach-Zehnder-type interferometer sequence in a toroidal trapping potential. The time between the two  $\pi/2$  pulses is varied and a varying fringe spacing is expected. The solid line shows the expected fringe spacing according to Eq. (3.49) and the dashed line incorporates the drift of the resting atomic ensemble, which reduces the time needed to achieve a spatial overlap.

The resulting parameters for the fringe spacing are shown in Fig. 5.37. Alongside the experimental data is the expected fringe period plotted. The numerical solution of  $\alpha$  was used to determine the fringe spacing  $d$  with Eq. (3.49). The parameter  $\Delta x$  in a toroidal trap has to take into account the periodicity of the potential. Therefore  $\Delta x$  is determined by:

$$\Delta x(t) = (t - t_{4\hbar k}) \times 4v_R, \quad (5.9)$$

for an interferometer with momentum transfer to  $|4\hbar k\rangle$ .  $t_{4\hbar k} = 46.2$  ms denotes the round trip time of an ensemble of  $^{87}\text{Rb}$  atoms with a momentum of  $4\hbar k$  in the toroidal wave guide. In addition the dashed line shows the expected fringe period for a drifting resting ensemble. As shown in Sec. 5.3 a resting cloud has shown to move up to  $20 \mu\text{m}$  after a time of  $45 \mu\text{s}$ . According to the movement direction of the displacement the overlap point of the interferometer to apply the second  $\pi/2$  pulse is reached earlier.

The experimental data does not show any dependency on the parameter  $\Delta x$ . As the numerical data would imply a shift in the displacement should induce a changed spatial frequency, hence a changed fringe spacing. This could not be observed. Instead the fringe spacing remains constant throughout the

whole parameter area. The parameter is also independent from the potential depth in radial or  $z$  direction. With Eq. (3.49) a value for the phase gradient  $\alpha = (105 \pm 46) \times 10^{-6} \mu\text{m}^{-2}$  can be derived from the experimental data. The value is by at least four orders of magnitude lower than the expected value of  $\approx \alpha = 0.4 \mu\text{m}^{-2}$  calculated with Eq. (2.40).

To make sure that each lattice pulse creates the desired momentum distribution the sequence was performed without the application of both but only one pulse. The timing of the remaining experimental setup was not altered. First the second lattice pulse was omitted and the achieved density distribution was investigated. In an additional measurement the first lattice pulse was omitted. Both systems produced the expected momentum distribution which evolved according to its momentum in the guiding structure.

In order to prove that the observed density distribution is not a product of accelerated atom ensembles with different relative momenta of  $2\hbar k$  or  $4\hbar k$  the evolution of the fringe spacing was observed. Fig. 5.38 shows the mean values of the measured fringe period of up to 60 single shots per data point. The error bars are the statistical errors of the average values. The obtained data illustrates that the fringe distance of the density modulation achieved in the experiment is changing. The slope  $m = (5.19 \pm 0.44) \mu\text{m}/\text{ms}$  obtained from the fit of a linear equation to the data point shows that the velocity differs significantly from the velocity of the momentum states  $|2\hbar k\rangle$  and  $|4\hbar k\rangle$ . The equivalent velocities are  $11.77 \mu\text{m}/\text{ms}$  and  $23.54 \mu\text{m}/\text{ms}$ . If the structures would be a simple product of the application of multiple  $\pi/2$  pulses without the addition of a coherent relation between the wave packets relative velocities of  $23.54 \mu\text{m}/\text{ms}$  should be observable. This is not the case. Under the assumption that one of the two lattice pulses does not perform as desired, and excitation of the non-desired momentum state  $|2\hbar k\rangle$  is occurs, relative velocity of  $11.77 \mu\text{m}/\text{ms}$  would be observed. Both relative velocities cannot be observed. The measured slope of  $m = (5.19 \pm 0.44) \mu\text{m}/\text{ms}$  is not achievable with a momentum transfer by an optical lattice for  $^{87}\text{Rb}$ . Therefore it can be ruled out that the observed density patterns are created solely from non-coherent processes.

---

## 5.6.2 Discussion on limiting factors for matter wave interferometers in wave guides

---

As shown in the previous section interferometric measurements have been performed, but the expected behaviour could not be confirmed. In contrast to successful implementations of guided matter wave interferometers [161] no consistent dependence on the parameters could be observed. Instead a constant density modulation occurred. This section will discuss possible experimental uncertainties and their consequences for the implementation of matter wave interferometers in toroidal wave guides.

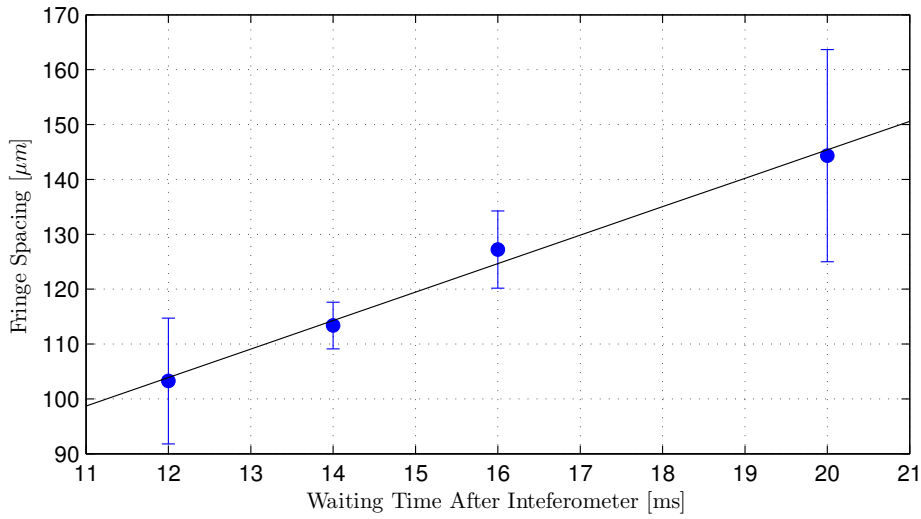


**Figure 5.38:** Fringe spacing depending on the additional waiting time after the second interferometer pulse. The data points shown are the mean values of multiple measurements. The solid line represents a linear fit to the data points and has a slope of  $m = (5.19 \pm 0.44) \mu\text{m}/\text{ms}$ .

---

#### Different evolution of phase gradients for both interferometer arms

---

In order to guide a wave packet with  $4\hbar k$  moment in the toroidal wave guide the potential has to be at least  $16 E_R$  deep in order to hold the atoms on the circular wave guide. In order to achieve said potential heights the intensity of the Ti:Sa laser used to produce the wave-guiding ring structure has to be increased. The free expansion along the azimuthal direction discussed in Sec. 5.3.5 is diminished by an increased optical power. As shown before the increased trap depth yields a non-spreading atom ensemble in the loading area of the BEC. Since the expansion of the wave and the phase gradient are dependent on each other this occurrence yields a modified phase gradient. Because only the moving cloud experiences a diminished expansion, different phase gradients in each of the interferometric legs evolve. Eq. (3.49) gives the fringe period under the assumption that both clouds feature the same phase gradient  $\alpha$  during the complete duration of the interferometric process. By introducing two different phase gradients  $\alpha_1$  and  $\alpha_2$ , Eq. (3.49) has to be altered accordingly. Eq. (3.45) becomes:

$$F(x) = 2N \times \cos \left( - \left( \frac{\alpha_1 - \alpha_2}{2} \right) x^2 + (\alpha_1 \Delta x + 2\beta) x + C \right), \quad (5.10)$$

and  $\kappa$  is now defined as by:

$$\kappa(x) = \left( \frac{\alpha_1 - \alpha_2}{2} \right) x + \alpha_1 \Delta x. \quad (5.11)$$

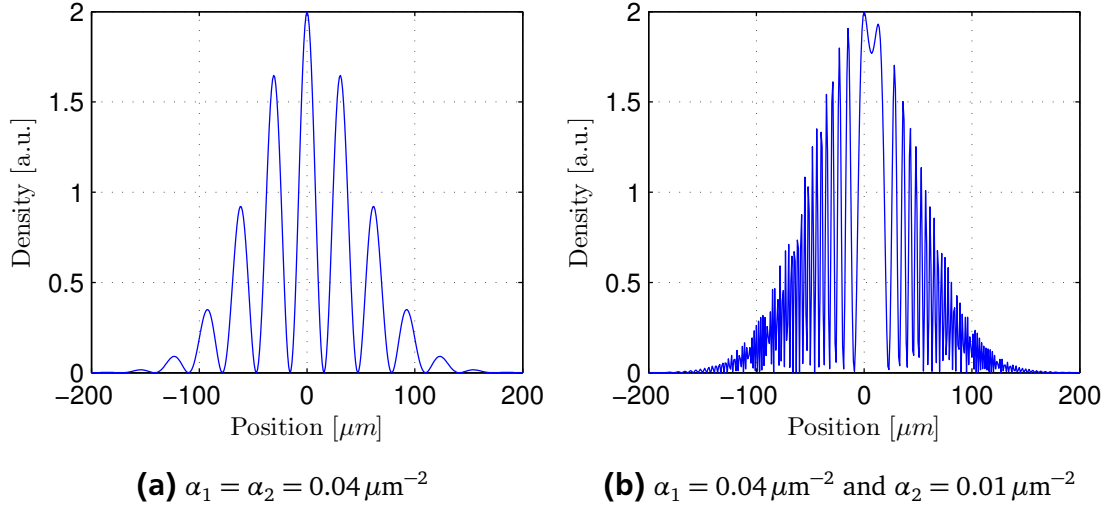


**Figure 5.39:** Calculated density distributions for different values of the phase gradient  $\alpha_1$  and  $\alpha_2$  for the respective atomic distributions.

In contrast to the previous discussion an additional term is introduced: a space dependent oscillation frequency  $\kappa(x)$  of the spatial density modulation. For  $\alpha_1 = \alpha_2$  the term vanishes and the definition of  $\kappa(x)$  is the same as Eq. (3.47). Fig. 5.39 illustrates the behaviour of the density modulation of different values of  $\alpha$ . Both density distribution feature the same set of experimentally obtained values. The density distribution consists of a Gaussian envelope with a sinusoidal oscillation on top. The width of the Gaussian is  $100\ \mu\text{m}$ . The amplitude of the Gaussian has been set to one as well as the amplitude of the oscillation. The position of the centre of mass has been set to zero. Fig. 5.39(a) shows the density modulation obtained with  $\alpha_1 = \alpha_2 = 0.04\ \mu\text{m}^{-2}$ . The density distribution shows a single-frequency modulation. The fixed period is very well in the detectable region of the ATOMICS experiment. Fig. 5.39(b) shows the density distribution obtained for  $\alpha_1 = 0.04\ \mu\text{m}^{-2}$  and  $\alpha_2 = 0.01\ \mu\text{m}^{-2}$  [63]. The space dependent oscillation frequency  $\kappa(x)$  yields a very fast increasing oscillation frequency as the distance increases from zero. The obtained fringe spacing reaches a regime of under  $30\ \mu\text{m}$ , a lower bound for the detectable spatial period of the optical system. Even though the resolution is  $5.3\ \mu\text{m}$ , to fully observe two density modulations as separate fringes at least  $30\ \mu\text{m}$  of separation are favourable. The calculations do not take into account fluctuations of the density due to imperfect lattice beams and noise, effects that further diminish the observable parameter regime.

---

## Azimuthal width of the clouds

---

Due to the processing time of at least 45 ms the azimuthal width of the condensate is at least a third of the complete toroidal wave guide. This yields additional problems in regards of the lattice pulses used to accelerate and decelerate the atomic ensemble. Due to the large waist of the lattice pulses the position of the atoms in the ring is of no problem. The problem arises from the curvature of the toroidal wave guide and the acceleration direction of the optical lattice. Atoms at the loading point of the toroidal trap are accelerated tangentially in the ring direction. This is also possible on the opposite side of the toroidal potential where the lattice beams are also aligned tangentially with the ring potential. Accelerating the atoms at other positions in the ring is also possible but yields excitation of radial oscillations or even atom losses. In certain places this behaviour is useful, e.g. to measure the trap frequency of the toroidal wave guide [65] or to measure the trap depth (see Sec. 5.3.4). In the case of interferometric measurements this non-desired behaviour inhibits the quality of the seconds  $\pi/2$  pulse. Atom losses during the interferometric process yield a reduced contrast of the interferometer and should be avoided. In addition the excitation of radial oscillations inhibits the possibility to observe density modulations [136, 162].

---

## Dependence of the motion of atoms on the lightsheet potential

---

The lightsheet potential used to support atoms against gravity is known to feature inequalities in its spatial intensity distribution. This yields modulated potential depths also in the area of the ring potentials guiding structure [63]. It could be shown that the free expansion of an atom cloud in the toroidal wave guide is possible (see Sec. 5.3.5) and therefore the influence of the lightsheet is negligible. Nevertheless in this respect a different effect has been observed. The azimuthal position of an accelerated ensemble in the toroidal trap changes with varying intensity of the lightsheet beam. To further investigate the behaviour of atoms for different lightsheet depth a ensemble of ultra cold atoms was accelerated inside the toroidal guiding structure. Fig. 5.40 shows the position of an atom ensemble after the acceleration to a momentum of  $4\hbar k$  and subsequent waiting time of 35 ms after the lattice pulse. The time of 35 ms was chosen to have the maximum rotation time of the atoms in the ring without interacting with atoms resting at the loading point. After 35 ms 75 % of the full circumference of the ring have been travelled.

The solid black line shows the expected position of the centre of mass of the wave packet at  $x = v \times t = 22.5 \mu\text{m}/\text{ms} \times 35 \text{ ms} = 789 \mu\text{m}$ . The ring potential was kept constant at a wavelength of 792.5 nm and repulsive outer ring height of  $24.2 E_R$ . The position of the centre of mass has the expected position after moving with a momentum of  $4\hbar k$  for 35 ms for low lightsheet power. For in-

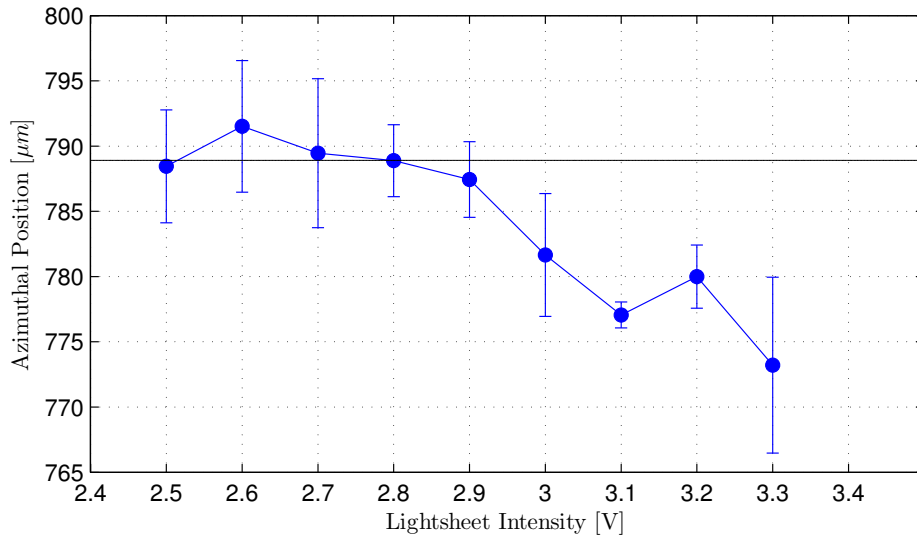


**Figure 5.40:** Position of the centre of mass of an accelerated atom ensemble in the toroidal waveguide. The atoms are accelerated to a momentum of  $4\hbar k$  and after 35 ms their expected azimuthal position with respect to the point of acceleration is  $789 \mu\text{m}$ . Depending on the optical power of the lightsheet the position varies.

creasing power the position of the centre of mass is reduced to smaller values indicating that an increased lightsheet depth introduces a potential gradient or corrugations along the ring guiding structure. These effects influence the free movement of the atoms by decreasing their momentum. This results in a false estimation  $\Delta x$  for the interferometer sequence.

In order to implement a perfect interferometer this drift has to be taken into account. The relative position of the two clouds  $\Delta x$  has to be adjusted appropriately if the influence of the lightsheet cannot be eliminated. The induced displacement due to the lightsheet's potential depth is in the order of  $10 \mu\text{m}$  for the experimentally achievable optical power. This displacement does not change the overall spatial density modulation by a large factor. A well-defined spatial density modulation should still be observable.

---

### 5.6.3 Consequences for future interferometric measurements

---

The implementation of a Mach-Zehnder-type interferometer for ultra-cold atoms has not been successful in a quantitative manner. The expected dependence of the fringe period on the displacement  $\Delta x$  could not be observed.

The measured phase gradient of the BEC of  $\alpha = (105 \pm 46) \times 10^{-6} \mu\text{m}^{-2}$  is by four orders of magnitude smaller than the expected value of  $\alpha_{\text{calc}} = 0.04 \mu\text{m}^{-2}$ . Also the assumption that both clouds feature the same phase profile  $\alpha$  has to be reconsidered. The implementation of a free expanding cloud has been shown

---

in shallow ring potentials. Guiding potentials deep enough to guide accelerated atoms with a momentum of  $4\hbar k$  did not show this behaviour.

In general the implementation of a smaller ring structure would decrease a multitude of problems. On the one hand the transport times for all processes in the ring system would decrease and on the other hand the reduced transport time would yield smaller azimuthal expansion of the atomic ensembles. The reduced ring size could also be used with less optical power. A Mach-Zehnder-type interferometer in a smaller ring could be implemented using  $2\hbar k$  momentum, which would also prevent the reduced contrast experienced in higher order Bragg interferometers.

---

## 6 Novel three dimensional dark focus trap

Traps for atoms come in a multitude of different implementations. All-optical trapping geometries have the advantage that they can trap all magnetic states of an atom simultaneously [26]. They also feature flexibility and can be shaped according to a given application [163]. A drawback of trapped atoms in attractive dipole potentials is, that they suffer from different energy shifts depending on the state and intensity of the trap. The fidelity of high precision measurements based on dipole traps also suffer from coherence loss caused by inhomogeneous differential light shifts [164]. These shifts can be compensated with appropriate arrangements but would not arise in principle in a so called 'dark trap'. A dark trap features large repulsive potentials enclosing the trapping region confining the atomic ensemble spatially. Normally, dark traps consist of a combination of multiple repulsive potentials. Conical refraction offers the possibility to create true three-dimensional dark trap with a single beam. A perspective application of these beams is found in quantum computation, where large registers of atomic ensembles are used to store quantum information in atomic states. The applicability of the involved operations is highly depended on the dephasing effects which are partly caused by the differential ac Stark shift [165]. By using micro-lens arrays a two-dimensional register of dark traps can be realised to create a new way of storing atoms without the drawback of the differential ac Stark shift at the traps centre.

In this chapter, the experimental implementation of a three dimensional dark traps is presented. Sec. 6.1 characterizes a complete experimental setup of a dark trap. Trapping of atoms and Bose-Einstein condensates is demonstrated in Sec. 6.2. The chapter concludes with a discussion of future applications of dark traps in quantum information processing and presents an approach towards the generation of a two dimensional register of qubits in dark traps (see Sec. 6.3).

---

### 6.1 Experimental realization of a three dimensional dark focus trap

---

In addition to the general discussion on the three-dimensional dark focus in Sec. 4.4.2, a complete characterization of experimentally realized potential has been done. Sec. 6.1.1 shows the experimental creation of the bottle beam. The intensity distribution along the propagation direction will be discussed in Sec. 6.1.2 and the properties of the focal plane will be shown in Sec. 6.1.3.

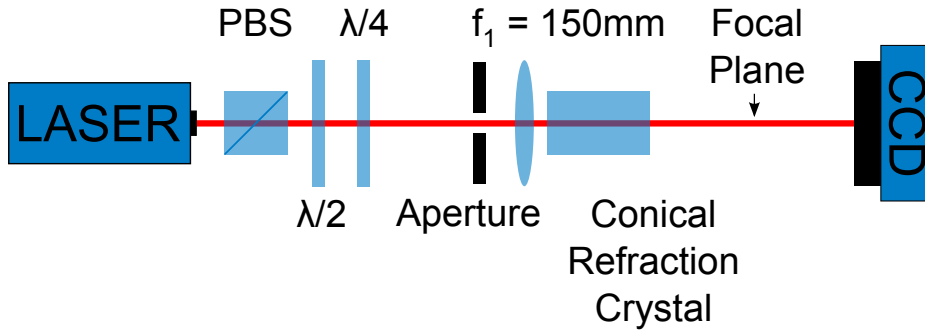


**Figure 6.1:** Setup for the characterization of the three dimensional dark focus beam. The polarization of the laser beam is purified by a polarizing beamsplitter and can be adjusted by a combination of a  $\lambda/2$  and  $\lambda/4$  waveplate. The focal plane of the focussing lens  $f_1$  is imaged by a CCD camera.

### 6.1.1 Experimental setup of a three dimensional dark focus beam

The experimental setup to create a three dimensional dark focus is shown in Fig. 6.1. The shown setup is part of the setup used to trap atoms with the three dimensional dark focus described in Sec. 6.2. Collimated light out of a laser passes a polarizing beamsplitter cube and is guided through a  $\lambda/4$  waveplate to create circular polarized light. In order to compensate inequalities of the polarization an additional  $\lambda/2$  waveplate is used. The light is then guided through a focussing lens with a focal length of  $f_1 = 150$  mm. In order to optimize the optical beam path an aperture is placed in front of the focussing lens  $f_1$ . The aperture limits the waist and yields a well defined beam profile. With an incident beam waist of  $w_i = 1$  mm Eq. (2.6) gives a calculated beam waist of  $w_{0,\text{calc}} = 37.9 \mu\text{m}$  and a Rayleigh range of  $z_R = 5.88$  mm. The conical refraction crystal used is a  $\text{KGd}(\text{WO}_4)_2$  crystal with a length of  $l = 2.2$  mm. The remaining properties of the crystal are the same as the properties of the crystal used for the creation of the double ring structure. In particular it features the same half opening angle of  $\alpha = 1^\circ$ . The radius of the ring structure is given by  $R_0 = \alpha \times l = 38.4 \mu\text{m}$ . The created ring structure is imaged with a CCD camera mounted on a translation stage. To avoid damage of the CCD camera a low optical power was used.

The lens in front of the conical refraction crystal in combination with an aperture produces a focus of size  $w_0 = 42.7 \mu\text{m}$ . The Rayleigh range of the beam is  $z_R = 5.42$  mm. For the given values for the bottle beam,  $\rho_0 = 0.90$  which is close to the ideal value of 0.92.

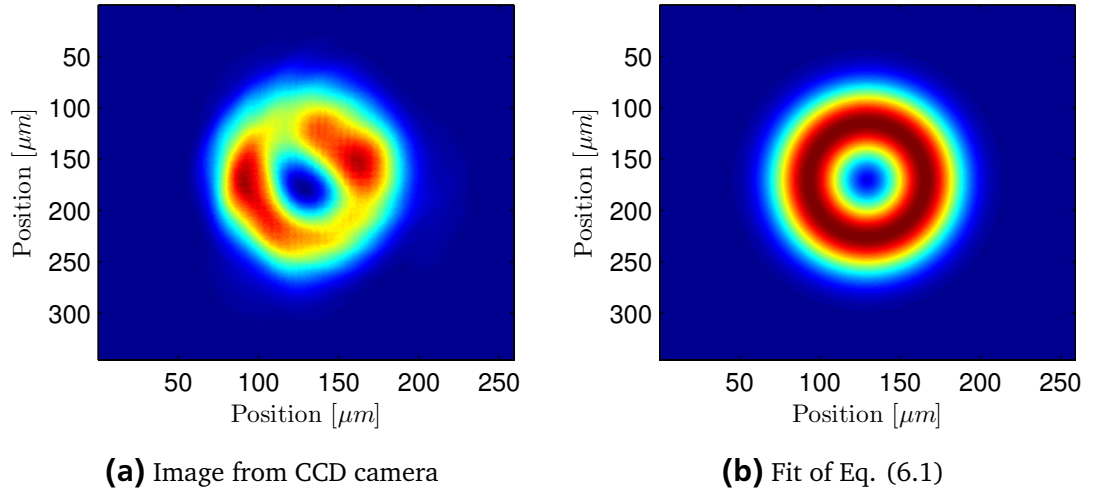


**Figure 6.2:** Comparison of an experimental intensity distribution of the three-dimensional dark focus in the focal plane and a fit of Eq. (6.1). The azimuthal asymmetry of the potential yields an overall reduced trap depth in the radial direction and is unfavourable.

### 6.1.2 Intensity distribution along the beam path

The beam profile of the three-dimensional dark focus has been measured in detail in order to investigate the structure for the future use for atom trapping. To obtain parameters like the radius and the width of the intensity distribution a two-dimensional Gaussian distribution of the following form was fitted to the experimental data:

$$I(x, y) = I_0 \times e^{-0.5 \frac{\left( \sqrt{(x-x_0)^2 + (y-y_0)^2} - \gamma(z) \right)^2}{\sigma^2}} + C, \quad (6.1)$$

where  $\gamma(z)$  gives the radius of the ring in each plane  $z$  structure and  $\sigma_r$  the radial width of the ring.  $I_0$  denotes the amplitude of the intensity and  $C$  a constant background.  $x_0$  and  $y_0$  are used to position the ring in the centre of the radial structure. The intensity distribution  $I(x, y)$  does not feature a dependency on an azimuthal angle in order to represent the radial symmetry of the numerical solution of the potential. Deviations of  $I(x, y)$  to the experimental values are discussed later and used to determine the radial symmetry of the potential.

The experimental data presents the intensity distribution of the three-dimensional dark focus in the focal plane and azimuthal asymmetries are clearly visible (Fig. 6.2a). Fig. 6.2b depicts the obtained fit of Eq. (6.1) and shows the very good agreement with the experimental data. The ring radius as well as the width of the ring wall can be extracted without problem. For  $z$  positions near the focal plane, this fit gives easy access to experimental values. Near

the Raman spot, the width of the ring walls is larger than the ring radius and the obtained fitting parameters have to be handled with more care. Especially amplitude  $A$  and the constant background  $C$  have to be reconsidered.

---

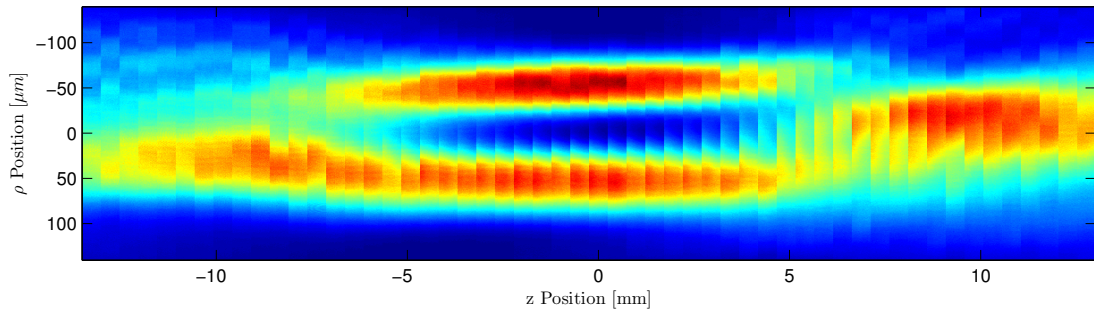
## Beam Profile

---

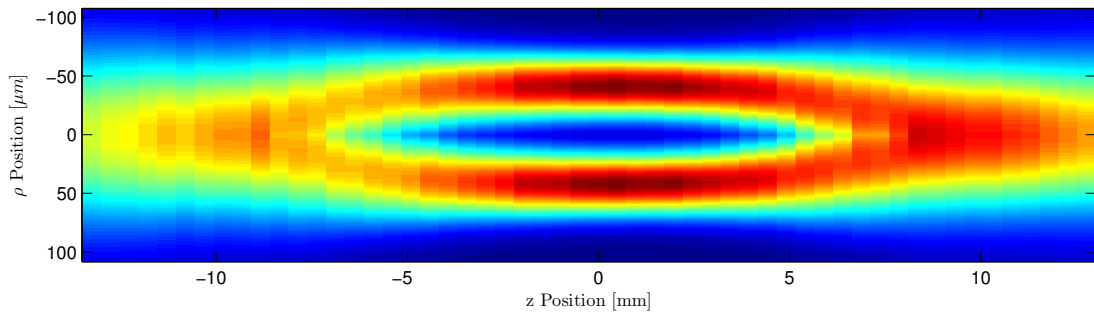
Fig. 6.3 shows the comparison of the experimentally obtained dark focus and the solution of Eq. (4.14) using experimental values determined in the focal plane. Fig. 6.3(a) compiles experimental images taken every 0.5 mm along the direction  $z$  around the focal plane. The composition was built by using a cut through the experimentally obtained image. The numerical solution of Eq. (4.14) was carried out for the values of  $w_0 = 42.7 \mu\text{m}$  and  $\rho_0 = 0.9$  and is shown in Fig. 6.3(c). The bottle beam shows a good agreement with the numerical solution of Eq. (4.14) but also features some important differences. In addition Fig. 6.3(b) shows Eq. (6.1) with the obtained fitting parameters during analysis.

As discussed in Sec. 4.4.2, the beam propagation along the  $z$ -direction shows a symmetric intensity distribution around the focal plane. The dark focus in the  $z$  direction is limited by the Raman spot and the focal plane was determined experimentally by choosing the middle points between the two Raman spots. The Raman spots themselves are calculated to be positioned at  $z_{\text{Raman}} = \pm 7.23 \text{ mm}$  (see Eq. (4.13)). The experimental position of the Raman spot is determined to be at  $z_{\text{Raman}} = \pm 7.7 \text{ mm}$ . The focussing lens and the crystal are positioned to the left of  $z = 0$  and the beam propagates in positive  $z$  direction. The overall agreement of the numerical calculations to the experimentally obtained intensity distributions is very good. Form and shape of the potential match. In addition the experimental results show an asymmetry along the radial direction. In the upper part of the experimental image shows a strong trend to higher distances from the initial axis of propagation and features an increased intensity. The position just before the Raman spot at  $z = 6 \text{ mm}$  shows a larger decrease in intensity as expected. Also the Raman spot to the left of the focal plane at  $z = -7.7 \text{ mm}$  features a smaller radial width by a factor of 1.7 in respect to the Raman spot after the focal plane at  $z = 7.7 \text{ mm}$ . A broadening of the structure in  $z$  direction indicates is not collimated perfectly.

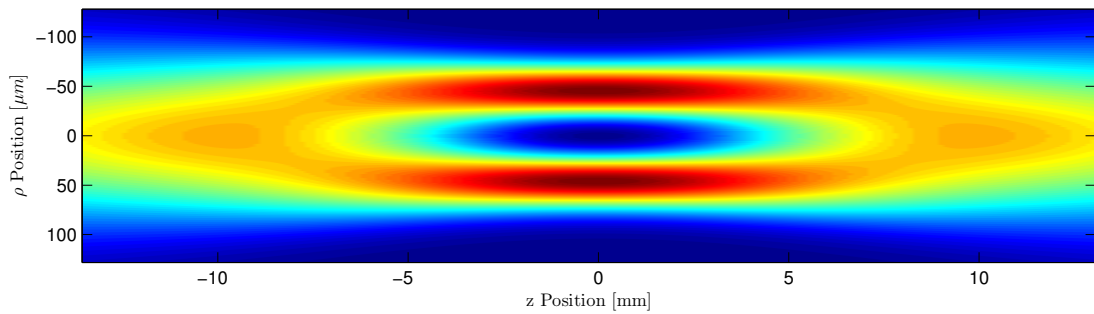
To characterize the azimuthal variation of the intensity distribution in each plane, the deviation of a perfect radially symmetric beam to the measured intensity distribution was calculated. Fig. 6.4 shows the relative deviation normalized to the mean intensity in each plane. The mean deviation along the full ring is 6.7% whereas the maximum mean deviation is 10%. The data shows a minimum deviation in the focal plane of 5.1%. The maximum deviation of the intensity in azimuthal along  $\gamma(z)$  is also shown plotted and the minimum intensity of the ring is 45% of the mean intensity. The obtained data shows that the radial symmetry is not perfect but the deviation should not hinder the



**(a)** Measured beam profile



**(b)** Fit of Eq. (6.1) to the measured intensity distribution



**(c)** Calculated beam profile

**Figure 6.3:** Comparison of the experimental and calculated intensity distribution of a three dimensional dark focus along the beam propagation axis  $z$ . (a) Each slice of the measured intensity distribution is a cut of  $10 \mu\text{m}$  through centre of the ring shaped intensity distribution. The position is given as  $\rho = \sqrt{x^2 + y^2}$ . Points of lower intensity show the variation of intensity in the azimuthal direction of the intensity distribution. (b) The solution of the fit of Eq. (6.1) to the intensity distribution of each plane. The asymmetry of the measured images with respect to the fit is clearly visible. (c) The numerical solution of Eq. (4.14) was made with parameters matching the experimental values:  $w_0 = 42 \mu\text{m}$  and  $\rho_0 = 0.9$ .

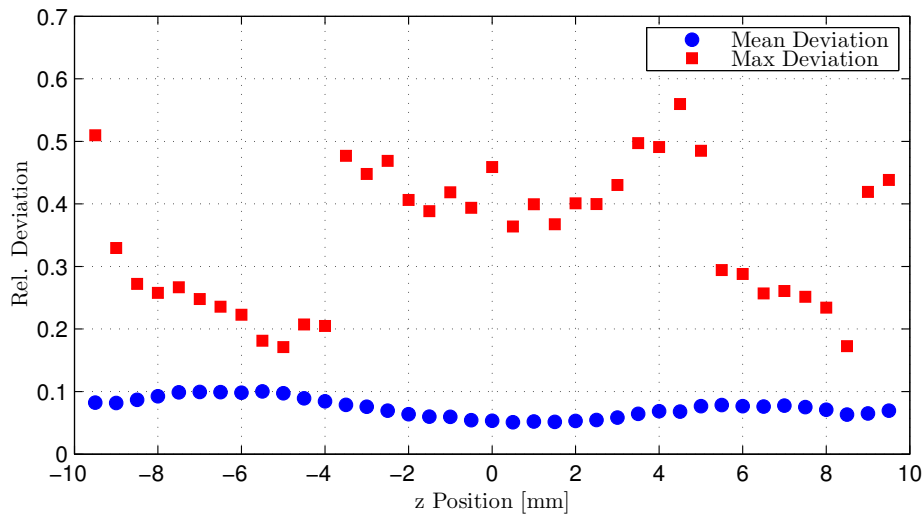


**Figure 6.4:** Relative deviation of the measured intensity distribution in each plane along the  $z$  direction from a perfectly radial symmetric intensity distribution of equal power. The mean deviation shows a minimum at the focal plane, where ultra-cold atoms and BECs will be trapped in experiments. Additionally, the intensity drops about 40 % in the azimuthal direction around the ring.

trapping of ultra-cold atoms. The obtained intensity distribution in the focal plane differs in a second setup used to measure the influences of spatial apertures in front of the focussing lens. This implies that the overall setup used to create conical refraction patterns is strongly prone to variations in the beam-shaping process and should be revised for future implementations. Sec. 6.2 shows that the implemented setup is able to trap atoms despite its inequalities and that a three-dimensional dark focus is a robust system that is also usable with non-perfect beam shapes.

---

### Radial size of the potential

---

As previously discussed, the radial size of the measured intensity distribution is not as homogeneous and symmetric as expected (see Fig. 6.3(a)). Therefore, the obtained radii of the fits of Eq. (6.1) have been investigated. Fig. 6.5 shows the obtained values of the radius for each image along the beam propagation axis. As before, the solid line represents the numerical solution of Eq. (4.14). The radius of the numerical solution was determined by taking the distance from the optical axis to the position of maximum intensity in radial direction. The measured radii show a very good agreement with the expected evolution but fall short of the maximum achievable radius. The maximum measured radius is  $40.4 \mu\text{m}$  and positioned at  $z = 0$ . The radii decrease symmetrically for increasing distance to  $z = 0$ , as expected. At the position of  $z = \pm 7.7 \text{ mm}$  the

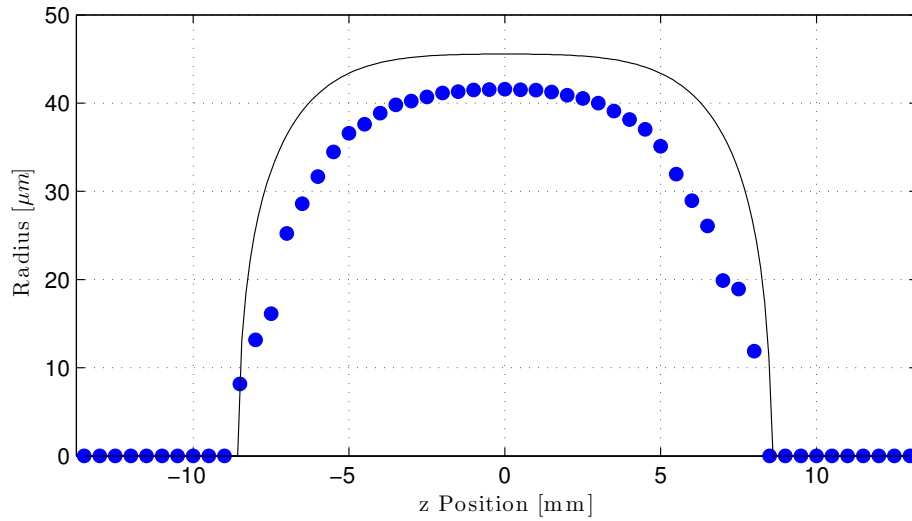


**Figure 6.5:** Radial dilatation of the three-dimensional dark focus depending on the position along the beam propagation. The solid line represents the distance of the position of maximum intensity from  $\rho = 0$  for each plane along the  $z$ .

measured radius of the ring is zero. This point lies behind the Raman spot and shows that the Raman spot still features a small intensity at  $\rho = 0$ . The measured radius in the focal plane is by  $4\mu\text{m}$  short of the calculated radius of the numerical solution. The reason for the difference between the calculated radius and the measured radius is unknown. The not perfectly collimated beam before the focussing lens could be the reason the measured intensity distribution diverges from the calculated one.

---

### Confining potentials in a three-dimensional dark focus

---

The main application of the three-dimensional dark focus is going to be the trapping of ultra-cold atoms and BECs. To build a trap, a tight confinement in both, the radial as well as the longitudinal direction is important. As discussed in Sec. 2.1, the trap depth is directly dependent on the detuning of the incident light as well as the intensity. The dark focus is created with blue-detuned light, therefore in a repulsive geometry. This potential stores atoms at locations of low intensity. In the case of the three-dimensional dark focus, atoms will be trapped around  $z = 0$  and  $\rho = 0$ .

To determine the trap depth in radial direction intensity difference between the lowest point of intensity and the highest points of intensity in the ring structure, i.e. the outer wall confining the potential, has to be determined. This is done by measuring the intensity at  $\rho = 0$  and at  $\rho = \gamma(z)$  along the transversal direction  $z$  of the structure.

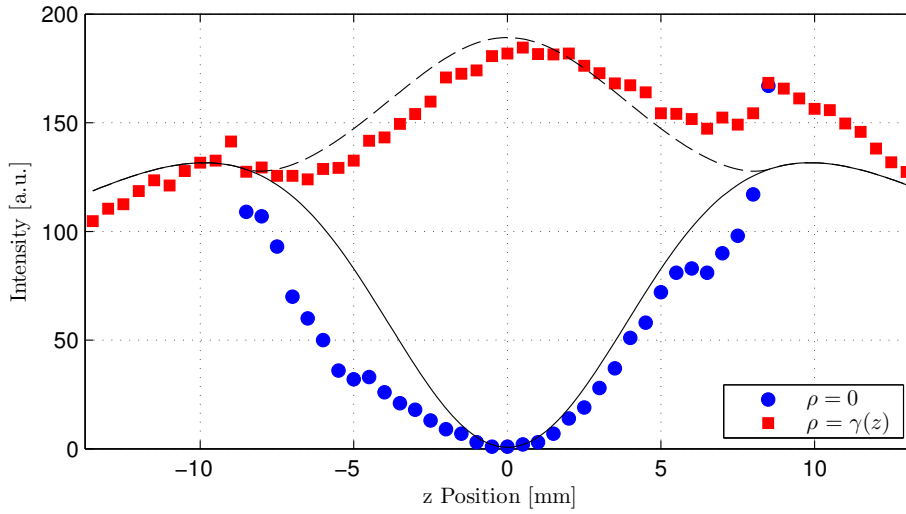


**Figure 6.6:** Axial structure of the intensity at the points of minimum ( $\rho = 0$ ) and maximum ( $\rho = \gamma(z)$ ) intensity. The solid line shows the numerical solution of Eq. (4.14) with at  $\rho = 0$  and the dashed line at  $\rho = \gamma(z)$ . The numerical solution has been rescaled to match the total optical power.

Fig. 6.6 shows the mean intensity measured in each plane of the observed intensity distribution, together with the intensity at  $\rho = 0$ . The underlying solid line shows the solution of Eq. (4.14) for  $\rho = 0$  and the dashed line shows the intensity at  $\rho = r$ . Both lines have been rescaled to match the optical power used by the experimental setup. The values of the solid and the dashed line meet at the Raman spot. The measured intensity shows the same behaviour as predicted by the numerical calculations and the previous discussed features of the experimental implementation are also visible. As the most important feature an intensity of zero can be observed in the focal plane showing that a dark state trap is possible. In addition the intensity distribution shows a minimum at  $z = 0$  for  $\rho = 0$  and a maximum for  $\rho = \gamma(z)$ . This shows that the maximum trap depth will be present in the focal plane. The intensity along  $z$  for  $\rho = 0$  rises until the Raman spot is met at  $z = \pm 7.7$  mm. Up until this point the intensity distribution of  $\rho = r$  follows the expected behaviour having a maximum around the focal plane. The previously discussed asymmetry of the potential is clearly visible in the experimental data as the maximum intensity is shifted to higher values of  $z$ .

The obtained trap depth is now calculated by the difference of the intensities in each plane and is plotted in Fig. 6.7. As discussed before the ring wall has a maximum in the focal plane and the intensity in the centre of the trap is zero. This yields a maximum trap depth in the focal plane and has been confirmed experimentally. The trap depth along the axial direction is lower and the difference length scales have to be taken into account. The trap size in the radial

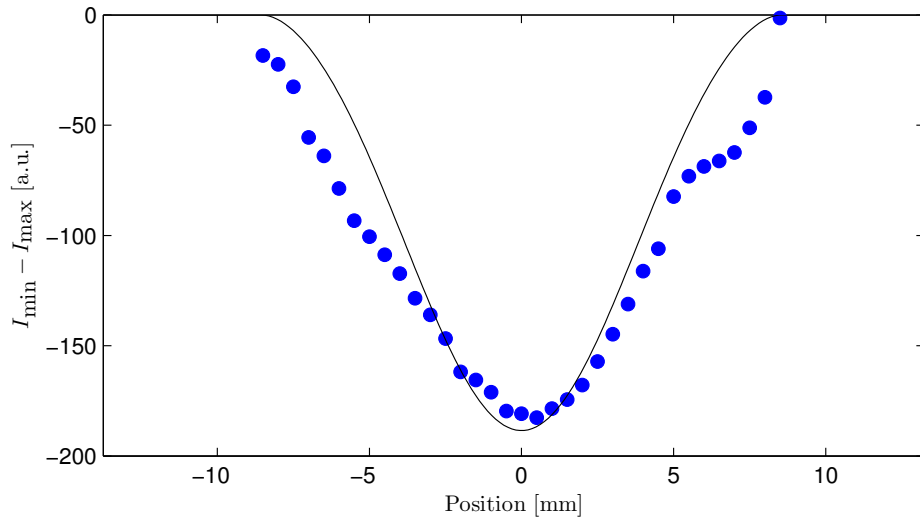


**Figure 6.7:** Intensity difference along the axial direction  $z$ . The difference of the maximum and the minimum intensity is shown. The maximum intensity was determined as the azimuthal averaged intensity of the radial intensity distribution at  $\rho = \gamma(z)$ . The minimum intensity is the intensity at  $\rho = 0$ . The solid line shows the difference of the intensity at  $\rho = 0$  and  $\rho = \gamma(z)$  calculated by Eq. (4.14). The data has been rescaled to match the total optical power.

direction yields a much smaller trap, with a diameter of  $\approx 80 \mu\text{m}$ , and therefore higher trapping frequencies for equal intensities. In the axial direction, the trap has a size of  $\approx 15 \text{ mm}$  which yields far lower trapping frequencies. These properties will be discussed in Sec. 6.2 where the three-dimensional dark focus is used to trap atoms.

---

### 6.1.3 Properties of the focal plane

---

As shown in the previous section, the focal plane define the position of maximum trap depth for dipole potentials and features an intensity minimum equal to zero. These properties give the focal plane ideal properties to serve as a trap for ultra-cold atoms. The previously discussed asymmetry of the azimuthal intensity distribution could reduce the quality of the trap as it could lower the overall trap depth and therefore increase losses.

Fig. 6.2 depicts the intensity distribution in the focal plane recorded with the CCD camera. In contrast to the theoretical predictions, the intensity distribution features a modulation of intensity along its azimuthal evolution. The reduction of intensity is in the order of 45% and therefore halves the achievable trapping depth. The image shows, that with a rotation of  $90^\circ$  the intensity changes between maximum and minimum values. This modulation is unlikely to originate from polarization problems as the polarization changes along the ring and

---

points with equal intensity have orthogonal polarization. It is likely, that the incident, non-perfectly collimated light features asymmetries which produce these patterns.

To further investigate on the quality of the obtained intensity distribution a second beam line was set up to investigate on effects of a mechanical aperture in front of the focussing lens. The overall setup was chosen to be identical to the one already described in Sec. 6.1.1. With the extra aperture placed in front of the focussing lens a second set of measurements was performed for comparison. The experimental images are presented in Fig. 6.8 depict the influence of the aperture. Fig. 6.8(a) shows the experimental image of the focal plane of a three-dimensional bottle beam without aperture. The beam features a radial intensity distribution with the same radial asymmetry already present in the previous implementation of the setup. The modulation is less pronounced indicating that the overall beam quality and collimation is better. Fig. 6.8(b) depicts the same intensity distribution with an additional optical aperture in front of the focussing lens. The aperture is used to increase the spatial coherence of the input beam and to transform it into an ideally round Gaussian beam that is then focussed through the conical refraction crystal. The focussed Gaussian beam shows a less pronounced azimuthal intensity modulation and is close to the numerical solution of Eq. (4.14) shown in Fig. 6.8(c). This indicates that non-circular symmetric beam shaped introduce intensity modulations along the ring structure that can be avoided by the use of an aperture. The aperture had a diameter of slightly less than 1 mm increasing the width of the focus  $w_0$ . The increased focus yields an increased ring wall width which is visible in the two different experimental implementations.

In order to further observe the influences of the aperture, linear polarized light was used. Fig. 6.8(d) shows the experimental image obtained without an aperture. The image features the typical moon-shape intensity distribution of a linear polarized conical refraction beam. Opposite of the maximum intensity is an intensity minimum visible that is more pronounced as expected. With the implementation of the same aperture used previously the unexpected intensity vanishes (see Fig. 6.8(e)). For comparison the numerical solution of Eq. (4.15) is shown in Fig. 6.8(f) which has a very good agreement to the overall shape and size of the obtained intensity distribution in the focal plane. As before, the radial width of the structure increases due to an increased  $w_0$ .

The observed values of the intensity distribution have been further investigated in Fig. 6.9. By applying the same algorithm described in Chapter 5 to calculate the radial intensity distribution, fluctuations can be studied in more detail.

Without an aperture, the intensity distribution along the ring drops by 35% in respect to the maximum value of intensity. By using an aperture the reduction in intensity can be reduced to 9%. The intensity modulations along the ring are greatly reduced. The mean relative deviation of the rings intensity modulation along the full ring structure is reduced from 11.8% to 2.6% showing a

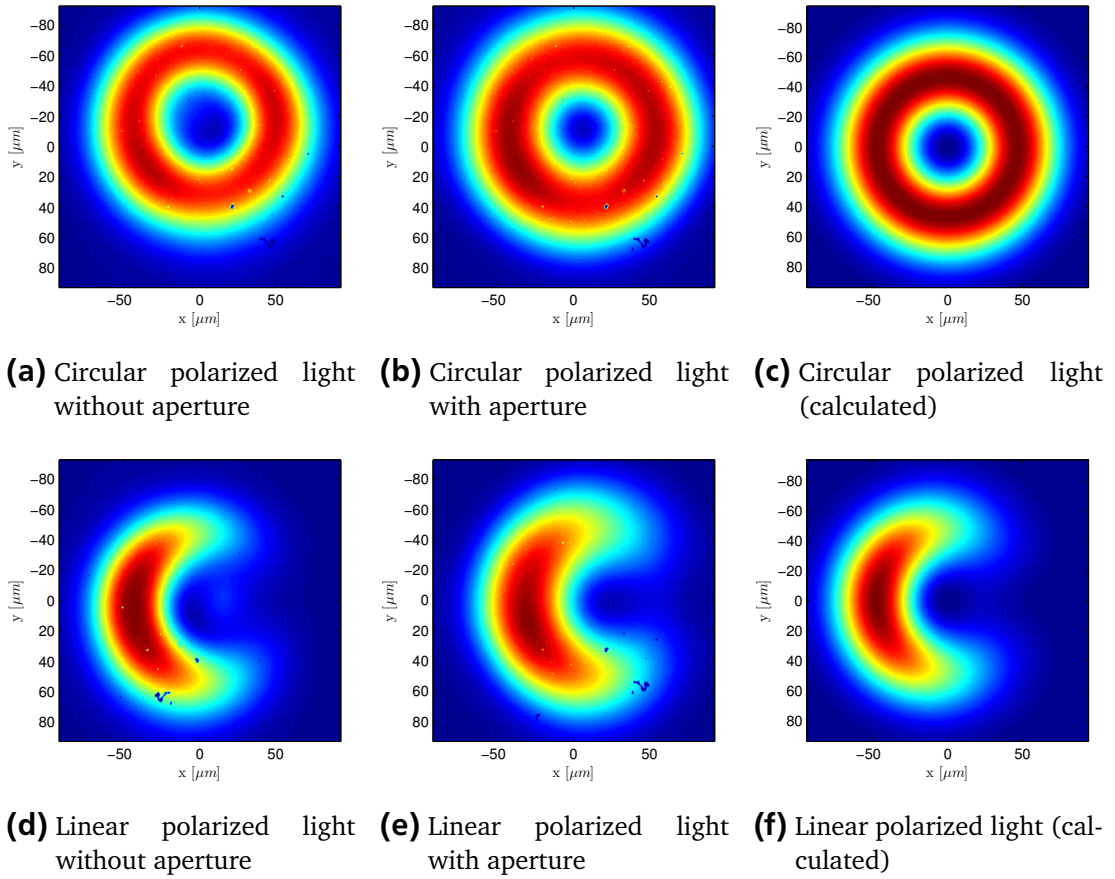


**Figure 6.8:** Intensity distribution of the focal plane of three-dimensional dark focus. Fig. (a) and Fig. (d) show experimental images without an aperture in front of the focussing lens. Fig. (b) and Fig. (e) show the same experimental properties with an additional aperture in front of the focussing lens. Fig. (c) and Fig. (f) show the numerical solution of Eq. (4.14) and Eq. (4.15) respectively for the values of  $\rho_0 = 0.92$  and  $w_0 = 42 \mu\text{m}$ .

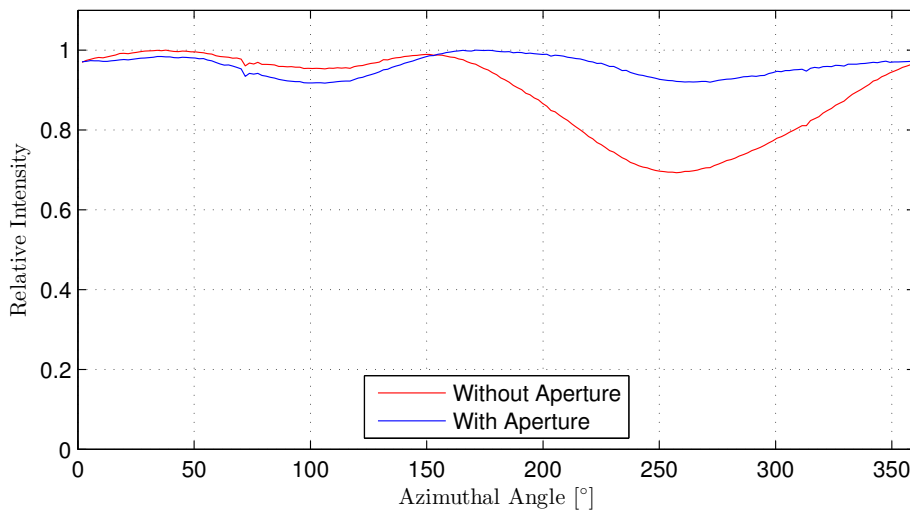


**Figure 6.9:** Intensity distribution in the focal plane of the three dimensional dark focus. The insertion of an aperture in front of the focussing lens yields a decreased intensity modulation of the ring structure.

significant improvement. This confirms that the implementation of an aperture to shape the input Gaussian beam is a useful addition of the creation of a three-dimensional dark focus. It could also yield an improved double ring structure if applied to the setup explained in Chapter 5. The differences in beam quality between the two setups also shows that a rebuilt of the main setup should be investigated in order to improve the symmetry of the intensity distribution.

---

## 6.2 Atom trapping in a three-dimensional dark focus

---

The experimental realization of a three-dimensional dark focus has been demonstrated in Sec. 6.1. This section shows that trapping atoms with a three-dimensional dark focus is possible and that it is valuable as a storage structure for ultra-cold atoms and BECs.

---

### 6.2.1 Experimental alignment

---

The experimental implementation of the dark focus beam is done in the same way as the previously described positioning of the Poggendorff dark ring (see Sec. 5.1). To be able to switch between both potentials fast, a second beam line was implemented. The light for the second beam line is branched off from the beam line of the Poggendorff dark ring right before its focussing lens in front of the crystal. After the creation of the beam, it is recombined with the beam path with a second mirror, before the non-polarizing beamsplitter. By removing these two mirrors, the first beam line for the Poggendorff dark ring can be used without additional alignment.

Fig. 6.10 shows the experimental setup of the three dimensional dark focus beam. The same laser system and intensity stabilization as described in Sec. 5.1 is used. Right after the combination of a  $\lambda/2$  and  $\lambda/4$  waveplates the used aperture and the focussing lens with  $f_1 = 150$  mm are placed. The beam passes through the conical refraction crystal and in the focal plane the expected intensity distribution of a single ring is observed. The focal plane is re-imaged by a combination of two achromatic lenses with  $f_2 = f_3 = 400$  mm. The re-imaged focal plane features the same intensity distribution and is not magnified or demagnified. As with the Poggendorff dark ring the three dimensional dark focus is aligned on top of the vertical absorption imaging beam of the ATOMICS experiment (see Sec. 2.3.3). This is done with a non-polarizing beamsplitter. The splitting of the non-polarizing beamsplitter varies between 50% for p-polarized light and 52% for s-polarized light. Since conical refraction potentials rely on equal intensity distribution for all linear polarization components of the incident light, the azimuthal intensity distribution along the ring was monitored after the beamsplitter. The polarisation was adjusted with the combination of  $\lambda/2$  and  $\lambda/4$  waveplates in front of the conical refraction crystal. The lenses  $f_4$  and  $f_5$  re-imaged the focal plane into the vacuum chamber at the place of the atoms. The creation of the three dimensional dark focus follows the implementation discussed in Sec. 6.1.1. The lens in front of the conical refraction crystal in combination with an aperture produces a focus of size  $w_0 = 42.7 \mu\text{m}$ . The Rayleigh range of the beam is 5.42 mm. The  $\text{KGd}(\text{WO}_4)_2$  conical refraction crystal has a length of  $l = 2.2$  mm which yields a ring radius of  $R_0 = 38.4 \mu\text{m}$  directly behind the crystal. The ratio between the radius  $R_0$  and the beam waist  $w_0$  is  $\rho_0 = 0.90$  which is near the desired ratio of 0.92. The ring is demagnified by the second pair of lenses  $f_4$  and  $f_5$  in front of the vacuum chamber by a factor of 0.75. This results in a ring radius at the place of the atoms of  $28.8 \mu\text{m}$ . The Rayleigh range for  $\lambda = 792.5$  nm is  $z_R = 3.28$  mm.

Since the conical refraction crystal has no anti-reflection coating, about 30% of the incident light is reflected backwards and lost for the creation of the dark focus. In addition, the non-polarizing beamsplitter that combines the dark focus light with the axis of the detection beam introduces additional 50% losses. The optical power remaining in front of the pair of lenses  $f_4$  and  $f_5$  is 29% of the initial optical power.

In contrast to the double ring potential the three dimensional dark focus features a confinement in the all three spatial dimensions, if used with blue-detuned light. Due to the large Rayleigh range, the Raman spot is positioned at  $z_{\text{Raman}} = \pm 3.41$  mm (see Eq. (4.13)) and the resulting confinement in the z-direction is too weak to hold atoms against gravity. Therefore the lightsheet potential already used with the Poggendorff dark ring is used to hold atoms against gravity (see Sec. 5.1.2). By reducing the Rayleigh range, the need for an additional potential could potentially vanish. A possible solution is to switch to another experimental vacuum chamber that features a shorter beam path

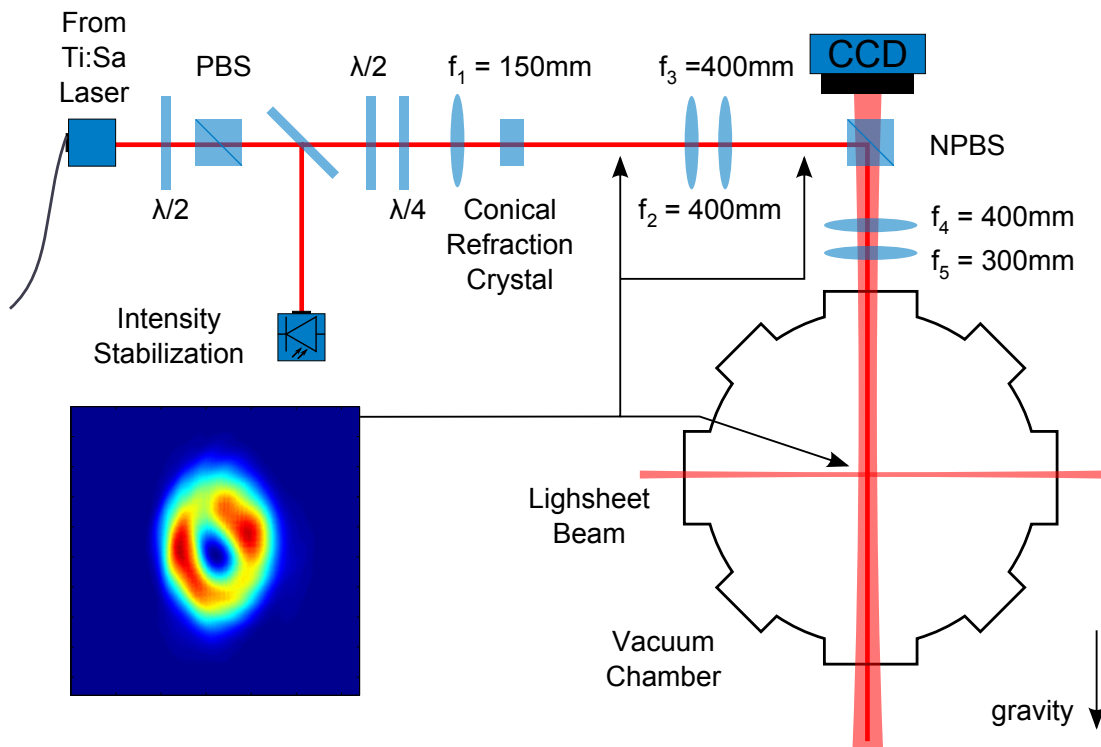


**Figure 6.10:** Experimental beam preparation for the three-dimensional dark focus. The collimated light beam is focused through the conical refraction crystal and is re-imaged twice into the experimental chamber. The second re-imaging process demagnifies the light field by a factor of 0.75.

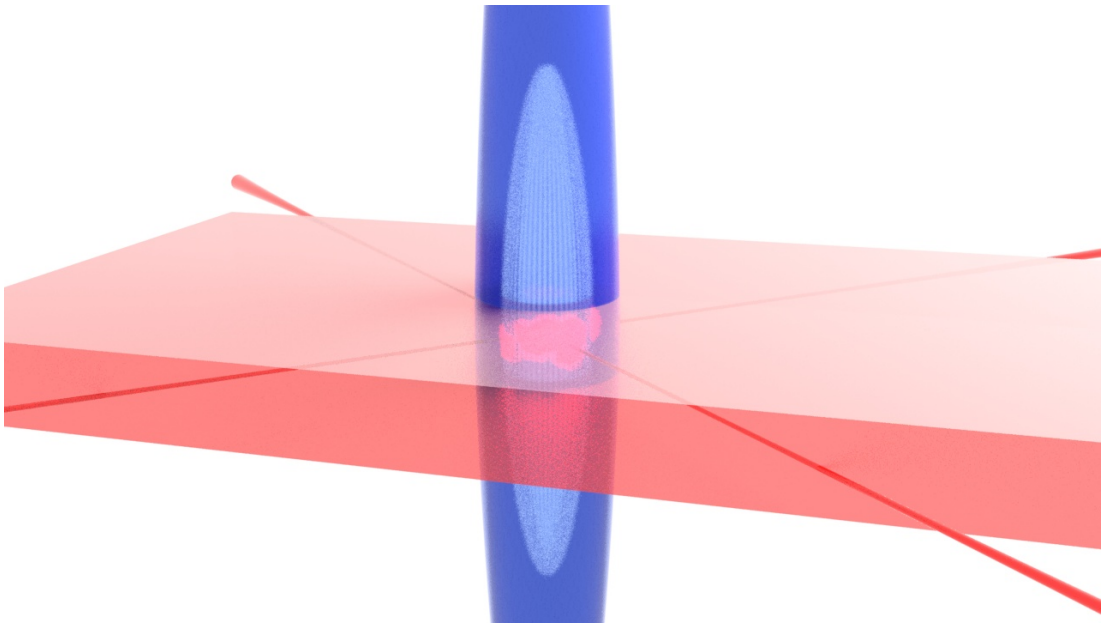


**Figure 6.11:** Combination of optical dipole traps to create a three-dimensional trapping potential. Due to the weak confinement of the dark focus trap in the  $z$ -direction an additional lightsheet potential is used to hold atoms against gravity. The dark focus is positioned on top of the crossed optical dipole trap and the BEC is loaded into the trapping geometry.

from the last optical element to the experimental plane in the vacuum chamber, allowing for an increased de-magnification. This would help with the creation of a tight confinement along the propagation axis  $z$ .

Fig. 6.11 shows a three-dimensional representation of the trapping geometry. The crossed optical dipole trap is aligned in the focal plane of the three dimensional dark focus. The three-dimensional dark focus is aligned along the  $z$ -axis to provide a ring shaped potential barrier in the  $xy$ -direction. The  $z$ -direction is supported by the lightsheet potential.

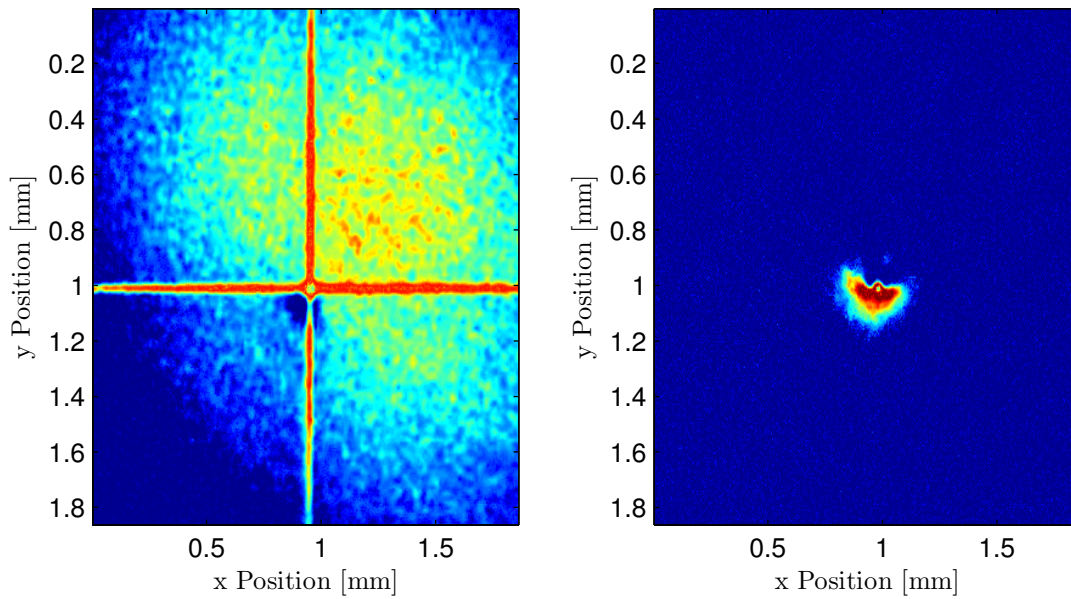
---

## 6.2.2 Vertical alignment and trapping of ultra-cold atoms

---

The vertical alignment of the beam is done in two steps. First, the beam itself is positioned in the MOT without the use of the conical refraction crystal. Second, the conical refraction crystal is placed in the beam line between the focussing lens  $f_1$  and its focal point and the beam is re-positioned in the MOT.

For positioning the focussed Gaussian beam in the magneto-optical trap, several tools are available to accelerate the alignment process. Since the beam is positioned along the detection axis of the vertical imaging system, the two beams can be aligned on top of each other. This is done by reducing the power of the Ti:Sa laser system to an approximate value of the power of the detection



**(a)** Focused gaussian beam imaged into the MOT in combination with the crossed optical dipole trap **(b)** Dark focus trap in a cloud of atoms released from the crossed optical dipole trap

**Figure 6.12:** Experimental images obtained during the alignment of the dark focus trap.

beam. By choosing two points before the non-polarizing beamsplitter a beam walk can be performed to overlay the beams at two spots. Due to the transfer optics  $f_2$  and  $f_3$  a large beam path is available which give the opportunity to fine tune the position nicely. The re-imaging lens systems of the three-dimensional dark focus also images the magneto-optical trap illuminated by the detection light in counter-propagating direction. Due to the low intensity of the detection beam the MOT produces a shadow that can be observed in the focal plane of the re-imaging and in the focal plane of the lenses  $f_4$  and  $f_5$  in front of the non-polarizing beamsplitter. This points can also be used to aid the initial positioning of the beam line.

After the beam has been aligned on top of the counter-propagating detection beam it should already be visible in the MOT. By imaging the MOT with the vertical detection system this can be observed. The intensity of the laser beam from the Ti:Sa laser should be as high as possible and the detuning to the  $D_1$  transition of  $^{87}\text{Rb}$  should be reduced to a minimum. This yields stronger interactions between the incident light and the atoms trapped in the MOT. A blue-detuned focussed beam produces a hole in the MOT whereas its red-detuned counterpart creates an area of increased density. Both should be circularly shaped.

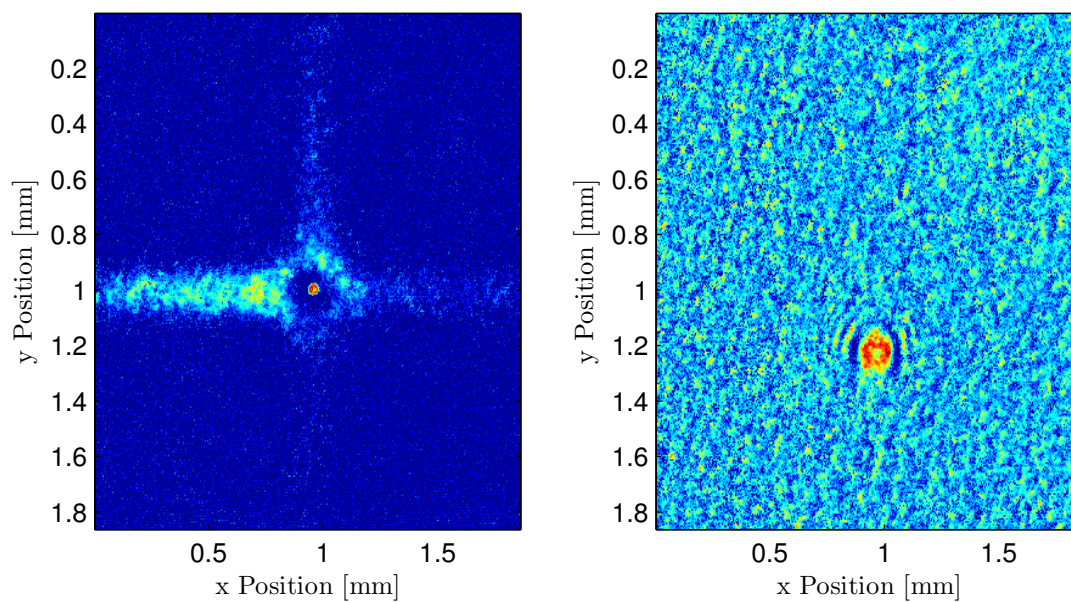
Fig. 6.12 shows images of the alignment process. The focussed gaussian beam is near the cross section of the crossed optical dipole trap in Fig. 6.12(a). The

---

blue detuned potential creates a hole in the density distribution along its propagation direction. To aid with the vertical positioning of the focal plane the diameter of the hole can be utilized. A minimum diameter should be achieved if the focal plane lies inside the magneto-optical trap. Since the MOT has a large diameter of more than 1 mm this method can only be used to give a good starting point for a following fine tuning. Also the side detection camera system can be used. Due to the small diameter of the focussed beam with respect to the diameter of the MOT the observable density modulation induced by the light field is barely visible. After the positioning of the focus is done, the conical refraction crystal can be adjusted in the beam path. This can be done with a CCD camera to directly image the focal plane after the conical refraction crystal. In order to optimize the beam path each re-imaged focal plane was observed with a CCD camera.

Fig. 6.12(b) the ongoing alignment process after the conical refraction crystal has been inserted in the beam path. After the position of the dark focus has been adjusted near the cross section of the crossed optical dipole trap, the alignment procedure was adapted. Instead of observing the interaction the incident light with the atoms from the MOT, atoms from the crossed optical dipole trap were used to image the influence of the dark focus. This was accomplished by aborting the evaporation procedure on purpose and by switching off the crossed optical dipole trap. An additional waiting time of 4 ms ensured that the expansion of the ultra-cold atom cloud was sufficient to cover the whole area of the dark focus focal plane. The alignment was done with blue-detuned light, and therefore repulsive interaction. The light is present during the complete process of loading the MOT and loading the crossed optical dipole trap. Fig. 6.12(b) shows that the angle with respect to the detection axis is critical for a good alignment of the dark focus trap. The dark focus beam hits the evolving cloud of thermal atoms and its repulsive interaction creates a hole in the otherwise circular density distribution. The expected circular shape is present. Due to the lower intensity of the intensity distribution in the centre of the ring shaped structure, atoms are expected to be occupying said region. Instead, because of the tilt with respect to the detection axis only a small fraction of atoms is visible as a circular distribution next to the centre of the crossed optical dipole trap. The angle between the dark focus beam path and the detection beam path can be reduced by the combination of mirrors used to align the two beams on top of each other. By carefully beam walking the dark focus beam, the small cloud of atoms in the centre of the ring structure can be maximized. Fig. 6.13(a) shows a perfect alignment of the two beam lines on top of each other. The dark focus is directly aligned on top of the crossed optical dipole trap. After the release of the atoms from the crossed optical dipole trap the atoms are held in place by the repulsive ring of the dark focus.

For higher waiting times the atoms start to fall due to gravity. As already mentioned the trapping force of the dark focus trap against gravity is not sufficient



- (a)** Perfectly aligned dark focus inside the crossed optical dipole trap. The atoms are released from the potential and the central part of the atoms is confined in the dark focus.
- (b)** Atoms falling in the direction of gravity and being scattered by the repulsive interaction with the Raman spot.

**Figure 6.13:** Experimental images obtained during the fine tuning of the horizontal position of the dark focus traps. Atoms are loaded directly from the crossed optical dipole trap without additional evaporation.

---

to support the atoms completely. As they begin to accelerate towards the bottom of the trapping potential they pass the Raman spot and encounter a barrier along the direction of gravity. The barrier yields a conical splitting of the atom cloud and a ring shaped density distribution appears. Fig. 6.13(b) shows the obtained density distribution for a total fall time of 30 ms.

---

### 6.2.3 Loading of BECs into the dark focus potential

---

To support atoms against gravity the lightsheet potential introduced in Sec. 5.1.2 with identical parameters is used. To create a tight radial confinement the wavelength of the Ti:Sa laser is set to  $\lambda = 793.8 \text{ nm}$  and the power to 9.7 mW at the place of the atoms. The resulting trap depth in the radial direction is given by Eq. (4.25):  $U = 25 E_R$ .

To load the potential with ultra-cold atoms, the same loading scheme previously demonstrated with the Poggendorff dark ring is used (see Sec. 5.3). For a linear ramping time exceeding 12.7 ms, the calculated adiabaticity criterion as discussed in Sec. 5.3.2 is fulfilled. An applied ramping time of 40 ms gives additional margin and should yield an adiabatically loaded ensemble of atoms. The experimental result of the loading scheme is depicted in Fig. 6.14. The image shows a confined ensemble of ultra-cold atoms of  $^{87}\text{Rb}$  loaded from the crossed optical dipole trap. The maximum loading efficiency achieved is  $95 \pm 2\%$ . Atoms lost during the loading procedure are visible for a period of up to 10 ms in the region of the trapping potential. Due to the lack of spatial confinement in the lightsheet potential they disperse quickly and are no longer detectable. The remaining atoms are stored in the potential and their lifetime will be discussed in the following section.

---

### 6.2.4 Lifetime of atoms in the dark focus trap

---

The applicability of the dark focus trap depends on the achievable trapping durations. These are highly dependent on the scattering of photons [166, 167] as well as on the density of the trapped gas [168]. Spontaneous scattering of photons is described by Eq. (2.1) and is controllable in the experiment by either using a large detuning with respect to resonant transitions of the trapped atoms or by lowering the optical power. Blue-detuned traps feature the advantage that atoms are stored in the region of low intensity which should increase coherence as well as storage times. In the current implementation of the dark focus trap, an additional red-detuned light field is used, the lightsheet, adds to the losses of the conical refraction based optical potential. As discussed before the scattering rate of atoms in the lightsheet potential is  $\approx 2.4 \text{ s}^{-1}$ .

The experimental procedure was as follows: after the creation of a BEC in the crossed optical dipole trap the atoms are loaded into the combination of dark

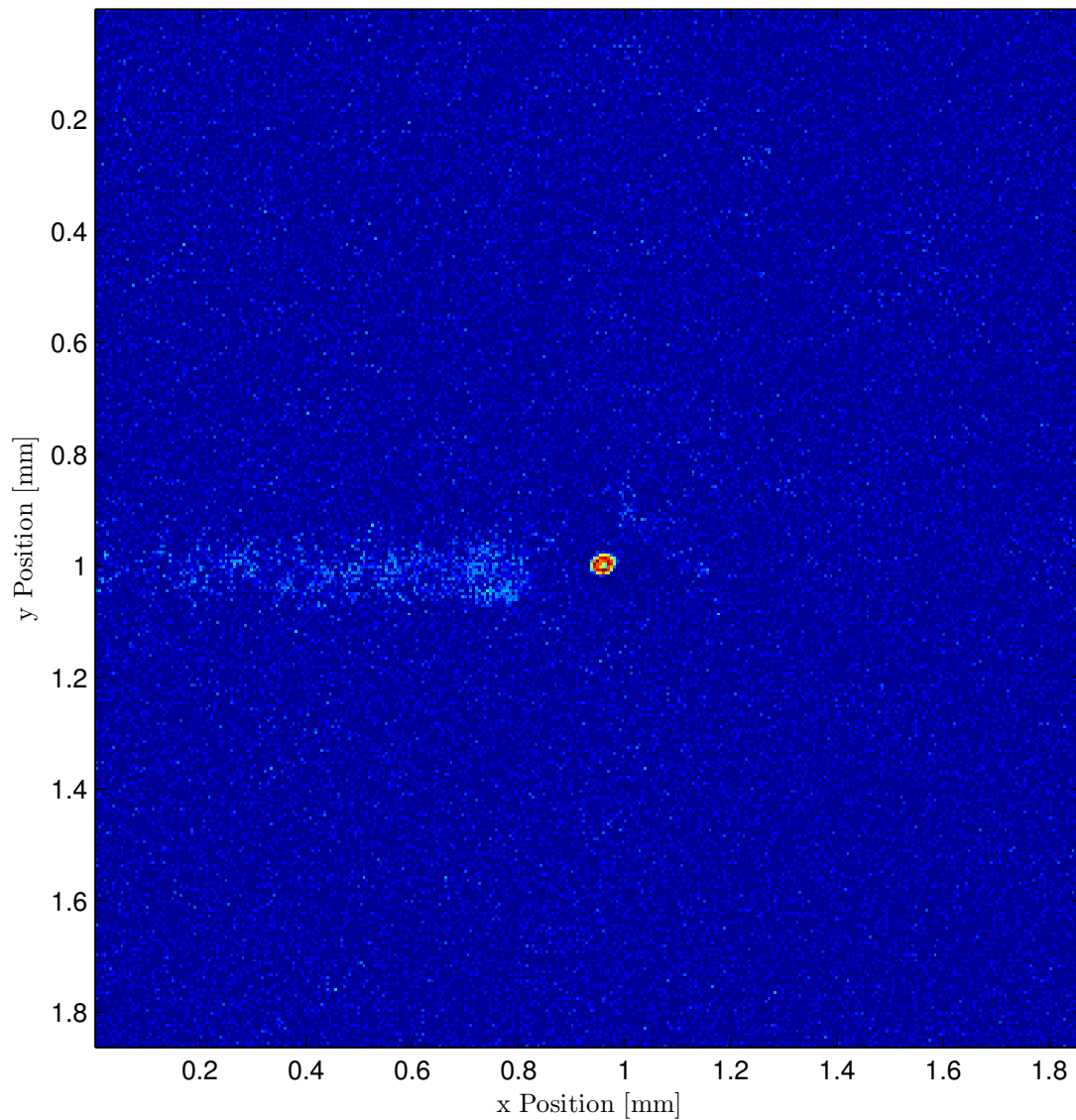


**Figure 6.14:** Trapped BEC in the dark focus trap 18 ms after the atoms have been loaded into the trapping geometry. A red-detuned light-sheet potential is used in addition to support atoms against gravity. The radial confinement traps the atoms efficiently in a three-dimensional potential.

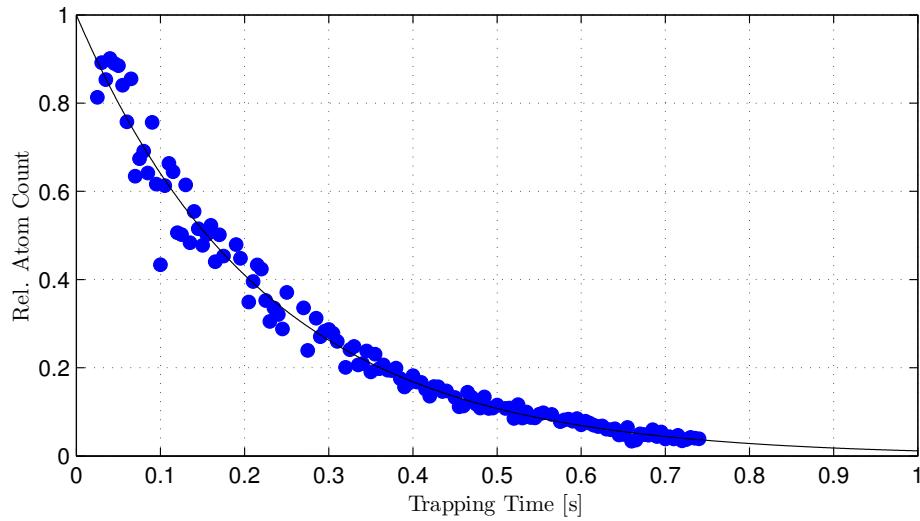


**Figure 6.15:** Relative atom count for variable trapping times in the dark focus trap. In addition to the dark focus trap an additional lightsheet potential is used to support atoms against gravity. The solid line depicts the fit of a combination of two exponential functions. The loss coefficient is  $\alpha = (4.4 \pm 0.3) \text{ s}^{-1}$

focus trap an lightsheet potential. The loading procedure consists of the lowering of optical power of the crossed optical dipole trap legs and the simultaneous increase of optical power for both, the dark focus and the lightsheet potentials. After the crossed optical dipole trap has been shut off completely an additional waiting time is applied. After the waiting time the atom count is determined by integrating the density distribution over the trapping region of trap.

Fig. 6.15 shows the experimentally obtained atom number in the combination of dark focus trap and lightsheet as a function of the trapping time. The trapping time is defined as the time after the crossed optical dipole trap has been shut off. The atom number is derived by summing up the density of each of the experimentally obtained density distribution. About 95% of the atoms leave the potential until 0.65 s. The lifetime of the atoms, defined as the time after which the initial atom number dropped to  $1/e$  times its initial value, is 227 ms. The underlying solid line shows a fitted exponential curve. Its decay coefficient is  $\alpha = (4.4 \pm 0.6) \text{ s}^{-1}$ . The uncertainty of the fitted parameter originates from the large spreading of the experimental data in the first 300 ms. Higher order losses due to many-body collisions are not incorporated in the fit. The observed temporal evolution of the atom number in the combined trapping geometry shows that trapping in a dark state focus is possible. On the one hand the lightsheet potential provides support for the atoms to achieve a long storage times. On the other hand the lightsheet seems to also be one of the main limiting factors of the lifetime, due to its large loss rate of  $2.4 \text{ s}^{-1}$ .

---

## 6.2.5 Trapping frequencies of the dark focus potential

---

To measure the radial trapping frequency of the dark focus confinement, a BEC was loaded into the trapping geometry of dark focus ring and lightsheet and was collectively accelerated with a double Bragg pulse. The lattice pulse was chosen to be a  $\pi/2$ -pulse so that all atoms are in motion. The Ti:Sa laser was set to an optical power of 24 mW which results in a calculated trap depth of  $31 E_R$  (including the losses of the non-polarizing beamsplitter). Because of the radial asymmetry of the confining ring potential, a trap depth well above the needed depth of  $4 E_R$  was chosen to guarantee that all atoms are trapped even after they are set in motion with a double Bragg lattice pulse of the order  $n = 1$ . The accelerated atoms were trapped inside three-dimensional geometry for variable times  $t_{\text{trap}}$ . After the applied trapping time the atoms are released from the potential, by switching off the dark focus light, and left for free expansion for an additional 18 ms

Due to the acceleration experienced by the double Bragg pulse the atomic ensemble oscillates in the confining potential. Because the atoms were accelerated orthogonally with respect to gravity the resulting oscillation frequency is given by the radial confinement of the trap. During the trapping time in the potential the atoms oscillate, transferring kinetic energy and potential energy depending on the position in the trap. The oscillation eigenfrequency of the confining potential: the radial trapping frequency  $\omega_R$ . Because double Bragg pulses are used to accelerate the atoms, two clouds are oscillating in opposite directions and are oscillating with a phase difference of  $180^\circ$ .

Fig. 6.16 shows the measured mean momentum of an atomic ensemble after the previously introduced procedure. For simplicity only the position of the atomic ensemble to the left of the position of the trap is considered. Depending on the trapping time in the confining dark focus the position of the cloud changes. In conjunction with the time of free evolution the mean momentum of the cloud is calculated. Since only the side to the left is considered it should vary between 0 and  $2\hbar k$ . An oscillation of the momentum depending on the trapping time can be observed. The expected oscillation between the momentum states is not covered in total. Instead the atoms do not return to zero momentum after a full revolution. This can be attributed to the fitting routine used to determine the position of the clouds and does not hinder determining the oscillation frequency. The black solid line shows the fitted sinusoidal oscillation to the momentum oscillation and gives a frequency of  $\omega_\rho = 2\pi \times (283 \pm 16)$  Hz. The fit already takes into account that the shown frequency in the plot is twice the trapping frequency. The calculated trapping frequency using the experimental parameters give a trapping frequency of  $\omega_{\rho,\text{calc}} = 2\pi \times 311$  Hz (see Eq. (4.27)). The calculated trapping frequency already incorporates 50% losses introduced by the non-polarizing beamsplitter and assumes the same losses along the optical beam path as experienced before with the toroidal trapping potential of

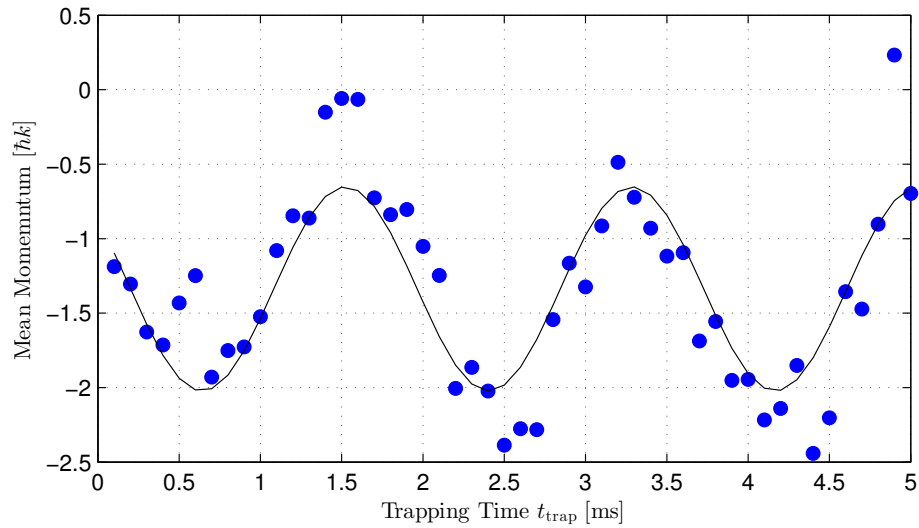


**Figure 6.16:** Mean momentum of an oscillating atom ensemble in the trap as a function of trapping time  $t_{\text{trap}}$ . The atomic ensemble is split into two packets with momenta of  $-2\hbar k$  and  $2\hbar k$  which oscillate in the trapping potential. After varying times the atomic ensemble is released from the trap and moves according to its kinetic energy. For simplicity only the left side of the trapping region is considered. The opposing side behaves equally.

20%. The calculated value is slightly above the expected value. These discrepancies are likely to originate from the radial asymmetry lowering the mean trapping frequency atoms experience as they oscillate in the  $xy$ -plane of the toroidal dark focus geometry. In addition the vertical positioning  $Z$  of the dark focus potential is critical for the calculation of the trapping frequency. Even though the shape between the two Raman spots is only varying slightly, the trapping frequency in the radial direction is decreasing for  $Z \neq 0$ .

---

### 6.3 Two dimensional array of dark-foci

---

The creation of a single dark focus for atom trapping in the previous section is a concept that can be applied to create a two-dimensional array of trapped atoms. The application of such a two-dimensional array of cold atoms has been investigated before [169–172]. Typically they are produced by two-dimensional arrays of micro-lenses generating focussed Gaussian beams with attractive potential. These potentials are prone to the differential ac Stark shift which has to be compensated manually [164]. Three-dimensional dark-trap implemented with conical refraction offers a new way to create these multi-site trapping potentials.

This section will give an introduction on two-dimensional trapping potentials and show important parameters for the applicability of a scalable register of

---

atom traps. The chosen register will be presented and its properties are characterized (Sec. 6.3.1). Next Sec. 6.3.2 demonstrates the implementation of a two-dimensional array of three-dimensional dark-foci and their properties. Differences to single focus implementations are reviewed and a possible experimental implementation to trap atoms is outlined.

---

### 6.3.1 Two-dimensional lens arrays

---

In order to create a two-dimensional array of dark foci, a system of identical Gaussian beams is needed. This system can be built with a two-dimensional lens array that features a discrete arrangement of lenses that each produces a near Gaussian focus. The two important properties of the lens array for the creation of an array of dark foci are the pitch  $d_{\text{pitch}}$  and the achievable beam waist  $w_0$  in the focal plane. The pitch describes the distance of two neighbouring lenses. The lenses used in this work feature a quadratic lens array, meaning that distances in the horizontal and in the vertical direction are identical. An in depth discussion on these types of lenses can be found in [173–179].

In order to create a dark focus trap with zero intensity in the focal plane for  $\rho = 0$  a ratio of  $\rho_0 = 0.92$  is needed. The present crystal for the generation of a dark focus has a length of 2.2 mm and creates a ring radius of  $R_0 = 38.4 \mu\text{m}$ . In order to create a perfect ratio  $\rho_0$  a waist of  $w_0 = 41.7 \mu\text{m}$  for each foci of the micro-lens array would be needed. In addition the pitch of the micro-lens has to be at least twice the size of  $w_0$ . Otherwise neighbouring traps would overlap and could potentially create additional substructures. The aim of the implementation was to avoid these unwanted structures.

Micro-lens arrays feature additional effects that need to be considered. The two main effects are the Talbot effect and the modification of the focal plane due to a low Fresnel Number. The Talbot effect describes the appearance of additional planes with focal spots near the focal plane. The parameters of these planes are related to the properties of the focal plane and can be modified likewise [153]. Typically, the Talbot planes show a modified waist  $w_0$  as well as a reduced pitch [180]. These properties may be utilized to further modify the implemented system. In addition, the micro-lens arrays typically used for the creation of two-dimensional arrays of traps feature a very low Fresnel Number. This introduces chromatic aberration which reduces the effective focal length and can yield a second spatially separated focus [181].

---

### 6.3.2 Experimental realisation of a two-dimensional array of dark foci

---

The experimental realisation of a two-dimensional array of dark foci is done by implementing the setup depicted in Fig. 6.17. A diode laser is used to illuminate a two dimensional array of micro-lenses and the focal plane of the lens array is

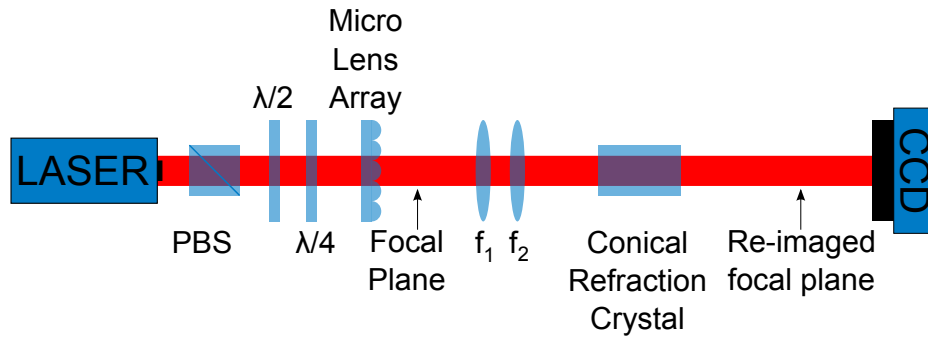


**Figure 6.17:** Measurement setup for a two-dimensional array of dark-foci. The polarization of the laser beam is purified by a polarizing beam-splitter and can be adjusted by a combination of a  $\lambda/2$  and  $\lambda/4$  waveplate. The focal plane of the microlens array is re-imaged by a combination of the lenses  $f_1$  and  $f_2$ . The conical refraction crystal is positioned between the lens  $f_2$  and the re-imaged focal plane in propagation direction. The resulting two dimensional array of dark foci is imaged by a CCD camera.

re-imaged onto a CCD camera.

The re-imaging process is not necessary in general but the limited space after the micro-lens mounting and the needed space for the conical refraction crystal give rise to this implementation. The advantage of the use of transfer optics is the possibility to tune the focal size as well as the pitch of the foci in the focal plane. Table 6.1 shows the compilation of transfer optics used. The values of  $f_1$  and  $f_2$  refer to the implemented setup depicted in Fig. 6.17. Before the conical refraction crystal was put into place the combination of lenses and their resulting focal plane was investigated. An experimental image of the focal plane of a two-dimensional array of foci is shown in Fig. 6.20. An array of Gaussian foci is present in the focal plane creating a set of red-detuned trapping potentials for ultra-cold atoms. The pitch of the foci was initially  $110\ \mu\text{m}$  and is magnified by the chosen telescope. A total of three different magnifications were implemented and will be discussed in the following section.

Fig. 6.18 shows a three-dimensional sketch of the implemented array of three-dimensional dark foci. An incident Gaussian beam is aligned on a micro-lens array that creates a two-dimensional array of focussed beams. The focussed beams are guided through a conical refraction crystal with the propagation direction is aligned along one of the optical axis of the crystal. The resulting intensity distribution in the focal plane is a two-dimensional register of dark foci.

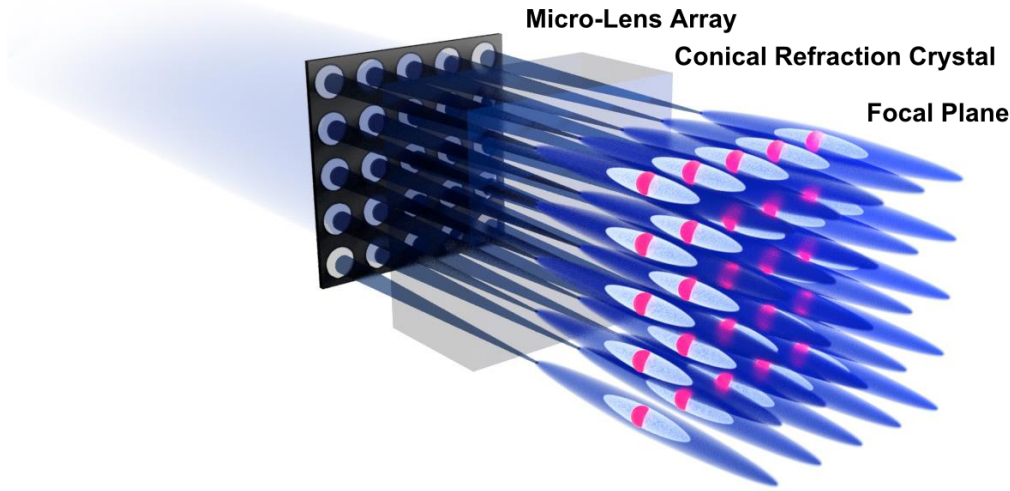


**Figure 6.18:** Three-dimensional representation of the implemented scheme. A micro-lens array creates a two-dimensional register of foci. The light is guided through a conical refraction crystal and an array of dark foci is created in the focal plane.

---

### Comparison of different magnifications

---

Since the obtained waist of the foci in the focal plane of the micro-lens array did not match the required criterion of  $\rho_0 = 0.92$  it had to be magnified. The magnification should be chosen to yield a perfect ratio of  $\rho_0$  but due to the special properties of micro-lens array foci the expected magnification could only be achieved approximately.

Fig. 6.19 shows the experimental measurement of the waists of various re-imaged micro-lens foci after magnification. The underlying solid lines represent fits of Gaussian distributions to determine the minimum waist  $w_0$  of the beam. The implemented magnification  $M = 1.25$  and  $M = 1.5$  yield values of  $w_0$  too small for the implementation of a three-dimensional dark focus. A magnification of  $M = 1.78$  gives a focus size of  $w_0 = 44.8 \mu\text{m}$ . The resulting pitch after magnification is  $d_{\text{pitch}} = 196 \mu\text{m}$ . Table 6.1 shows the compilation of three sets of lenses used to create the desired focal beam waist. The used magnification for future discussion is shown bold and features a ratio of  $\rho_0 = 0.86$ . The others two magnifications yields values way above  $\rho_0 = 1$  and are not of interest for the creation of a three-dimensional dark focus. Using too small magnifications yields structures discussed in Sec. 4.5.2, where the ring shaped intensity distribution features an additional intensity in its centre.

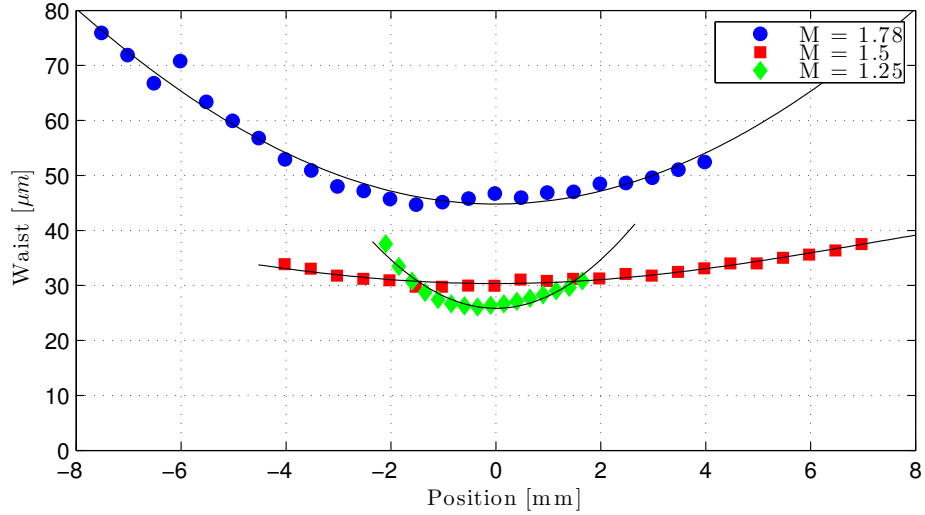


**Figure 6.19:** Measured radial waist  $w(z)$  for three different magnifications of the utilized micro-lens array. The experimental data has been obtained without the conical refraction crystal using a CCD camera.

Magnification M	Focal length [mm]		Waist [ $\mu\text{m}$ ]	$\rho_0$
	$f_1$	$f_2$	$w_0$	
<b>1.78</b>	<b>80</b>	<b>150</b>	<b><math>44.8 \pm 2.4</math></b>	<b>0.86</b>
1.5	100	150	$30.3 \pm 1.6$	1.27
1.25	80	100	$25.9 \pm 1.3$	1.48

**Table 6.1:** Compilation of experimental data obtained for the three different re-imaging lens systems. The bold line shows the lens combination used to realize a two-dimensional register of dark-foci.

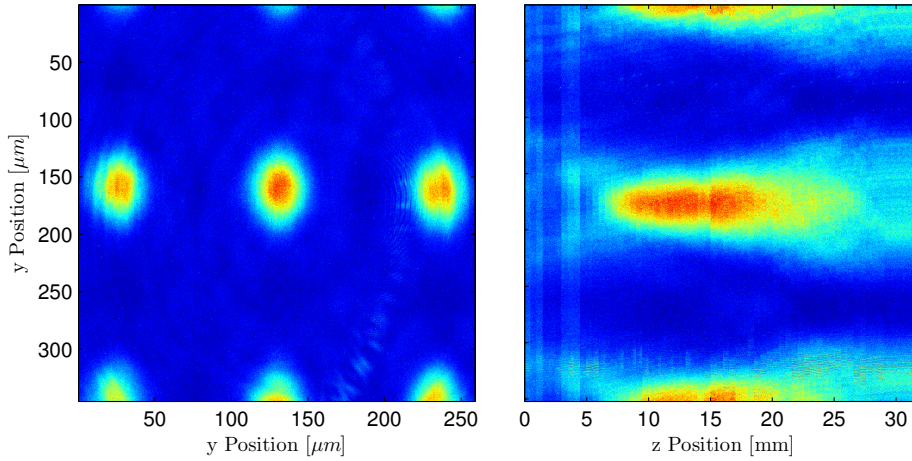


**Figure 6.20:** Experimental image of the foci produced by the micro-lens array and an additional transfer optic (left). Intensity distribution along the propagation axis of the focussed beam.

---

### Properties of the light field for the chosen magnification

---

The selected magnification of  $M = 1.78$  and the achieved waist of  $w_0 = 44.8 \mu\text{m}$  yields a Rayleigh range of  $z_R = 7.9 \text{ mm}$  at a wavelength of  $\lambda = 780 \text{ nm}$ . Fig. 6.20 shows the obtained intensity distribution in the focal plane (left) and along the beam propagation axis (right). Even though the magnification of the foci itself did not show the desired dependency as expected the magnification of the pitch has followed the predicted behaviour. The initial pitch of  $d_{\text{pitch}} = 110 \mu\text{m}$  has been increased to  $d_{\text{pitch}} = 196 \mu\text{m}$ . The waist of the focus in beam direction is  $19 \text{ mm}$  and therefore above the calculated Rayleigh range of  $2 \times z_R = 15.7 \text{ mm}$ . The obtained properties have been validated for the surrounding foci of the central spot.

---

### 6.3.3 Experimental implementation of a two-dimensional array of dark foci

---

The characterized optical system is used to create a two-dimensional array of dark foci. Due to the limited incident area of the conical refraction crystal some of the foci are not passing through the crystal but are blocked by the crystal mount. The alignment procedure of the beam path follows the alignment of a single trap. First, each of the foci creates a pair spots with high intensity obtained due to the birefringence of the crystal. Upon approaching the optical axis of the crystal with the beams propagation direction the circular shape begins to emerge. This process happens simultaneously for all foci in the focal plane of the re-imaged micro-lens array. The obtained intensity distribution is shown in Fig. 6.21. For each of the previously obtained foci in the focal

---

plane a ring structure emerges showing a total of  $10 \times 8$  full ring structures. The overall structure is convoluted by the Gaussian intensity distribution of the incident beam and the central part of the array features the highest overall intensity. The distribution of the rings is aligned in a way that the central ring shows the best possible symmetry along its azimuthal intensity distribution. As the distance to the central trap increases asymmetries begin to show up more strongly. This effect has been observed during the setup of the system multiple times and can be attributed to a slight divergence of the incident beam. If the alignment is optimized for the central dark focus and the beam is divergent, off-centre micro-lenses experience a tilt with respect to the optical axis of the conical refraction crystal. The tilt increases, the more the foci is distant to the optimized focus and introduces asymmetries in the focal intensity distribution. It is important to notice that the transfer optics used to magnify the focal plane of the micro-lens has shown to be prone to introduce these errors and has to be aligned very carefully. A discussion on the differences of central traps and off-centre traps will be given later (see Sec. 6.3.4).

The pitch of the ring shaped structure is  $d_{\text{pitch}} = 196 \pm 4 \mu\text{m}$ . It was measured by determining the centre of each ring structure and by calculating the distance to the nearest neighbour in vertical and horizontal direction. This has been done for a square of  $5 \times 5$  ring structures in the central region.

As discussed before, the polarization of the ring shaped structure is linear along the azimuthal directions of the ring and changes along the ring. To show that this behaviour is also valid for arrays of lenses a  $\lambda/2$  waveplate was used in order to create linear polarized light. By shifting the  $\lambda/2$  plate the gap in the intensity distribution can be moved around the ring. This process happens for all traps simultaneously and the hole is positioned under the same angle for each of the conical refraction rings.

---

### 6.3.4 Comparison of central traps and off-centre traps

---

In order to compare the performance of the trapping geometry in respect to the performance of a single dark focus trap, two ring structures of the focal plane were taken as a benchmark. Both ring structures were examined the same way the single trap was examined previously in Sec. 6.1.

The beam profile along the beam propagation axis is shown in Fig. 6.22. Fig. 6.23(a) shows the intensity distribution of the central ring trap and Fig. 6.23(b) shows the intensity distribution for an off centre trap. The trap chosen for the analysis was the third off-centre trap to the top of the central trap. The fit of Eq. (6.1) was used to determine the ring radius  $\gamma(z)$  as well as the length of the trapping potential by joining cuts of each image together. The focal plane in each of the plots was determined as the point of maximum ring diameter  $2\gamma(z)$ . The numerical solution for the initial values of  $w_0 = 44.8 \mu\text{m}$  and  $\rho_0 = 0.86$  are

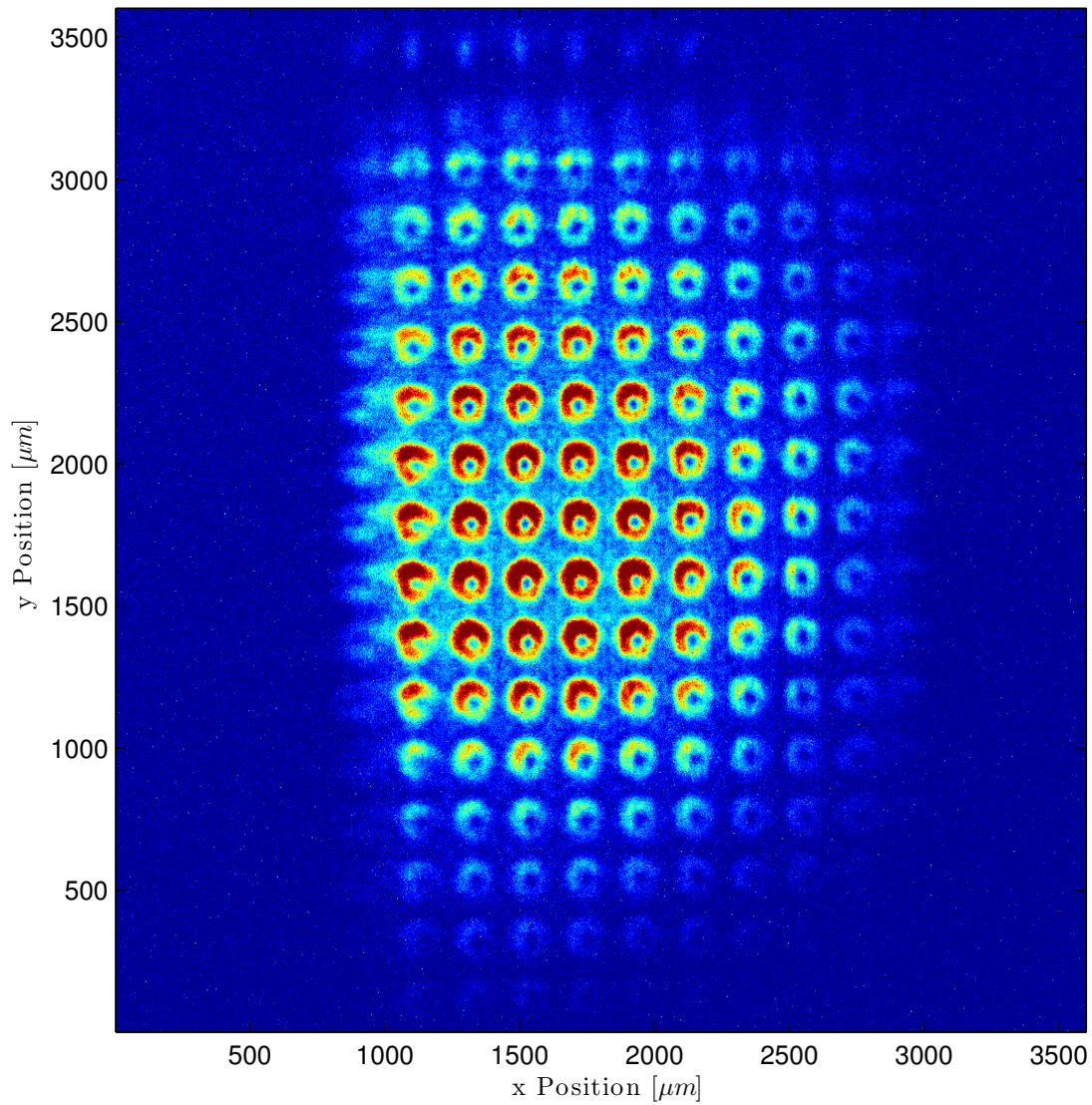


**Figure 6.21:** Experimental image of a two-dimensional array of three-dimensional dark traps. The light on the left side is blocked by the mount of the crystal.

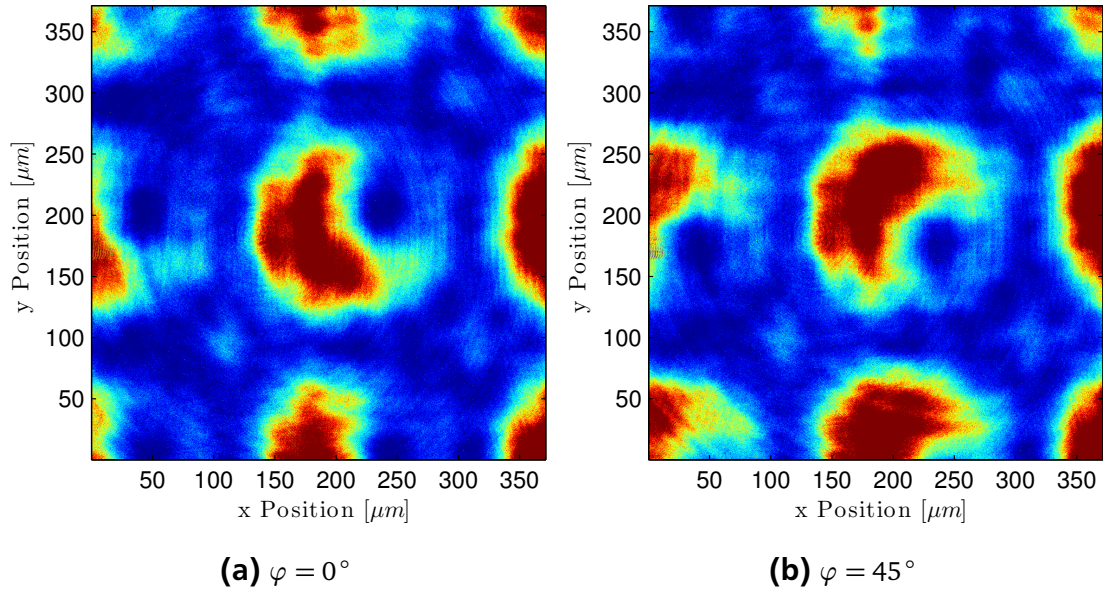
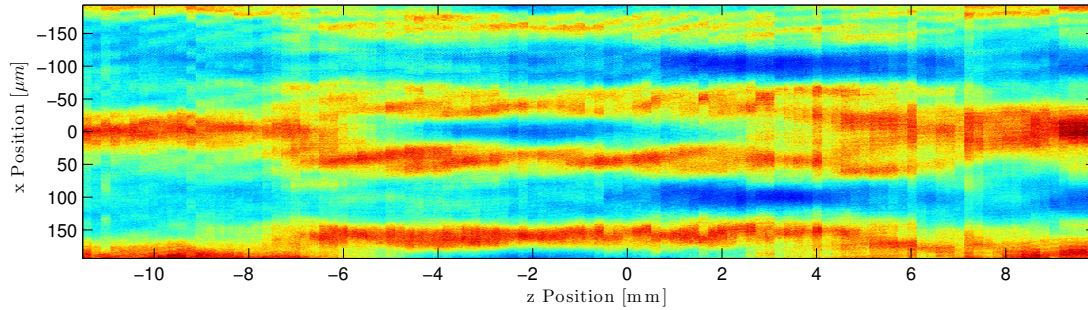


**Figure 6.22:** Experimental images of a two-dimensional array of dark focus traps with linear polarized light. The  $\lambda/2$  waveplate is rotated by  $\Delta\varphi = 45^\circ$  from Fig. (a) to Fig. (b) and the created gap in the azimuthal intensity distribution rotates accordingly.

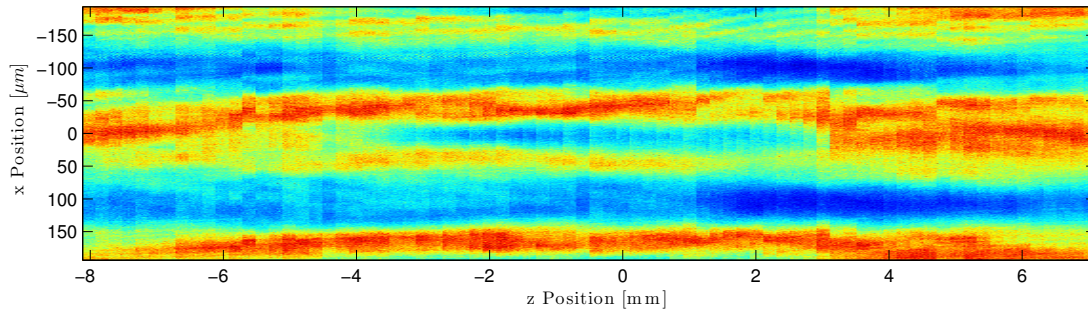
shown in Fig. 6.23(c). In contrast to the experimental values only a single trap is shown for the numerical solution.

The overall distribution of intensity around the focal plane is in agreement with the numerical calculations. The density distribution shows a radial symmetric structure near the focal plane that converges to a point where the potential is closed. The intensity along the azimuthal direction is nearly constant for the central trap. Since the alignment of the beam has been optimized for exactly this trap, it should indeed be the best trap. The off-centre trap features a completely different behaviour. Instead of a rotationally symmetric profile a clear loss of intensity at one side of the intensity distribution is observed. In the region between  $z = -2\text{ mm}$  and  $z = 1\text{ mm}$  the intensity is reduced significantly. The possibility to trap atoms would be completely lost since atoms could simply leave the ring potential without experiencing a trapping force in said direction. Also the length of the trap in beam direction is greatly reduced. To determine the spread of the potential in beam direction the ring radius  $r$  is used.

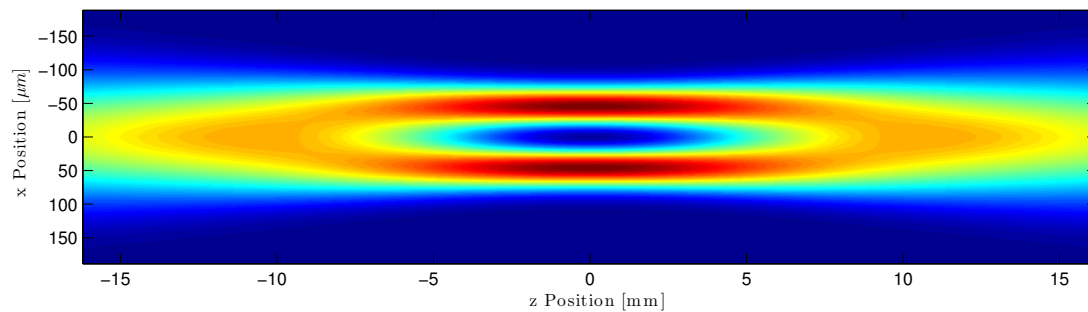
The ring radius  $\gamma(z)$  is shown in Fig. 6.24 and is obtained by fitting Eq. (6.1) to the intensity distribution of each plane. As the single focus beam, the radius of both, the central and the off-centre trap are below the expected radius of  $44.8\ \mu\text{m}$ . The maximum radius of the centre trap is  $43.5\ \mu\text{m}$  and the maximum radius of the off-centre trap is  $42.3\ \mu\text{m}$ . As already visible with Fig. 6.22 the length of the trap in  $z$  direction does not match the expected width of  $\approx 19\text{ mm}$ , which is twice the distance of the Raman spot (see Eq. (4.13)). The extent of



**(a)** Central trap



**(b)** Off centre trap



**(c)** Numerical solution of Eq. (4.14)

**Figure 6.23:** Comparison of two experimental beam profiles to the numerical solution of Eq. (4.14). Fig. (a) shows the central trap of the Gaussian intensity distribution along the axial direction. Fig. (b) shows a trap three pitches away to the top of the central trap and Fig. (c) shows the calculated beam profile. The values for the numerical solution were chosen to be  $w_0 = 44.8 \mu\text{m}$  and  $\rho_0 = 0.86$ .

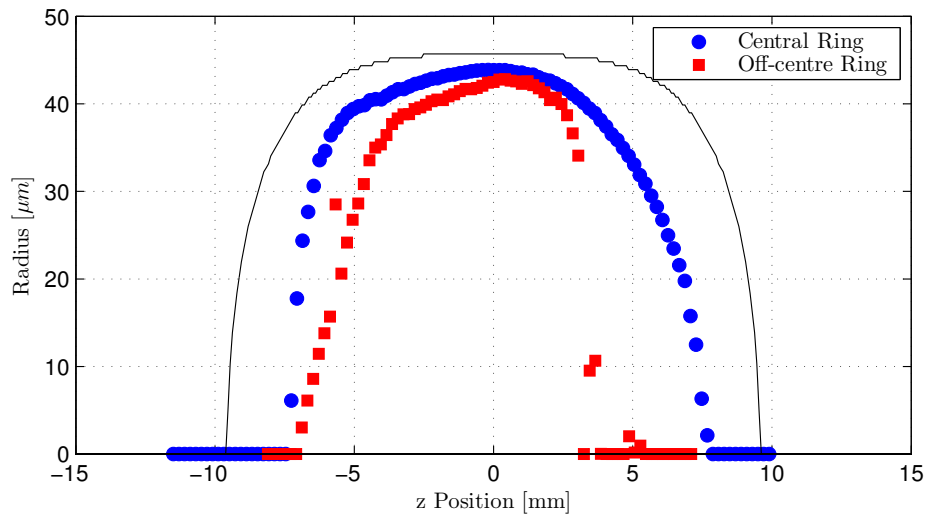


**Figure 6.24:** Radius of the trapping potential along the  $z$  direction. The radius is obtained by fitting Eq. (6.1) to each obtained experimental image. The solid line shows the numerical solution of Eq. (4.14). The radius is obtained by calculating the distance of the point of maximum intensity to the point  $\rho = 0$  for each plane.

the off-centre trap is short by 8 mm and the central trap by 4 mm.

In addition to the reduced length of the potential the symmetry of the trap has been reduced. Fig. 6.25 shows the deviation of the measured intensity distribution in respect to the numerical solution of Eq. (4.14). The central ring shaped intensity distribution shows a mean deviation of 16%. The mean deviation of the outer rings distribution gives 28%. Both distributions show higher intensity modulations than the single beam implementation of the three-dimensional dark focus. In addition to the reduced longitudinal length of the structure the difference is unexpected. Especially the position of the Raman spot has been shown to be robust. Maybe the influences of the non-Gaussian beam profile of a micro-lens focus is of more importance than expected.

---

### 6.3.5 Towards two-dimensional registers of atoms traps with conical refraction

---

The demonstration of the two-dimensional distribution of multiple dark focus traps has shown to be a new tool in atom optics. Instead of the expected behaviour unexpected problems occurred that could potentially hinder the usefulness of the presented system. Especially the huge dependence on the position of the ring in the focal plane on the trap quality creates the need to further improve the optical system. A possible solution for this problem could be the broadening of the Gaussian beam in front of the micro-lens array in order to minimize effects of wavefront curvature or divergence of the incident beam.

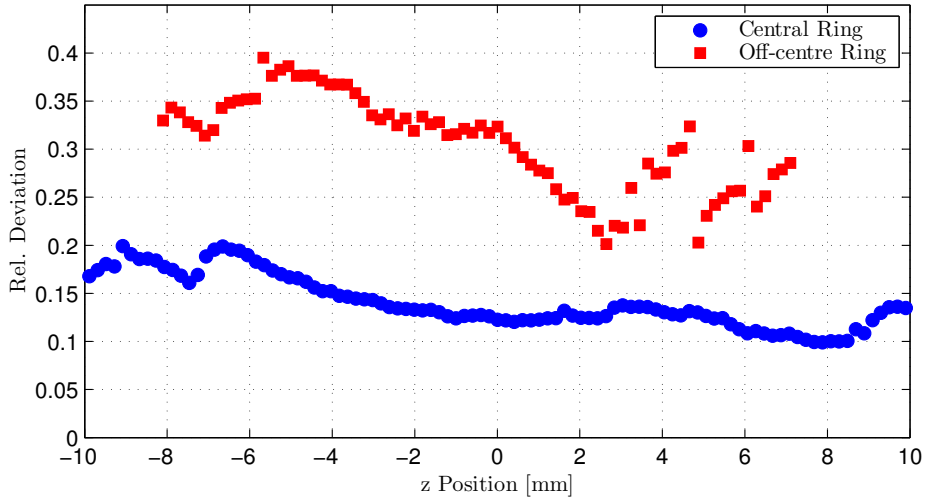


**Figure 6.25:** Mean deviation of the intensity distribution from a fully rotationally symmetric intensity distribution. In order to gain a symmetric intensity distribution with equivalent intensity Eq. (6.1) has been fitted to the measured intensity distribution.

For the future application of the two-dimensional array additional parameters have to be adjusted. Current implementations of quantum registers aim to utilize the Rydberg blockade in order to implement two gate operations [182]. To fulfil the experimental properties a smaller pitch as well as a smaller trapping ring radius  $R_0$  would be needed. Typical values for the distance of two traps would be  $d_{\text{pitch}} < 8 \mu\text{m}$  in order to experience Rydberg blockade [183]. The ring radius should be chosen appropriately in order to create still separated traps. In combination with an additional transfer optic an appropriate system to store ultra-cold atoms would be realizable nevertheless.

---

## 7 Summary and Outlook

This work has investigated novel optical potentials and the dynamics of ultra-cold atoms and Bose-Einstein condensates in these potentials. A Bose-Einstein condensate of 25000  $^{87}\text{Rb}$  atoms has been used to characterize these potentials and to study the first experimental realisation of double Bragg diffraction.

Optical lattices are widely used for Bragg diffraction in atom optic experiments and have shown to be a valuable tool. The first experimental implementation of double Bragg diffraction in this work expands these possibilities to novel applications. Double Bragg diffraction not only simplifies building matter wave beamsplitters, it is also a valuable tool for interferometric measurements. This work could also demonstrate second and third-order double Bragg diffraction and the implementation of highly efficient beamsplitters. In addition a Ramsey-type interferometer with first and second-order double Bragg diffraction for autocorrelation measurements of Bose-Einstein condensates has been demonstrated.

For future experiments, the optical setup of the double Bragg diffraction lattice should be expanded with an intensity stabilization. Day-to-day fluctuations and fluctuations between single pulses would be reduced and the stability of interferometric measurements will be increased. Such a system could be a valuable tool for Mach-Zehnder-type interferometers in combination with a toroidal wave guide.

The ongoing experimental improvements could be advanced with the use of a new vacuum chamber. Multiple experimental results have shown that the current setup limits the optical access as well as the resolution of the imaging system. Especially interferometric measurements and the detection of small spatial structures would greatly benefit from higher resolution imaging. The advanced planning of the new vacuum system could result in a fast transition between the two experimental vacuum setups.

Additional work should be targeted in the improvement of the current optical potentials. Especially the lightsheet potential is an important factor in the overall performance of the system. Because the lightsheet potential is used with the toroidal guiding potential as well as the dark focus trap, its performance determines the quality of the measurements in all experiments. Major improvements of the lightsheet system solved problems caused by diffraction and enabled the first ever observation of free expansion of an ultra-cold ensemble of  $^{87}\text{Rb}$  atoms in a toroidal waveguide created with conical refraction. The optical setup of a double-layer lightsheet based on conical refraction has already been demonstrated, the replacement of the current lightsheet setup

---

would facilitate additional trapping geometries. For example, a completely blue-detuned trap for ultra-cold atoms could be implemented, created by the blue-detuned dark focus and the blue-detuned double-layer lightsheet introduced in Sec. 4.5.1.

In addition Sec. 4.5.2 introduced a ring shaped trapping geometry with an additional intensity maximum in the centre of the ring. This geometry has never been investigated before and features unique characteristics with regard to its scalability. Competitive systems up until now need multiple light fields or complex combinations of magnetic trapping potentials to achieve similar shapes. The study of persistent current and the implementation of Josephson junctions or SQUID-like systems would be the obvious application for these geometries. The scalability and simplicity of conical refraction based systems makes it an interesting system for Atomtronics - the creation of circuit-like devices with atoms [154].

The experimental investigation of the toroidal ring guide and the dark focus trap should be continued further. The toroidal ring guide has shown to be a competitive implementation of a quasi one-dimensional trapping potential, that can trap, store and guide ultra-cold atoms and BECs. The limited lifetime can be surpassed by switching to different wavelength for both, the conical refraction based potential and the lightsheet potential. Increased lifetimes would then simplify the observations of atom optic experiments immensely due to the increased contrast of the absorption imaging process. The possibility to guide atoms with a momentum of up to  $6\hbar k$  in the toroidal trapping geometry has been shown in this work. In conjunction with the implementation of highly efficient beamsplitters for matter waves, a promising system for matter wave interferometry has been built. Experimental problems have been discussed and a way to further improve the system to implement a Mach-Zehnder-type interferometer has been presented. By rescaling the potential to smaller diameters faster process times for interferometer sequences are possible. The reduced process time also has positive impact on the atom number as well as the coherence of the wave packets. Since the experimental setup allows easy switching between multiple beam lines, different implementations of the waveguide can be studied side by side. A smaller geometry would also aid the ongoing studies of the dynamic loading process of the ring shaped guiding structure. After the first successful demonstration of the loading process, the outcoupling process should be studied in detail. Being able to load and unload wave packets on demand would produce an efficient storage structure for coherent matter waves. This structure could be expanded further to a velocity selective filter of neutral atoms via spatial adiabatic passage [184].

The first experimental realisation of a dark focus trap created with conical refraction should be followed by ongoing experimental characterization measurements. The dark focus potential opens a completely new set of trapping geometries, which are simple and scalable. Especially the experimental im-

---

provement of the beam shape should be the focus of ongoing investigations. Because additional setups have shown that a nearly perfect azimuthal homogeneous experimental implementation of a dark focus is possible, the existing optical setup should be redesigned. The blue-detuned dark focus could also be used as ring-shaped barrier to create disc-potentials, which are important for the studies of turbulences [137]. A red-detuned homogeneous ring potential on the other hand, would be perfectly usable for the investigation of persistent current experiments. On top of the applications for single dark focus potentials is the experimental realization of two-dimensional array of dark-foci. As measurements in this work have shown, micro-lens arrays in combination with conical refraction crystals create a scalable and simple system for quantum information processing. Trying to trap atoms in these potentials would allow to deepen the knowledge on how quantum information processing in these potentials could be achieved. In addition, the implementation of traps for quantum information processing could also be realized by trapping atoms with red-detuned light at the Raman spot of the dark focus. Its properties have not been investigated before, and could result in favourable trapping parameters compared to Gaussian foci. The multitude of possible applications shows, that conical refraction is a versatile tool that could drive forward research of ultra-cold atoms and their properties in many different ways.



---

# Appendix

---



# A Rb Data

## A.1 $^{87}\text{Rb}$ level scheme

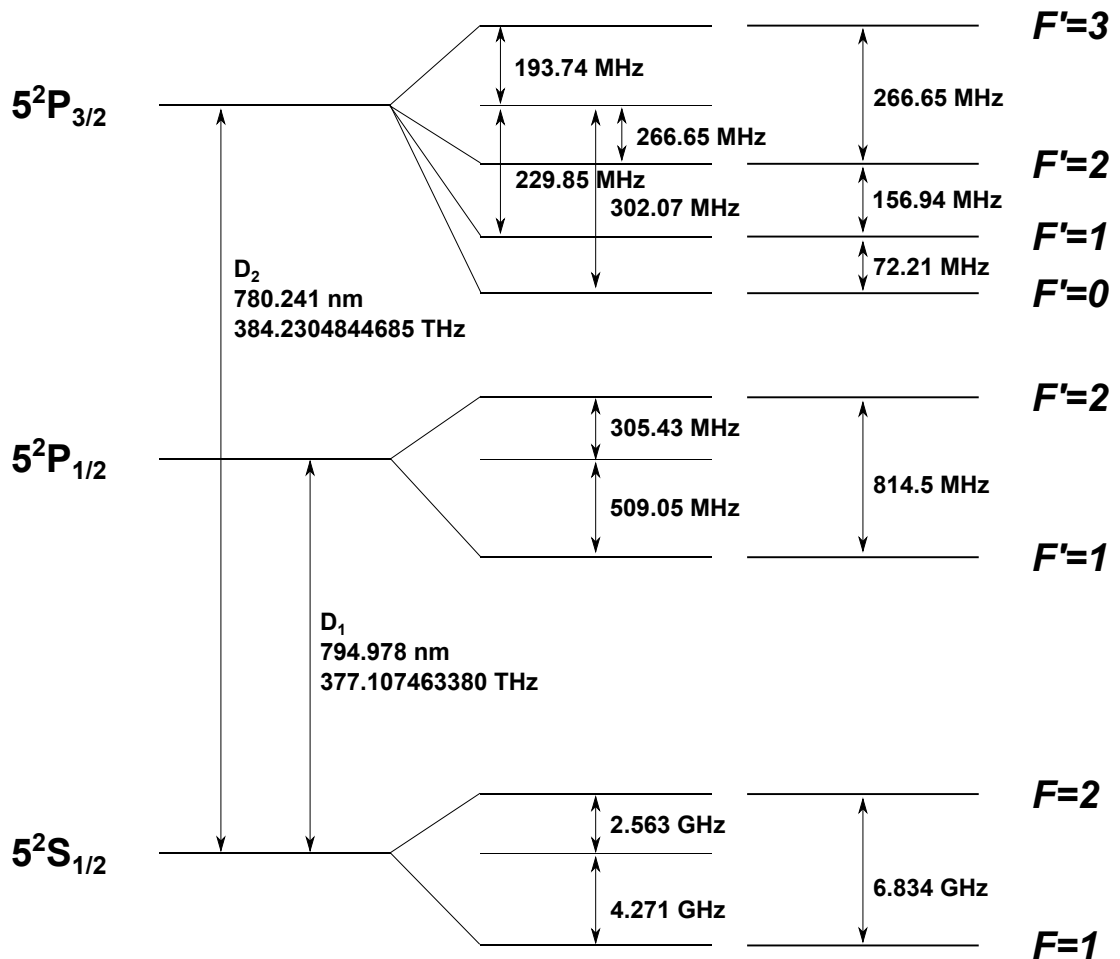


Figure A.1: Hyperfine structure of the  $D_1$  and  $D_2$  transition of  $^{87}\text{Rb}$  [52].

## A.2 <sup>87</sup>Rb properties

Name	Symbol	Value
Proton Count	Z	37
Nucleon Count	N + Z	87
Atomic Mass	m	$1.44160648(72) \times 10^{-25}$ kg
Rel. Natural Occurrence		27.83 %
Half-life	$t_{1/2}$	$4,88 \times 10^{10}$ years
Nuclear Spin	I	3/2
s-wave Scattering Length	a	$(110 \pm 4) a_B$ [185]
<i>D</i> <sub>1</sub> Transition		
Wavelength(vacuum)	$\lambda$	794.978851156(23) nm
Lifetime	$\tau$	27.679(27) ns
Natural Linewidth	$\Gamma_1$	$2\pi \times 5.7500(18)$ MHz
Recoil Frequency	$\omega_R$	$2\pi \times 3.6325$ kHz
Doppler Temperature	$T_D$	138 $\mu$ K
<i>D</i> <sub>2</sub> Transition		
Wavelength(vacuum)	$\lambda$	780.241209686(13) nm
Lifetime	$\tau$	26.2348(77) ns
Natural Linewidth	$\Gamma_1$	$2\pi \times 6.0666(18)$ MHz
Recoil Frequency	$\omega_R$	$2\pi \times 3.7710$ kHz
Doppler Temperature	$T_D$	146 $\mu$ K

**Table A.1:** Important parameters of <sup>87</sup>Rb. Data has been taken from [52]

## A.3 <sup>87</sup>Rb in optical lattices

Order	Frequency detuning (kHz)	Velocity (mm/s)
n	$\Delta\omega = n \times 4\omega_R$	$v = n \cdot 2v_R$
1	15.08	11.77
2	30.17	23.54
3	45.25	35.3
4	60.37	47.08
5	75.42	58.85
6	90.5	70.61

**Table A.2:** Compilation of values for Bragg and double Bragg diffraction of <sup>87</sup>Rb. The order n corresponds to Eq. (3.1).

---

---

## B ATOMICS Experiment

---

### B.1 Lightsheet properties

---

Wavelength	$\lambda_{LS}$	783.55 nm
Optical power		137 mW
Vertical waist	$w_z$	$(26.2 \pm 0.5)$ mW
Vertical Rayleigh range	$z_R$	$(2752 \pm 42)$ mW
Vertical trap depth	$U_{LS}/k_B$	1.24 $\mu$ K
Vertical trapping frequency	$\omega_z$	$2\pi \times (169 \pm 1.5)$ Hz
Horizontal waist	$w_y$	$(3643 \pm 30)$ mW
Scattering rate	$\Gamma_{SC,LS}$	$\approx 3s^{-1}$

**Table B.1:** Compilation of experimental values of the lightsheet potential used in Chpt. 5 and Chpt. 6. The values for the optical power and the vertical trapping frequency are typical values sufficient to hold atoms against gravity.

## B.2 Double ring potential properties

Name	Symbol	Value	
General properties			
Ratio $R_0/w_0$	$\rho_0$	14.3	
Focal plane			
Poggendorff Radius	$\rho_{\text{PDR}}$	290 $\mu\text{m}$	
Ring Waist	$w_0$	20.4 $\mu\text{m}$	
1st re-imaged plane			
Poggendorff Radius	$\rho_{\text{PDR}}$	232 $\mu\text{m}$	
Ring Waist	$w_0$	16.3 $\mu\text{m}$	
At the place of the atoms			
Poggendorff Radius (measured)	$\rho_{\text{PDR}}$	$(173 \pm 2) \mu\text{m}$	
Ring Waist	$w_0$	12.2 $\mu\text{m}$	
		Left	Right
Radial Trapping frequency	$\omega_R/2\pi$	$(325 \pm 5) \text{Hz}$	$(290 \pm 4) \text{Hz}$
Ratio Inner/Outer Ring		1:2.6	1:3.8

**Table B.2:** Experimental values of the double ring potential created by conical refraction used in Chapter 5

### B.3 Dark focus beam properties

Name	Symbol	Value
General properties		
Ratio $R_0/w_0$	$\rho_0$	0.90
Focal plane		
Ring Radius	$R_0$	$38.4 \mu\text{m}$
Gaussian Focus Without Aperture	$w_0$	$37.9 \mu\text{m}$
Gaussian Focus With Aperture	$w_0$	$42.7 \mu\text{m}$
At the place of the atoms		
Ring Waist With Aperture	$R_0$	$32 \mu\text{m}$
Radial Trapping frequency	$\omega_R$	$2\pi \times (283 \pm 16) \text{Hz}$

**Table B.3:** Experimental values of the dark focus potential created by conical refraction used in Chapter 6



# C Conical Refraction

## C.1 Overview on conical refraction crystals

Name	Formula	Indices of Refraction			Angle	source
		$n_1$	$n_2$	$n_3$		
$\alpha$ -HIO <sub>3</sub>	$\alpha$ -HIO <sub>3</sub>	1.8247	1.9424	1.9664	1.57°	[186]
BIBO	BiB <sub>3</sub> O <sub>6</sub>	1.7664	1.7947	1.9308	1.98°	[187]
BNN	Ba <sub>2</sub> NaNb <sub>5</sub> O <sub>15</sub>	2.1913	2.2866	2.2869	0.16°	[188]
CBO	CsB <sub>3</sub> O <sub>5</sub>	1.5241	1.5461	1.5798	1.01°	[189]
CTA	CsTiOAsO <sub>4</sub>	1.8642	1.8791	1.9387	0.90°	[190]
DLAP	C <sub>4</sub> H <sub>7</sub> D <sub>12</sub> N <sub>4</sub> PO <sub>7</sub>	1.5003	1.5647	1.5719	0.79°	[191]
KB5	KB <sub>5</sub> O <sub>8</sub> ·4H <sub>2</sub> O	1.4168	1.4303	1.482	1.05°	[192]
<b>KGW</b>	<b>KGd(WO<sub>4</sub>)<sub>2</sub></b>	<b>2.02</b>	<b>2.06</b>	<b>2.11</b>	<b>1.00°</b>	[122]
KTA	KTiOAsO <sub>4</sub>	1.7938	1.7997	1.8850	0.72°	[193]
KTP	KTiOPO <sub>4</sub>	1.7494	1.7577	1.8463	0.89°	[194]
KN	KNbO <sub>3</sub>	2.2909	2.2476	2.1425	1.72°	[195]
LBO	LiBO <sub>5</sub>	1.5699	1.5699	1.6116	0.72°	[196]
LCB	La <sub>2</sub> CaB <sub>10</sub> O <sub>19</sub>	1.6730	1.6738	1.7273	0.23°	[197]
LFM	LiCOOH·H <sub>2</sub> O	1.4564	1.5832	1.6367	2.98°	[198]
LGS	LiGaS <sub>2</sub>	2.1221	2.1649	2.1671	0.26°	[199]
LGSe	LiGaSe <sub>2</sub>	2.2992	2.3576	2.3595	0.25°	[199]
LIS	LiInS <sub>2</sub>	2.1557	2.1950	2.2026	0.45°	[200]
LISe	LiInSe <sub>2</sub>	2.3345	2.3810	2.3888	0.46°	[201]
LRB4	LiRbB <sub>4</sub> O <sub>7</sub>	1.5070	1.5309	1.5386	0.51°	[202]
NdGdMO	Nd:Gd <sub>2</sub> (MoO <sub>4</sub> ) <sub>3</sub>	1.8253	1.8258	1.8765	0.15°	[203]
NbKTP	Nb:KTiOPO <sub>4</sub>	1.7512	1.7611	1.8594	1.02°	[204]
NdGdCOB	Nd:GdCa <sub>4</sub> O(BO <sub>3</sub> ) <sub>3</sub>	1.69212	1.7183	1.7269	0.50°	[205]
RTA	RbTiOAsO <sub>4</sub>	1.8159	1.8235	1.8983	0.75°	[206]
RTP	RbTiOPO <sub>4</sub>	1.7795	1.7892	1.8766	0.93°	[207]
YCOB	YCa <sub>4</sub> O(BO <sub>3</sub> ) <sub>3</sub>	1.6734	1.7044	1.7149	0.61°	[208]

**Table C.1:** Compilation of birefringent crystals offering two optical axis [209]. Index of refraction is given by the Sellmeier equation for each crystal, the temperature of T = 293K, and the wavelength of 780nm. The opening angle is calculated using Eq. (4.9).



---

## D Computer-operated laboratory monitoring system

To successfully operate multiple experiments with high-precision lasers one needs well defined environmental conditions. Important factors include temperature, air pressure, and humidity. Day to day fluctuations can disturb and even destroy measurements and experimental hardware. To keep variations as small as possible and to maintain constant working conditions air conditioning and air dehumidifiers are used. In addition to controlling these parameter a monitoring system was developed and implemented successfully in each of the laboratories in the APQ group at the TU Darmstadt.

The system offers a simple and small setup and can be installed easily. In addition to the four setups in the main laboratories a reference system has been installed outside of the building.

An overview of the used hardware and software will be shown as well as a short manual and installation instructions for additional units. First important observations are discussed.

---

### D.1 Hardware

---

By using a RaspberryPi [210] we ensure that our system is small and energy efficient. We use Raspbian [211] as operating system. Raspbian is a Debian [212] Linux [213] distribution specifically optimized for RaspberryPi. The system itself is designed to be small and its current consumption is less than 5W. The Tinkerforge measurement system is connected via USB and the used components from are:

- **Master Brick 2.0** is connected to the RaspberryPi via USB and serves as a host for the sensor bricklets
- **Temperature Bricklet** is connected to the master bricklet and measure the temperature with an accuracy of 0.5 K in a range from  $-40^{\circ}\text{C}$  to  $125^{\circ}\text{C}$ . Not to be confound with the IR Temperature Bricklet
- **Humidity Bricklet** is connected to the master bricklet and measures the relative humidity in steps of 0.1 %
- **Barometer Bricklet** is connected to the master bricklet and measures the air pressure with a resolution of 0.012 mbar in the range of 10 mbar to 1200 mbar

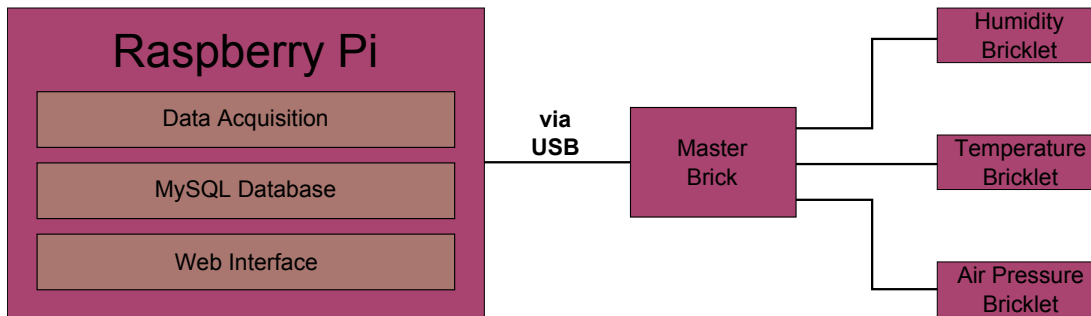


**Figure D.1:** Schematic of the data acquisition setup. A python script connects to the master brick via USB. The master brick provides an interface to the three bricklets and the obtained data is saved to a MySQL database. The user can view the gathered information by connecting to the RaspberryPi with a standard browser over LAN.

Fig. D.1 shows a schematic of the installed system. Each of the bricklets connected to the master brick which is connected by with the RaspberryPi via USB. A python script running on the RaspberryPi connects to the master brick, reads the relevant data and writes it into the database. The user can connect to the RaspberryPi via standard web browser and the frontend of the system shows data put into graphs on a website.

---

## D.2 Software

---

### D.2.1 Setup of a new monitoring system

---

To install or reinstall a new monitoring system the following steps need to be performed.

1. Copy a boot image of Raspbian on the SD card.  
A current version of Raspbian can be found at <https://github.com/debian-pi/raspbian-ua-netinst>. This step has to be made on a different PC that features an SD card reader. The provided image is a netinstall package, which means the installation process need an active internet connection on the RaspberryPi to download additional files. A tutorial on how to prepare the SD card is provided at the github repository for linux and windows systems.
2. Boot the new RaspberryPi for the first time and make sure that network access is available.  
The system needs to be connected to the internet in order to download additional files and will install itself on the SD card automatically. In principle the system is configurable over SSH out of the box, but a keyboard and monitor can also be used to complete the installation.

- 
3. Create user with appropriate username/password combination  
The standard user name was chosen to be 'pi' and the password can be chosen freely.
  4. Install necessary packages of the operating system:  
In order to provide the monitoring systems basic software infrastructure the following packages have to be installed:

```
apt-get install vim python-yaml python-mysqldb mysql-server libusb-1.0-0 libudev0 python  
python-qt4 python-qt4-gl python-qt5-qt4 python-opengl subversion iptables
```

5. Each monitoring setup should be provided with a static IP to simplify the day-to-day usage. To set a fixed IP in the APQ network the following entries in '/etc/network/interfaces' need to replace the DHCP configuration:

```
auto eth0  
iface eth0 inet static  
address 192.168.1.xxx  
netmask 255.255.255.0  
network 192.168.1.0  
broadcast 192.168.1.255  
gateway 192.168.1.1
```

6. Install NodeJS  
NodeJS is used as the webserver for the frontend representation of data:

```
# Load nodejs from the nodejs server  
wget http://nodejs.org/dist/v0.10.4/node-v0.10.4-linux-arm-pi.tar.gz  
# unpack and copy nodejs to the appropriate directory  
tar xvzf node-v0.10.4-linux-arm-pi.tar.gz  
cp -R node-v0.10.4-linux-arm-pi/* /opt/node/  
# register nodejs and npm globally in raspbian  
ln -s /opt/node/bin/node /usr/bin/node  
ln -s /opt/node/bin/npm /usr/bin/npm  
# install pm2  
npm install -g pm2
```

to redirect http port 80 to nodejs default port (3000) insert into /etc/rc.local:

```
iptables -A PREROUTING -t nat -i eth0 -p tcp --dport 80 -j REDIRECT --to-port 3000
```

7. Fetch software from SVN repository  
The software is hosted on the APQs internal SVN server.

```
# cd into user directory  
cd ~  
# checkout source code from SVN  
svn co https://130.83.3.168/svn/repos/pions/trunk/ ./  
# cd webserver directory  
cd webserver  
# install node packages  
npm install
```

8. Install TinkerForge software

```
dpkg -i tinkerforge/brickd_linux_latest_armhf.deb
```

## 9. Create MySQL User and Database

```
-- connect to mysql
mysql -u root -p
-- create database and user
CREATE DATABASE sensors;
```

and import mysql schema into the newly created database

```
# import mysql schema definitions
mysql -u root -p sensors < tinkerforge/scripts/schema.sql
```

insert bricklet ids and types in database

```
-- insert temperature bricklet
INSERT INTO sensors (id, sensor_uid, name, unit_id, node_id, room_id, callback_period)
VALUES (1, '***bricklet id***', 'temp', 1, 1, ***ROOM ID***, 60000)
-- insert humidity bricklet
INSERT INTO sensors (id, sensor_uid, name, unit_id, node_id, room_id, callback_period)
VALUES (1, '***bricklet id***', 'humid', 1, 1, ***ROOM ID***, 60000)
-- insert humidity bricklet (if installed)
INSERT INTO sensors (id, sensor_uid, name, unit_id, node_id, room_id, callback_period)
VALUES (1, '***bricklet id***', 'baro', 1, 1, ***ROOM ID***, 60000)
```

create user and grant privileges

```
CREATE USER 'pi'@'localhost' IDENTIFIED BY '***PASSWORD***';
GRANT ALL PRIVILEGES ON sensors.* to 'pi'@'%' identified by '***PASSWORD***';
```

## 10. Install CronJobs

```
@reboot /usr/bin/pm2 start /home/pi/webserver/app.js
@reboot /usr/bin/pm2 web
@reboot sleep 60 && exec /home/pi/tinkerforge/scripts/sensorDaemon.py
```

## 11. The system is now configured appropriately and should be rebooted

In order to ensure stable and secure operation third party software should be updated regularly. This creates the need to update the manual to the appropriate version number for each software change. Software updates should be distributed over the central version control system.

---

### D.2.2 Overview of the installed systems

---

Table D.1 gives an overview over the currently installed monitoring setups.

---

### D.3 Export data via command line

---

In the event of supply voltage loss the RaspberryPi automatically reboots once supply voltage is regained. The data acquisition script is automatically started by the operating system and gathers a new set of data every 60 seconds.

Room ID		IP	Brick ID	Bricklet ID		
		192.168.1	Master	Temp	Humid	Baro
Neon	1	.81	5VH6Cv	dB3	eDj	-
GSI	2	.82	6DcNJe	dzq	eD3	-
Outdoor	3	.83	68VPvs	dSj	fSW	g1w
Atomics	4	.84	6qzTf1	dSb	fQk	-
Quips	5	.85	6R61eW	e1L	fSY	-

**Table D.1:** Compilation of the currently installed monitoring systems at the different experiments.

```
SELECT UNIX_TIMESTAMP(date), value INTO OUTFILE '/tmp/data.csv' FIELDS TERMINATED BY ','
OPTIONALLY ENCLOSED BY '"' ESCAPED BY '\\\'' ESCAPED BY '\\n' FROM sensor_data WHERE sensor_id
= '1' AND date > '2014-03-01 00:00:00';
```

The created file can be copied from the RaspberryPi to another computer via SCP [214] or SFTP [215] (for example with FileZilla [216]).

## D.4 First experimental observations

Fig. D.2 shows the first experimental observation made with the newly installed monitoring system. The temperature as a function of time is shown as well as the frequency of a stabilized laser system. The laser system is used for high precision spectroscopy of tellurium as well as Rydberg excitation of  $^{87}\text{Rb}$  atoms [217].

The laser frequency is shown in reverse direction to show the observed correlation between the temperature and the stabilized frequency. Most likely the temperature dependence originates from the used accusto-optical modulators, used in the laser system. The decoupling of the system from the laboratory temperature is currently being researched.

In addition the quality of fibre couplings has shown to have a huge temperature dependence and is currently being monitored.

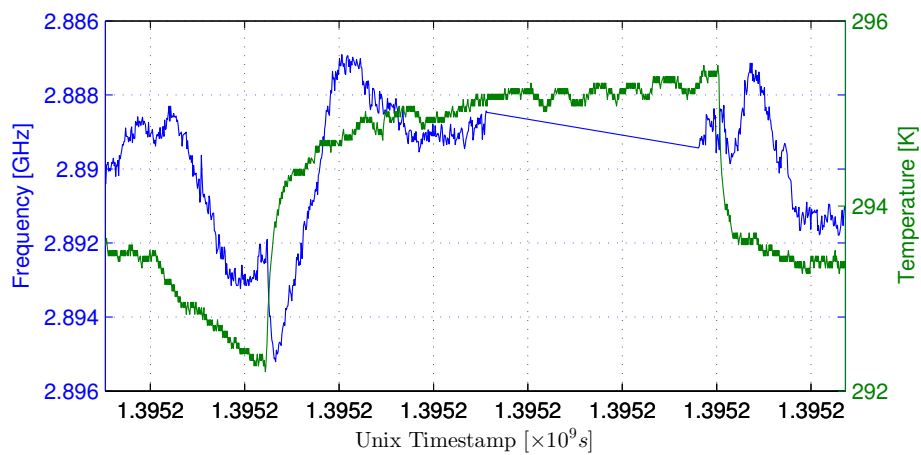


**Figure D.2:** Temperature and laser frequency as a function of time. The temperature and the frequency show a strong correlation which most likely originates from the acousto-optical modulators used in the optical setup.

---

---

## Bibliography

- [1] A. Abramovici *et al.*, *LIGO: The Laser Interferometer Gravitational-Wave Observatory*, *Science* **256**, 325 (1992).
- [2] E. M. Frohman, J. G. Fujimoto, T. C. Frohman, P. A. Calabresi, G. Cutter and L. J. Balcer, *Optical coherence tomography: a window into the mechanisms of multiple sclerosis*, *Nature Clinical Practice Neurology* **4**, 664 (2008).
- [3] A. A. Michelson and E. W. Morley, *On the Relative Motion of the Earth and the Luminiferous Ether*, *American Journal of Science* **34**, 333 (1887).
- [4] L. de Broglie, *Recherches sur la Theorie des Quanta*, type, Sorbonne, Paris, (1924).
- [5] D. P. Mitchell and P. N. Powers, *Bragg Reflection of Slow Neutrons*, *Phys. Rev.* **50**, 486 (1936).
- [6] C. Davisson and L. H. Germer, *The Scattering of Electrons by a Single Crystal of Nickel*, *Nature* **119**, 558 (1927).
- [7] W. Bragg, *The diffraction of X-rays by crystals*, *Physics* pp. 370–382 (1922).
- [8] M. Kasevich and S. Chu, *Measurement of the gravitational acceleration of an atom with a light-pulse atom interferometer*, *Applied Physics B* **54**, 321 (1992).
- [9] A. Peters, K. Y. Chung and S. Chu, *High-precision gravity measurements using atom interferometry*, *Metrologia* **38**, 25 (2001).
- [10] A. Peters, K. Y. Chung and S. Chu, *Measurement of gravitational acceleration by dropping atoms*, *Nature* **400**, 849 (1999).
- [11] M. Kasevich and S. Chu, *Atomic interferometry using stimulated Raman transitions*, *Phys. Rev. Lett.* **67**, 181 (1991).
- [12] S. Gupta, K. Dieckmann, Z. Hadzibabic and D. E. Pritchard, *Contrast Interferometry using Bose-Einstein Condensates to Measure  $h/m$  and  $\alpha$* , *Phys. Rev. Lett.* **89**, 140401 (2002).

- 
- [13] M. Cadoret, E. de Mirandes, P. Cladé, S. Guellati-Khélifa, C. Schwob, F. m. c. Nez, L. Julien and F. m. c. Biraben, *Combination of Bloch Oscillations with a Ramsey-Bordé Interferometer: New Determination of the Fine Structure Constant*, Phys. Rev. Lett. **101**, 230801 (2008).
- [14] R. Geiger *et al.*, *Detecting inertial effects with airborne matter-wave interferometry*, Nature **2** (2011).
- [15] T. van Zoest *et al.*, *Bose-Einstein Condensation in Microgravity*, Science **328**, 1540 (2010).
- [16] H. Müntinga *et al.*, *Interferometry with Bose-Einstein Condensates in Microgravity*, Phys. Rev. Lett. **110**, 093602 (2013).
- [17] A. Einstein, *Quantentheorie des einatomigen idealen Gases*, Sitzungsberichte der Preußischen Akademie der Wissenschaften zu Berlin **22**, 261 (1924).
- [18] A. Einstein, *Quantentheorie des einatomigen idealen Gases, Zweite Abhandlung*, Sitzungsberichte der Preußischen Akademie der Wissenschaften zu Berlin **1**, 3 (1925).
- [19] Bose, *Plancks Gesetz und Lichtquantenhypothese*, Zeitschrift für Physik **26**, 178 (1924).
- [20] M. H. Anderson, J. R. Ensher, M. R. Matthews, C. E. Wieman and E. A. Cornell, *Observation of Bose-Einstein Condensation in a Dilute Atomic Vapor*, Science **269**, 198 (1995).
- [21] K. B. Davis, M. O. Mewes, M. R. Andrews, N. J. van Druten, D. S. Durfee, D. M. Kurn and W. Ketterle, *Bose-Einstein Condensation in a Gas of Sodium Atoms*, Phys. Rev. Lett. **75**, 3969 (1995).
- [22] T. Hänsch and A. Schawlow, *Cooling of gases by laser radiation*, Optics Communications **13**, 68 (1975).
- [23] W. D. Phillips and H. Metcalf, *Laser Deceleration of an Atomic Beam*, Phys. Rev. Lett. **48**, 596 (1982).
- [24] S. Chu, L. Hollberg, J. E. Bjorkholm, A. Cable and A. Ashkin, *Three-dimensional viscous confinement and cooling of atoms by resonance radiation pressure*, Phys. Rev. Lett. **55**, 48 (1985).
- [25] E. L. Raab, M. Prentiss, A. Cable, S. Chu and D. E. Pritchard, *Trapping of Neutral Sodium Atoms with Radiation Pressure*, Phys. Rev. Lett. **59**, 2631 (1987).

- 
- [26] R. Grimm, M. Weidemüller and Y. B. Ovchinnikov, *Optical Dipole Traps for Neutral Atoms*, in *Optical Dipole Traps for Neutral Atoms*, Vol. 42 of *Advances In Atomic, Molecular, and Optical Physics*, M. W. u. Y. B. O. R. Grimm, ed., (Academic Press, 2000), pp. 95 – 170.
- [27] C. S. Adams, H. J. Lee, N. Davidson, M. Kasevich and S. Chu, *Evaporative Cooling in a Crossed Dipole Trap*, *Phys. Rev. Lett.* **74**, 3577 (1995).
- [28] M. D. Barrett, J. A. Sauer and M. S. Chapman, *All-Optical Formation of an Atomic Bose-Einstein Condensate*, *Physical Review Letters* **87**, 010404 (2001).
- [29] W. Hamilton, *Third supplement to an Essay on the Theory of Systems of Rays*, *Transactions of the Royal Irish Academy* **17**, 1 (1937).
- [30] H. Lloyd, *On the phenomena presented by light in its passage along the axes of biaxial crystals*, *Transactions of the Royal Irish Academy* **17**, 145 (1837).
- [31] A. M. Belskii and A. P. Khapalyuk, *Propagation of confined light beams along the beam axes (axes of single ray velocity) of biaxial crystals*, *Optics and Spectroscopy* **44**, 312 (1978).
- [32] A. Belsky and M. Stepanov, *Internal conical refraction of coherent light beams*, *Optics Communications* **167**, 1 (1999).
- [33] A. Belsky and M. Stepanov, *Internal conical refraction of light beams in biaxial gyrotropic crystals*, *Optics Communications* **204**, 1 (2002).
- [34] D. P. O'Dwyer, K. E. Ballantine, C. F. Phelan, J. G. Lunney and J. F. Donegan, *Optical trapping using cascade conical refraction of light*, *Opt. Express* **20**, 21119 (2012).
- [35] A. Abdolvand, K. G. Wilcox, T. K. Kalkandjiev and E. U. Rafailov, *Conical refraction Nd:KGd(WO<sub>4</sub>)<sub>2</sub> laser*, *Opt. Express* **18**, 2753 (2010).
- [36] C. F. Phelan, D. P. O'Dwyer, Y. P. Rakovich, J. F. Donegan and J. G. Lunney, *Conical diffraction and Bessel beam formation with a high optical quality biaxial crystal*, *Opt. Express* **17**, 12891 (2009).
- [37] O. Morsch and M. Oberthaler, *Dynamics of Bose-Einstein condensates in optical lattices*, *Rev. Mod. Phys.* **78**, 179 (2006).
- [38] P. J. Martin, B. G. Oldaker, A. H. Miklich and D. E. Pritchard, *Bragg scattering of atoms from a standing light wave*, *Phys. Rev. Lett.* **60**, 515 (1988).
- [39] P. L. Gould, G. A. Ruff and D. E. Pritchard, *Diffraction of atoms by light: The near-resonant Kapitza-Dirac effect*, *Phys. Rev. Lett.* **56**, 827 (1986).

- 
- [40] O. Carnal and J. Mlynek, *Young's double-slit experiment with atoms: A simple atom interferometer*, Phys. Rev. Lett. **66**, 2689 (1991).
- [41] M. Anderson, J. R. Ensher, M. R. Matthews, C. E. Wieman and E. A. Cornell, *Observation of Bose-Einstein Condensation in a Dilute Atomic Vapor.*, Science **269**, 198 (1995).
- [42] K. B. Davis, M. O. Mewes, M. R. Andrews, N. J. van Druten, D. S. Durfee, D. M. Kurn and W. Ketterle, *Bose-Einstein Condensation in a Gas of Sodium Atoms*, Physical Review Letters **75**, 3969 (1995).
- [43] K. M. R. van der Stam, E. D. van Ooijen, R. Meppelink, J. M. Vogels and P. van der Straten, *Large atom number Bose-Einstein condensate of sodium.*, The Review of Scientific Instruments **78**, 013102 (2007).
- [44] T. Lauber, *Bose-Einstein-Kondensation in einer gekreuzten Dipolfalle*, Diploma thesis, TU Darmstadt, Darmstadt, (2008).
- [45] J. Nes, *Cold Atoms and Bose-Einstein Condensates in Optical Dipole Potentials*, Ph.d. dissertation, TU Darmstadt, Darmstadt, (2008).
- [46] T. Kraemer, J. Herbig, M. Mark, T. Weber, C. Chin, H.-C. Nägerl and R. Grimm, *Optimized production of a cesium Bose-Einstein condensate*, Applied Physics B: Lasers and Optics **79**, 1013 (2004).
- [47] J.-F. Clément, J.-P. Brantut, M. Robert-de Saint-Vincent, R. A. Nyman, A. Aspect, T. Bourdel and P. Bouyer, *All-optical runaway evaporation to Bose-Einstein condensation*, Physical Review A **79**, 061406 (2009).
- [48] K. J. Arnold and M. D. Barrett, *All-optical Bose-Einstein condensation in a 1.06 $\mu$ m dipole trap*, Optics Communications **284**, 3288 (2011).
- [49] T. Kinoshita, T. Wenger and D. S. Weiss, *All-optical Bose-Einstein condensation using a compressible crossed dipole trap*, Physical Review A **71**, 011602 (2005).
- [50] K. B. Davis, M. O. Mewes and W. Ketterle, *An analytical model for evaporative cooling of atoms*, Applied Physics B: Lasers and Optics **60**, 155 (1995).
- [51] H. Metcalf and P. van der Straten, *Laser Cooling and Trapping*, Graduate Texts in Contemporary Physics (Springer New York, 1999).
- [52] D. A. Steck, *Rubidium 87 D Line Data*, 2010, <http://steck.us/alkalidata/>.
- [53] I. Bloch, *Ultracold quantum gases in optical lattices*, Nature Physics **1** (2005).

- 
- [54] C. Pethick and H. Smith, *Bose-Einstein Condensation in Dilute Gases* (Cambridge University Press, 2002).
- [55] M. Ueda, *Fundamentals and New Frontiers of Bose-Einstein Condensation* (World Scientific, 2010).
- [56] L. Pitaevskii and S. Stringari, *Bose-Einstein Kondensation* (Oxford University Press, 2003).
- [57] T. Fließbach, *Statistische Physik, Lehrbuch zur theoretischen Physik* (Spektrum Akademischer Verlag GmbH, 2010).
- [58] Y. Castin and R. Dum, *Bose-Einstein Condensates in Time Dependent Traps*, Phys. Rev. Lett. **77**, 5315 (1996).
- [59] Y. Kagan, E. L. Surkov and G. V. Shlyapnikov, *Evolution of a Bose-condensed gas under variations of the confining potential*, Phys. Rev. A **54**, R1753 (1996).
- [60] F. Dalfovo, S. Giorgini, L. P. Pitaevskii and S. Stringari, *Theory of Bose-Einstein condensation in trapped gases*, Rev. Mod. Phys. **71**, 463 (1999).
- [61] O. Wille, *Manipulation von Bose-Einstein-Kondensaten in optischen Dipolpotentialen*, Ph.d. dissertation, TU Darmstadt, Darmstadt, (2010).
- [62] W. Ertmer, R. Blatt, J. L. Hall and M. Zhu, *Laser Manipulation of Atomic Beam Velocities: Demonstration of Stopped Atoms and Velocity Reversal*, Phys. Rev. Lett. **54**, 996 (1985).
- [63] F. Schmaltz, *Kohärenzeigenschaften von Bose-Einstein-Kondensaten in ringförmigen Dipolpotentialen*, Master thesis, TU Darmstadt, Darmstadt, (2013).
- [64] N. Coleman, *Aufbau und Stabilisierung eines MOPA-Systems zur Laserkühlung von Rubidium*, Diploma thesis, TU Darmstadt, Darmstadt, (2007).
- [65] T. Lauber, *Kohärente Dynamik von Bose-Einstein-Kondensaten in Dipolpotentialen*, Ph.d. dissertation, TU Darmstadt, Darmstadt, (2012).
- [66] M. Krutzik, *Bose-Einstein Kondensate und ringförmige mikrooptische Dipolpotentiale*, Master thesis, University of Wisconsin-Madison, (2008).
- [67] S. Hertsch, *Bose-Einstein Kondensate und optische Wellenleiterstrukturen*, Master thesis, TU Darmstadt, Darmstadt, (2008).
- [68] T. Lauber, J. Küber, O. Wille and G. Birkl, *Optimized Bose-Einstein condensate production in a dipole trap based on a 1070-nm multifrequency laser: Influence of enhanced two-body loss on the evaporation process*, Phys. Rev. A **84**, 043641 (2011).

- 
- [69] M. D. Barrett, J. A. Sauer and M. S. Chapman, *All-Optical Formation of an Atomic Bose-Einstein Condensate*, Phys. Rev. Lett. **87**, 010404 (2001).
- [70] W. Ketterle, D. S. Durfee and D. M. Stamper-Kurn, *Making, probing and understanding Bose-Einstein condensates*, cond-mat/9904034 (1999).
- [71] M. Brinkmann, *Optimierung der Detektion und Auswertung von Rb-Spinor-Kondensaten*, Diploma thesis, Universität Hamburg, Hamburg, (2005).
- [72] *Python Programming Language*, <http://www.python.org>, 2014.
- [73] W. Bragg, *The diffraction of X-rays by crystals*, Nobel Lectures **1901-1921**, 370 (1922).
- [74] Kunze, S., Dürr, S. and Rempe, G., *Bragg scattering of slow atoms from a standing light wave*, Europhys. Lett. **34**, 343 (1996).
- [75] M. K. Oberthaler, R. Abfalterer, S. Bernet, J. Schmiedmayer and A. Zeilinger, *Atom Waves in Crystals of Light*, Phys. Rev. Lett. **77**, 4980 (1996).
- [76] D. M. Giltner, R. W. McGowan and S. A. Lee, *Theoretical and experimental study of the Bragg scattering of atoms from a standing light wave*, Phys. Rev. A **52**, 3966 (1995).
- [77] M. Kozuma, L. Deng, E. W. Hagley, J. Wen, R. Lutwak, K. Helmerson, S. L. Rolston and W. D. Phillips, *Coherent Splitting of Bose-Einstein Condensed Atoms with Optically Induced Bragg Diffraction*, Phys. Rev. Lett. **82**, 871 (1999).
- [78] J. J. Kinnunen and M. J. Holland, *Bragg spectroscopy of a strongly interacting Bose-Einstein condensate*, New Journal of Physics **11**, 013030 (2009).
- [79] J. Stenger, S. Inouye, A. P. Chikkatur, D. M. Stamper-Kurn, D. E. Pritchard and W. Ketterle, *Bragg Spectroscopy of a Bose-Einstein Condensate*, Phys. Rev. Lett. **82**, 4569 (1999).
- [80] M. R. Andrews, C. G. Townsend, H. j. Miesner, D. S. Durfee, D. M. Kurn and W. Ketterle, *Observation of Interference Between Two Bose Condensates*, Science **275**, 637 (1997).
- [81] E. Giese, A. Roura, G. Tackmann, E. M. Rasel and W. P. Schleich, *Double Bragg diffraction: A tool for atom optics*, Phys. Rev. A **88**, 053608 (2013).
- [82] Bogoliubov, N.N. and Mitropolskii, I.U.A., *Asymptotic Methods in the Theory of Non-linear Oscillations*, International monographs on advanced mathematics and physics (Hindustan Publishing Corporation, stamped, 1961).

- 
- [83] J. Küber, *Bose-Einstein-Kondensate in eindimensionalen optischen Gittern*, Master thesis, TU Darmstadt, Darmstadt, (2009).
- [84] C. G. Shull, *Observation of Pendellösung Fringe Structure in Neutron Diffraction*, Phys. Rev. Lett. **21**, 1585 (1968).
- [85] A. F. Bernhardt and B. W. Shore, *Coherent atomic deflection by resonant standing waves*, Phys. Rev. A **23**, 1290 (1981).
- [86] M. Marte and S. Stenholm, *Multiphoton resonances in atomic bragg scattering*, Applied Physics B **54**, 443 (1992).
- [87] W. Schleich, *Quantum Optics in Phase Space* (Wiley-VCH, 2001).
- [88] L. Allen and J. Eberly, *Optical Resonance and Two-level Atoms*, Dover Books on Physics Series (Dover, 1987).
- [89] S. Gupta, A. E. Leanhardt, A. D. Cronin and D. E. Pritchard, *Coherent manipulation of atoms with standing light waves*, Comptes Rendus de l'Académie des Sciences - Series IV - Physics **2**, 479 (2001).
- [90] F. C. Hauptert, *Diffraction of a Bose-Einstein Condensate and the Path to an Atom Laser*, type, The University of Auckland, (2007).
- [91] S. S. Szigeti, J. E. Debs, J. J. Hope, N. P. Robins and J. D. Close, *Why momentum width matters for atom interferometry with Bragg pulses*, New Journal of Physics **14**, 023009 (2012).
- [92] P. A. Altin *et al.*, *Precision atomic gravimeter based on Bragg diffraction*, New Journal of Physics **15**, 023009 (2013).
- [93] D. F. James and J. Jerke, *Effective Hamiltonian theory and its applications in quantum information*, Canadian Journal of Physics **85**, 625 (2007).
- [94] H. Müller, S.-w. Chiow and S. Chu, *Atom-wave diffraction between the Raman-Nath and the Bragg regime: Effective Rabi frequency, losses, and phase shifts*, Phys. Rev. A **77**, 023609 (2008).
- [95] J. Schütz, *Stoßwechselwirkungen in Isotopen- und Spinmischungen lasergekühlter metastabiler Neonatome*, Ph.d. dissertation, TU Darmstadt, Darmstadt, (2013).
- [96] X. Baillard, A. Gauguet, S. Bize, P. Lemonde, P. Laurent, A. Clairon and P. Rosenbusch, *Interference-filter-stabilized external-cavity diode lasers*, Optics Communications **266**, 609 (2006).
- [97] A. Castrillo, E. Fasci, G. Galzerano, G. Casa, P. Laporta and L. Gianfrani, *Offset-frequency locking of extended-cavity diode lasers for precision spectroscopy of water at 1.38  $\mu\text{m}$* , Opt. Express **18**, 21851 (2010).

- 
- [98] H. M. Frydrych, *Computergestützte Steuerung und Auswertung von Experimenten mit lasergekühlten Atomen*, Bachelor thesis, TU Darmstadt, Darmstadt, (2008).
- [99] T. A. Savard, K. M. O'Hara and J. E. Thomas, *Laser-noise-induced heating in far-off resonance optical traps*, Phys. Rev. A **56**, R1095 (1997).
- [100] A. Siegman, *Lasers* (University Science Books, 1986).
- [101] Y. B. Ovchinnikov, J. H. Müller, M. R. Doery, E. J. D. Vredenbregt, K. Helmerson, S. L. Rolston and W. D. Phillips, *Diffraction of a Released Bose-Einstein Condensate by a Pulsed Standing Light Wave*, Phys. Rev. Lett. **83**, 284 (1999).
- [102] P. L. Kapitza and P. A. M. Dirac, *The reflection of electrons from standing light waves*, Mathematical Proceedings of the Cambridge Philosophical Society **29**, 297 (1933).
- [103] J. H. Denschlag, J. E. Simsarian, H. Häffner, C. McKenzie, A. Browaeys, D. Cho, K. Helmerson, S. L. Rolston and W. DPhillips, *A Bose-Einstein condensate in an optical lattice*, Journal of Physics B: Atomic, Molecular and Optical Physics **35**, 3095 (2002).
- [104] C. Bergmann, L. und Schaefer, *Lehrbuch der Experimentalphysik Band 3: Optik*, 10 ed. ed. (Springer Verlag, 2004).
- [105] M. Mark, *Wechselwirkungseffekte eines Cäsium-BEC in eindimensionalen Gittern*, Diploma thesis, Leopold-Franzens-Universität Innsbruck, (2007).
- [106] D. L. Freimund, K. Aflatooni and H. Batelaan, *Observation of the Kapitza-Dirac effect*, Nature **413**, 090405 (2001).
- [107] H. Batelaan, *The Kapitza-Dirac effect*, Contemporary Physics **41**, 369 (2000).
- [108] S. Wu, Y.-J. Wang, Q. Diot and M. Prentiss, *Splitting matter waves using an optimized standing-wave light-pulse sequence*, Phys. Rev. A **71**, 043602 (2005).
- [109] Y.-J. Wang, D. Z. Anderson, V. M. Bright, E. A. Cornell, Q. Diot, T. Kishimoto, M. Prentiss, R. A. Saravanan, S. R. Segal and S. Wu, *Atom Michelson Interferometer on a Chip Using a Bose-Einstein Condensate*, Phys. Rev. Lett. **94**, 090405 (2005).
- [110] K. Bongs, S. Burger, S. Dettmer, D. Hellweg, J. Arlt, W. Ertmer and K. Senstock, *Waveguide for Bose-Einstein condensates*, Phys. Rev. A **63**, 031602 (2001).

- 
- [111] S. Dettmer, *Experimentelle Untersuchungen zum Einsatz von Bose-Einstein Kondensaten in der hochauflösenden Interferometrie*, Ph.d. dissertation, Universität Hannover, (2003).
- [112] N. F. Ramsey, *A Molecular Beam Resonance Method with Separated Oscillating Fields*, Phys. Rev. **78**, 695 (1950).
- [113] W. Demtröder, *Laserspektroskopie 1*, SpringerLink : Bücher (Springer, 2011).
- [114] B. Bransden and C. Joachain, *Physics of Atoms and Molecules*, Pearson Education (Prentice Hall, 2003).
- [115] F. Riehle, T. Kisters, A. Witte, J. Helmcke and C. J. Bordé, *Optical Ramsey spectroscopy in a rotating frame: Sagnac effect in a matter-wave interferometer*, Phys. Rev. Lett. **67**, 177 (1991).
- [116] K. Zeiske, G. Zinner, F. Riehle and J. Helmcke, *Atom interferometry in a static electric field: Measurement of the Aharonov-Casher phase*, Applied Physics B **60**, 205 (1995).
- [117] Ch.J. Bordé, *Atomic interferometry with internal state labelling*, Physics Letters A **140**, 10 (1989).
- [118] J. E. Simsarian, J. Denschlag, M. Edwards, C. W. Clark, L. Deng, E. W. Hagley, K. Helmerson, S. L. Rolston and W. D. Phillips, *Imaging the Phase of an Evolving Bose-Einstein Condensate Wave Function*, Phys. Rev. Lett. **85**, 2040 (2000).
- [119] F. Harris, *On the use of windows for harmonic analysis with the discrete Fourier transform*, Proceedings of the IEEE **66**, 51 (1978).
- [120] Y. Torii, Y. Suzuki, M. Kozuma, T. Sugiura, T. Kuga, L. Deng and E. W. Hagley, *Mach-Zehnder Bragg interferometer for a Bose-Einstein condensate*, Phys. Rev. A **61**, 041602 (2000).
- [121] M. Born, E. Wolf and A. Bhatia, *Principles of Optics: Electromagnetic Theory of Propagation, Interference and Diffraction of Light* (Cambridge University Press, 1999).
- [122] T. K. Kalkandjiev and M. A. Bursukova, *Conical refraction: an experimental introduction*, Proc. SPIE **6994**, 69940B (2008).
- [123] M. Berry and M. Jeffrey, *Chapter 2 Conical diffraction: Hamilton's diabolical point at the heart of crystal optics*, in *Chapter 2 Conical diffraction: Hamilton's diabolical point at the heart of crystal optics*, Vol. 50 of *Progress in Optics*, E. Wolf, ed., (Elsevier, 2007), pp. 13 – 50.

- 
- [124] A. M. Belskii and A. P. Khapalyuk, *Internal conical refraction of bounded light beams in biaxial crystals*, Optics and Spectroscopy **44**, 436 (1978).
- [125] A. J. Schell and N. Bloembergen, *Laser studies of internal conical diffraction. I. Quantitative comparison of experimental and theoretical conical intensity distribution in aragonite*, J. Opt. Soc. Am. **68**, 1093 (1978).
- [126] M. V. Berry, *Conical diffraction asymptotics: fine structure of Poggendorff rings and axial spike*, Journal of Optics A: Pure and Applied Optics **6**, 289 (2004).
- [127] A. Turpin, V. Shvedov, C. Hnatovsky, Y. V. Loiko, J. Mompart and W. Krolikowski, *Optical vault: A reconfigurable bottle beam based on conical refraction of light*, Opt. Express **21**, 26335 (2013).
- [128] C. Raman, V. Rajagopalan and T. Nedungadi, *Conical refraction in naphthalene crystals*, Proceedings of the Indian Academy of Sciences - Section A **14**, 221 (1941).
- [129] G. S. Sokolovskii, D. J. Carnegie, T. K. Kalkandjiev and E. U. Rafailov, *Conical Refraction: New observations and a dual cone model*, Opt. Express **21**, 11125 (2013).
- [130] A. Turpin, J. K. andand F. Schmaltz, J. Mompart and G. Birkl, blue-detuned optical ring trap for Bose-Einstein condensates based on conical refraction (to be published).
- [131] J. Küber, A. Turpin, F. Schmaltz, J. Mompart and G. Birkl, trapping of Bose-Einstein condensates in a dark focus trap generated by conical refraction (to be published).
- [132] A. Turpin, Y. V. Loiko, T. K. Kalkandjiev, H. Tomizawa and J. Mompart, *Wave-vector and polarization dependence of conical refraction*, Opt. Express **21**, 4503 (2013).
- [133] R. Sulzbach, *Realisierung von zweidimensionalen registern dunkler Fokii mittels eines Mikrolinsenregisters und konischer Refraktion*, Bachelor thesis, TU Darmstadt, Darmstadt, (2014).
- [134] C. Ryu, M. F. Andersen, P. Cladé, V. Natarajan, K. Helmerson and W. D. Phillips, *Observation of Persistent Flow of a Bose-Einstein Condensate in a Toroidal Trap*, Phys. Rev. Lett. **99**, 260401 (2007).
- [135] B. E. Sherlock, M. Gildemeister, E. Owen, E. Nugent and C. J. Foot, *Time-averaged adiabatic ring potential for ultracold atoms*, Phys. Rev. A **83**, 043408 (2011).
- [136] A. Turpin and Y. V. Loiko, *personal communication*, .

- 
- [137] T. Gericke, F. Gerbier, A. Widera, S. Fölling, O. Mandel and I. Bloch, *Emergence of order from turbulence in an isolated planar superfluid*, Journal of Modern Optics (2014).
- [138] C. McDougall, R. Henderson, D. J. Carnegie, G. S. Sokolovskii, E. U. Rafailov and D. McGloin, *Flexible particle manipulation techniques with conical refraction-based optical tweezers*, Proc. SPIE **8458**, 845824 (2012).
- [139] A. Lenef, T. D. Hammond, E. T. Smith, M. S. Chapman, R. A. Rubenstein and D. E. Pritchard, *Rotation Sensing with an Atom Interferometer*, Phys. Rev. Lett. **78**, 760 (1997).
- [140] T. Müller, M. Gilowski, M. Zaiser, P. Berg, C. Schubert, T. Wendrich, W. Ertmer and E. M. Rasel, *A compact dual atom interferometer gyroscope based on laser-cooled rubidium*, The European Physical Journal D **53**, 273 (2009).
- [141] W. Ping, L. Run-Bing, Y. Hui, W. Jin and Z. Ming-Sheng, *Demonstration of a Sagnac-Type Cold Atom Interferometer with Stimulated Raman Transitions*, Chinese Physics Letters **24**, 27 (2007).
- [142] M. Maik, P. Buonsante, A. Vezzani and J. Zakrzewski, *Dipolar bosons on an optical lattice ring*, Phys. Rev. A **84**, 053615 (2011).
- [143] W. H. Heathcote, E. Nugent, B. T. Sheard and C. J. Foot, *A ring trap for ultracold atoms in an RF-dressed state*, New Journal of Physics **10**, 043012 (2008).
- [144] Matthieu Vangeleyn and Barry M Garraway and Hélène Perrin and Aidan S Arnold, *Inductive dressed ring traps for ultracold atoms*, Journal of Physics B: Atomic, Molecular and Optical Physics **47**, 071001 (2014).
- [145] K. Henderson, C. Ryu, C. MacCormick and M. G. Boshier, *Experimental demonstration of painting arbitrary and dynamic potentials for Bose–Einstein condensates*, New Journal of Physics **11**, 043030 (2009).
- [146] S. A. Kennedy, G. Biedermann, J. Farrar, T. Akin, S. Krzyzewski and E. Abraham, *Confinement of ultracold atoms in a Laguerre–Gaussian laser beam created with diffractive optics*, Optics Communications **321**, 110 (2014).
- [147] F. Moscatelli, C. Sackett, S. Du and E. Oh, *Far-off-resonant ring trap near the ends of optical fibers*, Phys. Rev. A **76**, 043404 (2007).
- [148] M. Hasch, *Loading Bose-Einstein Condensates into a Ring-shaped Dipole Potential*, Master thesis, TU Darmstadt, Darmstadt, (2010).

- 
- [149] F. Schmitt, *Ab-Initio Quantum Phase Diagrams of Ultracold Atomic Gases in Optical Lattices*, Ph.d. dissertation, TU Darmstadt, Darmstadt, (2009).
- [150] L. Görgen, *Dynamik von Bose-Einstein-Kondensaten in eindimensionalen optischen Ringpotentialen*, Bachelor thesis, TU Darmstadt, Darmstadt, (2009).
- [151] D. A. Kokorowski, A. D. Cronin, T. D. Roberts and D. E. Pritchard, *From Single- to Multiple-Photon Decoherence in an Atom Interferometer*, Phys. Rev. Lett. **86**, 2191 (2001).
- [152] N. Davidson, H. Jin Lee, C. S. Adams, M. Kasevich and S. Chu, *Long Atomic Coherence Times in an Optical Dipole Trap*, Phys. Rev. Lett. **74**, 1311 (1995).
- [153] M. Schlosser, *Bereitstellung und kohärente Kontrolle von Einzel-Atom-Quantensystemen in zwei-dimensionalen Quantenregistern*, Ph.d. dissertation, TU Darmstadt, Darmstadt, (2013).
- [154] A. Benseny, S. Fernández-Vidal, J. Bagudà, R. Corbalán, A. Picón, L. Roso, G. Birkl and J. Mompart, *Atomtronics with holes: Coherent transport of an empty site in a triple-well potential*, Phys. Rev. A **82**, 013604 (2010).
- [155] I. Lesanovsky and W. von Klitzing, *Time-Averaged Adiabatic Potentials: Versatile Matter-Wave Guides and Atom Traps*, Physical Review Letters **99**, 083001 (2007).
- [156] T. Isoshima, M. Nakahara, T. Ohmi and K. Machida, *Creation of a persistent current and vortex in a Bose-Einstein condensate of alkali-metal atoms*, Phys. Rev. A **61**, 063610 (2000).
- [157] Y. Loiko, V. Ahufinger, R. Corbalán, G. Birkl and J. Mompart, *Filtering of matter-wave vibrational states via spatial adiabatic passage*, Phys. Rev. A **83**, 033629 (2011).
- [158] T. Lauber, P. Massignan, G. Birkl and A. Sanpera, *Atomic wave packet dynamics in finite time-dependent optical lattices*, Journal of Physics B: Atomic, Molecular and Optical Physics **44**, 065301 (2011).
- [159] T. Gericke, F. Gerbier, A. Widera, S. Fölling, O. Mandel and I. Bloch, *Adiabatic loading of a Bose-Einstein condensate in a 3D optical lattice*, Journal of Modern Optics **54**, 735 (2007).
- [160] B. Sun and M. S. Pindzola, *Slow collisions of Bose-Einstein condensates in both ground and excited states*, Journal of Physics B: Atomic, Molecular and Optical Physics **41**, 155302 (2008).

- 
- [161] T. L. Gustavson, A. Landragin and M. A. Kasevich, *Rotation sensing with a dual atom-interferometer Sagnac gyroscope*, *Classical and Quantum Gravity* **17**, 2385 (2000).
- [162] J. Polo and V. Ahufinger, *Soliton-based matter-wave interferometer*, *Phys. Rev. A* **88**, 053628 (2013).
- [163] A. L. Gaunt and Z. Hadzibabic, *Robust Digital Holography For Ultracold Atom Trapping*, *Sci. Rep.* **2**, 4091 (2012).
- [164] N. Lundblad, M. Schlosser and J. V. Porto, *Experimental observation of magic-wavelength behavior of Rb87 atoms in an optical lattice*, *Phys. Rev. A* **81**, 031611 (2010).
- [165] J. I. Cirac and P. Zoller, *Quantum Computations with Cold Trapped Ions*, *Phys. Rev. Lett.* **74**, 4091 (1995).
- [166] J. D. Miller, R. A. Cline and D. J. Heinzen, *Photoassociation spectrum of ultracold Rb atoms*, *Phys. Rev. Lett.* **71**, 2204 (1993).
- [167] A. M. Smith, K. Burnett and P. S. Julienne, *Semiclassical theory of collision-induced loss from optical traps*, *Phys. Rev. A* **46**, 4091 (1992).
- [168] E. A. Burt, R. W. Ghrist, C. J. Myatt, M. J. Holland, E. A. Cornell and C. E. Wieman, *Coherence, Correlations, and Collisions: What One Learns about Bose-Einstein Condensates from Their Decay*, *Phys. Rev. Lett.* **79**, 337 (1997).
- [169] M. Schlosser, S. Tichelmann, J. Kruse and G. Birkel, *Scalable architecture for quantum information processing with atoms in optical micro-structures*, *Quantum Information Processing* **10**, 907 (2011).
- [170] A. Lengwenus, J. Kruse, M. Schlosser, S. Tichelmann and G. Birkel, *Coherent Transport of Atomic Quantum States in a Scalable Shift Register*, *Phys. Rev. Lett.* **105**, 170502 (2010).
- [171] M. Schlosser, J. Kruse, C. Gierl, S. Teichmann, S. Tichelmann and G. Birkel, *Fast transport, atom sample splitting and single-atom qubit supply in two-dimensional arrays of optical microtraps*, *New Journal of Physics* **14**, 123034 (2012).
- [172] J. Kruse, C. Gierl, M. Schlosser and G. Birkel, *Reconfigurable site-selective manipulation of atomic quantum systems in two-dimensional arrays of dipole traps*, *Phys. Rev. A* **81**, 060308 (2010).
- [173] A. Lengwenus, *Manipulation der internen und externen Freiheitsgrade neutraler Atome in optischen Mikropotentialen*, Ph.d. dissertation, TU Darmstadt, Darmstadt, (2008).

- 
- [174] S. Teichmann, *Characterizing Microlenses for Optical Dipole Trap Arrays*, Bachelor thesis, TU Darmstadt, Darmstadt, (2008).
- [175] F. Schmaltz, *Charakterisierung von Transportverfahren für Dipolfallenregister*, Bachelor thesis, TU Darmstadt, Darmstadt, (2011).
- [176] D. O. de Mello, *Dynamische Positionierung optischer Mikrofallenregister*, Bachelor thesis, TU Darmstadt, Darmstadt, (2012).
- [177] L. Kreher, *Charakterisierung von Mikrolinsenregistern*, Project report, TU Darmstadt, Darmstadt, (2010).
- [178] M. Volk, *Kalte Atome für die Quanteninformationsverarbeitung*, Ph.d. dissertation, Universität Hannover, Hannover, (2005).
- [179] L. Hohmann, *Untersuchung eines Mikrolinsenregisters*, Project report, TU Darmstadt, Darmstadt, (2010).
- [180] E. Bonet, P. Andrés, J. Barreiro and A. Pons, *Self-imaging properties of a periodic microlens array: versatile array illuminator realization*, Optics Communications **106**, 39 (1994).
- [181] P. Ruffieux, T. Scharf, H. P. Herzig, R. Völkel and K. J. Weible, *On the chromatic aberration of microlenses*, Opt. Express **14**, 4687 (2006).
- [182] L. Isenhower, E. Urban, X. L. Zhang, A. T. Gill, T. Henage, T. A. Johnson, T. G. Walker and M. Saffman, *Demonstration of a Neutral Atom Controlled-NOT Quantum Gate*, Phys. Rev. Lett. **104**, 010503 (2010).
- [183] E. Urban, T. Johnson, T. Henage, L. Isenhower, D. Yavuz, T. G. Walker and M. Saffman, *Observation of Rydberg blockade between two atoms*, Nature **5**, 110 (2009).
- [184] Y. Loiko, V. Ahufinger, R. Menchon-Enrich, G. Birkl and J. Mompert, *Coherent injecting, extracting, and velocity filtering of neutral atoms in a ring trap via spatial adiabatic passage*, The European Physical Journal D **68** (2014).
- [185] T.-L. Ho, *Spinor Bose Condensates in Optical Traps*, Phys. Rev. Lett. **81**, 742 (1998).
- [186] S. Kurtz, in *Nonlinear Optical Materials*, Vol. 1 of *Laser Handbook*, F. Arecchi and E. Schulz-Dubois, eds., (North-Holland, Amsterdam, 1972).
- [187] H. Hellwig, J. Liebertz and L. Bohatý, *Linear optical properties of the monoclinic bismuth borate BiB<sub>3</sub>O<sub>6</sub>*, Journal of Applied Physics **88**, 240 (2000).
- [188] S. Singh, D. A. Draegert and J. E. Geusic, *Optical and Ferroelectric Properties of Barium Sodium Niobate*, Phys. Rev. B **2**, 2709 (1970).

- 
- [189] K. Kato, *Tunable UV generation to 0.185  $\mu\text{m}$  in CsB3O5*, Quantum Electronics, IEEE Journal of **31**, 169 (1995).
- [190] T. Mikami, T. Okamoto and K. Kato, *Sellmeier and thermo-optic dispersion formulas for CsTiOAsO4*, Journal of Applied Physics **109**, (2011).
- [191] D. Eimerl, S. Velsko, L. Davis, F. Wang, G. Loiacono and G. Kennedy, *Deuterated L-arginine phosphate: a new efficient nonlinear crystal*, Quantum Electronics, IEEE Journal of **25**, 179 (1989).
- [192] N. Umemura and K. Kato, *Phase-matched UV generation at 0.1774  $\mu\text{m}$  in KB5O8·4H2O*, Appl. Opt. **35**, 5332 (1996).
- [193] K. Kato, N. Umemura and E. Tanaka, *90° Phase-Matched Mid-Infrared Parametric Oscillation in Undoped KTiOAsO4*, Japanese Journal of Applied Physics **36**, L403 (1997).
- [194] K. Kato and E. Takaoka, *Sellmeier and Thermo-Optic Dispersion Formulas for KTP*, Appl. Opt. **41**, 5040 (2002).
- [195] N. Umemura, K. Yoshida and K. Kato, *Thermo-optic dispersion formula of KNbO3 for mid-infrared OPO*, In *Advanced High-Power Lasers*, O. M., P. H.T. and T. K., eds., Society of Photo-Optical Instrumentation Engineers (SPIE) Conference Series **3889**, 472 (2000).
- [196] K. Kato, *Temperature-tuned 90 deg; phase-matching properties of LiB3 O5*, Quantum Electronics, IEEE Journal of **30**, 2950 (1994).
- [197] Y. Wu, P. Fu, F. Zheng, S. Wan and X. Guan, *Growth of a nonlinear optical crystal La2CaB10O19 (LCB)*, Optical Materials **23**, 373 (2003), proceedings of the 8th International Conference on Electronic Materials, IUMRS-ICEM 2002.
- [198] H. Naito and H. Inaba, *Measurement of the refractive indices of crystalline lithium formate, HCOOLi·H2O*, Opto-electronics **5**, 256 (1973).
- [199] L. Isaenko, A. Yeliseyev, S. Lobanov, A. Titov, V. Petrov, J.-J. Zondy, P. Krinitsin, A. Merkulov, V. Vedenyapin and J. Smirnova, *Growth and properties of LiGaX2 (X = S, Se, Te) single crystals for nonlinear optical applications in the mid-IR*, Crystal Research and Technology **38**, 379 (2003).
- [200] Y. M. Andreev, L. G. Geiko, P. P. Geiko and S. G. Grechin, *Optical properties of a nonlinear LiInS2 crystal*, Quantum Electronics **31**, 647 (2001).
- [201] L. Isaenko, A. Yeliseyev, S. Lobanov, V. Petrov, F. Rotermund, G. Sleky and J.-J. Zondy, *LiInSe2 A biaxial ternary chalcogenide crystal for nonlinear optical applications in the midinfrared*, Journal of Applied Physics **91**, 9475 (2002).

- 
- [202] R. Komatsu, Y. Ono, T. Kajitani, F. Rotermund and V. Petrov, *Optical properties of a new nonlinear borate crystal LiRbB4O7*, Journal of Crystal Growth **257**, 165 (2003).
- [203] S. Singh, in *Nonlinear optical materials, Handbook of Lasers with Selected Data on Optical Technology*, R. Pressley, ed., (Chemical Rubber Co., Cleveland, 1971).
- [204] H. Shen, D. Zhang, W. Liu, W. Chen, G. Zhang, G. Zhang and W. Lin, *Measurement of Refractive Indices and Thermal Refractive-Index Coefficients of 7.5-mol.% Nb KTiOPO4 Crystal*, Appl. Opt. **38**, 987 (1999).
- [205] J. Wang, Z. Shao, J. Wei, X. Hu, Y. Liu, B. Gong, G. Li, J. Lu, M. Guo and M. Jiang, *Research on growth and self-frequency doubling OF Nd:ReCOB (Re=Y OR Gd) crystals*, Progress in Crystal Growth and Characterization of Materials **40**, 17 (2000), symposium L Fifth IUMRS International Conference on Advanced Materials IUMRS-ICAM 99.
- [206] K. Kato, E. Takaoka and N. Umemura, *Thermo-Optic Dispersion Formula for RbTiOAsO4*, Japanese Journal of Applied Physics **42**, 6420 (2003).
- [207] Y. Guillien, B. Ménaert, J. Fève, P. Segonds, J. Douady, B. Boulanger and O. Pacaud, *Crystal growth and refined Sellmeier equations over the complete transparency range of RbTiOPO4*, Optical Materials **22**, 155 (2003).
- [208] N. Umemura, H. Nakao, H. Furuya, M. Yoshimura, Y. Mori, T. Sasaki, KunioYoshida and K. Kato, *90° Phase-Matching Properties of YCa4O(BO3)3 and GdxY1-xCa4O(BO3)3*, Japanese Journal of Applied Physics **40**, 596 (2001).
- [209] P. D. N. P. Nikogosyan, *Nonlinear Optical Crystals: A Complete Survey* (Springer New York, 2005).
- [210] Raspberry Pi, <http://www.raspberrypi.org/>, 2014.
- [211] Raspbian free operating system based on Debian, <http://raspbian.org/>, 2014.
- [212] Debian - The universal operating system, <http://www.debian.org/>, 2014.
- [213] Linux - Operating System, <http://www.linuxfoundation.org>, 2014.
- [214] SCP - Secure copy, <http://nixdoc.net/man-pages/FreeBSD/scp.1.html>, 2014.
- [215] SSH File Transfer Protocol, <http://tools.ietf.org/html/draft-ietf-secsh-filexfer-13>, 2014.
- [216] FileZilla - The free FTP solution, <https://filezilla-project.org/>, 2014.

- 
- [217] S. Albrecht, *Ein Lasersystem zur Spektroskopie von hochgeladenen Ionen, Tellurmolekülen und Rubidium-Rydberg-Zuständen*, Ph.d. dissertation, TU Darmstadt, Darmstadt, (2014).



---

# Publications

T. Lauber, J. Küber, O. Wille, and G. Birkl

*Optimized Bose-Einstein-condensate production in a dipole trap based on a 1070-nm multifrequency laser: Influence of enhanced two-body loss on the evaporation process*, Physical Review A **84**, 043641 (2011).

T. Lauber, J. Küber, F. Schmaltz, J. Mompart, and G. Birkl

*Coherent propagation of Bose-Einstein condensates in a mesoscopic storage ring produced by conical refraction*, (submitted for publication).

J. Küber, F. Schmaltz, and G. Birkl

*Experimental realization of double Bragg diffraction beamsplitters and interferometers with Bose-Einstein condensates*, (to be submitted).

A. Turpin, J. Polo, Yu. V. Loiko, J. Küber, F. Schmaltz, T.K. Kalkandjiev, G. Birkl, V. Ahufinger, and J. Mompart

*Blue-detuned optical ring trap for Bose-Einstein condensates based on conical refraction*, (to be submitted).

J. Küber, T. Lauber, F. Schmaltz, and G. Birkl

*Experimental characterization of a one-dimensional ring-shaped dipole trap for ultra-cold atoms and Bose-Einstein Condensates created by conical refraction*, (in preparation).

J. Küber, A. Turpin, F. Schmaltz, J. Mompart, and G. Birkl

*Trapping of Bose-Einstein condensates in a dark focus trap generated by conical refraction*, (in preparation).



---

# Curriculum Vitae

## Personal Information

Johannes Stephan Peter Küber  
born on 14. July 1985  
in Frankfurt am Main

## Promotion

Nov. 2009 - Jul. 2014    Group of Prof. Birkl at Technische Universität Darmstadt, Germany  
Title: Dynamics of Bose-Einstein condensates in novel optical potentials

## Academic Studies

Mar. 2009 - Apr. 2009    Research visit at the Division of Physics and Applied Physics in the group of Prof. Dumke at Nanyang Technological University, Singapore

Sept. 2008 - Sept. 2009    Master Thesis in the group of Prof. Birkl at Technische Universität Darmstadt, Germany  
Title: Bose-Einstein condensates in one-dimensional optical lattices

Apr. 2008 - Sept. 2009    Master of Science at Technische Universität Darmstadt, Germany

Sept. 2007 - Nov. 2007    Bachelor Thesis in the group of Prof. Birkl at Technische Universität Darmstadt, Germany  
Title: Frequency stabilisation of a diode laser by stimulated magnetic field modulation

Oct. 2004 - Mar. 2008    Bachelor of Science  
Technische Universität Darmstadt, Germany

## Civilian Service

Aug. 2003 - Jun. 2004    Heilig Kreuz Gemeinde, Frankfurt am Main

## High School

Aug. 1995 - Jul. 2003    German diploma for university admission (Abitur)  
Edith-Stein Schule, Darmstadt, Germany



---

# Acknowledgements

Am Ende dieser Arbeit bleibt mir noch die große Freude mich bei den Leuten zu bedanken, die zum Gelingen dieser Arbeit beigetragen haben:

Bei Prof. Dr. Gerhard Birkl möchte ich mich in aller Form dafür bedanken, dass ich in seiner Arbeitsgruppe und unter seiner Leitung meine Forschungen zu dieser Dissertation durchführen konnte. Sein unablässiges Engagement schafft ein äußerst leistungsfähiges und angenehmes Arbeitsklima und die stets offene Tür ermöglicht einen sehr fruchtbaren Ideenaustausch. Die unzähligen wissenschaftlichen Diskussionen und der offene Meinungsaustausch tragen einen großen Anteil am Erfolg dieser Arbeit.

Bei Prof. Dr. Thomas Walther möchte ich mich für die Übernahme des Zweitgutachtens sowie die sympathische, unkomplizierte und sehr erfolgreiche Zusammenarbeit der letzten Jahre bedanken. Des Weiteren danke ich Prof. Walser sowie Prof. Vogel für den gemeinsamen Austausch zu meiner Arbeit.

Im Besonderen geht mein Dank an alle Vorgänger im ATOMICS Team, welche mir ein tolles Experiment hinterlassen haben. Die Zeit mit Oli und Thomas im Labor war nicht nur erfolgreich, sondern auch eine der Lehrreichsten in meinem Leben. Vielen Dank dafür. Ebenfalls möchte ich der aktuellen ATOMICS Besatzung danken. Allen voran Felix, ohne dessen Hilfe im Labor diese Arbeit nicht fertig geworden wäre. Ich wünsche dir viel Erfolg; jetzt bist du dran! Unserem Gast aus Barcelona, Alex, möchte ich für all das danken, was er innerhalb von nur drei Monaten auf die Beine gestellt hat. ¡Muchas gracias a barcelona! Ebenfalls danken möchte ich den weiteren Studenten am ATOMICS Experiment: Dominik Lohrey, Martin Hasch, Roman Sultzbach, Alexander Papak, Felix Sommer, Lutz Görden sowie Jörg Hoppe.

Ebenfalls bedanke ich mich bei der kompletten Arbeitsgruppe für all die Jahre der erfolgreichen Zusammenarbeit. Zu jeder Zeit konnte man die Ohren offen für Probleme und Ideen. Sei es im Labor, auf Tagungen oder bei völlig unphysikalischen Dingen. Im Besonderen möchte ich danken: mit euch war es nie langweilig! Vielen Dank Seppo, Sascha, Jan, Jens und Malte.

Ebenso möchte ich den fleißigen Helfern danken, die diese Arbeitsgruppe zusammenhalten. Durch ihre organisatorischen und fachlichen Fähigkeiten

---

wäre das Chaos das wir jeden Tag bekämpfen nicht zu bewältigen. An dieser Stelle besonders nennen möchte ich Gabi; die gute Seele der Arbeitsgruppe. An Herr Baumann und Herr Kringel von der Elektronikwerkstatt sowie an Herr Schmutzler von der Computerwerkstatt geht mein Dank für die langjährige unkomplizierte und erfolgreiche Zusammenarbeit. Beim kompletten Team der Feinmechanikwerkstatt, unter Leitung von Herr Kalbfleisch und Herr Weick, bedanke ich mich für die hervorragende und überaus schnelle Arbeit an sämtlichen Mechanikproblemen unserer Labore.

Des Weiteren möchte ich denen danken, die mit mir seit dem ersten Semester das Studium verbracht haben. Erstaunlich, das wir es alle auf die andere Seite geschafft haben. Sei es beim Lernen, Feiern, Lachen, Fluchen, Urlaub machen, diskutieren oder beim Ideenaustausch. Vielen Dank Tobi, Michel, Simon, Benni, Moritz und Basti. Ein weiterer Dank geht an die Leute, die zusammen mit mir die Promotion durchgestanden haben: Kamill, Alex, Stoppi, Stephan, Ben, Enzo und dem Metallager0031!

Ebenso möchten ich den Leuten danken, die mich seit meiner Schulzeit begleiten, und die durch ihre Einzigartigkeit dafür sorgen, dass sich meine Gedanken auch mal um andere Dinge drehen als Physik: Dirk, Stefan, Harry, Maike, Flo, Ingo, Martin, Christoph, Seppl und Steini.

Bei Alina möchte ich mich für die Unterstützung in dieser stressigen Zeit bedanken und ich freue mich darauf mit dir in Zukunft die Welt zusammen zu bereisen. Abschließend möchte ich meinen Eltern danken. Die Wurzeln und Flügel die sie mir geben haben, haben es mir ermögliehe mein Leben nach meinen Vorstellungen zu gestalten. Ohne sie wäre diese Arbeit nicht möglich gewesen. Vielen Dank.

---

# Erklärung zur Dissertation

Hiermit versichere ich, die vorliegende Dissertation ohne Hilfe Dritter nur mit den angegebenen Quellen und Hilfsmitteln angefertigt zu haben. Alle Stellen, die aus Quellen entnommen wurden, sind als solche kenntlich gemacht. Diese Arbeit hat in gleicher oder ähnlicher Form noch keiner Prüfungsbehörde vorgelegen.

Darmstadt, den 12. September 2014

---

(Johannes Küber, MSc)